

## ABSTRACT

### Experimental Investigation of Full Coverage Combustor Film Cooling and Airfoil Film Cooling for Advanced Gas Turbine Engines

Kyle R. Vinton, M.S.M.E.

Mentor: Lesley M. Wright, Ph.D.

Film cooling in modern gas turbine engines uses coolant from the compressor to protect the surface of the combustor lining and turbine airfoils from the hot mainstream gas. Pressure sensitive paint (PSP) is used to evaluate the effects of effusion cooling and hole shape for combustion film cooling. Results show that increasing row interaction increases superposition and lateral spreading of the coolant. PSP and stereoscopic particle image velocimetry (S-PIV) are used to investigate the effect of favorable pressure gradients and hole shape for turbine airfoil film cooling. Three-dimensional velocity and vorticity distributions obtained with S-PIV are coupled with the film cooling effectiveness distributions determined with PSP for six film cooling geometries. Results show that a favorable pressure gradient reduces jet separation and increases lateral spreading of coolant. Furthermore, adding contours to the hole shape can generate additional anti-kidney vortices and adding a racetrack shaped inlet improved film cooling effectiveness.

Experimental Investigation of Full Coverage Combustor Film Cooling and Airfoil Film Cooling  
for Advanced Gas Turbine Engines

by

Kyle R. Vinton, B.S.M.E.

A Thesis

Approved by the Department of Mechanical Engineering

---

Kenneth Van Treuren, Ph.D., Chairperson

Submitted to the Graduate Faculty of  
Baylor University in Partial Fulfillment of the  
Requirements for the Degree  
of

Master of Science in Mechanical Engineering

Approved by the Thesis Committee

---

Lesley M. Wright, Ph.D., Chairperson

---

Stephen T. McClain, Ph.D.

---

John M. Davis, Ph.D.

Accepted by the Graduate School

May 2017

---

J. Larry Lyon, Ph.D., Dean

Copyright © 2017 by Kyle R. Vinton

All rights reserved

## TABLE OF CONTENTS

LIST OF FIGURES .....	viii
LIST OF TABLES .....	xviii
NOMENCLATURE .....	xix
ACKNOWLEDGMENTS .....	xxiii
DEDICATION .....	xxvi
CHAPTER ONE .....	1
Introduction .....	1
General Gas Turbine Theory .....	1
Modern Gas Turbine Cooling Overview .....	3
Objectives of Study .....	11
CHAPTER TWO .....	13
Literature Review .....	13
Coolant-to-mainstream flow conditions .....	13
Effects of Hole Angle .....	17
Effect of Hole Shape .....	20
Effect of Freestream Pressure Gradient .....	34
Full Coverage Film Cooling .....	38
Flow Trends .....	41
CHAPTER THREE .....	45

Pressure Sensitive Paint for Film Cooling	45
Effectiveness Measurements	
General Film Cooling Measurement Background	45
Optical Film Cooling Effectiveness	46
Measurement Techniques	
Mass Transfer Film Cooling Measurement Techniques	49
General PSP Background	52
Literature Review of PSP for Film Cooling	53
PSP Experimental Procedure	54
Uncertainty Analysis	57
CHAPTER FOUR	59
Stereoscopic Particle Image Velocimetry in Film	59
Cooling Flows	
General PIV Background	59
General S-PIV Background	63
Experimental Technique and Uncertainty Analysis	67
CHAPTER FIVE	71
Experimental Setup for Combustor Liner Cooling	71
Overview of Experimental Facility	71
Flow Conditions	72
Combustor Cooling Coupon Details	73
CHAPTER SIX	76
Experimental Setup for Airfoil Cooling	76
Overview of Experimental Facility	76
Baseline Round Geometry	79

Base Diffuser-Shaped Geometry .....	80
Honeywell Shaped Geometries .....	82
Duck Foot Geometries .....	84
CHAPTER SEVEN .....	87
Combustor Liner Cooling Results .....	87
Validation of PSP for Full Coverage Film Cooling .....	87
Baseline Round Results .....	104
Baseline Shape Results .....	107
Double Hole Results .....	113
Comparison of Three Geometries .....	117
Summary of Effects .....	120
CHAPTER EIGHT .....	123
Film Cooling with Shaped Holes and FPG .....	123
Round Hole PSP Results .....	124
Round Hole S-PIV Results .....	130
Laidback, Fanshaped Hole PSP Results .....	135
Laidback, Fanshaped Hole S-PIV Results .....	141
Baseline Conclusions .....	147
Advanced Cooling Shapes .....	148
Honeywell Shaped 1 PSP Results .....	149
Honeywell Shaped 1 S-PIV Results .....	153
Honeywell Shaped 2 PSP Results .....	159
Honeywell Shaped 2 S-PIV Results .....	165

Duck Foot 1 PSP Results	.....	170
Duck Foot 1 S-PIV Results	.....	175
Duck Foot 2 PSP Results	.....	181
Duck Foot 2 S-PIV Results	.....	188
Summary of Effects	.....	195
CHAPTER NINE	.....	212
Conclusions	.....	212
Combustor Film Cooling	.....	212
Turbine Airfoil Film Cooling	.....	214
Future Recommendations	.....	217
APPENDIX A	.....	220
CAD Model of Round Combustor Cooling Coupon	.....	220
APPENDIX B	.....	221
CAD Models of Round and Laidback, Fanshaped Film Cooling Holes	.....	221
APPENDIX C	.....	223
PSP Data Analysis	.....	223
APPENDIX D	.....	238
Detailed PSP Uncertainty Analysis	.....	238
APPENDIX E	.....	247
S-PIV Uncertainty Analysis	.....	247
REFERENCES	.....	250

## LIST OF FIGURES

Figure 1.1: ALF502 turbofan developed by Honeywell (courtesy of Honeywell) .....	2
Figure 1.2: Specific core power increase due to RIT [1] .....	3
Figure 1.3: Internal cooling techniques for turbine airfoils [1] .....	6
Figure 1.4: External cooling techniques for turbine airfoils [1] .....	7
Figure 1.5: Illustration of film cooling .....	8
Figure 1.6: Illustration of film cooling jet [2] .....	9
Figure 2.1: Simple angle round hole with $\theta = 35^\circ$ .....	18
Figure 2.2: Round, compound angle holes at $\beta = 0^\circ$ and $\beta = 60^\circ$ [15] .....	19
Figure 2.3: Illustration of cylindrical, shaped, and fanshaped film cooling holes [3] .....	21
Figure 2.4: Schematic angled slot-hole film cooling [17] .....	22
Figure 2.5: Illustration of kidney pair and anti-kidney pair vortices produced by shaped hole [25] .....	26
Figure 2.6: Trenched hole configurations studied by Lu et al. [27] .....	27
Figure 2.7: Cratered hole configurations studied by Lu et al. [30] .....	29
Figure 2.8: Console hole configuration investigated by Sargison et al. [30] .....	27
Figure 2.9: Double jet film cooling hole geometry investigated by Wright et al. [32] .....	30
Figure 2.10: Antivortex geometries created by Heidmann and Ekkad [33] .....	31
Figure 2.11: Variation of antivortex geometries created by Leblanc et al. [35] .....	32

Figure 2.12: Asymmetric antivortex geometries created by Chi et al. [36]	.....	33
Figure 2.13: Louver (a), Dumbbell (b), Fanshaped (c), and Crescent (d) shaped hole geometries investigated by Kim et al. [37]	.....	34
Figure 2.14: Arrowhead-Shaped hole created by Okita and Nishiura [38]	.....	35
Figure 2.15: Selected trenched hole geometries from US 20130315710 A1 [39]	.....	36
Figure 2.16: Selected Multi Lobed Hole geometries from WO 2013165510 A31 [40]	.....	37
Figure 2.17: Example of effusion cooling used for combustor liner cooling [47]	.....	38
Figure 3.1: Fundamental principle of TLC paint [59]	.....	46
Figure 3.2: Experimental setup and calibration curve for TSP [64]	.....	49
Figure 3.3: Experimental setup for foreign-gas sampling [9]	.....	50
Figure 3.4: Calibration and sample ammonia-diazo trace [70]	.....	51
Figure 3.5: Fundamentals of PSP operation [2]	.....	52
Figure 3.6: PSP calibration setup	.....	55
Figure 3.7: PSP calibration curve	.....	56
Figure 3.8: Overview of the low speed wind tunnel with PSP experimental equipment	.....	57
Figure 4.1: Velocity field production from interrogation regions [59]	.....	61
Figure 4.2: 2D-PIV experimental setup [59]	.....	62
Figure 4.3: Camera orientation for S-PIV [59]	.....	64
Figure 4.4: Illustration of the Schiempflug adaptor [59]	.....	65
Figure 4.5: Overview of the low speed wind tunnel with S-PIV experimental equipment	.....	67
Figure 5.1: Low speed wind tunnel for effusion film cooling investigations	.....	71

Figure 5.2: Details of baseline round hole configuration	73
Figure 5.3: Shaped effusion film cooling coupon	74
Figure 5.4: Double hole effusion film cooling coupon	75
Figure 6.1: Low speed wind tunnel for film cooling investigations	76
Figure 6.2: Pressure gradient insert in wind tunnel	78
Figure 6.3: Validation of FPG insert	79
Figure 6.4: Baseline, simple angle, round hole	80
Figure 6.5: Laidback, fanshaped hole	81
Figure 6.6: Honeywell Shaped 1 – round inlet	82
Figure 6.7: Honeywell Shaped 2 – racetrack inlet	83
Figure 6.8: Duck Foot 1 – round inlet	85
Figure 6.9: Duck Foot 2 – racetrack inlet	86
Figure 7.1: Film cooling effectiveness distributions for all blowing ratios	88
Figure 7.2: Centerline film cooling effectiveness for all blowing ratios	91
Figure 7.3: Laterally averaged film cooling effectiveness for all blowing ratios	92
Figure 7.4: Local film cooling effectiveness for all blowing ratios at varying streamwise locations	93
Figure 7.5: Overall, area averaged film cooling effectiveness for all blowing ratios	95
Figure 7.6: Literature comparison for lateral average film cooling effectiveness for blowing ratios ranging from $M = 0.5$ to $3.0$	96
Figure 7.7: Sample of plate surface roughness	99
Figure 7.8: Sample roughness on the interior of holes	100
Figure 7.9: Centerline effectiveness comparison for DMLS and Objet ABS test plates	102

Figure 7.10 Film cooling effectiveness distributions for round holes at engine realistic blowing ratios .....	105
Figure 7.11: Centerline film cooling effectiveness for round holes at engine realistic blowing ratios .....	107
Figure 7.12: Laterally averaged film cooling effectiveness for round holes at engine realistic blowing ratios .....	108
Figure 7.13: Film cooling effectiveness distributions for shaped holes at engine realistic blowing ratios .....	110
Figure 7.14: Centerline film cooling effectiveness for shaped holes at engine realistic blowing ratios .....	111
Figure 7.15: Laterally averaged film cooling effectiveness for shaped holes at engine realistic blowing ratios .....	112
Figure 7.16: Film cooling effectiveness distributions for double holes at engine realistic blowing ratios .....	114
Figure 7.17: Centerline film cooling effectiveness for double holes at engine realistic blowing ratios .....	115
Figure 7.18: Lateral average film cooling effectiveness for double holes at engine realistic blowing ratios .....	116
Figure 7.19: Lateral average film cooling effectiveness for all three shapes for $M = 6.0$ .....	117
Figure 7.20: Local film cooling effectiveness for all three shapes for $M = 6.0$ at $y/d = 2.45$ .....	118
Figure 8.1: Round hole film cooling effectiveness distribution under a favorable pressure gradient: blowing ratio effect .....	124
Figure 8.2: Round hole centerline and laterally averaged film cooling effectiveness under a favorable pressure gradient: blowing ratio effect .....	125
Figure 8.3: Round hole film cooling effectiveness distribution under a favorable pressure gradient: density ratio effect .....	126
Figure 8.4: Round hole centerline and laterally averaged film cooling effectiveness under a favorable pressure gradient: density ratio effect .....	127

Figure 8.5: Round hole film cooling effectiveness distributions: FPG effect	.....	128
Figure 8.6: Round hole overall average film cooling effectiveness: FPG effect	.....	129
Figure 8.7: Effect of blowing ratio and freestream acceleration for round holes ( $x/d = DSE$ , $DR = 1.0$ )	.....	130
Figure 8.8: Influence of flow vorticity on surface film cooling effectiveness from round holes ( $x/d = DSE$ , $DR = 1.0$ )	.....	132
Figure 8.9: Effect of density ratio and freestream acceleration for round holes ( $x/d = DSE$ , $M = 1.5$ )	.....	133
Figure 8.10: Influence of flow vorticity on surface film cooling effectiveness from round holes ( $x/d = DSE$ , $M = 1.5$ )	.....	134
Figure 8.11: Effect of downstream location and freestream acceleration for round holes ( $M = 1.5$ , $DR = 1.0$ )	.....	135
Figure 8.12: Influence of flow vorticity on surface film cooling effectiveness from round holes ( $M = 1.5$ , $DR = 1.0$ )	.....	136
Figure 8.13: Shaped hole film cooling effectiveness distribution under a favorable pressure gradient: blowing ratio effect	.....	137
Figure 8.14: Shaped hole centerline and laterally averaged film cooling effectiveness under a favorable pressure gradient: blowing ratio effect	.....	138
Figure 8.15: Shaped hole film cooling effectiveness distribution under a favorable pressure gradient: density ratio effect	.....	139
Figure 8.16: Shaped hole centerline and laterally averaged film cooling effectiveness under a favorable pressure gradient: density ratio effect	.....	140
Figure 8.17: Shaped hole film cooling effectiveness distributions: FPG effect	.....	141
Figure 8.18: Shaped hole overall average film cooling effectiveness: FPG effect	.....	142
Figure 8.19: Comparison of baseline shaped and round with laterally averaged effectiveness under FPG	.....	143

Figure 8.20: Favorable pressure gradient overall average film cooling effectiveness: shape effect	.....	144
Figure 8.21: Effect of blowing ratio and freestream acceleration for shaped holes ( $x/d = DSE$ , $DR = 1.0$ )	.....	145
Figure 8.22: Influence of flow vorticity on surface film cooling effectiveness from shaped holes ( $x/d = DSE$ , $DR = 1.0$ )	.....	146
Figure 8.23: Effect of density ratio and freestream acceleration for shaped holes ( $x/d = DSE$ , $M = 1.5$ )	.....	147
Figure 8.24: Influence of flow vorticity on surface film cooling effectiveness from shaped holes ( $x/d = DSE$ , $M = 1.5$ )	.....	148
Figure 8.25: Effect of downstream location and freestream acceleration for shaped holes ( $M = 1.5$ , $DR = 1.0$ )	.....	149
Figure 8.26 Influence of flow vorticity on surface film cooling effectiveness from shaped holes ( $M = 1.5$ , $DR = 1.0$ )	.....	150
Figure 8.27: Comparison of round and shaped holes for varying blowing ratio ( $x/d = DSE$ , $DR = 1.0$ , FPG)	.....	151
Figure 8.28: Comparison of round and shaped holes through the influence of flow vorticity on surface film cooling effectiveness ( $x/d = DSE$ , $DR = 1.0$ , FPG)	.....	152
Figure 8.29: Honeywell Shaped 1 hole film cooling effectiveness distribution under a favorable pressure gradient: blowing ratio effect	.....	153
Figure 8.30: Honeywell Shaped 1 centerline and laterally averaged film cooling effectiveness under a favorable pressure gradient: blowing ratio effect	.....	154
Figure 8.31: Honeywell Shaped 1 hole film cooling effectiveness distribution under a favorable pressure gradient: density ratio effect	.....	155
Figure 8.32: Honeywell Shaped 1 hole centerline and laterally averaged film cooling effectiveness under a favorable pressure gradient: density ratio effect	.....	156
Figure 8.33: Honeywell Shaped 1 film cooling effectiveness distributions: FPG effect	.....	157

Figure 8.34: Honeywell Shaped 1 overall average film cooling effectiveness: FPG effect	158
Figure 8.35: Comparison of baseline shaped and HWS1 with laterally averaged effectiveness under FPG	159
Figure 8.36: Comparison of HWS1 and shaped with overall average film cooling effectiveness	160
Figure 8.37: Effect of blowing ratio and freestream acceleration for Honeywell Shaped 1 hole ( $x/d = DSE$ , $DR = 1.0$ )	161
Figure 8.38: Influence of flow vorticity on surface film cooling effectiveness from Honeywell Shaped 1 ( $x/d = DSE$ , $DR = 1.0$ )	162
Figure 8.39: Effect of density ratio and freestream acceleration for Honeywell Shaped 1 holes ( $x/d = DSE$ , $M = 1.5$ )	163
Figure 8.40: Influence of flow vorticity on surface film cooling effectiveness from Honeywell Shaped 1 holes ( $x/d = DSE$ , $M = 1.5$ )	164
Figure 8.41: Effect of downstream location and freestream acceleration for Honeywell Shaped 1 ( $M = 1.5$ , $DR = 1.0$ )	165
Figure 8.42: Influence of flow vorticity on surface film cooling effectiveness from Honeywell Shaped 1 holes ( $M = 1.5$ , $DR = 1.0$ )	166
Figure 8.43: Comparison of HWS1 and shaped holes for varying blowing ratio ( $x/d = DSE$ , $DR = 1.0$ , FPG)	167
Figure 8.44: Comparison of round and shaped holes through the influence of flow vorticity on surface film cooling effectiveness ( $x/d = DSE$ , $DR = 1.0$ , FPG)	168
Figure 8.45: Honeywell Shaped 2 hole film cooling effectiveness distribution under a favorable pressure gradient: blowing ratio effect	169
Figure 8.46: Honeywell Shaped 2 centerline and lateral average film cooling effectiveness under a favorable pressure gradient: blowing ratio effect	170
Figure 8.47: Honeywell Shaped 2 hole film cooling effectiveness distribution under a favorable pressure gradient: density ratio effect	171

Figure 8.48: Honeywell Shaped 2 hole centerline and laterally averaged film cooling effectiveness under a favorable pressure gradient: density ratio effect	....	172
Figure 8.49: Honeywell Shaped 2 film cooling effectiveness distributions: FPG effect	.....	173
Figure 8.50: Honeywell Shaped 2 overall average film cooling effectiveness: FPG effect	.....	174
Figure 8.51: Favorable pressure gradient lateral average film cooling effectiveness: Inlet shape effect	.....	175
Figure 8.52: Comparison of HWS1 and HWS2 with overall average film cooling effectiveness	.....	176
Figure 8.53: Effect of blowing ratio and freestream acceleration for Honeywell Shaped 2 hole ( $x/d = DSE$ , $DR = 1.0$ )	.....	177
Figure 8.54: Influence of flow vorticity on surface film cooling effectiveness from Honeywell Shaped 2 ( $x/d = DSE$ , $DR = 1.0$ )	....	178
Figure 8.55: Effect of density ratio and freestream acceleration for Honeywell Shaped 2 holes ( $x/d = DSE$ , $M = 1.5$ )	.....	179
Figure 8.56: Influence of flow vorticity on surface film cooling effectiveness from Honeywell Shaped 2 holes ( $M = 1.5$ , $DR = 1.0$ )	.....	180
Figure 8.57: Effect of downstream location and freestream acceleration for Honeywell Shaped 2 ( $M = 1.5$ , $DR = 1.0$ )	.....	181
Figure 8.58: Influence of flow vorticity on surface film cooling effectiveness from Honeywell Shaped 2 holes ( $M = 1.5$ , $DR = 1.0$ )	.....	182
Figure 8.59: Comparison of HWS1 and HWS2 holes for varying blowing ratio ( $x/d = DSE$ , $DR = 1.0$ , FPG)	.....	183
Figure 8.60: Comparison of HWS1 and HWS2 holes through the influence of flow vorticity on surface film cooling effectiveness ( $x/d = DSE$ , $DR = 1.0$ , FPG)	.....	184
Figure 8.61: Duckfoot 1 hole film cooling effectiveness distribution under a favorable pressure gradient: blowing ratio effect	.....	185

Figure 8.62: Duckfoot 1 centerline and lateral average film cooling effectiveness under a favorable pressure gradient: blowing ratio effect	.....	186
Figure 8.63: Duckfoot 1 hole film cooling effectiveness distribution under a favorable pressure gradient: density ratio effect	.....	187
Figure 8.64: Duckfoot 1 hole centerline and lateral average film cooling effectiveness under a favorable pressure gradient: density ratio effect	.....	188
Figure 8.65: Duckfoot 1 film cooling effectiveness distributions: FPG effect	.....	189
Figure 8.66: Duckfoot 1 overall average film cooling effectiveness: FPG effect	.....	190
Figure 8.67: Favorable pressure gradient laterally averaged film cooling effectiveness: Duckfoot outlet effect	.....	191
Figure 8.68: Comparison of HWS1 and DF1 with overall average film cooling effectiveness	.....	192
Figure 8.69: Effect of blowing ratio and freestream acceleration for Duckfoot 1 hole ( $x/d = DSE$ , $DR = 1.0$ )	.....	193
Figure 8.70: Influence of flow vorticity on surface film cooling effectiveness from Duckfoot 1 ( $x/d = DSE$ , $DR = 1.0$ )	.....	194
Figure 8.71: Effect of density ratio and freestream acceleration for Duckfoot 1 holes ( $x/d = DSE$ , $M = 1.5$ )	.....	195
Figure 8.72: Influence of flow vorticity on surface film cooling effectiveness from Duckfoot 1 holes ( $M = 1.5$ , $DR = 1.0$ )	.....	196
Figure 8.73: Effect of downstream location and freestream acceleration for Duckfoot 1 ( $M = 1.5$ , $DR = 1.0$ )	.....	197
Figure 8.74: Influence of flow vorticity on surface film cooling effectiveness from Duckfoot 1 holes ( $M = 1.5$ , $DR = 1.0$ )	.....	198
Figure 8.75: Comparison of HWS1 and DF1 holes for varying blowing ratio ( $x/d = DSE$ , $DR = 1.0$ , FPG)	.....	199
Figure 8.76: Comparison of HWS1 and DF1 holes through the influence of flow vorticity on surface film cooling effectiveness ( $x/d = DSE$ , $DR = 1.0$ , FPG)	.....	200

Figure 8.77: Duckfoot 2 hole film cooling effectiveness distribution under a favorable pressure gradient: blowing ratio effect	.....	201
Figure 8.78: Duckfoot 2 centerline and lateral average film cooling effectiveness under a favorable pressure gradient: blowing ratio effect	.....	201
Figure 8.79: Duckfoot 2 hole film cooling effectiveness distribution under a favorable pressure gradient: density ratio effect	.....	202
Figure 8.80: Duckfoot 2 hole centerline and lateral average film cooling effectiveness under a favorable pressure gradient: density ratio effect	.....	202
Figure 8.81: Duckfoot 2 film cooling effectiveness distributions: FPG effect	.....	203
Figure 8.82: Duckfoot 2 overall average film cooling effectiveness: FPG effect	.....	203
Figure 8.83: Favorable pressure gradient lateral average film cooling effectiveness: Inlet shape effect	.....	204
Figure 8.84: Figure 8.84: Comparison of DF1 and DF2 with overall average film cooling effectiveness	.....	205
Figure 8.85: Favorable pressure gradient lateral average film cooling effectiveness: Duckfoot effect	.....	205
Figure 8.86: Comparison of DF2 and HWS2 with overall average film cooling effectiveness	.....	206
Figure 8.87: Effect of blowing ratio and freestream acceleration for Duckfoot 2 hole ( $x/d = DSE$ , $DR = 1.0$ )	.....	206
Figure 8.88: Influence of flow vorticity on surface film cooling effectiveness from Duckfoot 2 ( $x/d = DSE$ , $DR = 1.0$ )	.....	207
Figure 8.89: Effect of density ratio and freestream acceleration for Duckfoot 2 holes ( $x/d = DSE$ , $M = 1.5$ )	...	207
Figure 8.90: Influence of flow vorticity on surface film cooling effectiveness from Duckfoot 2 holes ( $M = 1.5$ , $DR = 1.0$ )	.....	208
Figure 8.91: Effect of downstream location and freestream acceleration for Duckfoot 2 ( $M = 1.5$ , $DR = 1.0$ )	.....	208

Figure 8.92: Influence of flow vorticity on surface film cooling effectiveness from Duckfoot 2 holes ( $M = 1.5$ , $DR = 1.0$ )	.....	209
Figure 8.93: Comparison of DF2 and DF1 holes for varying blowing ratio ( $x/d = DSE$ , $DR = 1.0$ , FPG)	.....	209
Figure 8.94: Comparison of DF1 and DF2 holes through the influence of flow vorticity on surface film cooling effectiveness ( $x/d = DSE$ , $DR = 1.0$ , FPG)	.....	210
Figure 8.95: Comparison of HWS2 and DF2 holes for varying blowing ratio ( $x/d = DSE$ , $DR = 1.0$ , FPG)	.....	210
Figure 8.96: Comparison of DF2 and HWS2 holes through the influence of flow vorticity on surface film cooling effectiveness ( $x/d = DSE$ , $DR = 1.0$ , FPG)	.....	211
Figure A.1: CAD drawing of round combustor cooling coupon	.....	220
Figure B.1: CAD drawing of round film cooling hole plate	.....	221
Figure B.2: CAD drawing of laidback, fanshaped film cooling hole	.....	222
Figure D.1: Derivation of film cooling effectiveness in terms of measured effectiveness	.....	238
Figure D.2: Derivation of uncertainty as a function of measured intensity	.....	239
Figure D.3: Partial derivatives used to calculate uncertainty	.....	240
Figure D.4: Determination of percent uncertainty	.....	241
Figure D.5: Film cooling effectiveness and percent uncertainty	.....	241
Figure E.1: S-PIV uncertainty processing	.....	247
Figure E.2: Uncertainty in streamwise velocity	.....	248
Figure E.3: Uncertainty in lateral velocity	.....	248
Figure E.4: Uncertainty in normal velocity	.....	249

## LIST OF TABLES

Table 6.1: Momentum flux ratio equivalents of the density and blowing ratios used for this study .....	77
Table 7.1: Details of previous effusion cooling investigations .....	97

## NOMENCLATURE

$A$	Cross sectional area of film cooling hole inlet
$C_{fg}$	Oxygen concentration in foreign gas
$C_{Mix}$	Oxygen concentration in mainstream and coolant mixture
$C_{\infty}$	Oxygen concentration in mainstream
CFD	Computational fluid dynamics
$cl$	Centerline
CVP	Counter-rotating vortex pair
$d$	Film cooling hole diameter
DF1	Duck foot 1 film cooling hole
DF2	Duck foot 2 film cooling hole
DJFC	Double jet film cooling
$DR$	Density ratio, $\rho_c / \rho_m$
DSE	Downstream edge
EDM	Electrical discharge machining
$f$	Focal length
FPG	Favorable pressure gradient
$h$	Heat transfer coefficient
HSI	Hue, saturation, intensity
HWS1	Honeywell shaped 1 film cooling hole
HWS2	Honeywell shaped 2 film cooling hole

$I$	Momentum flux ratio, $\rho_c V_c^2 / \rho_m V_m^2$
$I$	Intensity
$I_{ref}$	Reference intensity
$I_b$	Intensity of black images
$I(P)_{ref}$	Intensity of reference images
$I(P)$	Intensity of coolant injection images
IRT	Infrared Thermography
$K$	Acceleration parameter
$L$	Hole interior length
LDA	Laser Doppler anemometry
LDV	Laser Doppler velocimetry
$M$	Blowing ratio, $\rho_c V_c / \rho_m V_m$
MRV	Magnetic resonance velocimetry
$n$	Number of samples for area averaged, mainstream velocity
$N$	Number of samples for mean velocity calculations
$P$	Pressure
$P_{ref}$	Reference pressure
$(P_{O_2})_{Air}$	Partial pressure of oxygen with air as coolant
$(P_{O_2})_{Mix}$	Partial pressure of oxygen with foreign gas as coolant
PIV	Particle image velocimetry
PSP	Pressure sensitive paint
RGB	Red, green, blue
RIT	Rotor inlet temperature

RMS	Root mean squared
$s$	Point of intersection between lens, image and object plane
$S$	Streamwise coordinate
SEM	Scanning electron microscope
$S-PIV$	Stereoscopic-particle image velocimetry
$T$	Temperature observed
$T_{ref}$	Reference temperature
$T_c$	Coolant temperature
$T_w$	Adiabatic wall temperature
$T_\infty$	Mainstream temperature
TBC	Thermal barrier coating
TLC	Thermochromic liquid crystal
TSP	Temperature sensitive paint
$Tu$	Turbulence intensity
$\bar{u}$	Local time averaged velocity of coolant in x-direction
$U_c$	Average coolant velocity
$u_i$	Instantaneous velocity in x-direction
$U_m$	Average mainstream velocity
$u'_{RMS}$	Local velocity fluctuation of coolant in x-direction
$\bar{v}$	Local time averaged velocity of coolant in y-direction
$v_i$	Instantaneous velocity in y-direction
$V$	Local time averaged velocity magnitude
$V_{avg}$	Area averaged, time averaged velocity of mainstream

$V_r$	Velocity ratio
$\bar{w}$	Local time averaged velocity of coolant in z-direction
$w_i$	Instantaneous velocity in z-direction
$x$	Streamwise distance along the flat plate
$y$	Spanwise distance along the flat plate
$z$	Normal distance from the flat plate
ZPG	Zero pressure gradient
$\alpha$	Fanshaped angle
$\beta$	Compound angle
$\gamma$	Laidback angle
$\varepsilon$	Roughness height
$\eta$	Film cooling effectiveness
$\bar{\eta}$	Laterally averaged film cooling effectiveness
$\overline{\bar{\eta}}$	Overall averaged film cooling effectiveness
$\eta_{CL}$	Centerline film cooling effectiveness
$\theta$	Streamwise inclination of the film hole
$\rho_c$	Coolant density
$\rho_m$	Mainstream density
$\omega$	Streamwise vorticity

## ACKNOWLEDGMENTS

The thesis that lies before you is the culmination of 18 months of hard work, but the credit for this work belongs first and foremost to Jesus Christ. The passion, talent, desire to work hard, curiosity, and perseverance required to complete this work are entirely derived from my heavenly Father. I also know that there are numerous other people who have encouraged and helped along this path, and they should be recognized for their value.

My wife Ashley has been wonderfully supportive through this time, despite the many late nights away from home, and the weekends spent trying to get S-PIV to work right. She has been more encouraging than I deserve, and there have been days where the desire to make you proud of me has been a primary factor in my desire to continue my work. I love you, sweetie.

My parents should also be acknowledged for nurturing my curious and hardworking nature. They have been supporting me for over two decades, and this work is absolutely a culmination of that support. I cannot thank them enough for their invaluable impact on my life.

Dr. Wright also deserves a significant share of credit for the countless hours spent with a red pen improving my words. I needed someone to be straight with me and tell me when something was poorly written or did not make any sense, and she was the perfect mentor for that. I have grown tremendously as an engineer and a person in the time I have

worked with her and my confidence and pride in my work are a direct result of her efforts.

I would also like to thank Honeywell Inc. and Stratasys for sponsoring the work and providing strong intellectual support. Mr. Dan Crites and Dr. Malak Malak from Honeywell Inc. have been invaluable to the development of this thesis. I would also like to specifically thank Andrew Carter from Stratasys for the intellectual support provided. My interest and understanding of real gas turbine technology was developed through this project, and I hope to soon have a career in this industry that will be at least partially due to the investment made by these companies.

There are two individuals who provided special technical support that was invaluable to the completion of this work. Dr. Bernd Zechmann with the Center for Microscopy and Imaging helped me obtain some really cool scanning electron microscope images that helped to reveal important aspects of DMLS technology. Additionally, Dr. Steve Anderson from LaVision Inc. helped me to get the S-PIV setup to work. The setup is complicated and there are so many little things that can be changed, and I would never have gotten it working without his help.

I so thoroughly appreciate Dr. Stephen McClain and Dr. John Davis for taking the time to invest in me and read this enormous document. Their effort to help me grow and push me to fully clarify and understand the material helped make this a better project. Many other members of the Baylor faculty have been tremendously helpful over these past five and a half years in Waco. There are too many to name here but their contributions have not gone unnoticed. Furthermore, my fellow graduate students have had a huge impact on my time. I would especially like to thank Sara Seitz, Travis

Watson, and Berkley Bonjonia for the countless hours of company in 107. They helped to keep my spirits up and finish this long project.

## DEDICATION

To God, who deserves all of the honor and glory  
And to Ashley for being my rock through all of the ups and downs

## CHAPTER ONE

### Introduction

#### *General Gas Turbine Theory*

Gas turbine engines have played a vital role in shrinking the globe and paving the way for the modern global economy. They have propelled countless airplanes across continents and oceans at fast and cost efficient speeds. They generate power for homes and businesses across the world. Even small improvements to the efficiency of a gas turbine engine can have globally significant ramifications.

Gas turbine engines generate power or thrust using a traditional Brayton cycle. Ambient air passes through a series of compression stages which input energy into the flow, increasing the mainstream air pressure by up to 40 times in modern compressors. This high pressure, moderate temperature air ( $\sim 650^{\circ}\text{C}$ ) is then passed to the combustion chamber, where energy is added through combustion. This energy increases the temperature to the maximum point of approximately  $1900^{\circ}\text{C}$ . This high temperature, high energy flow then moves through the turbine stage, where a series of vanes and rotors extract energy from the flow to power the compressor and provide thrust or electrical power (depending on the application). This applied Brayton cycle is shown with a cutaway of a Honeywell aircraft engine in *Figure 1.1*.

In order to maximize the power of this engine cycle, the rotor inlet temperature (RIT) should be maximized. The power of the engine is produced in the turbine, and higher temperature mainstream flows have more available energy for turbine blades to convert into shaft rotation. The relationship between RIT and specific core power of the

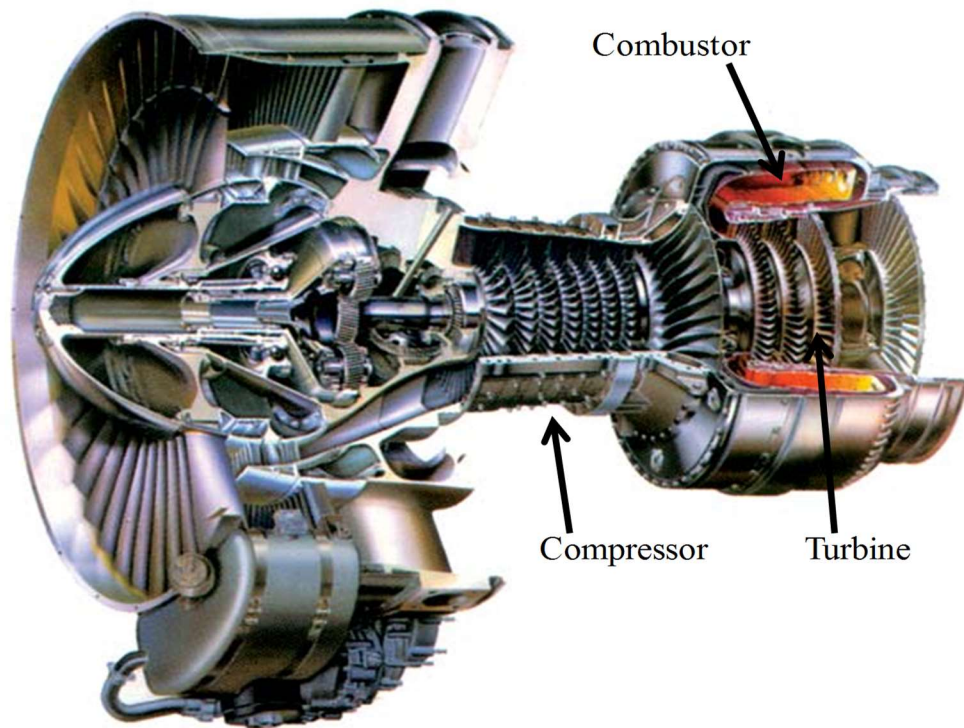


Figure 1.1: ALF502 turbofan developed by Honeywell (courtesy of Honeywell)

engine is shown in *Figure 1.2* [1]. As shown in the figure, specific core power has a nearly linear correlation with RIT. Increasing RIT has costs associated with it, such as more fuel required and higher compressor pressure ratios. The goal of engine design is to optimize the RIT.

The rotor inlet temperature cannot be increased indiscriminately, as the present material limitations do not allow for component temperatures exceeding  $1100^{\circ}\text{C}$  to  $1400^{\circ}\text{C}$ . Current mainstream rotor inlet temperatures can exceed  $1600^{\circ}\text{C}$ , which is far above the maximum allowable temperatures of the available materials. In order to facilitate rotor inlet temperatures above the material operational limits, various cooling techniques are employed.

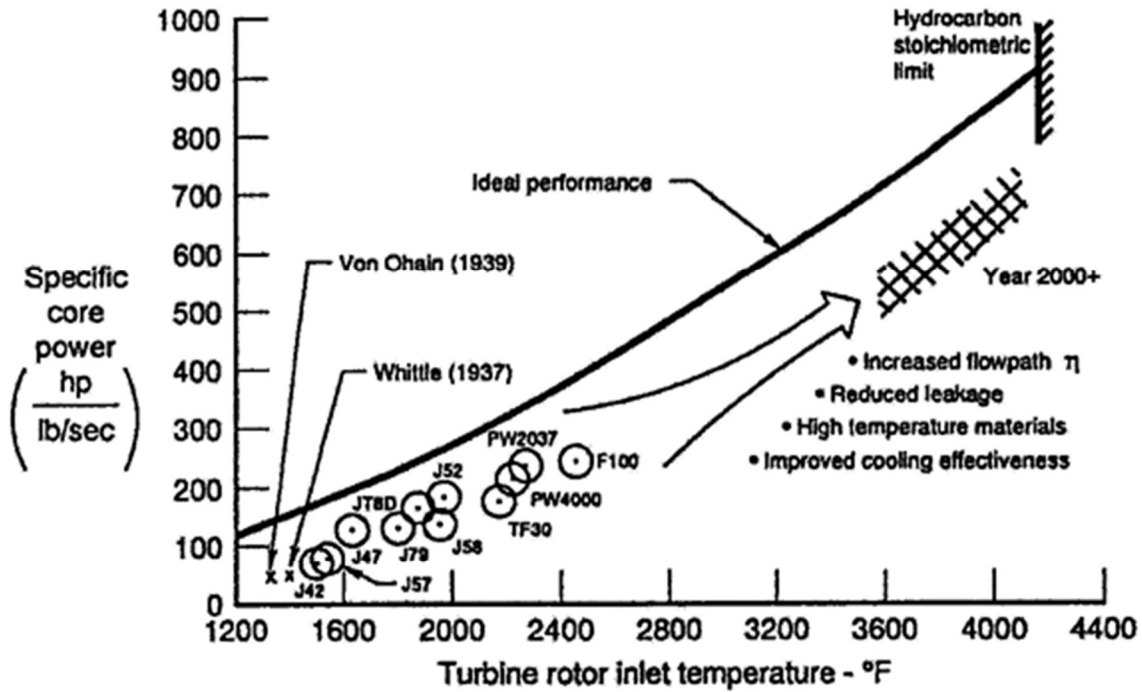


Figure 1.2: Specific core power increase due to RIT [1]

### *Modern Gas Turbine Cooling Overview*

Airfoil cooling is accomplished by extracting air from the compressor, bypassing the combustion chamber, and passing through hollow channels in the engine to cool the combustor liner and the turbine vanes and blades. Pulling air from the compressor reduces the mass flow rate through the turbine stages, reducing the overall power generated. In order to justify this reduction, the higher RIT must lead to an increase in specific power surpassing the loss of power from the reduced mass flow. The complexity of gas turbine blade cooling has forced engine designers to overcool engine components to ensure their safety, which limits efficiency in favor of reliability. The best way to improve the efficiency of a gas turbine engine is to limit overcooling, while still maintaining safe component temperatures.

Gas turbine blade and vane cooling is divided into two categories: internal and external cooling. Internal cooling works by passing the compressor bleed air through channels inside of the turbine blades. Heat is transferred from the hot engine components to the compressor bleed air by forced convection. The goal of internal cooling design is to find an optimum combination of heat transfer enhancement and flow rate of coolant. As the flow rate increases, so does the heat transfer, but increasing the flow rate reduces the overall maximum power production of the engine. The amount of heat transfer is characterized by the heat transfer coefficient ( $h$ ). Increasing the flow rate also increases the pressure loss through the channel due to the increased friction factor. The outlet pressure of the internal cooling passages must be maintained above the pressure of the mainstream gas near the outlets to avoid ingesting mainstream gas into the internal passages, which would be catastrophic. The pressure drop between the point of coolant extraction from the compressor and the internal cooling outlet determines the required inlet pressure of the coolant from the compressor. Increasing the pressure drop results in higher pressure and temperature coolant being used, which is undesirable. Therefore, the frictional losses should be minimized while maintaining sufficient protection of engine components.

There are four primary internal cooling techniques which have varying effects on the heat transfer coefficient and friction factor: jet impingement, pin fins, rib turbulators, and dimples. Jet impingement is the most aggressive form of internal cooling, and incurs the highest friction factor increase. It is only used in areas such as the leading edge, where hot mainstream air stagnates on the blade. With jet impingement, holes are added to the internal cooling passage to direct cooling air on to the interior walls of an airfoil.

The cooling air stagnates on the blade interior, creating high transfer at the expense of increased pressure loss. The mid-chord region of the airfoil is primarily cooled with rib turbulators and dimples, which increase the turbulence in the cooling channel. The increased turbulence leads to higher heat transfer coefficients within the channel without increasing the friction factor as drastically as jet impingement. The final method of internal cooling, pin fin cooling, is used in the trailing edge of the blade because of the extremely narrow areas in this region. Pin fins provide structural support to the blade while also increasing the heat transfer by increasing surface area and turbulence in the channel. Pin fins obstruct more of the flow than ribs or dimples, thus incurring a significantly higher pressure penalty, so they are primarily used in the thin trailing edge where structural support is necessary. Several of the internal cooling methods are illustrated in *Figure 1.3* [1].

Internal cooling alone is not sufficient to cool the blades. The other primary mode of engine component cooling is external, or film cooling. External cooling takes place in the combustor, on turbine vanes and blades, and even some high temperature compression stage impellers. Film cooling is accomplished through small holes that eject the cool air from the internal cooling passages onto the exterior surface of the component. In ideal film cooling operations, the cool air remains attached to the blade surface, acting as a blanketing layer of insulation between the engine component and the hot mainstream gas. This external cooling technique is illustrated in *Figure 1.4* [1].

The interaction of the coolant and mainstream flows in film cooling is shown in *Figure 1.5*, leading to the development of a film temperature between the coolant and

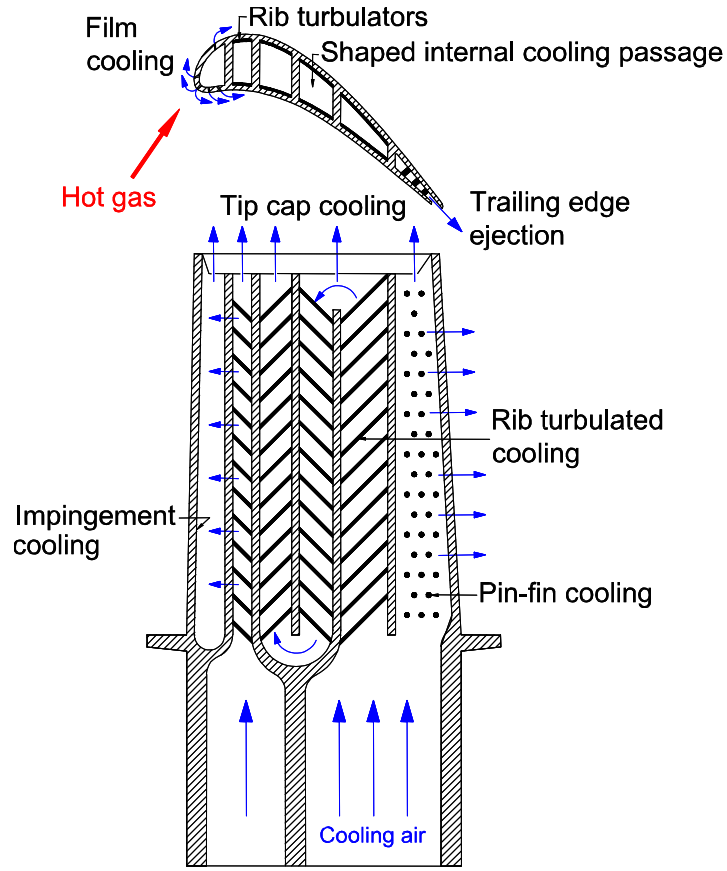


Figure 1.3: Internal cooling techniques for turbine airfoils [1]

mainstream temperatures. The film temperature is the temperature of the mixed mainstream and coolant that directly interacts with the turbine blade surface. The film cooling effectiveness ( $\eta$ ) is defined in equation 1.1.

$$\eta = \frac{T_{\infty} - T_F}{T_{\infty} - T_C} \quad (1.1)$$

When the wall, or film temperature ( $T_f$ ) is equal to the mainstream temperature ( $T_{\infty}$ ), the effectiveness is equal to zero. When the wall temperature is equal to the coolant temperature ( $T_C$ ), the effectiveness is equal to one. The film cooling effectiveness

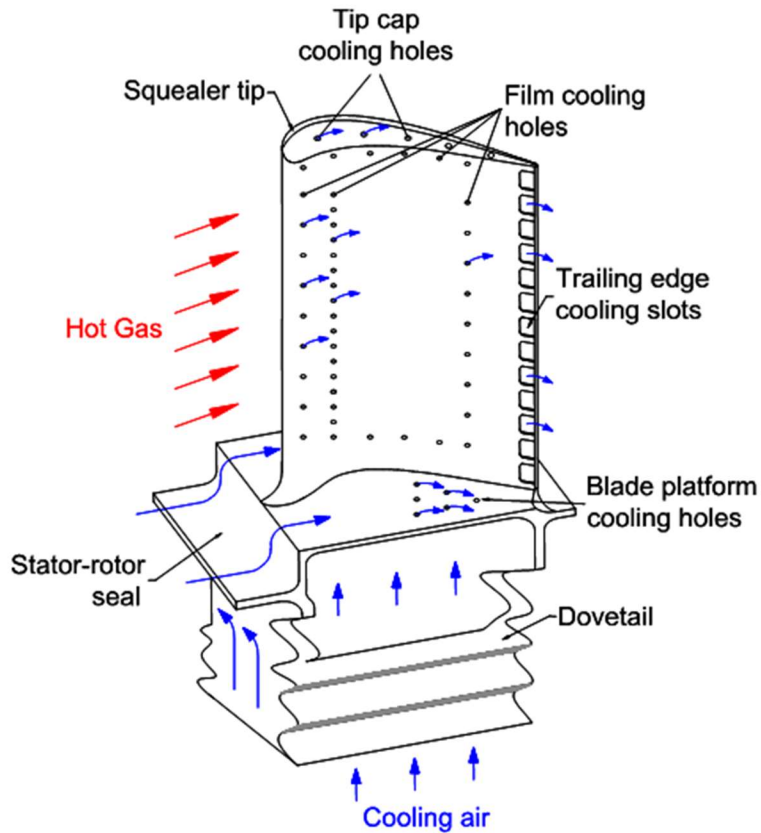


Figure 1.4: External cooling techniques for turbine airfoils [1]

represents the efficacy of the cooling scheme. The more coolant that is kept closer to the surface to protect the blade, the higher the film cooling effectiveness.

The film cooling effectiveness is effected by the mixing between the cooling jet and mainstream flow, which is illustrated in *Figure 1.6* [2]. The figure demonstrates the forces that prevent the coolant jet from perfectly adhering to the blade surface. It is not possible, from a manufacturing perspective, for the jet to exit the film cooling hole parallel to the turbine blade. Therefore, the jet will have momentum normal to the blade which reduces the film cooling effectiveness. Counter rotating vortices develop within the jet itself, pulling hot mainstream air down towards the surface. Additionally, the horseshoe vortices developing on the surface generate turbulence that increases jet

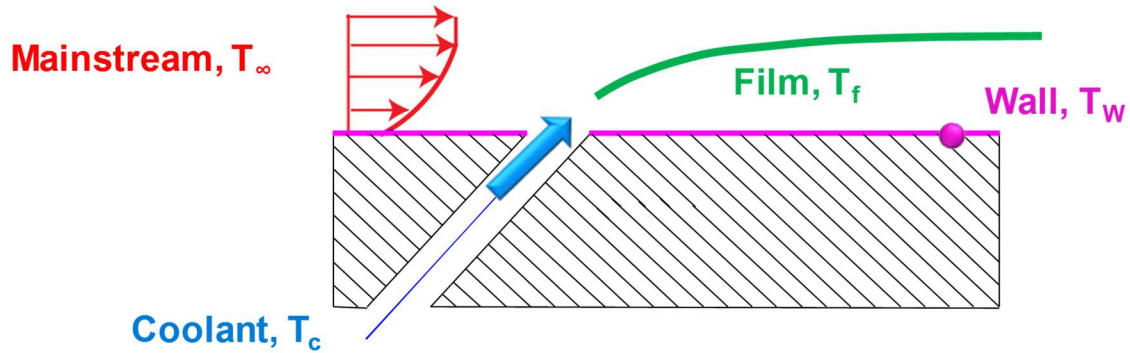


Figure 1.5: Illustration of film cooling

separation. Effective film cooling must limit the normal momentum of the jet and the formation of the counter rotating and horseshoe vortices.

The capacity of a film cooling hole to limit jet separation is a function of hole geometry and coolant to mainstream flow conditions. Hole geometry includes factors such as hole shape, spacing, and angle. Traditional film cooling had always utilized cylindrical film cooling holes created by laser drilling. Modern film cooling began to utilize shaped holes, which will be a focus of this thesis. Generically, shaped holes expand the hole exit cross sectional area, reducing the momentum of the jet and providing improved jet attachment. The only limit to the shape of modern shaped holes created with EDM (electro-discharge machining) is that they must be line of sight holes. Even more recent advancements in hole shape have come in the form of Direct Metal Laser Sintering (DMLS) technology, which is an additive manufacturing method applied to metals. More detail will be provided on DMLS in subsequent chapters, especially relating to combustor cooling applications. DMLS has high potential for film cooling applications because it is capable of creating non-line of sight holes. Non-line of sight holes allow for new creative designs to limit jet separation by stagnating the flow inside the hole and allowing the hole angle to approach parallel.

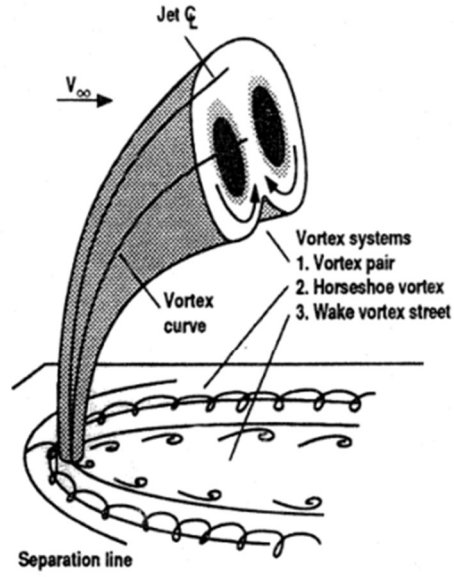


Figure 1.6: Illustration of film cooling jet [2]

Coolant-to-mainstream flow conditions are often characterized by four non-dimensional values: the velocity ratio ( $V_r$ ), the density ratio (DR), the mass flux ratio, or blowing ratio (M), and the momentum flux ratio (I), which are defined in equations 1.2-1.5.

$$V_r = \frac{V_c}{V_\infty} \quad (1.2)$$

$$DR = \frac{\rho_c}{\rho_\infty} \quad (1.3)$$

$$M = V_r * DR = \frac{V_c \rho_c}{V_\infty \rho_\infty} \quad (1.4)$$

$$I = V_r * M = \frac{V_c^2 \rho_c}{V_\infty^2 \rho_\infty} = \frac{M^2}{DR} \quad (1.5)$$

The velocity ratio is a simple ratio of coolant velocity to mainstream velocity. The density ratio is the ratio of coolant gas density to mainstream gas density. In gas turbine engines for aerospace applications, the density ratio is around 3 because of the difference in temperature of the mainstream and cooling flows. In actual laboratory settings, a density ratio of 3 is difficult to simulate. For this reason, the density ratio and velocity ratio are often combined using the mass flux ratio, which is simply the velocity ratio multiplied by the density ratio. The momentum flux ratio is also used by researchers because jet separation is thought to be a function of the momentum of the coolant jet relative to the momentum of the mainstream flow.

In addition to those four parameters, the freestream acceleration also impacts film cooling effectiveness. In real turbine blades, the mainstream air accelerates (or decelerates) because of the curvature of the blade. Most studies only consider zero pressure gradient flows, but the effect of favorable pressure gradient mainstream flow should be considered. All of these effects on film cooling effectiveness, including realistic engine density ratios, will be studied together throughout this investigation.

Combustor cooling is similar to turbine blade external cooling, except combustors are non-rotational. Turbine blade hole patterns are limited by the stress created by rotation, while combustor liner hole patterns can be much closer together. This method of cooling, wherein rows of holes are close enough to interact, is known as full coverage, or effusion film cooling. Most studies of full coverage film cooling have focused on blowing ratios that were effective for single row film cooling applications. Additionally, shaped film cooling holes have not previously been considered in effusion film cooling studies.

### *Objectives of Study*

The primary goal of this study is to help engine designers limit overcooling in gas turbine engines. The first experiment will focus on combustor cooling applications. The effect of hole shape and blowing ratio ( $M$ ) on full coverage film cooling effectiveness will be investigated with a pressure sensitive paint technique. The hole shape is studied to provide data on the impact of shaped holes in effusion cooling applications. In particular, non-linear shaped holes created using DMLS technology will be investigated to evaluate the potential to dramatically influence film cooling effectiveness. A wide range of blowing ratios is studied to determine the impact of row to row interaction. Modern engine designers often use high blowing ratios in combustion chambers to ensure safe operation, without accurately knowing the cooling effectiveness compared to single row turbine blade applications where lower blowing ratios are used.

The second experiment will use the stereoscopic particle image velocimetry technique alongside the previously mentioned PSP technique to investigate turbine airfoil cooling. The flow fields investigated using S-PIV will be used to aid in analysis of the film cooling effectiveness trends determined with PSP. The techniques will be used to evaluate the performance of round, traditional shaped, and four new shaped holes for a wide range of blowing ratios and engine-like density ratios. Furthermore, the effect of accelerating mainstream flow, as seen in real engine applications, will be investigated for all holes and flow conditions. The effect of freestream acceleration is not currently well understood, and the flow visualization provided by S-PIV combined with the effectiveness results provided by PSP may help resolve some of the discrepancies in the literature. Additionally, the impact of hole shape on the formation of secondary flows is

not fully understood, and this study will provide further characterization of those important film cooling scenarios.

## CHAPTER TWO

### Literature Review

#### *Coolant-to-Mainstream Flow Conditions*

As briefly discussed in the introduction, the film cooling effectiveness is a function of the flow conditions and the hole geometry. Bogard and Thole [3] completed a comprehensive review of film cooling literature up to 2006 in which they determined the most important factors for film cooling effectiveness. Bogard and Thole [3] noted six factors of primary importance for film cooling performance: mass flux ratio (M), momentum flux ratio (I), mainstream turbulence ( $Tu$ ), hole shape, hole inclination ( $\theta$ ), and surface curvature. Han et al. [1] provides a comprehensive text that explains the fundamentals of the effects listed above, along with the density ratio (DR), which will be included in this discussion. The goal of any engine designer is to achieve the optimum combination of flow conditions and hole geometry. Unfortunately, different aspects of the flow conditions do not affect film cooling effectiveness independently of each other, or of the hole geometry. For example, increasing the blowing ratio has different effects for round holes than it does for shaped holes. The number of factors that influence film cooling effectiveness is prohibitive of simultaneous testing of every single co-dependent factor. Therefore, fundamental understanding of each effect is necessary to design efficient film cooling schemes.

It should also be noted that film cooling effectiveness is only one part of explaining the interaction of film cooling and mainstream flows. Film cooling also impacts the local heat transfer coefficients which have an impact on the surface

temperature of the blades. However, for this thesis, heat transfer coefficients have not been investigated or considered, so the extensive literature detailing the effect of film cooling on the heat transfer coefficients is not discussed.

In order to gain fundamental understanding of the effect of various flow conditions, the standard round hole at a  $30^\circ$  incline in zero pressure gradient flow (no accelerating mainstream) with a density ratio of  $DR = 1.0$  will be considered. The effect of the mass flux ratio, or blowing ratio ( $M$ ), is relatively well understood for turbine blade applications. Baldauf et al. [4] used IR thermography to demonstrate that film cooling effectiveness is maximized between blowing ratios of  $M = 0.5$  and  $M = 1.0$ . Increasing the blowing ratio beyond  $M = 1.0$  resulted in reduced downstream effectiveness because the higher velocity coolant is less resistant to jet separation. Eriksen and Goldstein [5] showed that a blowing ratio of  $M = 0.5$  is the optimum for round holes. They both conclude that cooling flows with blowing ratios lower than  $M = 0.5$  lack sufficient momentum to travel downstream of the holes without getting swept into the mainstream. Coolant jets with blowing ratios greater than  $M = 1.0$  do not stay attached to the surface. The jet has sufficient momentum to penetrate the mainstream flow and the coolant is unable to protect the surface. Detailed film cooling effectiveness results provided by Russin et al. [6] validated previous results, while giving increased understanding for the separation and reattachment in the range of blowing ratios from  $M = 0.4$  to  $M = 1.0$ . It was determined that coolant separation occurred approximately one diameter downstream in this blowing ratio range, but would reattach downstream. The point of reattachment was highly dependent on blowing ratio. For this reason, increasing

the blowing ratio towards  $M = 1.0$  increases downstream the centerline effectiveness at the expense of near hole lateral effectiveness.

In addition to the blowing ratio, the effect of increasing the density ratio must be considered because modern engines operate with density ratios near  $DR = 3$  due to the temperature difference between the coolant and the mainstream. As the density ratio increases, the coolant is heavier and more resistant to jet separation. For a given blowing ratio, increasing the density ratio decreases the coolant velocity. The density ratio effect has been studied by Johnson et al. [7], Sinha et al. [8], and Pedersen et al. [9]. Johnson et al. [7] used PIV and PSP measurements to evaluate the density ratio effect on round hole film cooling. The PIV results were used to demonstrate that the flow would remain attached for low blowing ratios ( $M = 0.4$  and  $0.83$ ) regardless of whether air ( $DR = 1$ ) or  $CO_2$  ( $DR = 1.5$ ) was used as coolant. However, for higher blowing ratios ( $M = 1.7$ ), the PIV results clearly show that the air coolant separates from the plate, while the  $CO_2$  is able to stay closely attached to the surface. Sinha et al. [8] demonstrated that for round holes, increasing the density ratio to  $DR = 2$  specifically increased the lateral average and spread of the coolant. The effect was most pronounced at higher blowing ratios ( $M > 0.8$ ). The study attempted to correlate the effectiveness data with velocity ratio, mass flux ratio, and momentum flux ratio. It was determined that none of those parameters could completely explain the difference in effectiveness across varying density ratios. Increasing the density of the coolant has a fundamental effect on the effectiveness of film cooling, pulling it closer to the surface and dispersing the coolant over a wider area. Pedersen et al. [9] showed that very high density ratios ( $DR = 4.17$ ) improve the lateral average film cooling effectiveness by up to 400% at blowing ratios over  $M = 1.0$ . The reason that effectiveness improves so

drastically for high blowing ratios is the effect that the density ratio has on jet attachment and reattachment. As the blowing ratio increases the jet becomes more likely to separate from the surface, but increasing the density ratio causes it to reattach.

The momentum flux ratio is often used to combine the mass flux ratio and density ratio into a single parameter to correlate effectiveness. The momentum flux ratio is defined as the ratio of the momentum flux of the coolant to momentum flux of the mainstream. Thole et al. [10] showed that round jets could be clearly divided into three categories based on momentum flux ratio. For  $I < 0.4$ , the coolant remains completely attached in the region evaluated (10 diameters downstream of hole). In the intermediate category ( $0.4 < I < 0.8$ ), the coolant initially detaches immediately downstream of the hole but is quickly reattached. As the momentum flux ratio increases, that point of reattachment shifts further downstream. In the final category ( $I > 0.8$ ), the coolant fully detaches and does not reattach. The coolant has sufficient momentum to penetrate the mainstream flow and not get pushed back down to reattach to the surface. Saumweber et al. [11] showed that area average film effectiveness decreased as  $I$  increased for round holes but increased as  $I$  increased for shaped holes. The momentum flux ratio has become a common parameter used to correlate effectiveness, and it is generally assumed that it can be used to scale flows, combining  $M$  and  $DR$  into a single value.

The mainstream flow entering the turbine is highly turbulent in real engine applications. Turbulence intensity is defined as the turbulent fluctuations divided by the average velocity, as shown in equation 2.1,

$$Tu = u'_{rms} / \bar{u} \quad (2.1)$$

where  $u'_{rms}$  is the fluctuating component of velocity of fluid moving in the streamwise direction and  $\bar{u}$  is average velocity of fluid moving in the streamwise direction. The size of the turbulent eddies and the level of turbulent intensity vary according to the engine design, but a baseline turbulence intensity would be around 20%. Most film cooling studies use mainstream air with far lower turbulence, so it is important to understand the effect that real engine turbulence has on film cooling performance. Bons et al. [12] investigated film cooling effectiveness using a wind tunnel capable of generating a free stream turbulence level of  $Tu = 17.4\%$ . For round film cooling holes, immediately downstream of the holes, the film cooling effectiveness was drastically reduced by up to 70%. However, the elevated turbulence results in increased lateral spread of the coolant. In the area between the holes, the film cooling effectiveness is increased by up to 100% due to the elevated freestream turbulence. Fundamentally, realistic engine turbulence increases jet separation, but it also increases jet lateral spreading. For studies with minimal freestream turbulence, these effects should be accounted for when evaluating the data.

### *Effect of Hole Angle*

The angle between the ejected coolant and the mainstream flow has strong influence on the film cooling effectiveness. The primary angle of consideration is hole injection angle ( $\theta$ ), described in *Figure 2.1*. As  $\theta$  increases, the coolant exits the hole with increased normal momentum, which increases jet separation. Foster and Lampard [13] studied the effect of injection angle on round holes with a density ratio of  $DR = 2.0$  and blowing ratios of  $M = 0.5$  and  $1.4$ . Hole angles of  $35^\circ$ ,  $55^\circ$ , and  $90^\circ$  were investigated using a mass transfer technique to confirm the theory that increasing coolant momentum

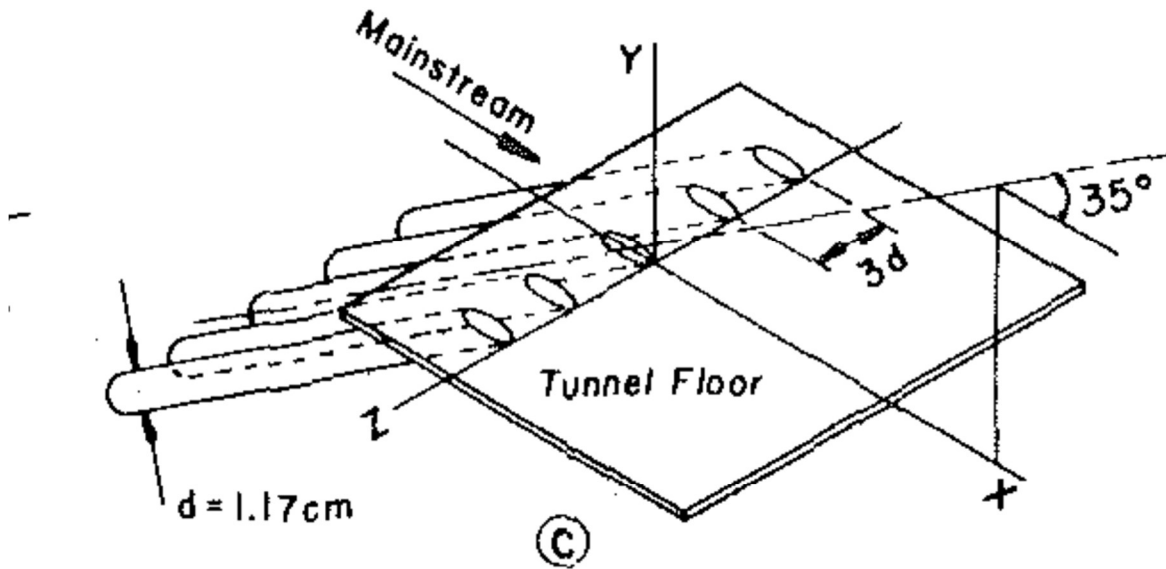


Figure 2.1: Simple angle round hole with  $\theta = 35^\circ$  [9]

normal to the mainstream flow reduces film cooling effectiveness. The study showed that for the lower blowing ratio, where round film cooling is near optimum, the hole angle of  $35^\circ$  out-performed the other injection angle holes by about 50% in the region near the hole (15 diameters). At the higher blowing ratio however, where round holes have lower effectiveness, the higher injection angles actually out-performed the injection angle of  $35^\circ$  by more than 100% in the near hole region (15 diameters). This unintuitive increase occurs because round jets with a blowing ratio of  $M = 1.5$  at a standard inclination angle experience jet separation, and then subsequent mainstream mixing that slowly leads to coolant reattachment. With an inclination angle of  $90^\circ$  the mixing actually occurs more rapidly, leading to reattachment closer to the hole. Kholi and Bogard [14] have also studied hole injection angles of  $35^\circ$  and  $55^\circ$  by varying the momentum flux ratio from  $I = 0.1$  to 0.6. Increasing the injection angle reduced the area average film cooling effectiveness by  $\sim 10\%$  at low momentum flux ratios, but for higher momentum flux

ratios, the area average effectiveness was reduced by over 30%. This contradicts the study of Foster and Lampard [13], making it difficult to completely clarify the fundamental effect of hole inclination angle at higher momentum flux ratios.

The secondary angle between ejected coolant and mainstream flow studied in film cooling literature is the oblique angle ( $\beta$ ), as shown in *Figure 2.2*. A hole with an oblique angle greater than  $\beta = 0^\circ$  is considered a compound angle hole, which ejects coolant that is not parallel to the mainstream flow. The purpose of rotating the hole is to reduce the streamwise momentum, which would potentially keep the coolant attached to the blade surface near the hole exit. Schmidt et al. [15] compared a compound hole angle ( $\beta = 60^\circ$ ) with a baseline round hole using thermocouple measurements. A hole inclination of  $\theta = 35^\circ$  was used to study the effect of the oblique angle on the spatially averaged film cooling of round holes while varying the blowing ratio from 0.6 to 1.25. Overall,

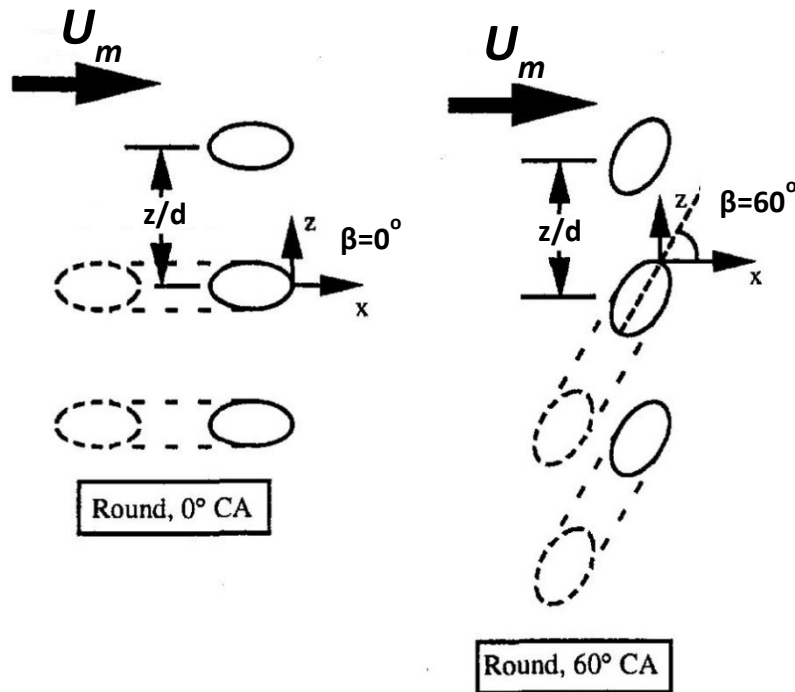


Figure 2.2: Round, compound angle holes at  $\beta = 0^\circ$  and  $\beta = 60^\circ$  [15]

compound angle film cooling improves the area average effectiveness. At a low blowing ratio, there was little difference between the compound angle hole and the simple angle hole. However, at the higher blowing ratios, the compound angle outperformed the simple angle hole by more than double. This distinction shows that compound angle holes can facilitate consistent effectiveness over a wide range of blowing ratios, unlike simple angle round holes. This occurs because the coolant does not eject parallel to the mainstream, and the interaction of the two flows increases the lateral dispersion of the coolant at higher blowing ratios.

More recently, Wright et al. [2] studied the effect of blowing ratio on compound angle film cooling using the PSP technique. Results showed that for low blowing ratios ( $M \sim 0.5$ ), the mainstream pushed the low momentum coolant in the streamwise direction, which created a more uniform spread of the coolant downstream. Higher blowing ratio coolant ( $M \sim 1.5$ ) had sufficient oblique momentum to maintain the path of the oblique angle and reduce the uniformity of the downstream effectiveness.

### *Effect of Hole Shape*

Film cooling began with round holes, but over the past several decades, many new film cooling hole shapes have been tested. The primary goal of any different hole shape design is to increase the hole exit area to diffuse the coolant, providing more uniform lateral coverage, and also to slow down the coolant to reduce local blowing ratio and jet separation. More advanced hole shapes have been designed with an additional goal of reducing vortex formation. The most common hole shape in literature and practice is a simple modification of the standard round hole with a laterally expanded exit, commonly referred to as fanshaped, and expansion into the surface, commonly

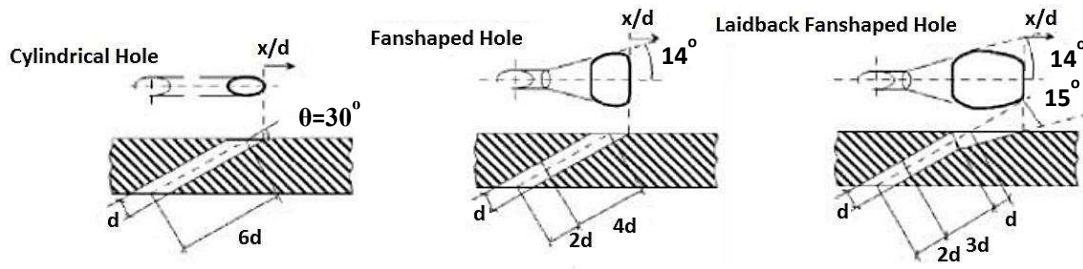


Figure 2.3: Illustration of cylindrical, shaped, and fanshaped film cooling holes [3]

referred to as laidback. The laidback and fanshaped holes are illustrated in *Figure 2.3*. Bunker et al. [16] notes five newer shaped holes in his comprehensive review of shaped film cooling, including the transonic wall jet, console, cratered hole, trenched hole, and tab overlays. All of the shaped holes commonly investigated have shown substantially higher film cooling effectiveness than round holes. The shaped holes reduce local blowing ratios, allowing coolant to remain attached to the surface for a wider range of blowing ratios and momentum flux ratios.

Before considering the effect of hole design, the ideal hole design must be discussed. The ideal cooling film is produced by a tangential, two-dimensional continuous slot used to evenly distributed coolant across the surface, as illustrated by *Figure 2.4* [17]. While this slot cooling is ideal, there are competing factors such as thermal and mechanical stresses which prevent slot cooling in most film cooling applications. Due to its impracticality, there have been fewer studies conducted for continuous slots than for singular holes or rows of cooling holes. Slot cooling is typically used for endwall film cooling, which has been studied by Zhang and Jaiswal [18] using PSP. The single row of discrete slots was compared to a double staggered row of holes.

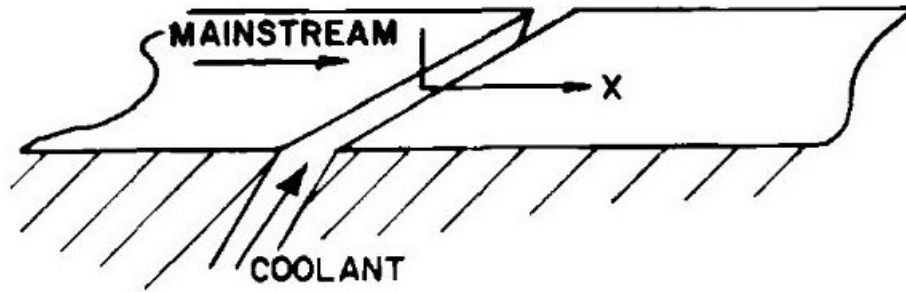


Figure 2.4: Schematic angled slot-hole film cooling [17]

At higher mass flux ratios, the discrete jets provided greater uniform effectiveness while the staggered holes provided better trailing edge coverage.

Some conclusions drawn from previous slot-hole studies were compiled by Jia et al. [19] and verified with their own experimental and numerical investigations of slot film cooling for varying angles of ejection. They concluded that for large injection angles ( $\theta > 30^\circ$ ), coolant quickly separates in the region downstream of the slot, overpowering the mainstream. The jet penetrates into the crossflow, increasing turbulence generation and reducing film cooling effectiveness. However, at elevated blowing ratios, the downstream film cooling effectiveness is actually increased due to a thickened thermal boundary layer and the presence of more available coolant. It was shown that recirculating coolant downstream of the slot exit is solely dependent on the angle of ejection. For large jet angles ( $\theta > 40^\circ$ ), the recirculation region is evident, but vanishes entirely for  $\theta < 40^\circ$ . Nevertheless, the size of the recirculation was found to be dependent on the velocity ratio, with a stronger jet flow leading to a reduced recirculation zone. For an angled slot-hole configuration, a  $30^\circ$  ejection angle was shown to maximize effectiveness.

The first study on shaped holes was performed by Goldstein et al. [20], which demonstrated that a  $10^\circ$  expanded film cooling hole offered improved protection by spreading the coolant near the surface. The coolant jet from the shaped hole did not penetrate nearly as far into the mainstream as the cylindrical hole. A simple angle cylindrical hole, fanshaped hole, and laidback, fanshaped hole with  $\theta = 30^\circ$ ,  $\alpha = 14^\circ$ , and  $\gamma = 15^\circ$  were compared by Gritsch et al. [21] using IR thermography for a range of blowing ratios from  $M = 0.5$  to  $1.5$ . It was determined that the fanshaped hole outperformed the cylindrical hole, especially at elevated blowing ratios. Furthermore, the laidback, fanshaped hole provided increased film cooling effectiveness over the simple fanshaped hole, especially due to increased lateral spreading of the jet created by the laidback hole geometry. Yu et al. [22] investigated similar geometries, comparing round holes to laidback shaped holes and the laidback, fanshaped hole with  $\theta = 30^\circ$ ,  $\alpha = 10^\circ$ , and  $\gamma = 10^\circ$ . The transient liquid crystal technique was used to confirm the work of Gritsch et al. [21] showing that the laidback, fanshaped hole outperforms the round hole along with the laidback hole. Additionally, the laidback hole shows moderate improvement compared to the round hole, but is significantly outperformed by the laidback, fanshaped hole. Laser-sheet flow visualization was used to compare the centerline of each hole to provide an explanation for the difference in the geometries. The flow visualization revealed that the laidback, fanshaped hole exhibits the thinnest boundary layer and lowest level of shear generation between the mainstream and cooling flows.

Khohli and Bogard [14] investigated the effect of increasing the hole injection angle to  $\theta = 55^\circ$ , along with increasing the laidback angle to  $\gamma = 25^\circ$ . Velocity field results

were obtained to demonstrate that the shaped hole improved the coolant flow along the surface. The improved downstream coverage was shown to be a result of merging coolant jets close to the hole exit. It was assumed that the increased laidback angle would provide improved performance. However, the increased laidback angle actually caused separation with the hole, leading to reduced film cooling performance. The study highlights the importance of proper hole design to optimize performance.

The effect of freestream turbulence on shaped hole film cooling was investigated by Saumweber and Schulz [23] by varying the turbulence intensity from  $Tu = 2\%$  to  $7.5\%$ . It was determined that the performance gain of fanshaped holes over cylindrical holes may be overestimated at low turbulence laboratory conditions. Shaped hole film cooling is more adversely affected by elevated freestream turbulence than cylindrical holes. Saumweber et al. [24] similarly investigated the effects of elevated freestream turbulence on shaped hole cooling performance (up to  $11\%$  turbulence intensity). The study determined that elevated freestream turbulence is detrimental to shaped hole film cooling effectiveness at all blowing ratios. While round holes at low blowing ratios experience similar effects, round holes were demonstrated to exhibit higher effectiveness at high blowing ratios ( $M \sim 2.5$ ) for increased freestream turbulence. It is important to consider the effect of freestream turbulence when evaluating shaped hole film cooling performance.

Before discussing more advanced film cooling hole designs, it must be noted that hole area expansion is not the only part of hole shape design that influences film cooling effectiveness. It has been exhaustively proven that discrete film cooling holes produce kidney bean vortices because of the friction between the jet and crossflow. Haven et al.

[25] observed the vortices created by shaped holes and found that they do not behave in the same way as cylindrical holes. Fanshaped holes, laidback holes, and fanshaped laidback holes were investigated using a water flow visualization technique which demonstrated that shaped holes exhibit two effects which impact the kidney bean vortex formation: lateral separation of the vortices and formation of anti-kidney vortices. The increased lateral separation of kidney bean vortices reduced their counterproductive effects. The anti-kidney bean vortices rotate opposite of the typical kidney bean vortices, as demonstrated in *Figure 2.5*. This anti-kidney vortex pair was inconsistent across the three shapes investigated, suggesting that the design of shaped holes has the potential to influence the formation of anti-kidney vortex pair. Ideally, the anti-kidney vortex pair could be positioned to counteract the effects of the standard kidney bean vortex pair and actually improve the film cooling effectiveness. Investigations of advanced shaped hole designs will focus on the hole's influence on the formation of anti-kidney vortices and the potential impact it may have on film cooling effectiveness.

Recently, in an effort to reproduce the more two-dimensional spread of coolant from slots without a significant increase in stress concentration, holes were embedded in trenches, as seen in *Figure 2.6*. Trench cooling was originally investigated because film cooling holes are often masked before the application of the thermal barrier coating (TBCs), and when the mask is removed, become embedded in a 2-D trench. The trench condition was first investigated by Ekkad et al. [26] with cylindrical holes. The trench effect was determined to improve film cooling downstream of the injection site by reducing the jet momentum for all flow conditions investigated. Lu et al. [27] studied the effects of trench width and depth for cylindrical holes and found that trenching the holes

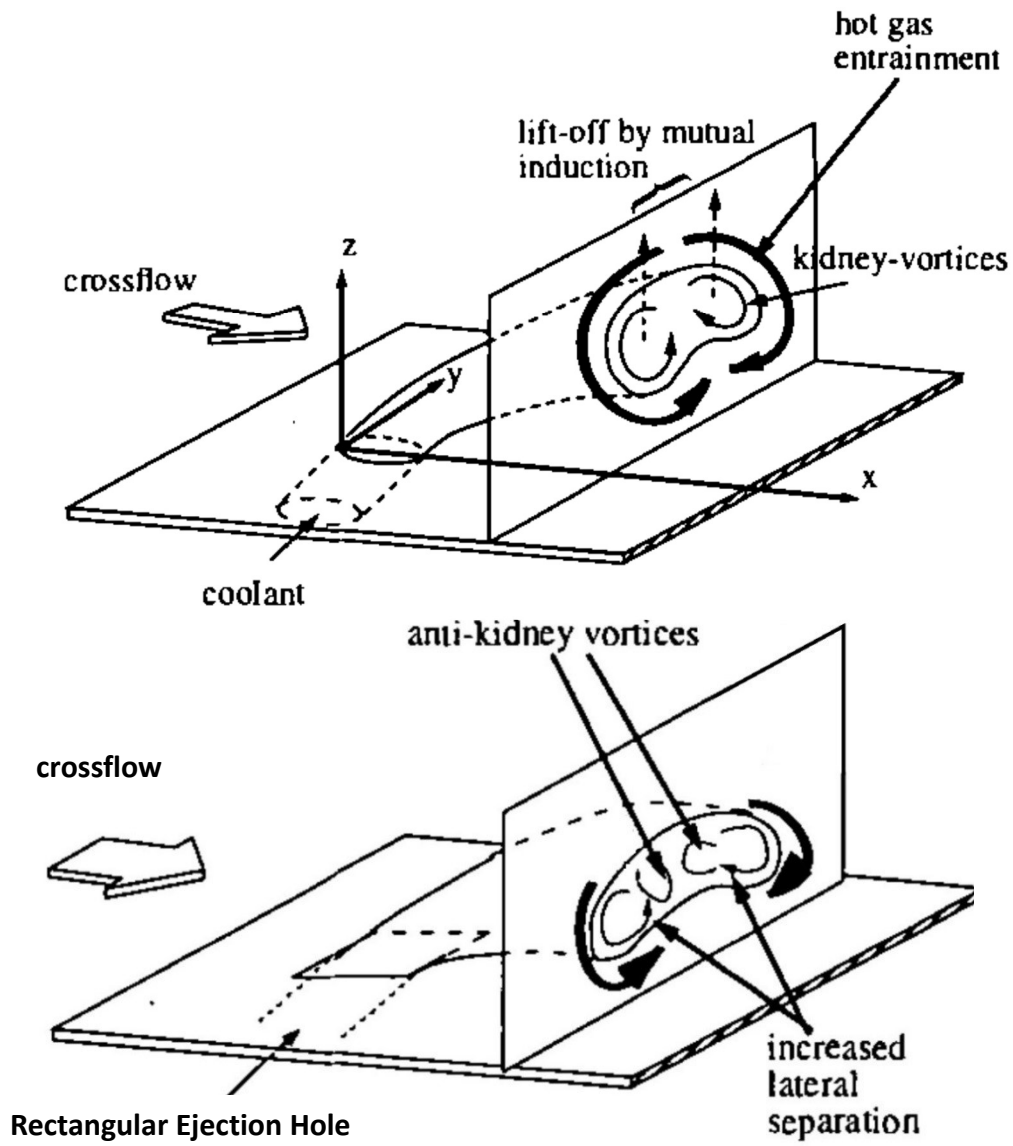


Figure 2.5: Illustration of kidney pair and anti-kidney pair vortices produced by shaped hole [25]

in a slot reduces the jet momentum at the exit and creates a similar effect as 2D slot cooling as opposed to the 3D nature of individual jets. Trenched shaped holes have been investigated by Dorrington et al. [28], who proposed that trenched shaped holes showed continued improvement after exceeding the optimum blowing ratio of untrenched shaped cooling holes. Similar to trenched cylindrical holes, trenched shaped holes reduce momentum exiting the hole, increasing the optimum blowing ratio.

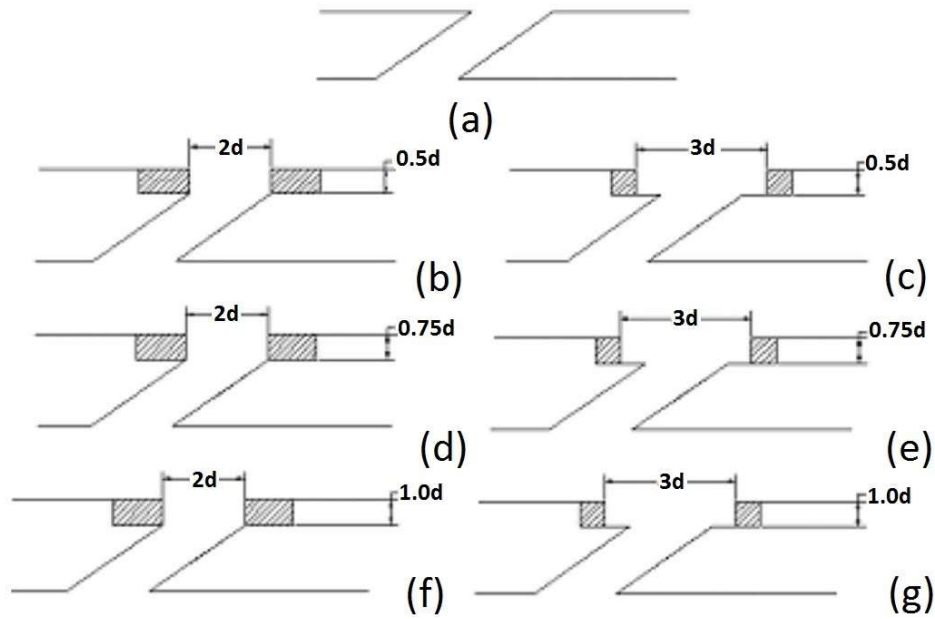


Figure 2.6: Trenched hole configurations studied by Lu et al. [27]

Cratered hole geometries, such as those seen in *Figure 2.7*, are similar to trenched holes and formed in a similar way by TBC application method. The effects of these cratered holes on film cooling have been studied by Lu et al. [29] using IR thermography to evaluate effectiveness and CFD to evaluate the flow fields caused by cratered holes. It was determined that cratered holes increased the film cooling effectiveness by about 50% over the baseline round case. The coolant spreading seen in trenched holes was not replicated in cratered holes, and furthermore, the jet maintained a clear three-dimensional structure, although with limited vortex strength. Overall, the cratered holes were less effective than trenched holes.

A converging slot-hole, also called console, was developed and tested by Sargison et al. [30]. The console shape, illustrated in *Figure 2.8*, is designed to improve the cooling and aerodynamic performance by mimicking a slot geometry without increasing mechanical stress concentrations. The cross section of the console extrudes from a row of

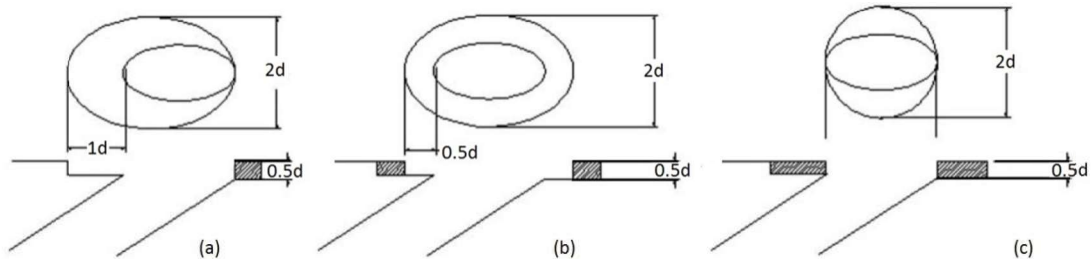


Figure 2.7: Cratered hole configurations studied by Lu et al. [29]

round holes into a slot. Coolant dispersed from a row of consoles was shown to provide increased lateral uniformity of the coolant, with some enhanced cooling between the discrete slots due to vortex interaction. Console shapes performed similarly to fanshaped holes, though with better aerodynamic performance.

A double-jet film cooling (DJFC) design, shown in *Figure 2.9*, is designed specifically to establish an anti-kidney vortex system. A single jet produces a dominating vortex, the combination of two mirrored, compound angle cylindrical holes is used to develop a symmetrical anti-kidney vortex pair. These vortices are designed to move coolant towards the wall, keeping hot, mainstream flow from being entrained under the jet and causing separation between the jet and the surface. Moreover, the cooling effectiveness may be improved by spreading the coolant in the lateral direction as compound angled holes have previously been shown to do. This design was first introduced by Kusterer et al. [31] and investigated using CFD. The DJFC configuration was shown to establish an anti-kidney vortex pair, protecting the jet from separation. The lateral distribution of the coolant is also increased as predicted. This design shows potential because cylindrical holes are much cheaper to manufacture than shaped holes.

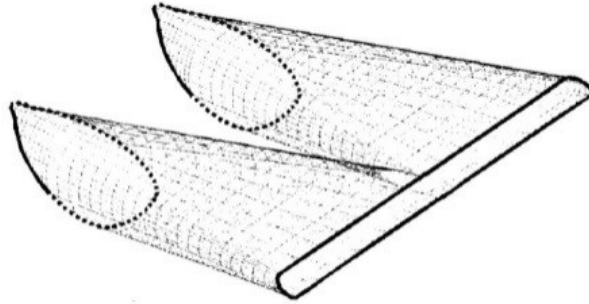


Figure 2.8: Console hole configuration investigated by Sargison et al. [30]

Wright et al. [32] compared the DJFC system to both round and shaped holes, concluding that the DJFC configuration did not outperform fanshaped, laidback holes. Further investigation revealed that, when separated, the two jets had lower momentum and offered improved coverage. However, once merged, the coolant stream from the DJFC system resembled a single, cylindrical hole, only with increased momentum and mainstream mixing because of the double mass flow. Even though the DJFC configuration did not outperform the shaped holes as hoped, the cylindrical holes are still significantly cheaper than the shaped holes and worth investigating the angle and spacing of the DJFC holes to determine if improvements can be made.

A tripod “antivortex” hole configuration was developed at NASA Glenn Research Center by Heidmann and Ekkad [33]. The design consisted of two compound angle, round holes with a smaller diameter branching out from a traditional cylindrical hole, as shown in *Figure 2.10*. The principle idea is that the branch holes will mitigate detrimental primary vortices by creating an antivortex (anti-kidney) pair. Additionally, the design is made entirely of round holes and therefore simpler to manufacture than shaped film cooling hole designs. Initial modeling suggests that the area averaged film cooling

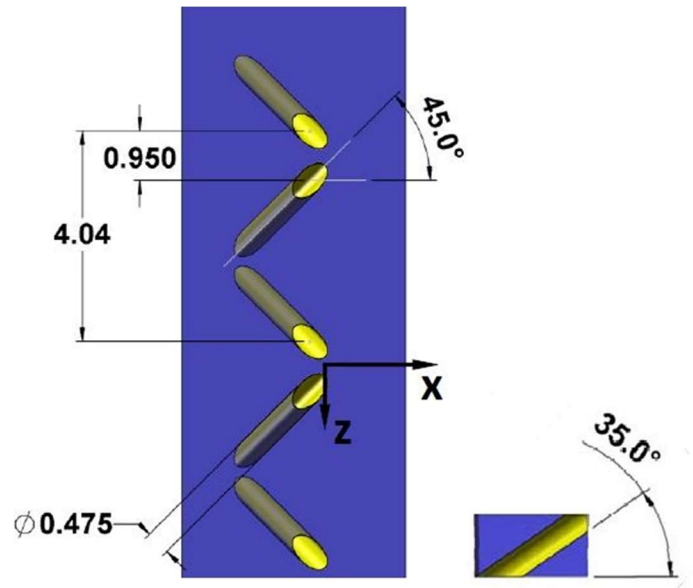


Figure 2.9: Double jet film cooling hole geometry investigated by Wright et al. [32]

effectiveness is significantly increased compared to the baseline round case. A number of variations of the anti-vortex geometries were tested and compared to a baseline shaped cooling hole by Dhungel et al. [34]. It appeared that kidney pair vortices were reduced due to the presence of antivortex holes, increasing lateral and downstream effectiveness over traditional cylindrical holes. However, the baseline shaped hole out-performed all six of the anti-vortex designs tested. The ideal scenario would have a cheaper hole design that outperformed the baseline shaped hole, but there is promise in the improvement over round holes and the simplicity of the design.

A variation of the tripod design, created by LeBlanc et al. [35], involved branching two supplemental anti-vortex holes, of the same diameter as the primary, at  $15^\circ$  angles from the primary root, as shown in *Figure 2.11*. Significant improvement in film cooling for all blowing ratios was reported, in contrast with traditional round holes.

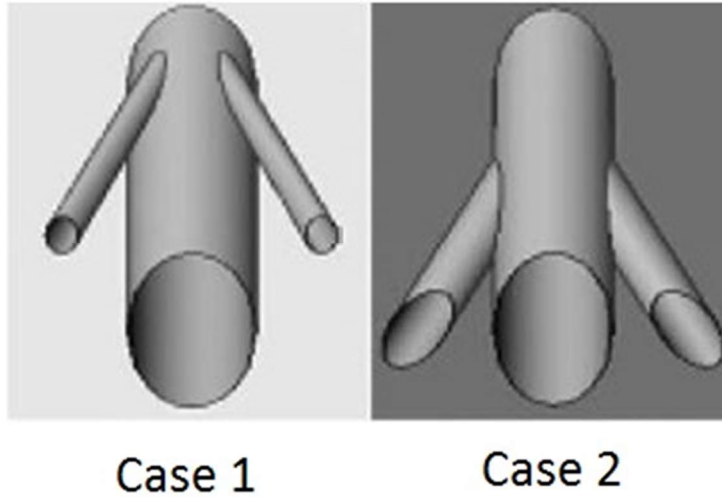


Figure 2.10: Antivortex geometries created by Heidmann and Ekkad [33]

Additionally, regardless of blowing ratio, the new design provided between 30%-40% higher film cooling for half the amount of coolant required by the baseline round holes.

Chi et al. [36] offered another variation of the anti-vortex hole with asymmetric branches, as demonstrated in *Figure 2.12*. It was determined that at the optimum configuration, the asymmetric tripod hole actually outperformed the shaped hole configuration for blowing ratios ranging from  $M = 0.5$  to 2.0. It should be noted that at high blowing ratios ( $M = 2.0$ ), the asymmetric tripod hole showed increased decay in the streamwise direction in comparison to the shaped holes.

Additional novel film cooling shapes have been investigated by Kim et al. [37]. The louver, dumbbell, and crescent shapes (*Figure 2.13*) were compared to the traditional shaped hole using numerical analysis. The louver hole was shown to be completely ineffective compared to the baseline shaped hole. The dumbbell hole and the crescent hole showed essentially the same spatially averaged effectiveness as the shaped hole for blowing ratios ranging from  $M = 0.5$  to 2.0. Okita and Nishiura [38] presented the arrowhead-shaped hole, as shown in *Figure 2.14*. The arrowhead-shaped hole was

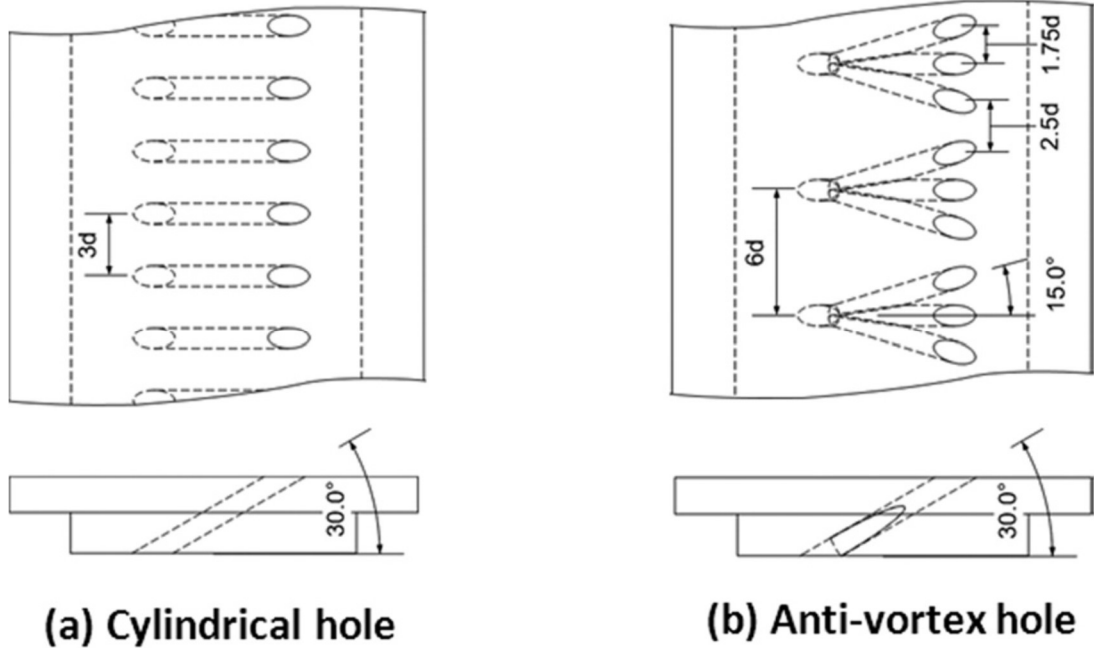


Figure 2.11: Variation of Antivortex geometries created by Leblanc et al. [35]

demonstrated to outperform laidback, fanshaped holes, especially at blowing ratios greater than  $M = 2.0$ . This improvement occurs because the arrowhead-shaped hole has a tendency to redirect the momentum of the coolant towards the surface, reducing jet penetration and mainstream mixing. Furthermore, various patents have been obtained for other shaped holes including hole trenches [39] (*Figure 2.15*) and the multi-lobed hole [40] (*Figure 2.16*).

There are numerous hole designs beyond the baseline shaped hole that have shown either an improvement in effectiveness, or the ability to maintain effectiveness with a simpler manufacturing design. Studies for new hole shapes are ongoing, and several new hole shapes will be presented in the following chapters. Laidback, fanshaped holes work well, but they are not the optimum film cooling hole shape. Presently, baseline shaped holes are the most common hole shape used in the industry due to manufacturing and the lack of sufficient data detailing the effectiveness of other, more

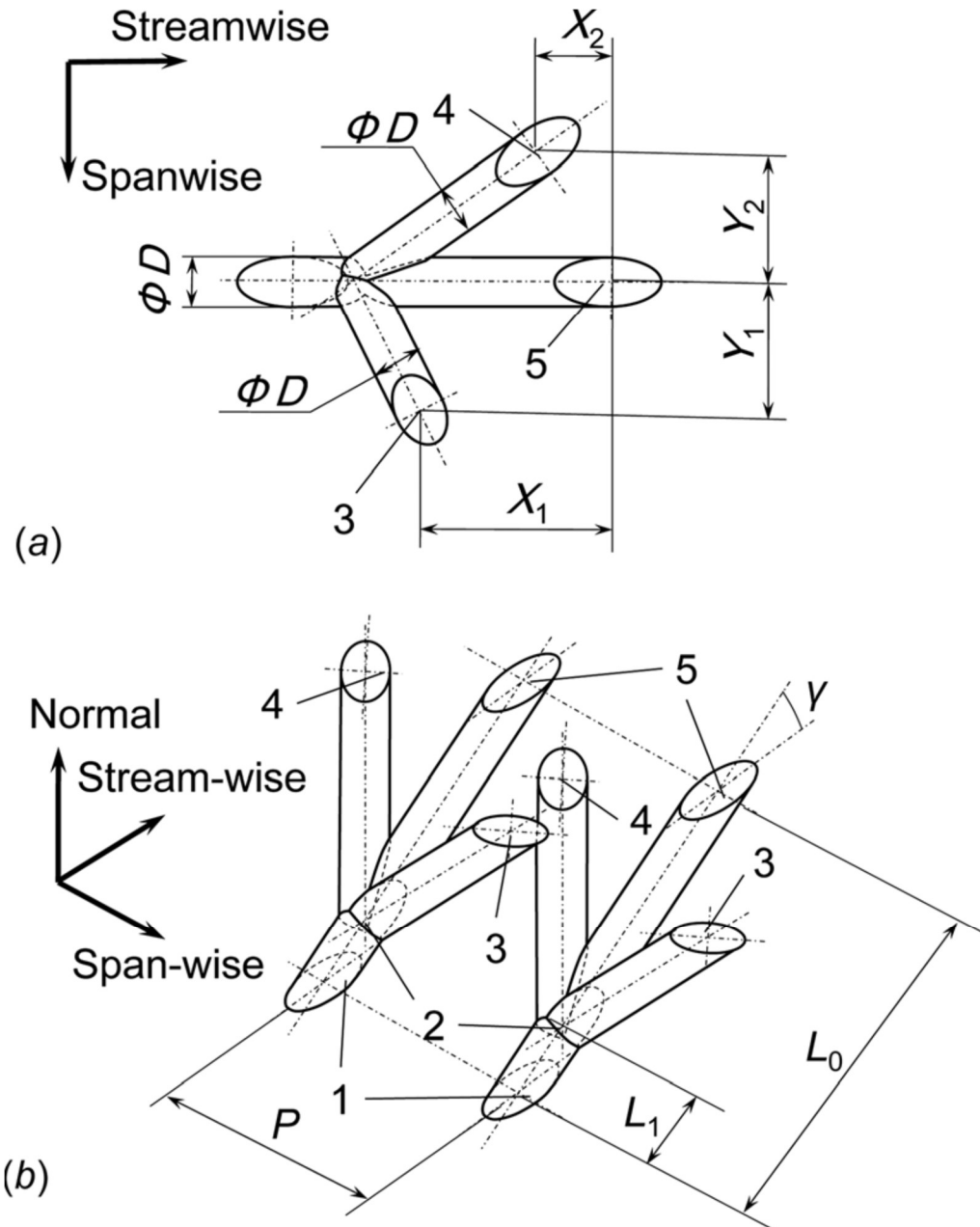


Figure 2.12: Asymmetric antivortex geometries created by Chi et al. [36]

complex geometries. It has been clearly demonstrated that hole shape has an impact on the secondary flows created by coolant and mainstream interaction. The anti-kidney vortices created by the hole are a function of the hole shape, and there must be an optimum shape that will completely counteract the kidney bean vortices that are detrimental to film cooling.

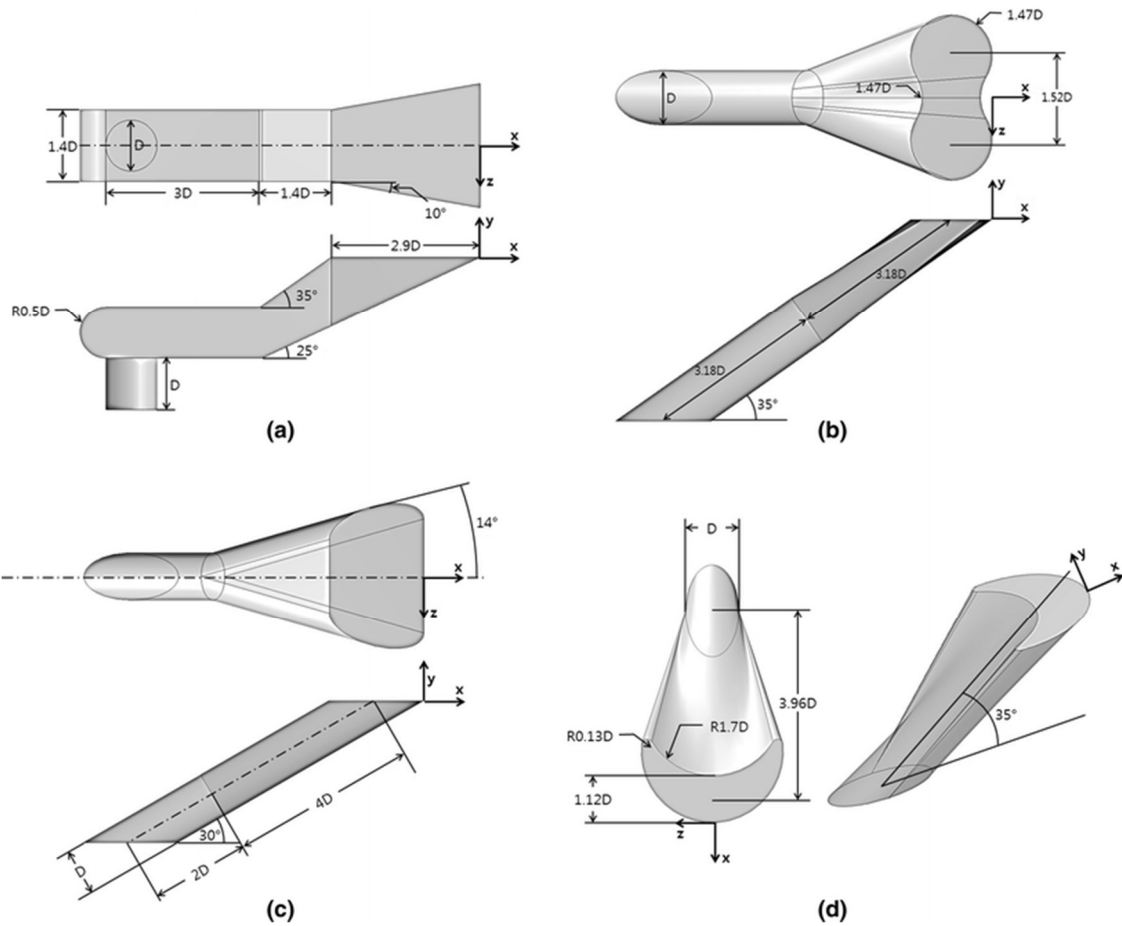


Figure 2.13: Louver (a), Dumbbell (b), Fanshaped (c), and Crescent (d) shaped hole geometries investigated by Kim et al. [37]

### *Effect of Freestream Pressure Gradient*

The effect of freestream pressure gradient is not thoroughly understood. It is important to understand this effect because engine turbine blades are curved and induce freestream acceleration (or deceleration) along the blade. Acceleration in the freestream certainly effects the secondary flows present in film cooling, but unfortunately, the existing literature is not clear on the fundamental effect of freestream acceleration.

The effect of using a curved opposite wall to create mainstream flow acceleration has been studied by various groups, including Lutum et al. [41], Teekaram et al. [42],

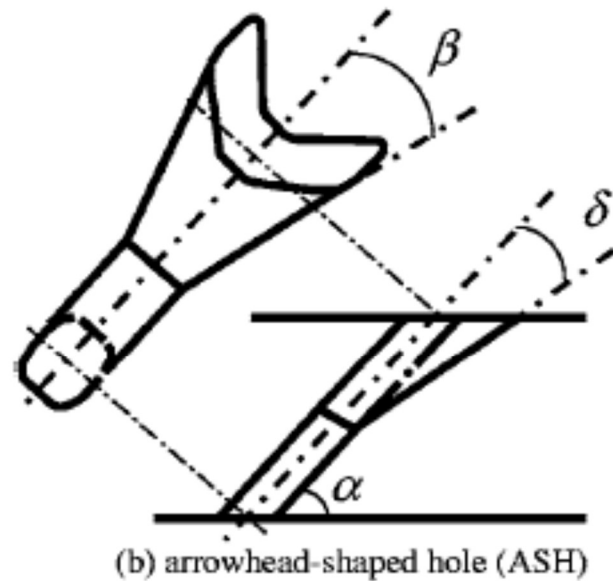
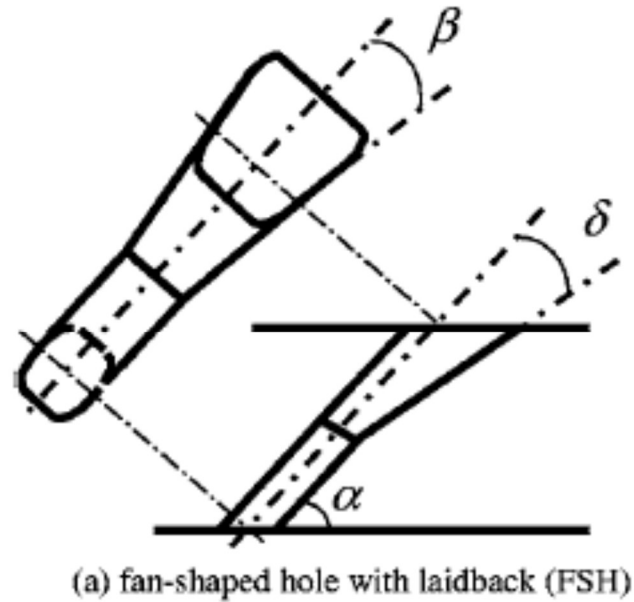


Figure 2.14: Arrowhead-Shaped hole created by Okita and Nishiura [38]

Liess et al. [43], Schmidt and Bogard [44], Launder and York [45], and Coletti et al. [46], with little to no agreement between data. All of these investigations were performed on round holes with acceleration parameters ranging from  $K = 0.8 \cdot 10^{-6}$  to  $K = 4.8 \cdot 10^{-6}$ .

Lutum et al. [41] showed considerable decrease in effectiveness, except in the near hole

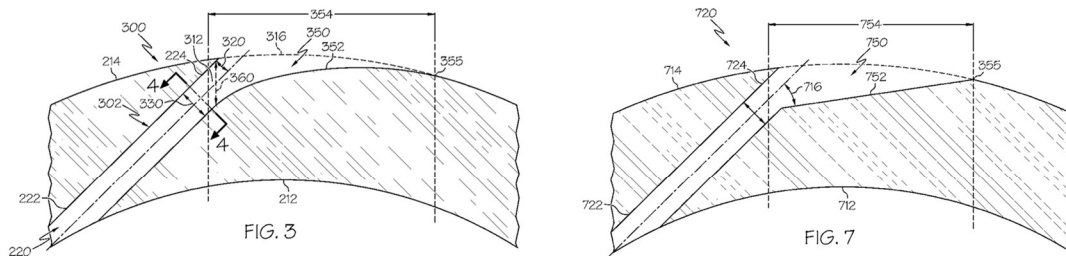


Figure 2.15: Selected trenched hole geometries from US 20130315710 A1 [40]

region using a curved opposite wall. Lutum et al. [41] theorizes that the increase in effectiveness in the near hole region is due to the reduction in jet separation caused by the accelerating freestream. No clear answer is given for the  $\sim 20\%$  reduction in downstream efficiency. Liess et al. [43] showed that there is limited favorable pressure gradient effect at high blowing ratios, but at blowing ratios below  $M = 1.0$  the effectiveness generally decreased in the presence of the pressure gradient. Teekaram et al. [42] shows that there is minimal improvement at low blowing ratios because the cooling jets are still attached to the cooling surface. However, at higher blowing ratios, Teekaram et al. [42] actually shows an increase in film cooling effectiveness in the region immediately downstream of the jet separation point. This data suggests that accelerating freestream flow impacts the point of jet separation. This is a relatively small effect, but nevertheless contrary to the effects shown by Lutum et al. [41] and Liess et al. [43]. Meanwhile, Schmidt and Bogard [44] investigated the effect of accelerating mainstream flow with a density ratio of  $DR = 1.6$  and blowing ratios ranging from  $M = 0.4$  to  $M = 1.5$ . Schmidt and Bogard [44] concluded that the effect of favorable pressure gradient flow is small, but non-negligible. It was determined that the maximum value of effectiveness occurs at slightly elevated blowing ratios. Additionally, the coolant dispersion was increased in the very near hole

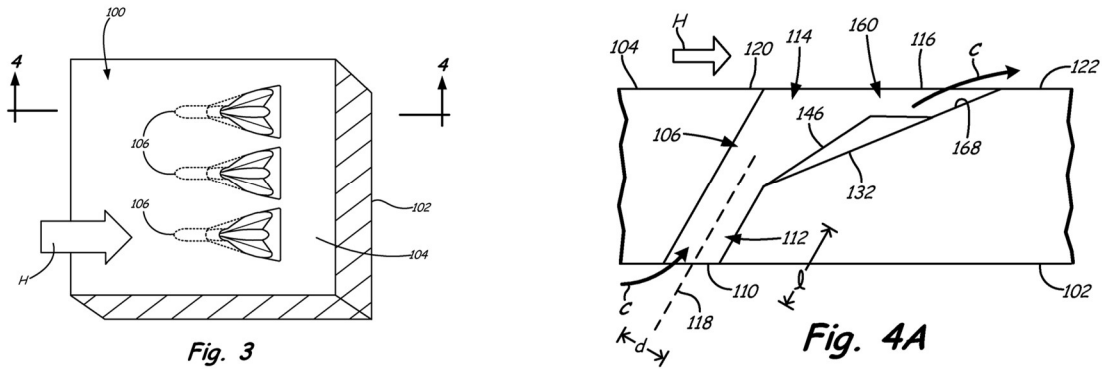


Figure 2.16: Selected Multi Lobed Hole geometries from WO 2013165510 A31 [41]

region. Launder and York [45] demonstrated that not only did the favorable pressure gradient reduce effectiveness, but it also specifically reduced lateral jet spreading. Coletti et al. [46] used magnetic resonance technology to visualize the flow field generated for round hole film cooling under a favorable pressure gradient. It was shown that the favorable pressure gradient caused the jet to remain more closely attached to the wall, improving the cooling performance. However, the counter rotating vortex pair (CVP) is intensified by the FPG which results in reduced spreading of the jet. There are competing fundamental effects from the pressure gradient and the literature has not yet been able to completely resolve them and clarify the interaction between film cooling and accelerating mainstream flows. Additionally, studies with accelerating flow for shaped holes have not been performed to determine the effect of engine mainstream pressure gradients on the film cooling effectiveness of various shaped hole schemes. It would be beneficial to evaluate shaped hole film cooling with accelerating mainstream flows. The turbulent interactions between the coolant and mainstream have been shown to be a function of mainstream flow acceleration. As shaped hole design is based on controlling these

turbulent interactions, it is important to determine whether or not mainstream flow acceleration effects that interaction.

### *Full Coverage Film Cooling*

On turbine blades, the rotation causes significant mechanical stresses that limit the spacing of the film cooling hole. In the combustor liner, however, there is no rotation to consider, which allows for less hole spacing because mechanical stress concentrations are less of a concern. An example of full coverage film cooling is shown in *Figure 2.17* [47]. Full coverage film cooling should be considered separately from single row film cooling applications. The fundamentals of single row film cooling apply to the first row or two of a full coverage film cooling application; but beyond that, row to row interaction begins to dominate over single row effects. The literature has shown that the interaction between rows of film cooling holes creates different flow scenarios that impact cooling performance. The flow condition trends discussed previously for single row applications no longer apply. For example, with single row applications, increasing the blowing ratio beyond  $M = 1$  decreases film cooling effectiveness. With full coverage film cooling

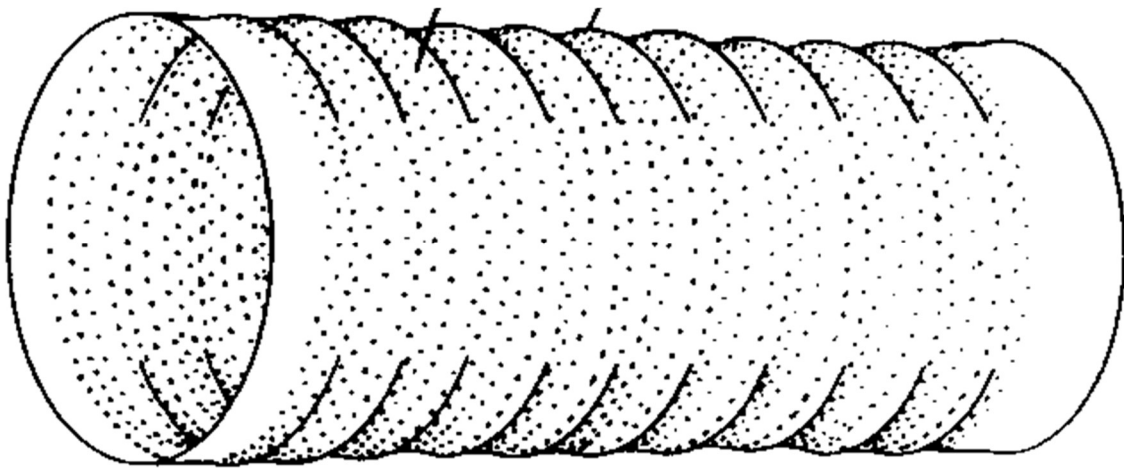


Figure 2.17: Example of effusion cooling used for combustor liner cooling [47]

applications, blowing ratios much higher than  $M = 1$  can lead to more effective film cooling. This occurs because the first row of holes acts as a sacrificial row that thickens the boundary layer and protects the downstream holes, allowing for the cooling jets to stay attached in the downstream region.

Full coverage, or effusion, film cooling has been investigated by Andrews et al. [48], Sasaki et al. [49], Lin et al. [50], Harrington et al [51] and Mayle and Camarata [52]. Andrews et al. [48] investigated simple angle holes inclined at  $\theta = 30^\circ$ , for blowing ratios ranging from 1 to 14. The study found that the film cooling effectiveness increased with each passing row. Additionally, it was determined that the overall film cooling effectiveness increased by 50% when the blowing ratio increased from 1 to 3. However, increasing the blowing ratio from 3 to 14 provided almost no further increase in overall film cooling effectiveness. Sasaki et al. [49] studied lower blowing ratios to determine the benefit of multiple rows over a single row. The accumulative benefit afforded by multiple rows of holes was clearly shown using IR thermography. For a streamwise row spacing of 10 diameters, the data agreed with simple, additive superposition; however, the data did not agree for a streamwise hole spacing of five diameters at a higher blowing ratio. For a higher blowing ratio and closer hole spacing, the coolant is staying attached to the surface and interacting with the coolant from the subsequent row. This interaction has a negative impact on the film cooling effectiveness after the third or fourth row, showing that the coolant is only traveling far enough to interact with subsequent rows after the initial rows of holes have blown into the boundary layer to protect the coolant from the mainstream.

Lin et al. [50] used a mass transfer technique to show that blowing ratios ranging from 1 to 4 had almost zero effect on film cooling effectiveness. Lin et al. [50] and Andrews et al. [48] show conflicting effects for blowing ratio from  $M = 1$  to  $M = 3$ . Harrington et al. [51] has investigated effusion film cooling for blowing ratios from 0.25 to 1, and compared the data to the superposition prediction similar to Sasaki et al. [48]. The results show that superposition results are not matched after a certain number of rows, and the number of rows that match superposition predictions is dependent on the blowing ratio. The region where the effectiveness reaches a maximum value, and falls short of superposition predictions is referred to as the “fully developed region”. This fully developed region corroborates the study performed by Sasaki et al. [48] that suggested that the film cooling performance of downstream rows is impacted by previous rows.

Mayle and Camarata [52] investigated various lateral hole spacing ( $P/d$ ) values for compound angle holes at blowing ratios between  $M = 0.5$  and  $M = 2.0$ . In the first few rows, the lateral spacing has little impact on lateral average film cooling at all blowing ratios studied. However, in the downstream region, the laterally averaged film cooling effectiveness was drastically reduced for high lateral hole spacing. This demonstrates that the interaction between holes is beneficial for full coverage film cooling. Additionally, it was confirmed that the effectiveness continued to increase beyond the optimal blowing ratio for single row applications, though the effectiveness was reduced for  $M = 2.0$ .

The fundamental effect of row-to-row interaction is not completely understood. It appears that the interaction increases the lateral spread of the coolant and creates a more uniform distribution of downstream coolant after the initial rows. There have not been any studies where shaped holes were tested for effusion cooling applications. It is unclear

what effect would result, though shaped film cooling dramatically improved single row film cooling. It is likely that shaped hole film cooling would similarly improve effusion cooling.

### *Flow Trends*

While most studies have focused on the film cooling performance, it is also important to investigate the film cooling flow field that determines film cooling performance. Many studies that investigate film cooling performance present theories about the interactions between the cooling and mainstream flows that cause the various film cooling results. Studying the flow itself is difficult and expensive, but various studies have been completed that measure the flow itself to clarify the secondary flows that determine film cooling performance. In order to fully characterize a flow field, the mean and instantaneous velocity must be determined at every point throughout the area of interest.

Simple flow field measurements, such as local mean velocity, can be obtained using pitot-static probes. Pitot-static probes are only capable of measuring local velocity in a single direction. Five-hole probes are capable of breaking down local, average velocity components into three orthogonal directions through an extensive calibration process as described by Morrison and Tung [53]. Five-hole probes are limited by only being able to take local measurements, and have no capacity for measuring instantaneous velocity because of a limited response time incapable of capturing turbulence.

Instantaneous velocity fluctuations in all three dimensions, however, can be obtained with triple-wire hot wire anemometry systems. Zhou and Wang [54] and Blair and Bennet [55] have previously used the triple-wire hot wire anemometry measurement

technique to measure instantaneous velocity fluctuations in a turbulent boundary layer. The probe impacts the flow field being measured, which limits the ability of the experimentalist to characterize turbulent flows.

Recent improvements have led to flow field measurements that do not intrude into the flow. The two new methods are laser doppler velocimetry (LDV), or laser Doppler anemometry (LDA), and particle image velocimetry (PIV). PIV, and more advanced versions of PIV such as stereoscopic particle image velocimetry (S-PIV) and volumetric PIV will be discussed extensively in chapter 4.

Laser Doppler velocimetry is a non-intrusive, optical measurement technique which captures the Doppler shift of reflected light from particles passing through a laser beam in a moving fluid. To begin operation, flow is seeded with reflective particles. Typically, a single laser beam is split in two. Special optics are then used to rejoin the separated beams at a desirable focal point within the flow. At the point of the beam intersection, the entrained particles passing through reflect light which is then collected by receiving optics and measured by a photodetector. The Doppler shift is observed between the reflected scattered light and incident light of the laser itself, allowing for a calculation of velocity [56]. Although employing a single laser produces only one vector of velocity for a point, this technique can be used to make turbulent velocity measurements in a film cooling boundary layer. To determine detailed velocity vector distributions of the flow with this technique, advanced systems include a traverse.

Pietrzyk et al. [57] evaluated the effect of density ratio on standard round hole film cooling by measuring the turbulence characteristics in the boundary layer downstream of the hole using LDV. It was shown that for  $DR = 2.0$  and  $1.0$ , the

maximum turbulence and shear values were similar immediately downstream of the hole. However, the higher density ratio flow maintained elevated turbulence and shear much farther downstream than the unity density ratio. Thole et al. [58] used LDV to visualize the effect of laidback and laidback, fanshaped holes by comparing them to the baseline round case. It was determined that the velocity gradients were dramatically reduced for the shaped holes, which reduced downstream turbulence production. The location of maximum turbulence for the shaped hole was actually found to be over the hole exit, whereas round hole turbulence peaks further downstream. The study showed that turbulent mixing actually begins inside the hole for shaped film cooling, which is important to confirm previous effectiveness results. Beyond that, it is also beneficial information for hole shape designers.

Unlike LDV, PIV is capable of measuring many points at once, leading to much higher spatial resolution. For this reason, PIV will be the method used to examine the film cooling flow fields related to this work. The method, application, and previous use of the various forms of PIV will be discussed in chapter four.

The primary purpose of this literature review is to present the complexity of factors that impact film cooling performance, and more importantly, film cooling design. Despite the effort and money poured into film cooling research, there is still a dearth of comprehensive studies that consider all of the effects that occur in modern film cooling applications. For this reason, the fundamental effect of each film cooling factor must be well understood. There are three primary factors noted in this chapter that are not yet fundamentally understood: effect of hole shape, effect of freestream acceleration, and effect of full coverage film cooling. The goal of this thesis is to investigate those three

factors for a range of blowing ratios and density ratios to clarify the fundamental nature of each factor. The goal of this thesis is to present data that film cooling designers can use to design film cooling holes to perform optimally.

## CHAPTER THREE

### Pressure Sensitive Paint for Film Cooling Effectiveness Measurements

#### *General Film Cooling Measurement Background*

In order to evaluate film cooling designs, the film cooling effectiveness ( $\eta$ ) must be measured experimentally. Han et al. [1] catalogued the variety of experimental techniques that have been employed for this purpose. The difficulty in measuring the film cooling effectiveness lies in the determination of the film temperature. Measuring the mainstream temperature and coolant temperature can be accomplished with thermocouples, as those temperatures do not experience sharp spatial gradients. The film temperature, however, changes significantly in space and requires determining the temperature in a boundary layer near a wall. High resolution, non-intrusive measurements are required to determine the film temperature. The film temperature can be measured by thermocouples and heat flux gauges, but it must be assumed that the film cooling surface is adiabatic. As this is never actually true in experimental setups, the heat loss must be calculated and the determination of the film temperature is difficult. Furthermore, thermocouples intrude into the boundary layer and affect the measured flow. For these reasons, the primary techniques used to evaluate the film temperature are optical techniques. Optical measurements are also preferred because of the high resolution, as each pixel is a measurement. Some of these optical techniques still require assuming the adiabatic wall condition, but others do not.

### Optical Film Cooling Effectiveness Measurement Techniques

One of the most widely used optical techniques takes advantage of the properties of thermochromic liquid crystals (TLC). Liquid crystals change phase when heat is transferred to them. While in the phase change, the color displayed by the crystal depends on the ratio of solid to liquid phase, and that ratio depends on the temperature of the crystal. When the crystal is not undergoing a phase change, no color is displayed. This transition is detailed in *Figure 3.1* [59]. Using an RGB camera, the red, green and blue “color” emitted by a film cooled surface coated in TLC can be converted to hue, saturation, and intensity (HSI). Intensity and saturation are controlled by maintaining uniform lighting and using software to control saturation. Image hue is then the variable of importance to determine temperature, which is directly related to the “color” of the TLC. The hue of the TLC is then converted into a surface temperature by comparing images of the TLC paint at known temperatures obtained by embedding a thermocouple in the painted surface. The film temperature, and then the film cooling effectiveness is

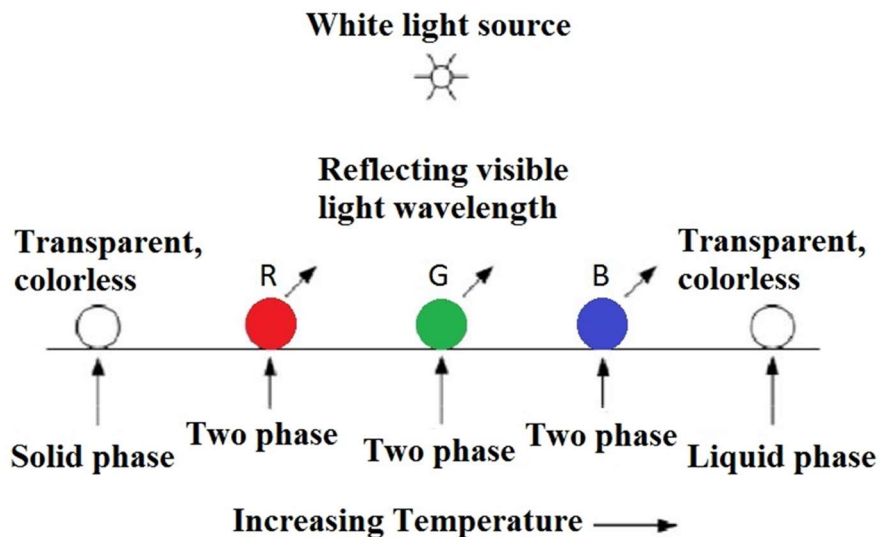


Figure 3.1: Fundamental principle of TLC paint [59]

either calculated with the steady state technique or the transient technique. The steady state technique requires that the adiabatic wall boundary condition is met, which requires that heat loss be accounted for. The transient technique allows for the film temperature to be calculated with the heat transfer coefficient by simultaneously solving equations 3.1 and 3.2.

$$\frac{T_{w1} - T_i}{T_f - T_i} = 1 - \exp\left(-\frac{h^2 \alpha t_1}{k^2}\right) \operatorname{erfc}\left(\frac{h\sqrt{\alpha t_1}}{k}\right) \quad (3.1)$$

$$\frac{T_{w2} - T_i}{T_f - T_i} = 1 - \exp\left(-\frac{h^2 \alpha t_2}{k^2}\right) \operatorname{erfc}\left(\frac{h\sqrt{\alpha t_2}}{k}\right) \quad (3.2)$$

The transient method can be used to determine the wall temperature at two separate times for each pixel. The transient TLC method has been used by Ekkad and Han [60] along with Kwak and Han [61] to evaluate film cooling effectiveness.

Infrared thermography (IR) can be used similarly to TLC methods as a non-intrusive measurement technique where the surface of a test plate is observed from outside the flow path and the wall temperatures can be quantified. IR thermography utilizes equation 3.3, which describes the net radiation heat flow between two objects.

$$Q = \varepsilon \sigma A (T_1^4 - T_2^4) \quad (3.3)$$

The emissivity ( $\varepsilon$ ) is defined as the measure of an objects efficiency in emitting radiation as compared to a black body. In order to determine the emissivity, the film cooling surface is painted black so that the emissivity can be known. The Boltzmann constant ( $\sigma$ ) is a known quantity, and the temperature of the IR sensor ( $T_2$ ) is held constant, so the surface temperature ( $T_1$ ) can be determined by measuring the heat flux. The heat flux is measured using quantum detectors capable of converting the energy in the IR wavelength

range into an electrical signal. The surface temperature of the film cooled surface is then determined and then the same steady state or transient technique mentioned previously for the transient liquid crystal method can be used to simultaneously calculate the film cooling effectiveness and heat transfer coefficients. The transient technique is often used in place of a steady state technique so that miscellaneous heat losses are not present. The spatial resolution is limited by the array of sensors rather than the camera pixels. The IR technique has been demonstrated to work in film cooling scenarios with both the transient method [62] and the steady state method [63].

The temperature sensitive paint (TSP) technique is an alternative optical heat transfer measurement technique that is commonly used to measure film cooling effectiveness. TSP is similarly unobtrusive with a high spatial resolution just as TLC methods, where every camera pixel is a measurement. When the paint is excited by incident light of a certain wavelength, it emits light at a different, yet quantifiable wavelength. When the molecules are excited by the incident light, the energy is either dissipated through emission of radiation or through radiationless deactivation. Radiationless deactivation, which is also referred to as thermal quenching, increases in likelihood with the temperature of the paint molecules. Thermal quenching involves releasing a photon, which then returns the molecule to the ground state. The intensity of light emitted by the paint molecule is a function of the temperature only. A calibration can be established by capturing images at known temperatures and determining the relationship between light intensity and temperature for the particular setup. The setup and process for TSP measurements is described by Liu et al. [64] and the calibration setup is shown in *Figure 3.2*. The setup has been used to determine film cooling

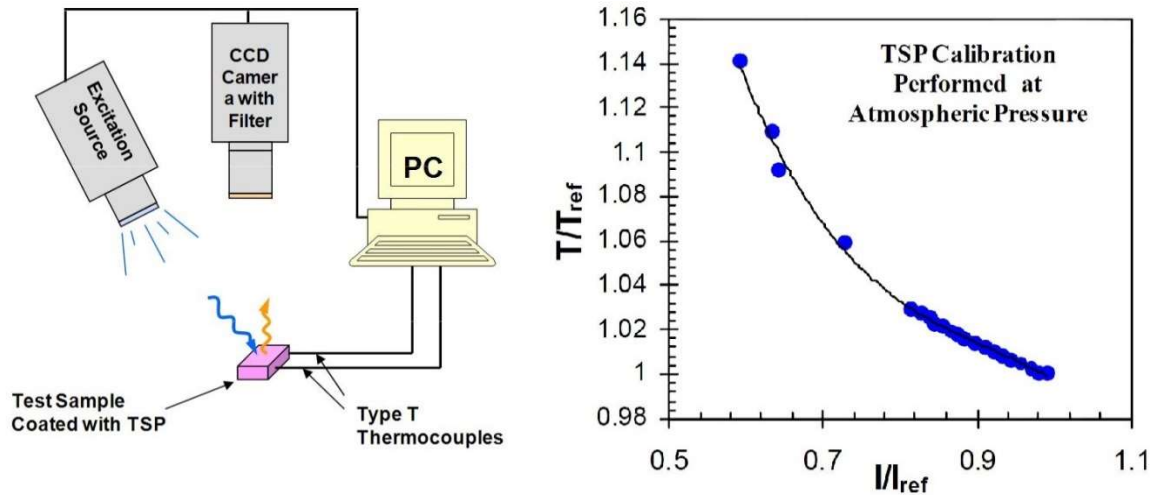


Figure 3.2: Experimental setup and calibration curve for TSP [64]

effectiveness with the steady state technique by Kunze et al. [65] and the transient technique by Russin et al. [66].

### *Mass Transfer Film Cooling Measurement Techniques*

The drawback for most of the previously mentioned methods for measuring the film temperature is that they either require an adiabatic wall assumption, or must use a transient test. It is impossible to create a truly adiabatic wall, so it can be preferable to use a mass transfer technique. Walls are impermeable to mass, so this difficulty in heat transfer techniques is avoided. Mass transfer techniques rely on the fundamental analogy that concentration can be directly related to temperature. If the coolant and mainstream flows have completely separate gases, then the mixture of the gases on the surface reflects the effectiveness of the coolant in staying attached to the surface, just as the film temperature determines the effectiveness of coolant in the same way. If the concentration of gas at the wall can be measured, then film cooling effectiveness can be determined.

Some of the approaches which employ this mass transfer analogy are foreign-gas concentration sampling, ammonia-diazo, and pressure sensitive paint (PSP).

Foreign gas sampling utilizes a gas not present in air as the “coolant”. Even though the coolant is at the same temperature as the mainstream, the technique functions by sampling the gas near the wall and measuring the concentrations of air and foreign gas. *Figure 3.3* [9] shows the method used to measure the gas concentrations at the wall. Tiny portholes are placed downstream of the film holes and the gas concentration is determined using gas chromatography. The holes are made to be small enough so that they do not influence the flow. This means that the effectiveness can only be determined at discrete locations, and the size of the holes required to sample the gas limits the spatial resolution of the measurements. The advantage of this technique is that it can simulate actual density ratios which occur inside real gas turbine engines without operating at high temperatures. Foreign gas sampling is described in detail by Pederson et al. [9], who

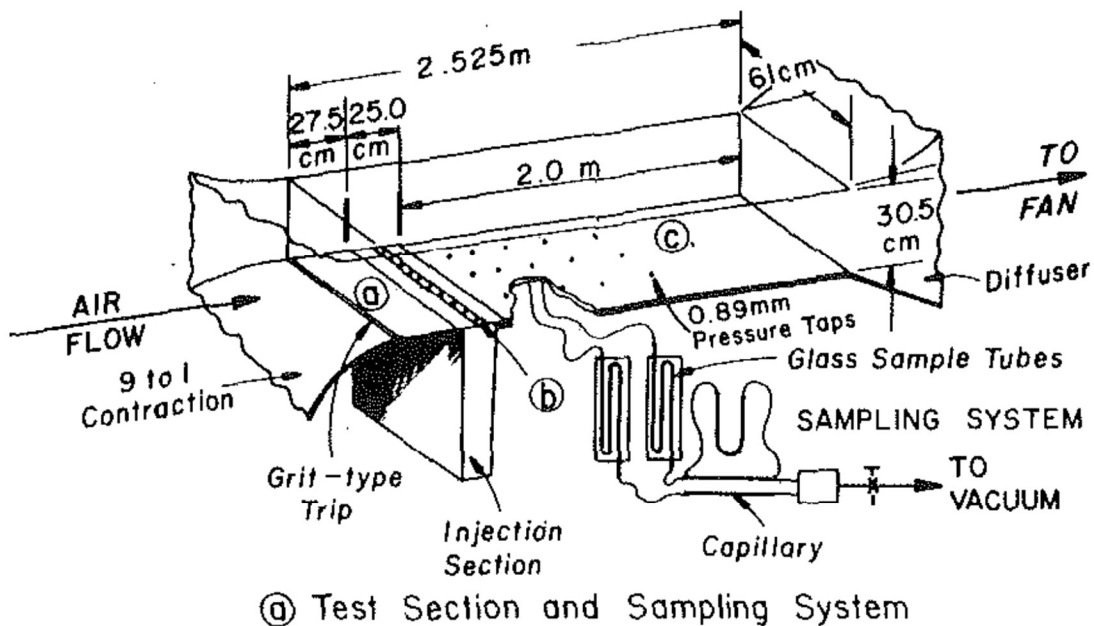


Figure 3.3: Experimental setup for foreign-gas sampling [9]

studied the effects of large density differences on round cooling holes. The technique has since been used by Goldstein and Chen [67] and Takeishi et al. [68] to evaluate film cooling effectiveness.

Another mass transfer method, the ammonia-diazo technique, was initially developed for flow visualization. The technique is based off of the reaction between ammonia gas and diazo paper. The film cooling surface is covered with a diazo-coated paper, and when pure ammonia gas passes over the surface, it leaves a dark trace. In order to perform the experiment, the coolant is seeded with ammonia and water vapor which reacts with the diazo and leaves traces as it is transported across the surface. The darkness of the traces is determined by the surface concentration of ammonia gas and water vapor. The first quantitative effectiveness measurements were obtained by Soechting et al. [69]. The technique was then improved by Friedreichs et al. [70], providing a method for calibrating the darkness of the ammonia gas traces to specific ratios of ammonia gas and water vapor on diazo paper (*Figure 3.4*). After conducting an experiment, the test surface is exposed to light and fixed to prevent further reaction, much

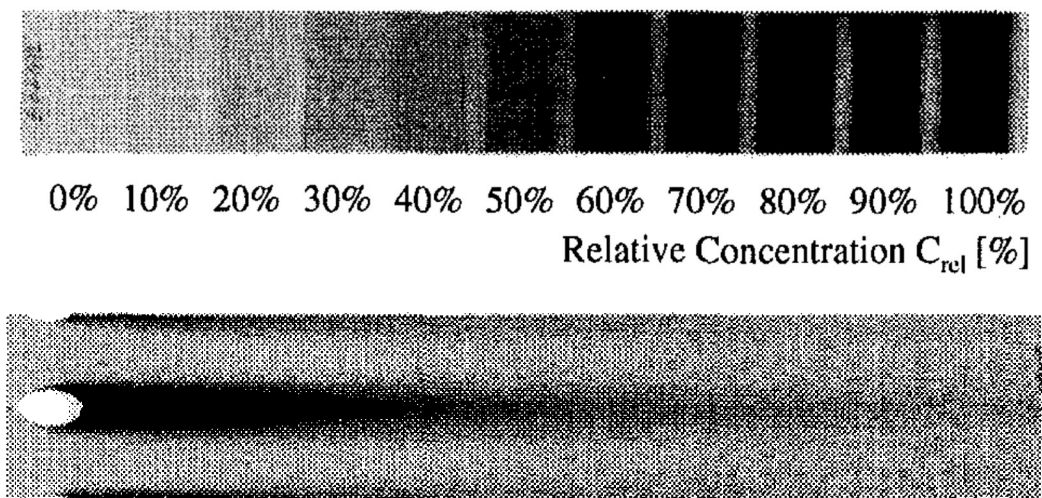


Figure 3.4: Calibration and sample ammonia-diazo trace [70]

like a photograph. Since the mainstream is not seeded with ammonia gas and water vapor, the concentration is zero. The adiabatic film cooling effectiveness is then determined from a ratio of the wall concentration of ammonia gas and water vapor over the concentration inside of the plenum from which the coolant is dispersed.

### General PSP Background

The mass transfer method of PSP, developed by Zhang et al. [71], utilizes a distinctive paint, composed of luminescent molecules suspended in a polymer binder. When the luminescent paint molecule is illuminated by an energy source such as an LED light, the molecule achieves an excited energy level. The molecules are oxygen quenched, which means that they will only emit a photon at this excited energy level when there is no oxygen present to return the molecule to the original state. This interaction is illustrated in *Figure 3.5*. This characteristic of the paint can be leveraged to determine film cooling effectiveness through a mass transfer analogy.

As previously discussed, the film cooling effectiveness can be determined by the concentrations instead of temperatures. In the case of PSP, the concentrations measured are defined as the concentration of oxygen because the paint responds to the concentration of oxygen. The concentration of oxygen in the foreign gas coolant should

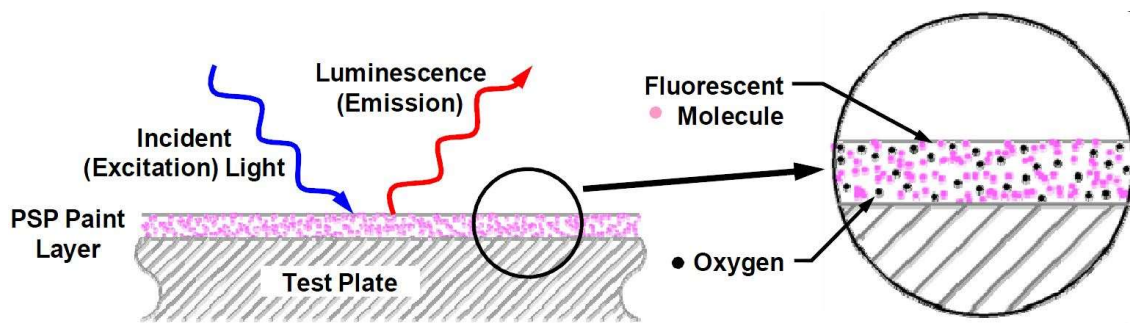


Figure 3.5: Fundamentals of PSP operation [2]

be negligible. The concentration at the wall can be directly related to the partial pressure of oxygen at the wall. The intensity of fluorescence from the paint is determined by the local partial pressure of oxygen. This series of equations is described in equation 3.4.

$$\eta = \frac{T_{\infty} - T_f}{T_{\infty} - T_c} = \frac{C_{\infty} - C_{Mix}}{C_{\infty} - C_{fg}} = \frac{(P_{O_2})_{Air} - (P_{O_2})_{Mix}}{(P_{O_2})_{Air}} \quad (3.4)$$

The film cooling effectiveness has been previously defined in equation 1.1, and  $C_{\infty}$  is the concentration of oxygen in the mainstream,  $C_{fg}$  is the concentration of oxygen in a foreign gas ( $C_{fg} = 0$ ), and  $C_{mix}$  is the concentration in the mixture of the mainstream and coolant. Then  $P_{O_2}$  is the partial pressure of oxygen for the given test. The method for determining the local partial pressure of oxygen is explained later in the experimental procedure section.

### *Literature Review of PSP for Film Cooling*

Before PSP became more widely used, it was validated against the more established heat transfer techniques that have been previously mentioned. It was necessary to confirm that the results were not a function of the new experimental method. Wright et al. [2] compared PSP to steady state TSP and IR Thermography on a flat plate, and found that the PSP measuring technique had a negligible influence on the results. Gao et al. [72] similarly compared PSP on a cylinder to transient IR thermography and determined that PSP returned similar results in this case as well. With the experimental technique well established through these comparisons, it has since been applied to investigate numerous film cooling flows. Zhang et al. [18] used PSP to evaluate film cooling flows on a flat endwall. Ahn et al. studied blade tips [73] and the blade leading edge in rotating flows [74,75] using the PSP technique. Suryanarayanan et al. [76] also

used PSP to investigate film cooling effectiveness on a rotating blade platform. It has been sufficiently demonstrated that PSP is a valid technique for obtaining detailed film cooling effectiveness distributions in a wide variety of conditions. PSP results are generally accepted and will be utilized to determine the film cooling effectiveness of various unique geometries.

### *PSP Experimental Procedure*

The theory has shown that film cooling effectiveness can be determined on a flat plate coated with PSP if the local partial pressure of oxygen is known. The local partial pressure of oxygen is difficult to measure, so a reference condition is established. A pressure ratio is established by dividing the local measured pressure by the reference pressure at 1 atm. Under 400 nm LED light, the intensity of fluorescence given off by each PSP molecule is related to the local partial pressure of oxygen. The intensity is captured by a 1600 x 1200 resolution 14-bit CCD (charge-couple device) camera, fitted with a 570 nm filter. The measured intensity is similarly referenced to atmospheric conditions so that it can be converted to the required pressure ratio. A reference image is taken with the LED light on, but without any flow. In order to remove optical noise from the camera, a black image is also taken (LED off, no flow) and subtracted from each measured intensity value. The intensity ratio is shown in equation 3.5,

$$\frac{I(P)_{ref} - I_b}{I(P) - I_b} = f(P; P_{ref}) \quad (3.5)$$

where  $I_b$  is the black intensity,  $I(P)_{ref}$  is the measured intensity for the reference images, and  $I(P)$  is the measured intensity for the given test. In order to determine the pressure

ratios required for film cooling effectiveness calculations, a calibration must be performed to convert measured intensities back to pressure ratios.

In order to generate the calibration curve, a small sample test plate is coated with Uni-FIB PSP (UF470-750) supplied by Innovative Scientific Solutions, Inc. (ISSI) in the exact same conditions as the film cooling plate. The test plate is placed inside a vacuum chamber in a similar position as the film cooling plate relative to the camera and light. In order to generate the intensity ratio shown in equation 3.5, images are taken with no light on (black), with LED on at atmospheric pressure (reference), and at various pressures controlled closely with the vacuum pump using the setup shown in *Figure 3.6*. In each case, 200 images are recorded and averaged to decrease the uncertainty. The measured intensity ratios and pressure ratios are related using a cubic regression as shown in *Figure 3.7*. With an established calibration, any measured intensity ratio can be converted to pressure ratio and then directly to film cooling effectiveness.

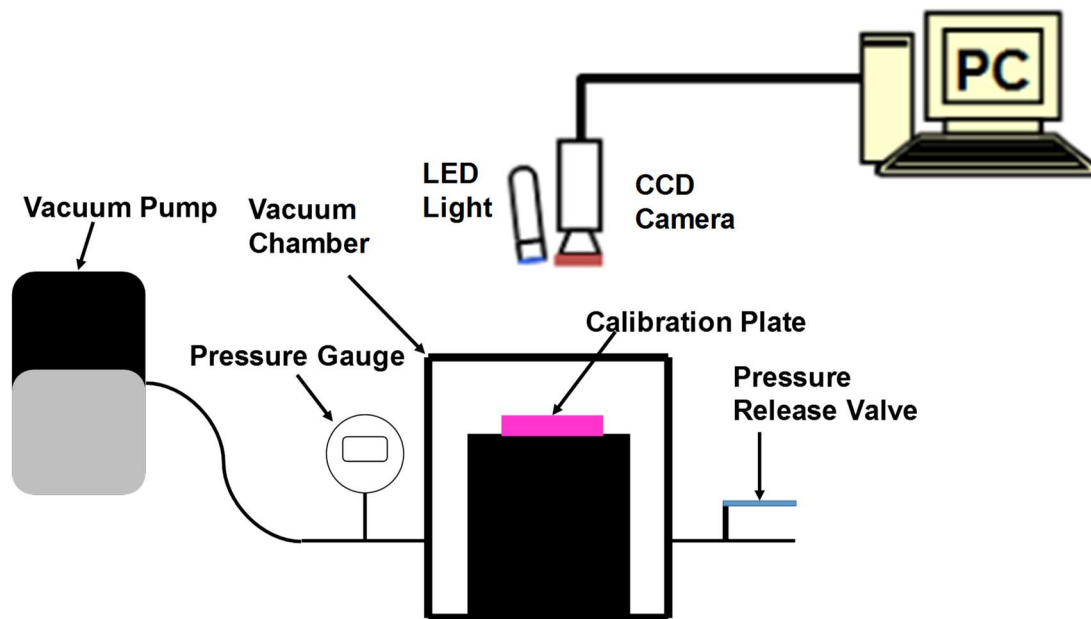


Figure 3.6: PSP calibration setup

It should be noted that according to Wright et al. [77], the measured pressure is a function of paint temperature, so the calibration and tests must be performed at the same temperature. Throughout this study, all PSP images were recorded at ambient room temperature.

Once the calibration is complete, the painted film cooling plate can be inserted into the test section. The camera and light are positioned such that the entire plate is captured by the camera and illuminated by the light. *Figure 3.8* shows the test section and optical equipment. Recall from equation 3.5 that two pressure ratios are required: air as coolant and a foreign gas (no oxygen) as coolant. In order to get the two intensity

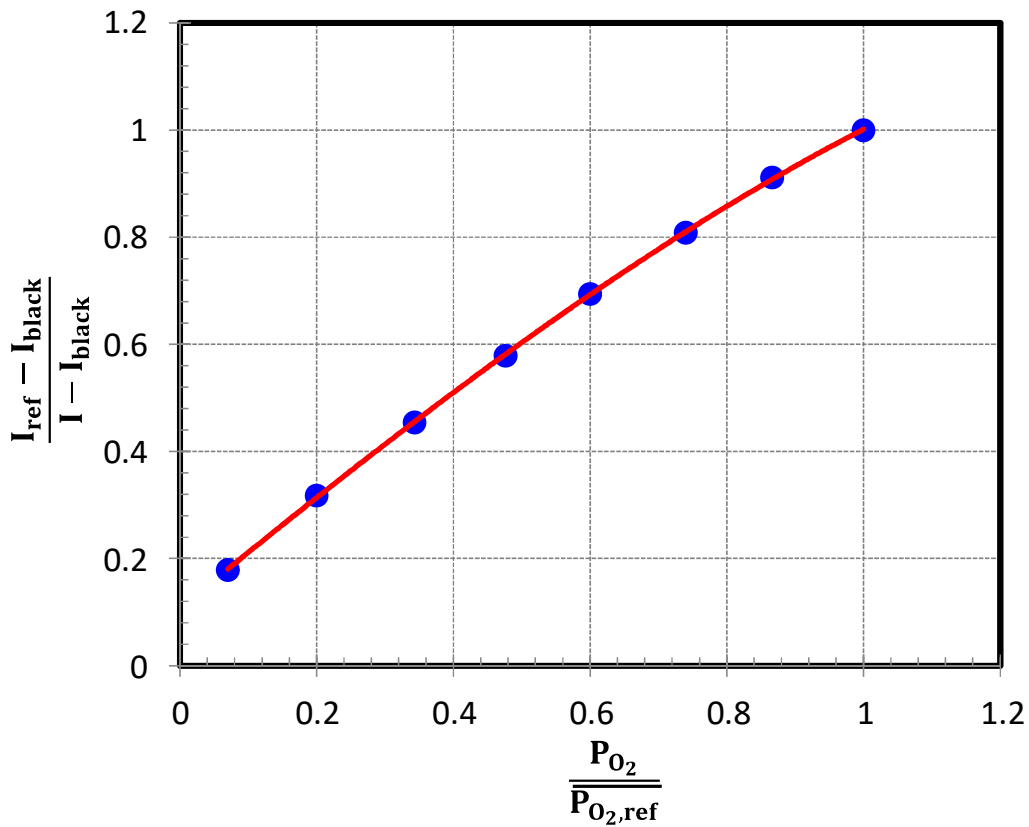


Figure 3.7: PSP Calibration Curve

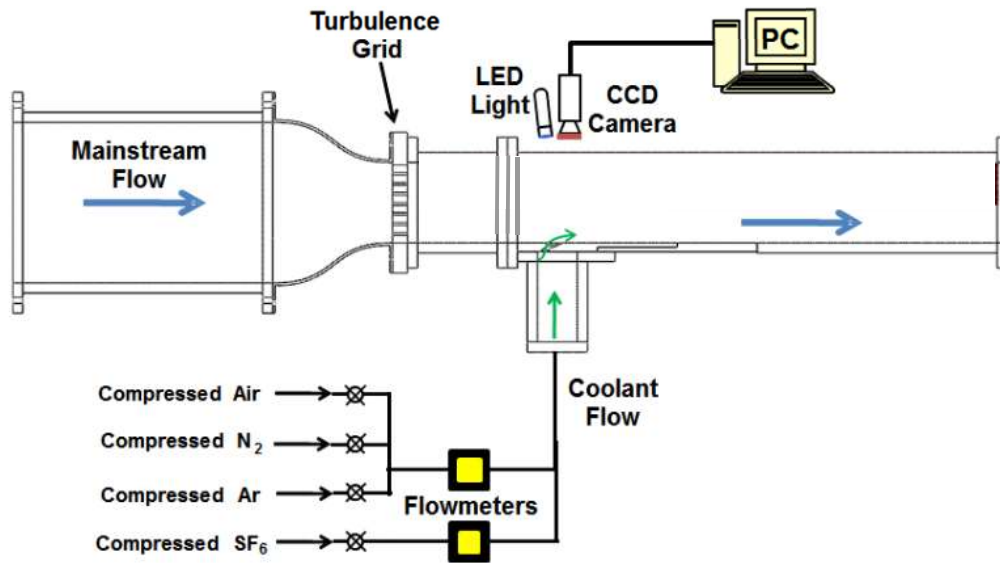


Figure 3.8: Overview of the low speed wind tunnel with PSP experimental equipment

ratios required, four images of the test plate are taken. One dark image (LED light off, no flow), one reference image at atmospheric pressure (LED light on, no flow), an air injection image (LED on, air as coolant), and a foreign gas injection image (LED on, foreign gas as coolant). The foreign gas used for this experiment is either nitrogen (N<sub>2</sub>) or some of argon (Ar) and sulfur-hexafluoride (SF<sub>6</sub>) depending on the desired density ratio. As with the calibration, 200 images are recorded and averaged for each case to remove turbulent fluctuations and reduce uncertainty.

### *Uncertainty Analysis*

The uncertainty of the PSP technique has been determined using the method established by Kline and McClintock [78]. As shown previously in equations 3.4-3.5, the film cooling effectiveness can be directly related to the measured intensity of light emitted for each of the 4 tests. The uncertainty is therefore different for each pixel. To

minimize the random uncertainty of the intensity measurements (black intensity, reference intensity, and test intensity), each image represents the average of 200 individual images. The procedure is also followed for the images recorded during the PSP calibration. The uncertainty of the intensity of each measured pixel is mostly a function of the uncertainty of the camera measurement, but also depends on the accuracy of the calibration. The calibration accuracy is considered to be negligible compared to the uncertainty of the camera, except for extremely low values of effectiveness ( $\eta < 0.05$ ), where the error of the calibration is much higher. As the intensity ratio approaches unity, the overall uncertainty increases, corresponding to effectiveness values approaching zero. When the film cooling effectiveness is measured to be 0.7, the experimental uncertainty is calculated to be 2.3%. As the measured effectiveness decreases to approximately 0.4, the experimental uncertainty increases to 7.9%, and as the measured effectiveness continues to decrease, the uncertainty increases. For all flow conditions presented in this study, the experiments are repeated to ensure the results can be replicated.

## CHAPTER FOUR

### Stereoscopic Particle Image Velocimetry in Film Cooling Flows

#### *General PIV Background*

Particle image velocimetry (PIV) is a non-intrusive flow field measurement technique, capable of determining a distribution of velocity and vorticity vectors simultaneously in a plane. Flow field measuring techniques such as PIV are vital for clarifying the physical effects that determine film cooling effectiveness results. While the effectiveness results provide the first step towards describing the interaction between the coolant and mainstream flows, they cannot give the full picture. In order to design an optimum film cooling scheme, full characterization of the primary and secondary flows involved in film cooling is necessary. Clearly defined measurement of vortex formation especially allows for improved hole shape design and evaluation.

Ideally, three dimensional mean velocity and instantaneous velocity fluctuation vectors would be known at a high resolution for an entire volume. This is possible, using a new technique called volumetric PIV, but the equipment cost and computing time are increased substantially. Two dimensional PIV is capable of determining mean and instantaneous velocity measurements in two dimensions within a plane using a single camera. Stereoscopic PIV (S-PIV) is capable of determining mean and instantaneous velocity measurements in three dimensions within a plane using two cameras. Two dimensional PIV and S-PIV can be employed strategically to approximate the ideal characterization of the entire volume.

PIV actually captures seed particle movement, rather than flow movement itself. In order for the data gathered by PIV to be accurate, the fundamental assumption that the tracked seed particles are behaving the exact same way as the untracked fluid must hold true. In order to ensure this, the solid particles must be extremely low density. In gas flows, the tracked particle must have a diameter of less than one micrometer. At this small size, the seed particle effectively has no inertia, so it will follow the air particles wherever they move without interfering in the flow [59].

In order to track a seed particle, it must be captured by a camera. To allow the camera to distinguish the particles, they must be illuminated. A laser sheet is used to illuminate the particles and establish a plane of interest. Only seed particles that are within the thickness of the laser plane will be captured by the camera. For two dimensional PIV, a camera is placed perpendicular to the laser sheet. The camera takes image pairs, separated by a large enough time that the particles move a perceivable amount, but the separation time must also be small enough to keep the particles within small regions called interrogation regions. In order to determine velocity vectors from the image pair, the images are divided into interrogation regions. Interrogation regions are based on the assumption that the region is small enough such that all of the particles within the region will have a uniform velocity. The regions must also be large enough to ensure that there are at least 10 particles in each interrogation region. However, decreasing the size of the interrogation regions increases the spatial resolution of vector distribution. Each interrogation region from image 1 is compared to the corresponding region in image 2, and a single velocity vector is determined for each interrogation region. The concept of interrogation regions is illustrated in *Figure 4.1*. There is no

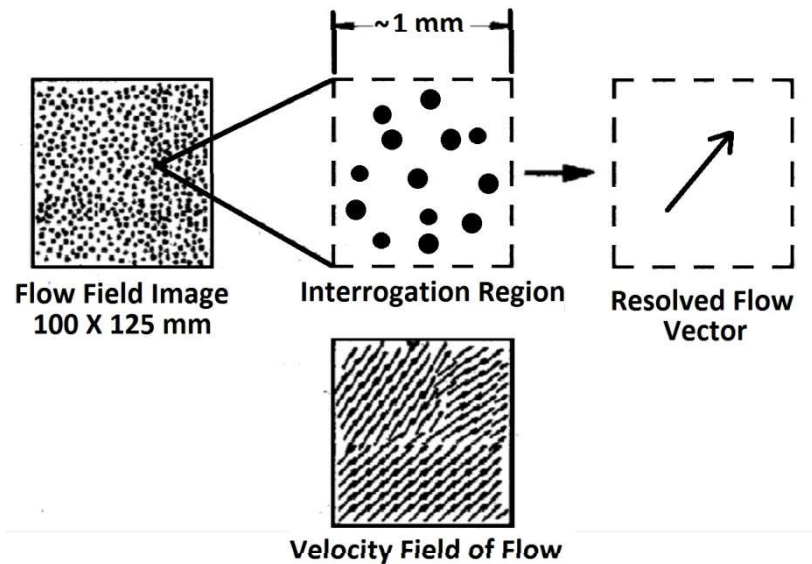


Figure 4.1: Velocity field production from interrogation regions [59]

guarantee that particles will not move out of the interrogation region during the separation time. Therefore, the particles cannot truly be tracked, but rather a statistically most likely velocity vector is established. A cross-correlation is used to determine the pixel displacement between the images. The separation time is known, so the velocity vectors can be determined if pixel displacement can be converted to physical distance. In order to do this, spatial calibrations are performed before beginning the test.

This task is accomplished by placing a calibration plate inside the test section such that it lines up directly with the laser light sheet. The camera can then be focused on the calibration plate, which has an added benefit of ensuring the camera is focused on the illuminated seed particles during the actual test. For a plate with known dimensions, an image is taken so that physical distance on the plane of interest is directly related to the pixel number. With the calibration in hand, the velocity vectors can be calculated for each interrogation region.

An example experiment is shown in *Figure 4.2*. To begin the experiment, desired flow conditions are set within the test section, and the flow is seeded. The laser light sheet is triggered to illuminate the seed particles in the desired plane and an image is recorded. After the separation time has passed, another laser pulse is triggered and a second image is recorded to complete the pair. The images are then analyzed to determine two dimensional velocity vectors within the plane.

Two dimensional PIV has been used by various groups to investigate and characterize the flow fields that result from film cooling. Simple angle cylindrical holes were observed using PIV by Gogineni et al. [79] for varying jet Reynolds numbers and turbulence intensities. Two dimensional velocity vectors and instantaneous vorticity distributions were presented for varying blowing ratios ( $M = 0.7$  to  $1.5$ ) and freestream turbulence ( $Tu = 1\%$  to  $17\%$ ) for a set jet Reynolds number ( $Re = 40,000$ ). Results indicated that at low blowing ratios ( $M = 0.7$ ) the size of eddies directly downstream of

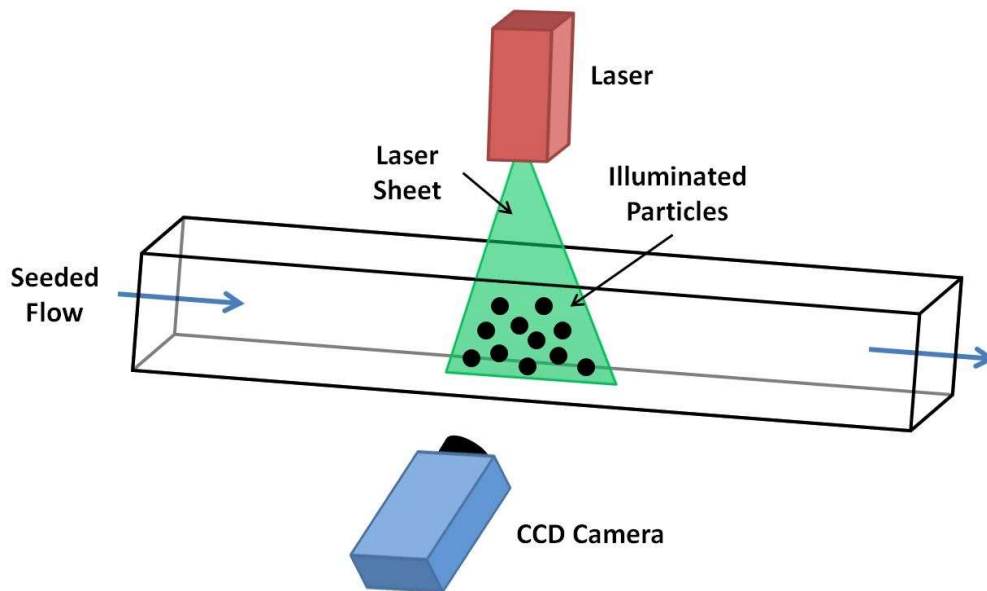


Figure 4.2: 2D-PIV experimental setup [59]

the film cooling holes was largely unaffected by enhanced turbulence. However, at high blowing ratios ( $M = 1.5$ ), eddies significantly increased in size due to the increased turbulence level. Wright et al. [80] was able to couple PIV directly with PSP in order to clarify the effect of freestream turbulence on round hole film cooling at various blowing ratios. The PIV results were used to determine the turbulent kinetic energy thickness and the turbulent shear stress thickness. Both of these measurements allowed for direct correlation of surface film cooling effectiveness distributions. With this detailed characterization of the mainstream flow along with the surface measurements, the door is opened for validation of sophisticated CFD models.

Two dimensional PIV offers the ability to visualize and quantify two dimensional flow fields, but it has some limitations. While 2D-PIV is comparatively much simpler and cheaper than S-PIV, highly three-dimensional flows simply cannot be resolved, which are important for film cooling flows. S-PIV has become increasingly popular as the cost of cameras and processing power has been reduced. S-PIV utilizes the same basic principles associated with 2-D PIV, with the added complexity of a second camera. S-PIV affords the powerful ability to resolve 3-D velocity vectors in a plane.

#### *General S-PIV Background*

S-PIV determines the third component of velocity in the same way that human eyes perceive depth. Adding the second camera allows for determination of the velocity vector normal to the laser plane. Both cameras view the same flow field from different angles, and a spatial calibration is applied in order to determine their locations in reference to a shared plane of interest. Once calibrated, the angle between the two cameras gives the S-PIV system perception to identify the out of plane velocity

components. Adding the additional camera does incur the cost of the camera, but beyond that, the cost of processing is significantly increased by applying the calibration between the two cameras to determine the three dimensional vectors.

For 2D-PIV, the camera is mounted perpendicular to the illuminated plane, which ensures that the entire laser light sheet is in focus. However, for S-PIV, the dual cameras must be set up at oblique angles to the laser plane to enable perception of the three-dimensional velocity, as shown in *Figure 4.3*. A generic lens is incapable of focusing the entire laser plane because the distance between the camera and the laser plane is not consistent across the plane. This is commonly referred to as the “Schiempflug condition”. In order to allow for focus across the plane, an existing camera lens is retrofitted with an adaptor, commonly called a “Schiempflug adapter”. The adaptor alters the angle between the lens plane and the image plane, as shown in *Figure 4.4*. The angle between the lens

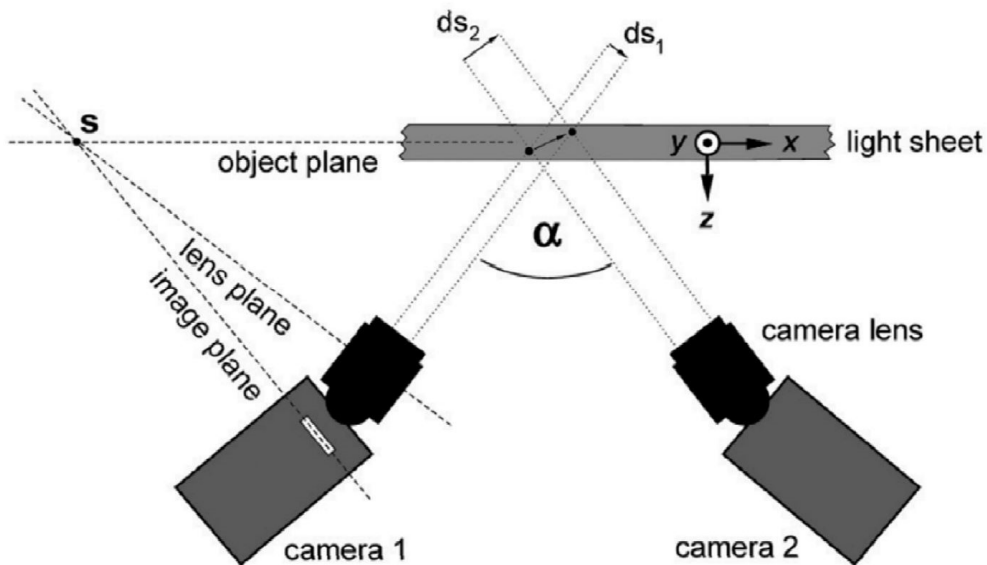


Figure 4.3: Camera orientation for S-PIV [59]

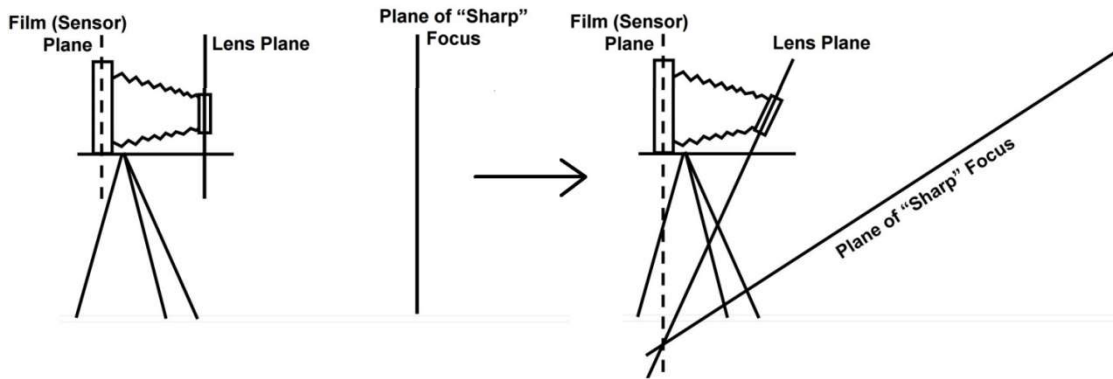


Figure 4.4: Illustration of the Schiempflug adaptor [59]

plane and image plane is called the “Schiempflug angle”, and must be carefully tuned to allow for good focus across the entire area of interest.

For the present study, it is desirable to capture cross flow, as opposed to the streamwise interactions of cooling hole jets and the mainstream traditionally captured by 2D-PIV. In order to facilitate this, the laser plane is oriented perpendicular to the bulk flow. The cameras are oriented at an oblique angle such that the camera is closer to perpendicular to the laser plane than parallel. This orientation is chosen because it more clearly shows flow trends such as kidney-pair vortices and horseshoe vortices which affect surface cooling. In order to accurately capture seed movement for this setup, laser separation time is now constrained such that approximately 75% of the particles remain inside the laser sheet (~1mm thick). For 2D-PIV, the particles were often traveling parallel to the laser plane, so the laser separation time was chosen to keep 75% of particles within an interrogation region. The laser separation time used in S-PIV is much smaller than 2D-PIV, which allows for the measurement of velocity vectors in much smaller time increments. The separation time is small enough to allow for instantaneous velocity measurements such that turbulence can be quantified. The determination of RMS

fluctuating components of velocity aids in characterizing and understanding the flow. However, due to the overwhelming volume of turbulence data, the data presented in this study is all time averaged.

S-PIV was used by Schabacker et al. [81] to investigate a U-channel with ribs. The S-PIV was able to quantify the secondary flows induced by the ribs close to the surface of the channel. More recently, the technique was employed by Brown et al. [82] to characterize the three-dimensional flow field over V-shaped dimple arrays. The technique was demonstrated to be capable of resolving flow near the surface of the channel. The 3-D velocity and vorticity distributions determined were used to clarify the turbulent secondary flows induced by the dimples. The data was utilized to aid in understanding a previous study [83] that showed an unintuitive impact of Reynolds number on heat transfer performance. S-PIV was also applied to film cooling by Aga et al. [84] in order to validate and calibrate a 3D computational fluid dynamics (CFD) model for compound angled, cylindrical film holes. The S-PIV was capable of detailing the effect of the compound angle hole, showing that the skewed vortex structure of the jet leads to the reduction of the classic counter rotating vortex pair, leaving only a single vortex. The data was also able to clearly explain why the compound angle holes resisted coolant liftoff at higher blowing ratios. Higher blowing ratios increase the boundary layer thickness on one side of the jet, allowing for better attachment on the thinner side. S-PIV has demonstrated utility for revealing secondary flows related to film cooling, especially near the surface.

### Experimental Technique and Uncertainty Analysis

The S-PIV system used to perform flow field research for this study was developed by LaVision, Inc. and the captured images were processed using DaVis 8.1.1 software. In order to capture the images for S-PIV, two high speed CMOS cameras, distributed by Vision Research (V211), were positioned on opposite sides of the wind tunnel, downstream of the test section, as shown in *Figure 4.5*. The cameras are capable of recording 2160 frames per second at their maximum resolution of 1280 by 800 pixels. Each camera was fitted with a 50mm focal length lens, and a Scheimpflug adapter to

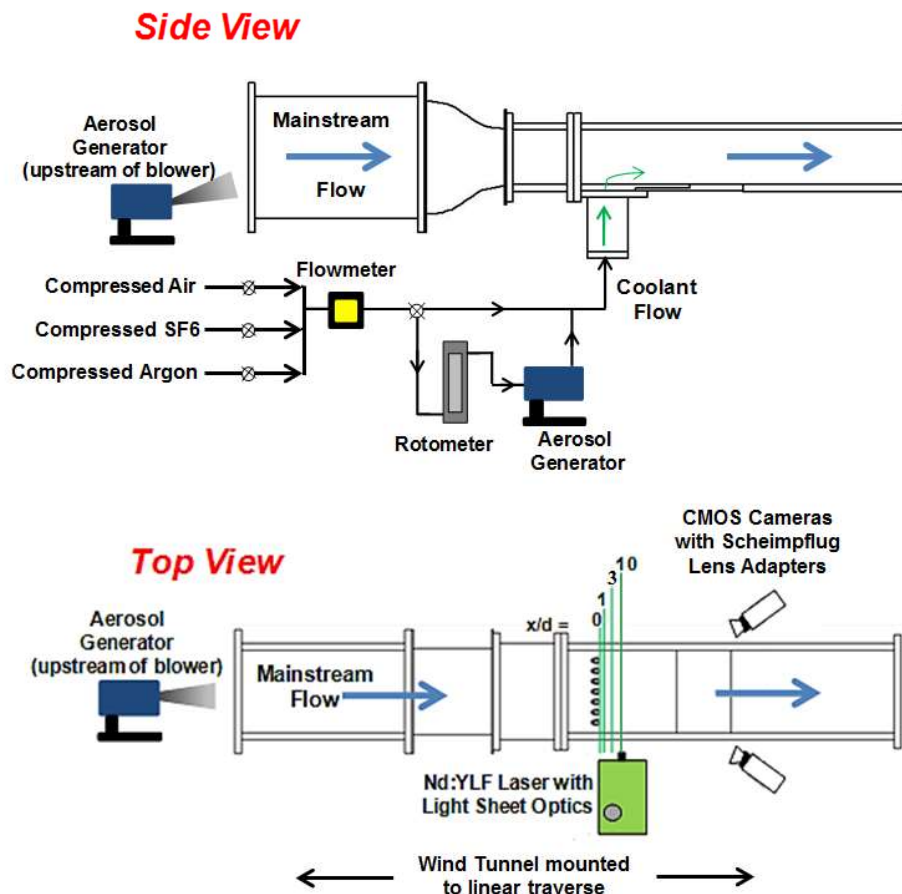


Figure 4.5: Overview of the low speed wind tunnel with S-PIV experimental equipment

focus on a row of film cooling holes at oblong angles to the camera lens. In the current study, 1000 image pairs were recorded by the CMOS cameras at 2000 frames per second.

The seed particles used to visualize the flow were generated by two LaVision aerosol seeders, which disperse oil droplets (Di-Ethyl-Hexyl-Sebecat) into the mainstream and coolant flows. Both seeders produce DEHS seed particles with a diameter on the order of 1  $\mu\text{m}$ . The oil seed particles are illuminated by an Nd:YLF dual cavity diode laser, produced by Photonics Industries. The laser produces a 532 nm wavelength laser beam at a repetition rate of up to 10 kHz per head. It utilizes a cylindrical lens with a focal length of  $f = -20$  mm to spread the beam into a laser light sheet with a thickness of approximately 1 mm. A laser separation time of 25  $\mu\text{s}$  is chosen because the mainstream flow is moving at 10 m/s, and no more than 25% of the seed particles should be allowed to move out of the laser sheet from the first image to the second.

Before the flow can be captured, both CMOS cameras are spatially calibrated by LaVision software. The calibration is accomplished by identifying the pixels on each of the two camera images that represent the same physical point in space. The distance between the pixels is specified in millimeters so that the pixels on each image can be converted to physical distance. The software uses the calibration to relate the interrogation regions from the two images so that the same physical point in space is compared between images. The calibration also compares the two images to determine the out of plane depth for each camera. After calibrating and capturing images, DaVis software first performs a self-calibration on the recorded images. The self-calibration works to fix the errors in the initial calibration by determining the average pixel deviation

between the two camera views. This aids in removing errors from inaccurate alignment of the calibration plate with the laser plane. DaVis is also used to post-process recorded images, utilizing a multi-pass, stereo-cross correlation technique which analyzes the spatial translation of oil droplets within the flow. Five passes, each with a 50% overlap of interrogation regions (three of a 32 x 32 pixel range and two of a 16 x 16 pixel range) are used to determine the flow velocity vectors of the calibrated images. Once the velocity vectors are calculated, the vectors which have a signal-to-noise threshold ratio less than 1.1 are removed.

The following equations are used to calculate the mean and instantaneous velocity components and magnitudes:

$$\text{(x-direction)} \quad \bar{u} = \frac{1}{N} \sum_{i=1}^N u_i \quad (4.1)$$

$$\text{(y-direction)} \quad \bar{v} = \frac{1}{N} \sum_{i=1}^N v_i \quad (4.2)$$

$$\text{(z-direction)} \quad \bar{w} = \frac{1}{N} \sum_{i=1}^N w_i \quad (4.3)$$

$$\text{(Velocity Magnitude)} \quad V = \sqrt{\bar{u}^2 + \bar{v}^2 + \bar{w}^2} \quad (4.4)$$

$$V_{\text{avg}} = \frac{1}{n} \sum_{j=1}^n V \quad (4.5)$$

$$\text{(Vorticity)} \quad \bar{\omega} = \left( \frac{dw}{dy} - \frac{dv}{dz} \right) \bar{i} + \left( \frac{du}{dz} - \frac{dw}{dx} \right) \bar{j} + \left( \frac{dv}{dx} - \frac{du}{dy} \right) \bar{k} \quad (4.6)$$

Vorticity is a measure of rotational nature of the velocity, and the  $\bar{i}$  component (vorticity in the x-direction) is the reported vorticity. The x-direction vorticity is used because it shows the rotation in the plane investigated. The velocity magnitude “V” is determined by the magnitude of the time averaged velocity components for each

interrogation region.  $V_{avg}$  is calculated by averaging the velocity magnitude from the set of interrogation regions where the velocity is approximately uniform. The velocities and vorticities are non-dimensionalized by referencing them to  $V_{avg}$ .

The systematic uncertainties associated with the S-PIV calculations are anticipated to be small compared to the random uncertainties. The laser timing is highly accurate and the spatial calibration is corrected with the self-calibration technique, which limits the systematic uncertainty. The random uncertainty is presented as the entire uncertainty. Wieneke [85] has developed a method used by the DaVis 3.2.2 software to calculate random uncertainty based on the standard deviation of the contribution of the differences in intensity to the correlation function using advanced statistical methods. The random uncertainty is determined from this correlation, and this method has been evaluated and validated using synthetic data with random Gaussian noise, varying particle density, and in and out of plane motion. The uncertainty of the in-plane directions (y and z) is relatively small ( $< 1$  m/s), but the uncertainty in the out of plane direction (x) is approximately 2 m/s for the average velocity vector. These uncertainties are calculated for each interrogation region for each image pair. Taking 1000 image pairs reduces the component of uncertainty due to random turbulence fluctuations. It is not currently feasible to determine exact values for S-PIV uncertainty, but the approximate order of the uncertainty shows that the technique can be used to observe trends in film cooling flow fields.

## CHAPTER FIVE

### Experimental Setup for Combustor Liner Cooling

#### *Overview of Experimental Facility*

The experiment used to determine the film cooling effectiveness for the effusion film cooling scenario was performed in a low speed, open loop wind tunnel. Ambient air flows through a 2:1 contraction, followed by a turbulence grid (used to create a turbulence intensity of 7.5%), before entering into a 15.24 cm X 10.16 cm test section. A variable speed blower is used to control the mainstream air velocity. *Figure 5.1* shows the configuration of the wind tunnel. This same setup has previously been used to complete film cooling investigations by Wright et al. [32]. The velocity of the mainstream air in the tunnel is maintained at 10 m/s throughout the test section. The velocity is monitored throughout the investigation with a pitot-static probe placed in the center of the tunnel, downstream of the film cooled plate. The film cooling plate is bolted to the bottom side

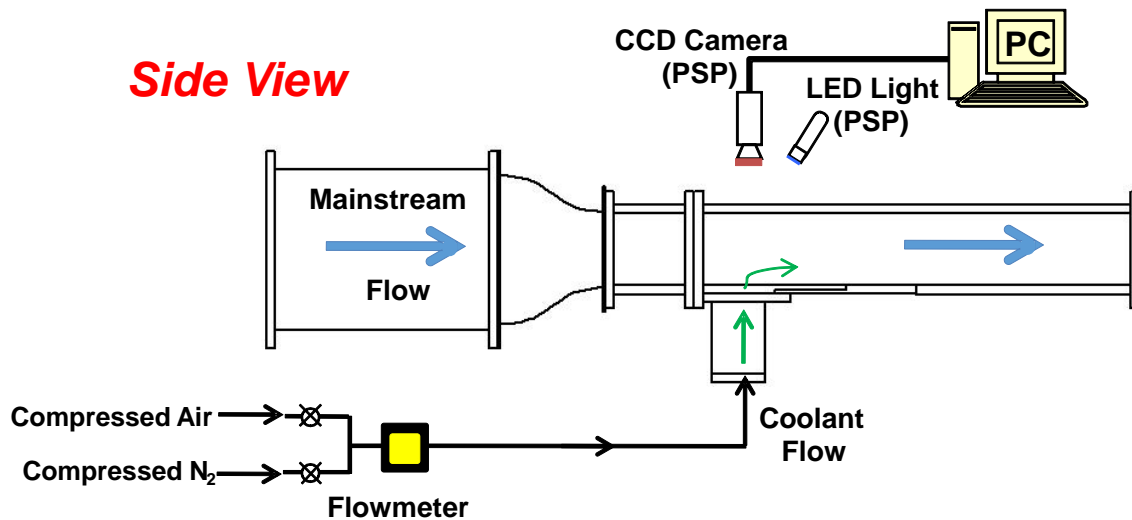


Figure 5.1: Low speed wind tunnel for effusion film cooling investigation

of the wind tunnel so that it can be easily switched out to investigate other geometries. The film cooling plate attaches directly to a plenum, which is used to distribute coolant evenly to all thirty-five holes. In effusion cooling investigations, influencing equal coolant mass flow through each hole is important to validate the results. The plenum is designed with an insert containing an array of small, evenly distributed holes to force the flow towards uniformity as it reaches the test coupon.

The film cooling test plate is painted using Uni-FIB PSP (UF470-750) provided by Innovative Scientific Solutions, Inc. (ISSI). The PSP is made to fluoresce under a 400 nm LED light, and a 1600 x 1200 resolution CCD camera with a 570 nm filter is used to capture the intensity of light emitted by the PSP. The positioning of the CCD camera and LED light are shown in Fig. 5.1.

### *Flow Conditions*

For the present study, the density ratio is maintained at  $DR = 1$  for all cases investigated. In order to validate the PSP setup, the baseline round holes are evaluated at a blowing ratio ranging from  $M = 0.5$  to  $M = 6.0$ . With the experimental setup validated, the baseline round holes, along with the more advanced shaped holes are evaluated at realistic engine blowing ratios. The blowing ratio effect is studied by varying the blowing ratio for  $M = 6.0$ ,  $7.5$ , and  $8.5$ . The blowing ratio reported is the average blowing ratio for all film cooling holes. The blowing ratio is set and measured using the flowmeter shown in Fig. 5.1 to keep the coolant mass flow in correct ratio to the pitot probe measurements of mainstream velocity.

### Combustor Cooling Coupon Details

The baseline film cooled surface is shown in *Figure 5.2*. The baseline test coupon, along with the other two coupons, was additively manufactured using direct metal laser sintering (DMLS) technology. An EOS M280 machine uses a 305 Watt, Yt-Fiber laser to melt the IN625 metal powder to form the coupon. The coupon was oriented in the machine so that the x-direction points vertically on the build surface; the layers are put down so that the coupon is built in the streamwise direction. Each layer of the coupon has a thickness of 40  $\mu\text{m}$ .

As shown in Fig. 5.2, the baseline film cooling surface consists of thirty-five standard cylindrical holes, each with a nominal diameter of 1.27 mm. To enhance attachment of the coolant to the surface, the holes have a simple inclination angle of  $\theta = 20^\circ$ . The length-to-diameter ratio for each hole is  $L/d = 9.8$ . The holes are laterally spaced with 9.8 diameters between each hole ( $P/d = 9.8$ ). This spacing prevents hole-to-hole jet

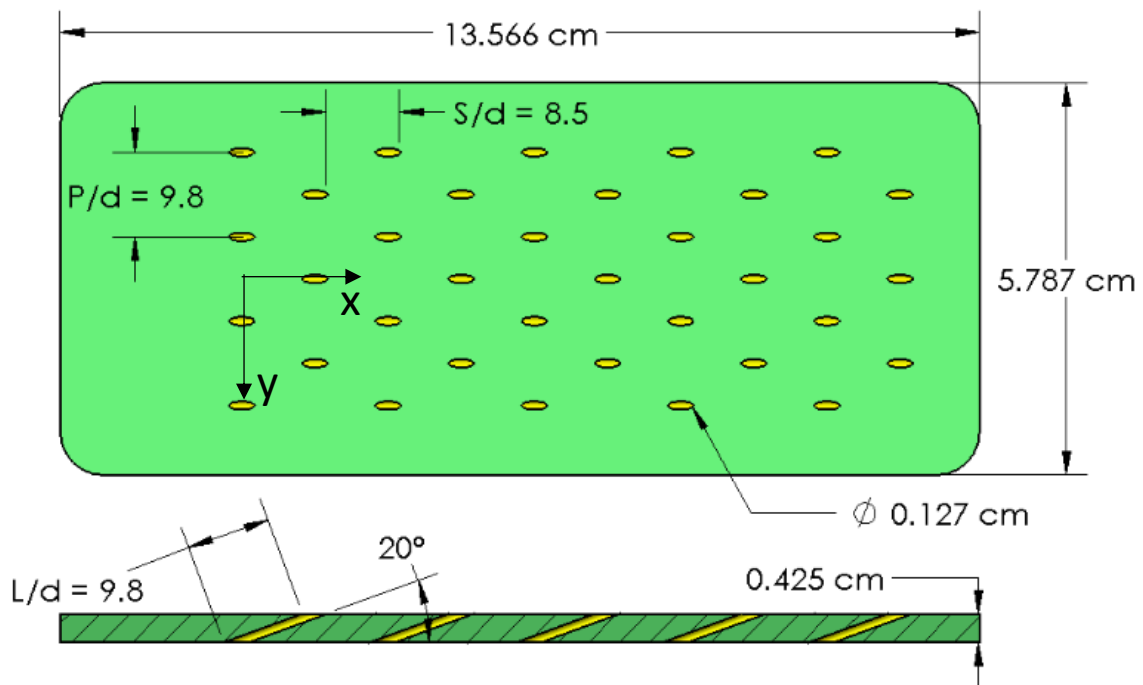


Figure 5.2: Details of baseline round hole configuration

interaction in the first several rows, though effusion effects overcome the lateral hole spacing after the first two rows. The holes are staggered, with 8.5 diameters between each row of holes in the streamwise direction ( $S/d = 8.5$ ). The origin is located at the lateral center of the plate, in the center of the first row of holes, as shown in Fig. 5.2.

The second geometry used consists of thirty-five laidback, fanshaped holes with the same hole spacing as the baseline hole. The geometry is shown in *Figure 5.3*. Due to proprietary concerns, the exact specifications of the shaped hole geometry cannot be disclosed. The DMLS technology is used to create non-line of site holes which should have some positive impact on the flow. However, for the purpose of this study, the geometry is used to evaluate the effect of shaped holes on effusion film cooling. For the purposes of comparison to the baseline hole, the origin is chosen to be in the same physical location on the coupon, as the true dimensions of the hole are unknown. The origin is located inside the expanding section of the hole. The third and final effusion cooling geometry evaluated with the PSP technique is shown in *Figure 5.4*. Each of the thirty-five inlet holes splits into two separate fanshaped holes which means that the mass flow rate through each hole exit is actually half that of all of the other holes. Similar to

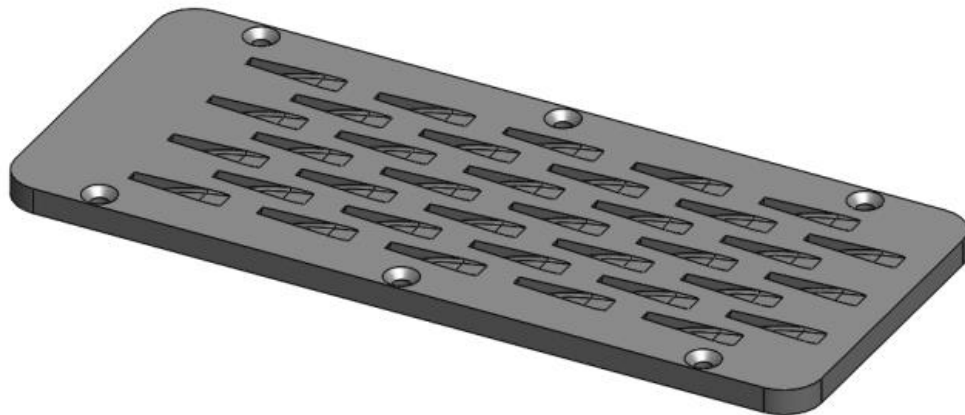


Figure 5.3: Shaped effusion film cooling coupon

the shaped hole effusion cooling geometry, proprietary concerns prevent the disclosure of the method involved in splitting the inlet hole into two exit holes. However, the hole spacing is the exact same as the baseline hole. The origin of the double hole is also chosen to be in the same physical location on the coupon as the baseline round hole, which places the origin on the upstream edge of the double holes.

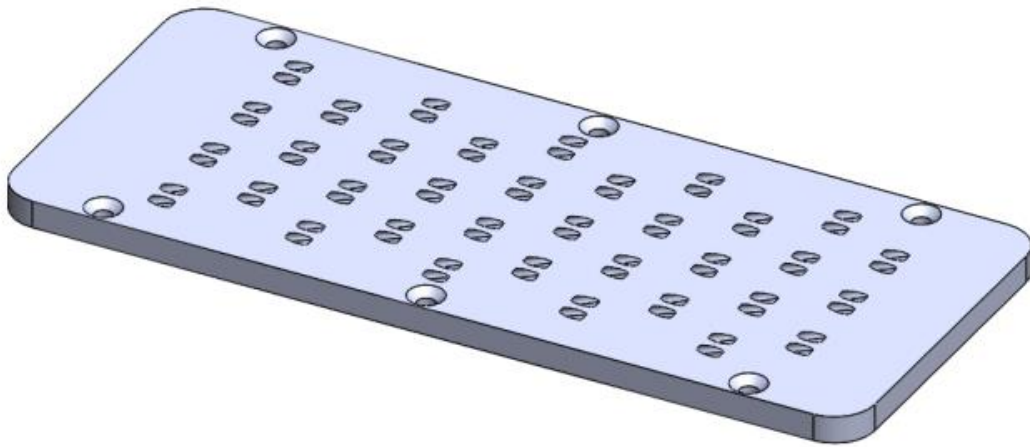


Figure 5.4: Double hole effusion film cooling coupon

## CHAPTER SIX

### Experimental Setup for Airfoil Cooling

#### *Overview of Experimental Facility*

The same wind tunnel discussed in chapter five to perform combustor cooling experiments is also used to evaluate various airfoil cooling scenarios. The wind tunnel configuration is shown in *Figure 6.1*. A traverse is used to move the wind tunnel to various planes of interest. The traverse is used to move the tunnel so that the cameras and

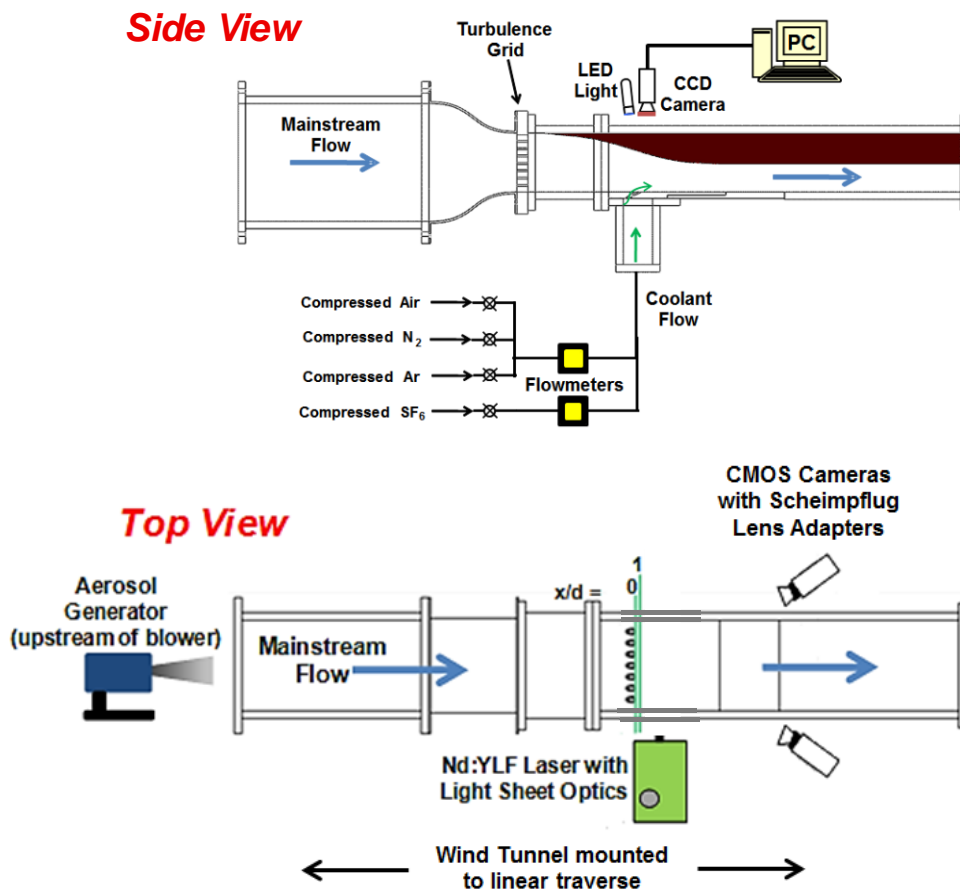


Figure 6.1: Low speed wind tunnel for film cooling investigations

laser are never required to move, and therefore, remain in focus for any plane of interest over the film cooled surface.

In order to evaluate various hole geometries, a support plate is developed using additive manufacturing that can be inserted into the bottom of the tunnel. The support plate connects to each film cooling plate so that the film cooling plates can be easily interchanged. The film cooling plate is also attached to a plenum which is used to evenly supply coolant to all five of the film cooling holes. The coolant used in this investigation is either  $N_2$  ( $DR = 1$ ) or a combination of argon and  $SF_6$  to create density ratios of  $DR = 2, 3$  and  $4$ . The coolant flow rate is monitored through flowmeters and set so that the blowing ratio can be controlled for  $M = 0.5, 1.0$ , and  $1.5$ . *Table 6.1* details the various flow conditions investigated, along with the resulting momentum flux ratio.

In order to study the effect of mainstream flow acceleration, an insert is created to curve the wall opposite of the film cooling plate. The insert used to create a favorable pressure gradient was cut from a single block of foam using a hot wire foam cutter. *Figure 6.2* shows the foam insert placed in the wind tunnel setup, where  $z$  is the unobstructed height of the tunnel and  $x$  is the streamwise distance from the origin. The foam insert was cut to match the acceleration parameter ( $K = 4.8 \cdot 10^{-6}$ ) with the flow

Table 6.1: Momentum flux ratio equivalents of the density and blowing ratios used for this study

Table 6.1: Momentum flux ratio equivalents of the density and blowing ratios used for this study

Density Ratio	I at $M = 0.5$	I at $M = 1.0$	I at $M = 1.5$
1.0	0.25	1.0	2.25
2.0	0.125	0.5	1.125
3.0	0.083	0.33	0.75
4.0	0.0625	0.25	0.5625

acceleration parameter used by Coletti et al. [46]. A 5<sup>th</sup> order polynomial was used to define the shape of the insert that would match the acceleration parameter of Coletti et al. [46]. The acceleration parameter is defined by equation 6.1:

$$K = \frac{\nu_{\infty}}{U_{\infty}^2} \frac{dU_{\infty}}{dS} \quad (6.1)$$

where  $\nu_{\infty}$  and  $U_{\infty}$  are the local freestream viscosity and velocity values and  $S$  is the streamwise coordinate. The derivative is evaluated in the region where it is nearly constant. As seen in *Figure 6.3*, the slope of the velocity profile is approximately constant in the range of  $-5 < x/d < 15$ . The acceleration is approximately constant for the region immediately before the holes and remains constant until the midpoint between the origin and the downstream edge of the plate. A hole was cut out of the foam insert so that the CCD camera would have a clear view of the film cooling plate. The size of the cutout viewing window was limited by the need to maintain the shape and rigidity of the insert. Transparent tape was placed such that it covered the viewing window to prevent airflow into the window and maintain the contour of the insert without blocking the camera. The insert was then affixed to the top of the wind tunnel such that the mainstream velocity over the center of the holes would be maintained at 10 m/s. An expected velocity profile

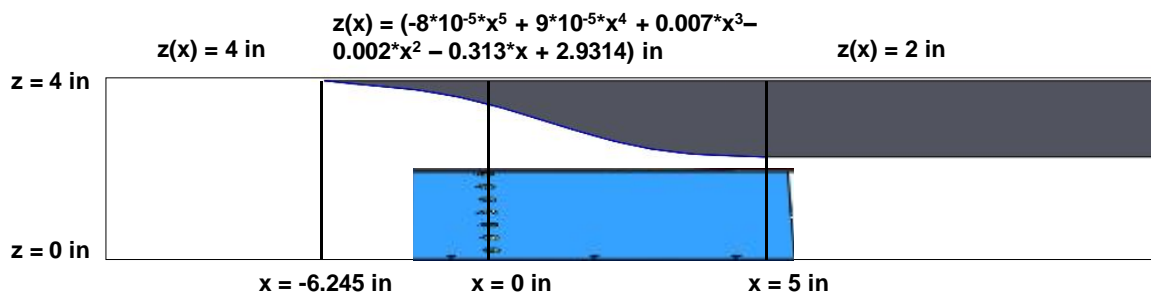


Figure 6.2: Pressure gradient insert in wind tunnel

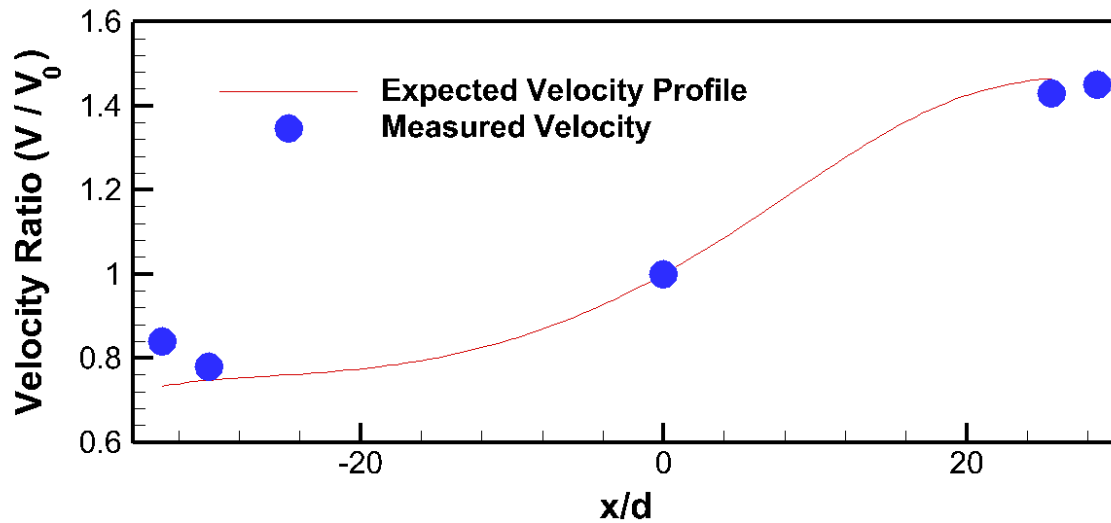


Figure 6.3: Validation of FPG insert

was developed given the assumption of maintaining 10 m/s mainstream velocity at the holes along with the known tunnel height for each  $x$  location. Pitot-static probes were inserted at three separate locations (upstream of pressure gradient, directly over holes, downstream into the flat region of pressure gradient) to confirm that the measured velocity at the three locations closely matched the expected velocity. Measured velocities matched predicted velocities, thus validating the pressure gradient insert. The measured velocities are presented in Fig 6.3.

#### *Baseline Round Geometry*

A total of six film cooling geometries were investigated for the current study. The first plate was chosen to match Issakhanian [86]. The baseline round cooling geometry shown in *Figure 6.4* was utilized to determine the improvement afforded by the new shaped holes, along with providing a method of direct comparison of the pressure gradient effect studied by Issakhanian [86]. The diameter of each hole was approximately 4.763 mm (0.1875 in) with a simple angle inclination of  $\theta = 30^\circ$  and a hole length of 4

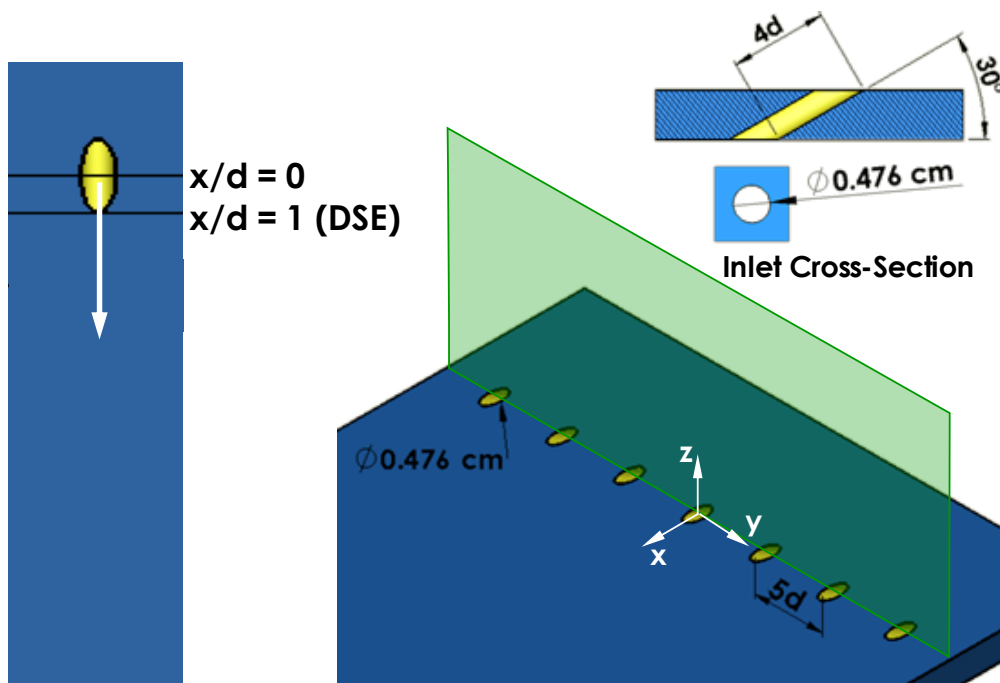


Figure 6.4: Baseline, simple angle, round hole

diameters ( $L/d = 4$ ). The hole spacing was chosen as five diameters ( $P/d = 5$ ) to ensure that there would be no interaction between the film cooling holes. The origin of the round hole film cooling plate was chosen to be in the center of the center hole in the plane of the film cooling surface. Cartesian coordinates were used, with the x-direction in the streamwise direction, y-direction in the lateral direction, and z-direction in the vertical direction as shown in Fig 6.3. For S-PIV, the round holes were investigated for  $x/d = 0$  and 1 (downstream edge).

#### *Base Diffuser-Shaped Geometry*

A standard laidback, fanshaped hole modeled after the diffuser shaped hole tested by Issakhanian et al. [86] is used as a baseline for shaped hole film cooling. More complex hole shapes are compared to the baseline to determine the film cooling improvement afforded by the more complex hole design. Additionally, the hole is

matched with Issakharian et al. [86] so that a direct comparison of the effect of mainstream flow acceleration on shaped hole film cooling can be made. The hole is inclined at a simple angle ( $\theta = 30^\circ$ ) with an inlet diameter of 4.763 mm (0.1875 in). After 4.5 diameters, the hole begins to expand in both the forward and lateral directions ( $\alpha = \gamma = 10^\circ$ ) for the next 1.5 diameters as shown in *Figure 6.5*. The film cooling surface is comprised of five identical holes evenly spaced 5 diameters apart ( $P/d = 5$ ). The planes of interest for S-PIV were  $x/d = 0$  and 3 (the downstream edge of the hole). The origin of the hole is determined where the axis of the round portion of the hole intersects the film cooling plane, as shown in Fig 6.5.

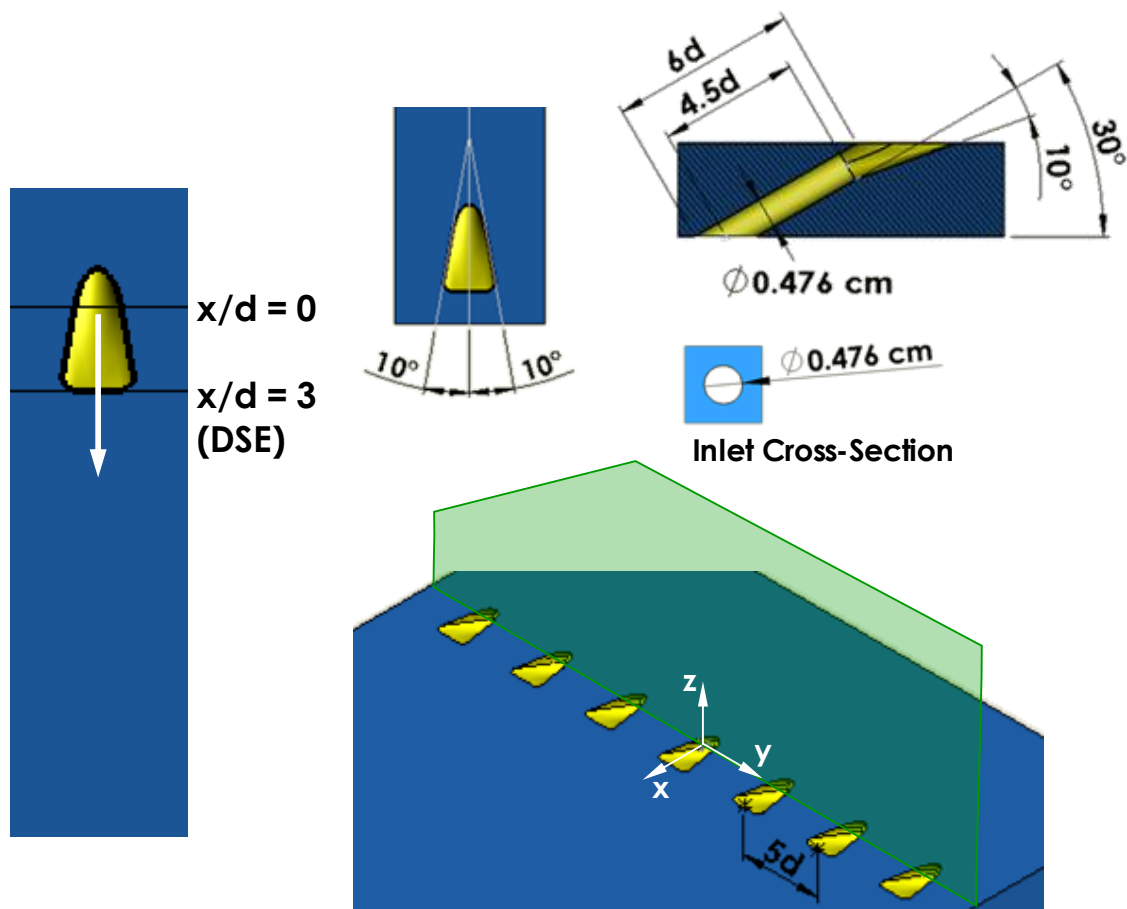


Figure 6.5: Laidback, fanshaped hole

### Honeywell Shaped Geometries

Two additional film cooling plates designed by Honeywell were investigated. The two laidback, fanshaped holes were completely identical except for the inlet. Both geometries contained five simple angle ( $\theta = 30^\circ$ ) laidback, fanshaped ( $\alpha = \gamma = 12^\circ$ ) film holes. The first geometry, designated “Honeywell Shaped 1” (HWS1), utilized a standard round inlet ( $d = 4.763 \text{ mm}$ ) with a metering length of 5.2 diameters at which point the shaped expansion continued for the final 0.8 diameters as shown in *Figure 6.6*. The planes of interest investigated using S-PIV for this geometry included  $x/d = 0$  and 3 (the

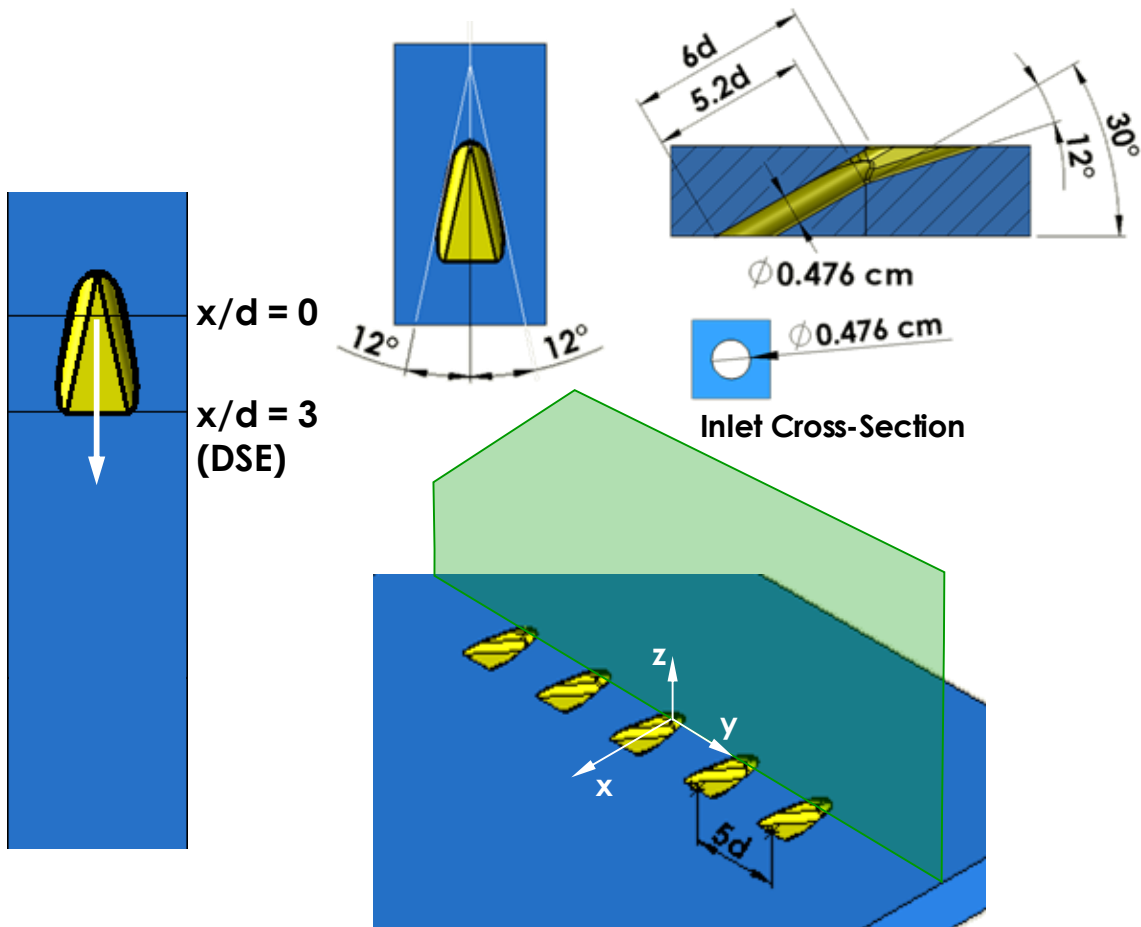


Figure 6.6: Honeywell Shaped 1 – round inlet

downstream edge of the hole). The origin of the hole is determined where the axis of the round portion of the hole intersects the film cooling plane, as shown in Fig 6.6.

The second design, designated “Honeywell Shaped 2” (HWS2) had identical simple, laidback, and fanshaped angles to HWS1. HWS2 is investigated to evaluate the effect of changing the shape of the hole inlet from round to racetrack as shown in *Figure 6.7*. The racetrack shape has the same cross-sectional area as the round inlet, with straight top and bottom edges (0.316 cm long) before curving at the sides. The curved sides had a diameter of 0.316 cm. The hydraulic diameter ( $D_H$ ) is defined in equation 6.2,

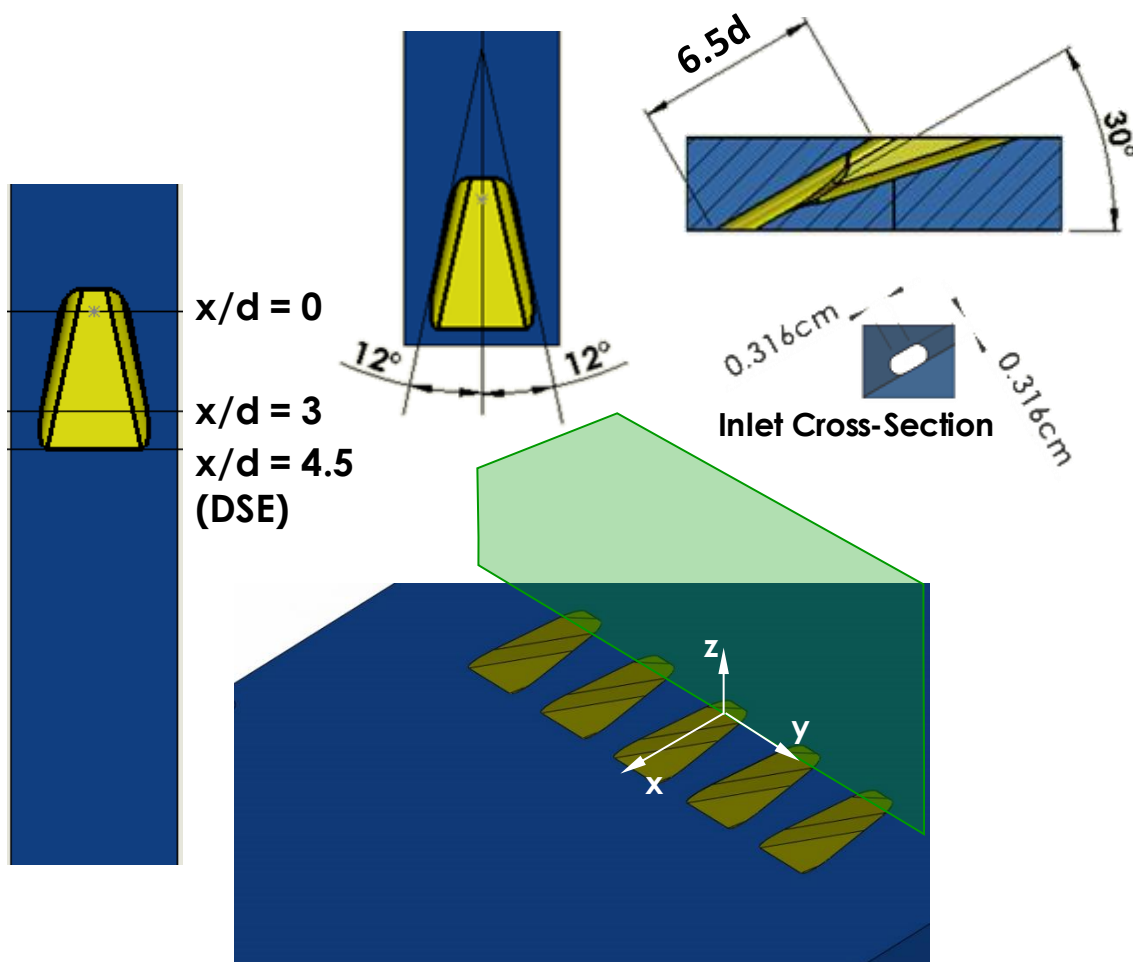


Figure 6.7: Honeywell Shaped 2 – racetrack inlet

$$D_H = \frac{4A_c}{P} \quad (6.2)$$

where  $A_c$  is the cross sectional area of the inlet, and  $P$  is the perimeter of the inlet. The hydraulic diameter will be used as the nominal diameter for all plots involving HWS2. Additionally, it should be noted that lateral expansion began at the curved sides of the racetrack inlet, widening the laidback, fanshaped exit area compared to HWS1. The planes of interest investigated using S-PIV included  $x/d = 0, 3$  (inside the laidback, fanshape), and 4.5 (the downstream edge of the hole). The origin of the hole is determined where the axis of the racetrack portion of the hole intersects the film cooling plane, as shown in Fig 6.7.

#### *Duck Foot Geometries*

Two innovative film cooling geometries developed by Honeywell have been investigated and compared to the baseline shaped holes. The hole design is reminiscent of a duck's footprint, with three webbed "toes" molded into the exit of the film hole, as described in *Figure 6.8* and *Figure 6.9*. The two geometries are identical except for the inlet. Duckfoot 1 (DF1) is the designation given to the first novel film cooling hole with the round inlet with a diameter of 4.76 mm. DF1 has a 4.8 diameter metering section, with hole expansion in both lateral and fanshaped directions ( $\alpha = \gamma = 12^\circ$ ) for an additional 1.2 diameters, similar to HWS1. The five holes on the plate for both duckfoot geometries had a hole spacing of five diameters. The planes of interest investigated with S-PIV for DF1 were  $x/d = 0, 3$  (inside the laidback, fanshape), and 5.7 (the downstream

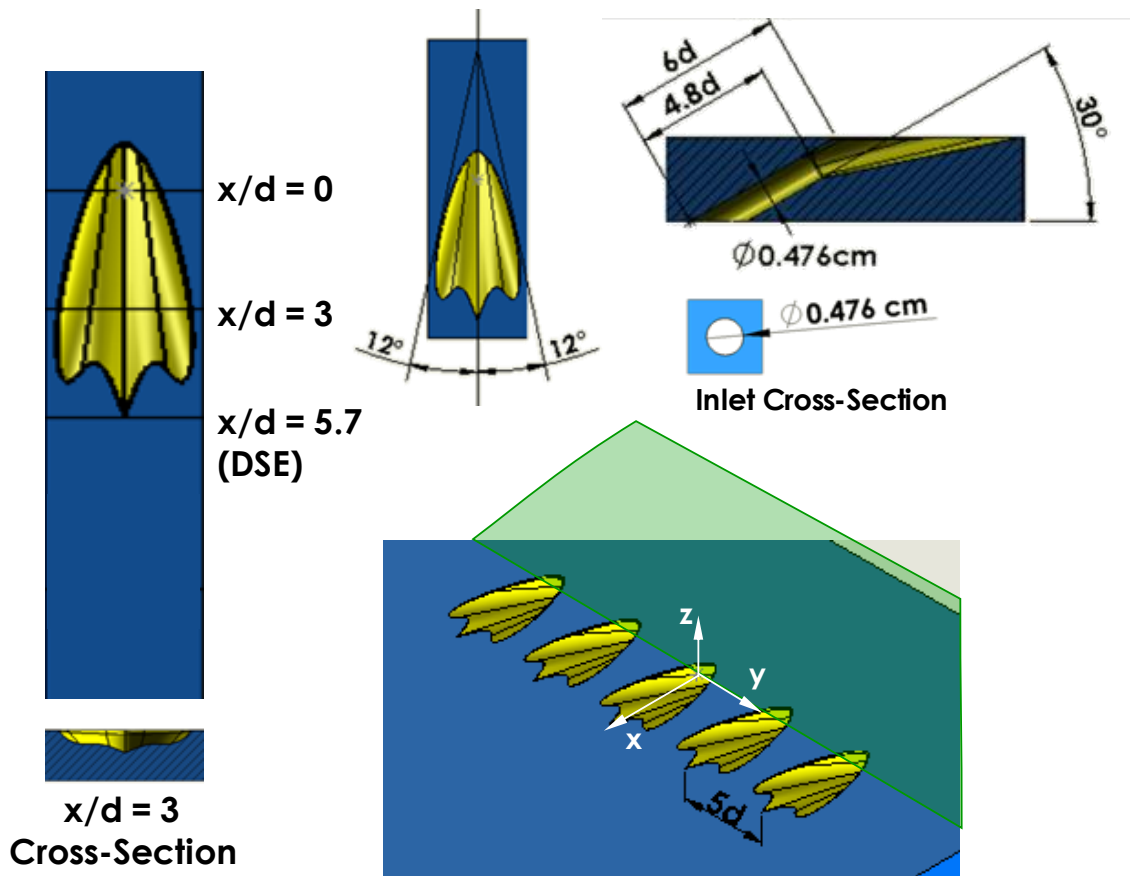


Figure 6.8: Duckfoot 1 – round inlet

edge of the hole). The origin of the hole is determined where the axis of the round portion of the hole intersects the film cooling plane, as shown in Fig 6.8.

The second duck foot film cooling design, designated “Duckfoot 2” (DF2), is identical to DF1, except the inlet is changed to a racetrack shape with identical dimensions as the racetrack inlet of HWS2. The planes of interest investigated with S-PIV were  $x/d = 0, 3$  (inside the laidback, fanshape), and 5.9 (the downstream edge of the hole). This film cooling geometry is thought to provide increased film cooling results from slot-like ejection provided by the laidback, fanshaped exit and the racetrack inlet.

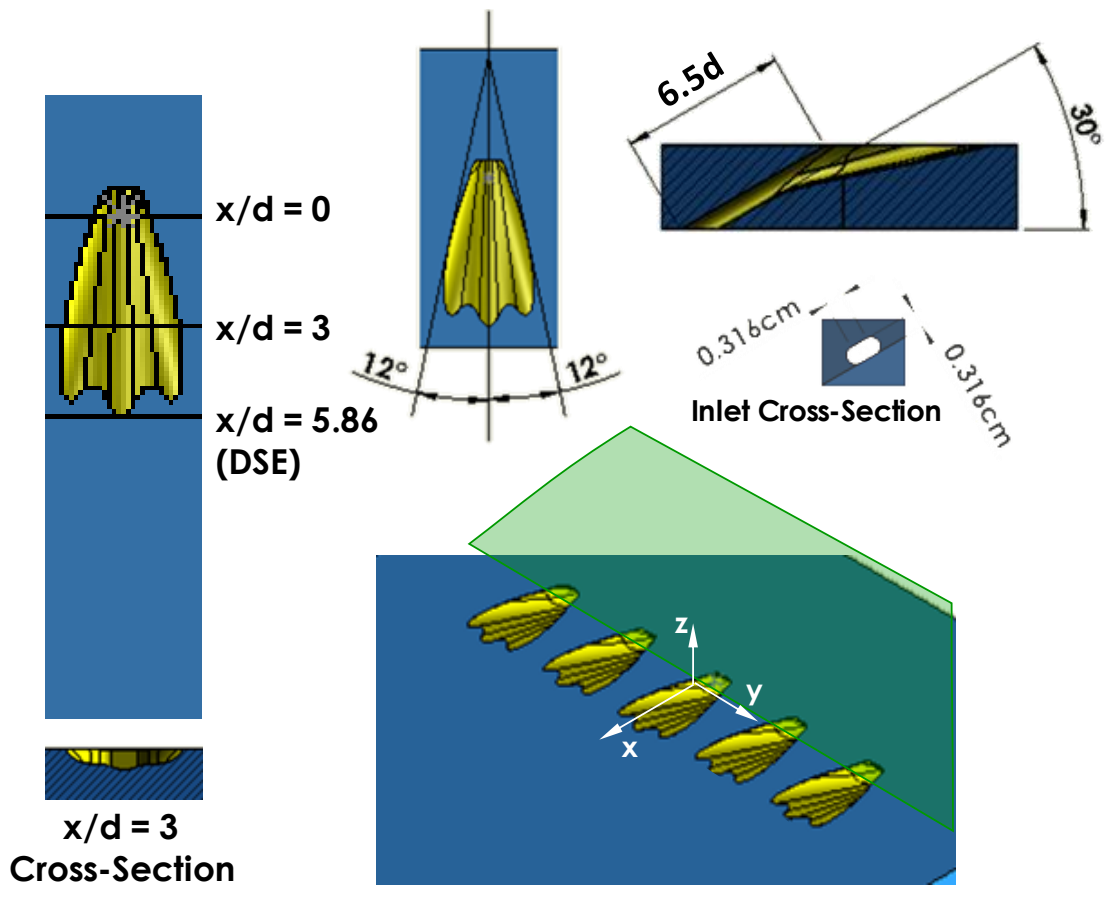


Figure 6.9: Duckfoot 2 – racetrack inlet

## CHAPTER SEVEN

### Combustor Liner Cooling Results

#### *Validation of PSP for Full Coverage Film Cooling*

The goal of this PSP investigation is to evaluate the capability of advanced shapes in an effusion film cooling scheme. Due to the proprietary nature of the shapes, there is no data available for a direct comparison. Furthermore, the shapes are evaluated at modern engine combustor blowing ratios which are much higher than blowing ratios traditionally studied in literature. Therefore, the baseline round holes will be evaluated for a range of blowing ratios commonly used in literature to develop a comparison and validate the PSP setup. Once the setup is validated, the advanced shapes can be compared to the baseline round holes.

Film cooling effectiveness distributions have been obtained for the baseline case for the blowing ratio range of  $M = 0.5$  to  $M = 6.0$ . The film cooling performance is also analyzed by considering centerline, laterally averaged, and overall area averaged effectiveness distributions. The data obtained from the baseline plate fabricated with the DMLS technique is compared to previous studies that used more established manufacturing techniques to create the film cooling plate. The trends related to effusion film cooling are analyzed through the film cooling distributions shown in *Figure 7.1*. In order to validate the results, it is vital to ensure that there is equal coolant mass flow through each hole. While the present facilities are not capable of measuring the actual flow rate through each hole, the distributions show that each film cooling hole is completely covered in film, with  $\eta \approx 1$  throughout the hole. The maximum of the scale

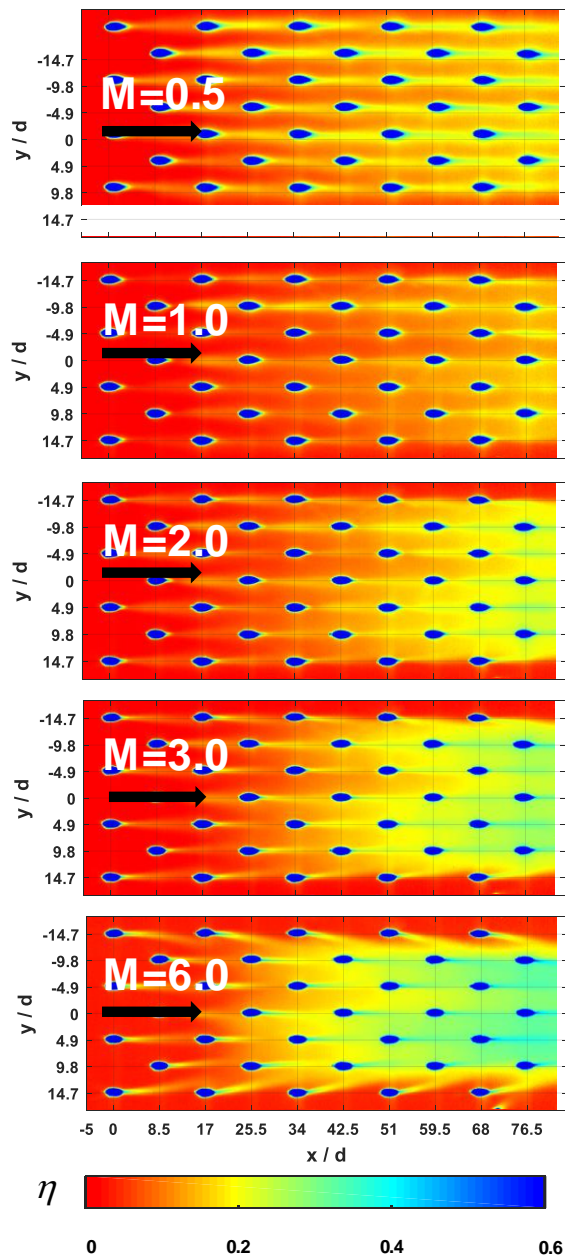


Figure 7.1: Film cooling effectiveness distributions for all blowing ratios

for Fig. 7.1 has been set to  $\eta = 0.6$  to more clearly show the color variance through the distribution, but the holes themselves are filled with coolant and have a minimum effectiveness of  $\eta = 0.95$  throughout the hole. Furthermore, the jet structure does not vary laterally across the plate, which shows that the plenum is delivering coolant evenly within each row. These indicators are sufficient to conclude that the coolant flow rate is approximately equal through each hole.

The initial row of holes actually shows improved effectiveness at elevated blowing ratios ( $M = 3.0$  and  $6.0$ ). It is expected from film cooling literature [4, 5] on single row applications that the lowest blowing ratio ( $M = 0.5$ ) should perform optimally. The lowest blowing ratio does outperform  $M = 1.0$  and  $2.0$  as expected from the literature; however, the highest blowing ratios ( $M = 3.0$  and  $6.0$ ) provide improved coverage immediately downstream of the hole. This could be caused by the relatively long ( $L/d = 9.8$ ) and shallow angle ( $\theta = 20^\circ$ ) holes compared to the standard holes investigated in single row film cooling applications. These factors could allow higher momentum flows to stay attached to the surface.

There are three primary effects of effusion film cooling that occur because the coolant jets interact with each other. Superposition occurs as the coolant that reaches the subsequent row is added to the coolant exiting that jet. Additionally, as the jets collide, the coolant spreads laterally. The spreading increases for each passing row. Furthermore, the initial row blows into the boundary layer to cause thickening. The boundary layer thickening protects the downstream rows from the mainstream. The effect of effusion film cooling can be seen most clearly for higher blowing ratios. For  $M \geq 2.0$ , the coolant has more momentum and travels further downstream, allowing more coolant to collide with the subsequent row. The final two rows of holes ( $x/d > 68$ ) show little lateral variation in film cooling effectiveness for the area given by  $-9.8 < y/d < 9.8$  because of the interactions between the holes that spread the coolant across the plate. Distributions for  $M = 0.5$  and  $1.0$  do not show this lateral spreading because the coolant does not have sufficient momentum to make it downstream to interact with the subsequent row of holes. Furthermore, at higher blowing ratios, this initial row blows more coolant into the

boundary layer, thickening the boundary layer more than for lower blowing ratios. As the boundary layer thickens, higher momentum coolant jets that would quickly separate from the surface in single row applications are capable of staying closely attached to the surface. The initial rows of holes actually act as a sacrifice, with low effectiveness immediately downstream of the first hole, but significantly improved effectiveness downstream.

For higher blowing ratios with increased hole-to-hole interaction, the outer rows of coolant jets actually curl towards the center of the plate. The outer jets are drawn inwards due to the increased hole-hole mixing which increases local turbulence. The elevated local turbulence in the center causes a pressure drop, drawing in some coolant from the outer holes. This effect increases the accumulation amongst the center three holes, but it also leaves the outer holes relatively unprotected.

The film cooling effectiveness distributions are also presented in terms of the effectiveness along the centerline ( $y/d = 0$ ) of the plate as shown in *Figure 7.2*. At each hole (along the centerline, the first hole occurs at  $x/d = 8.5$  due to staggering), the centerline effectiveness spikes to near  $\eta = 1$ , but the jets quickly separate from the plate until the film reaches the next hole. As the film accumulates along the length of the plate, the minimum centerline effectiveness is increased for each passing row in the streamwise direction. The coolant ejected through each new row is added to the remaining coolant from the previous row by superposition, which raises the minimum film effectiveness. For higher blowing ratios, the higher momentum coolant is sufficient to reach the subsequent row without entirely lifting off of the surface. Lower momentum flows, which are able to stay closely attached in the area immediately downstream of the hole, do not

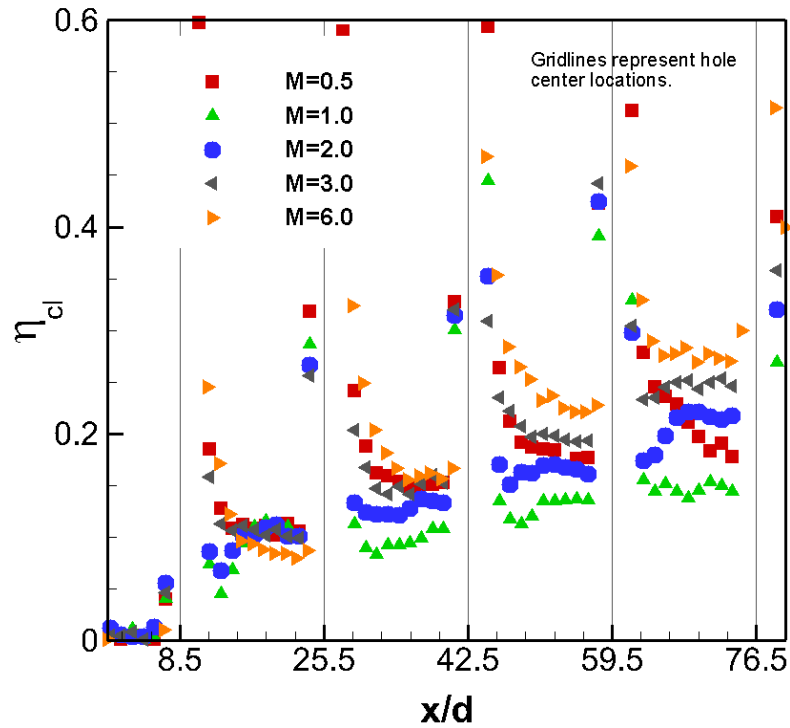


Figure 7.2: Centerline film cooling effectiveness for all blowing ratios

have sufficient momentum to maintain attachment all the way to the next row of holes. Furthermore, as higher momentum coolant is blown into the boundary layer in the initial row of holes, the boundary layer thickens and the coolant does not lift off as easily. This effect can be seen in Fig. 7.2 where the slope of coolant separation immediately downstream of the hole is reduced for each passing row at high blowing ratios.

The laterally averaged effectiveness is defined by averaging the film cooling effectiveness for  $-14.7 < y/d < 14.7$  at a given  $x/d$ , and is shown for all blowing ratios in *Figure 7.3*. The lateral average effectiveness confirms the impact of hole-to-hole interaction at the elevated blowing ratios. For the first five rows ( $x/d < 34$ ), the lowest blowing ratio ( $M = 0.5$ ) outperforms the rest as predicted by single row film cooling literature [4, 5]. However, in the region further downstream ( $x/d > 34$ ), the highest blowing ratios ( $M = 3.0$  and  $6.0$ ) dramatically outperform the other blowing ratios

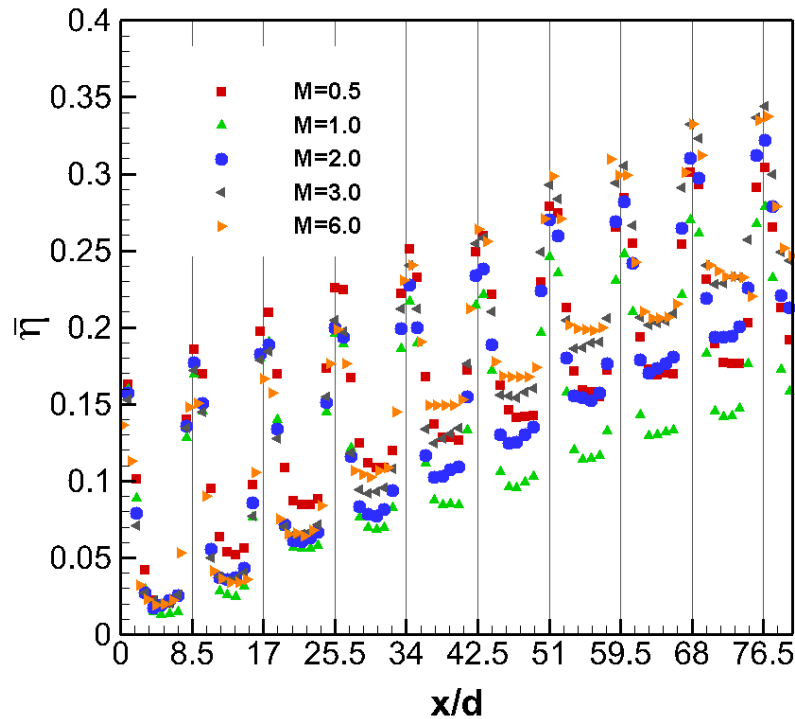


Figure 7.3: Laterally averaged film cooling effectiveness for all blowing ratios

because the higher momentum coolant allows for increased hole-to-hole interaction. When the coolant collides with the subsequent row, the coolant is deflected away from the streamline and spreads laterally, so the laterally averaged film cooling effectiveness is significantly increased. While coolant usage should be minimized in actual film cooling scenarios, it is important to note the improved performance at higher blowing ratios because it is contrary to the trends shown for single rows of round holes in film cooling literature [4, 5]. The discrepancy between the effectiveness for effusion film cooling and single row film cooling at elevated blowing ratios strongly suggests that the interaction between rows associated with effusion cooling has a fundamental impact on film cooling effectiveness.

The effect of blowing ratio on the interaction between rows is further illustrated by *Figure 7.4*, which shows the local film cooling effectiveness varying laterally at each

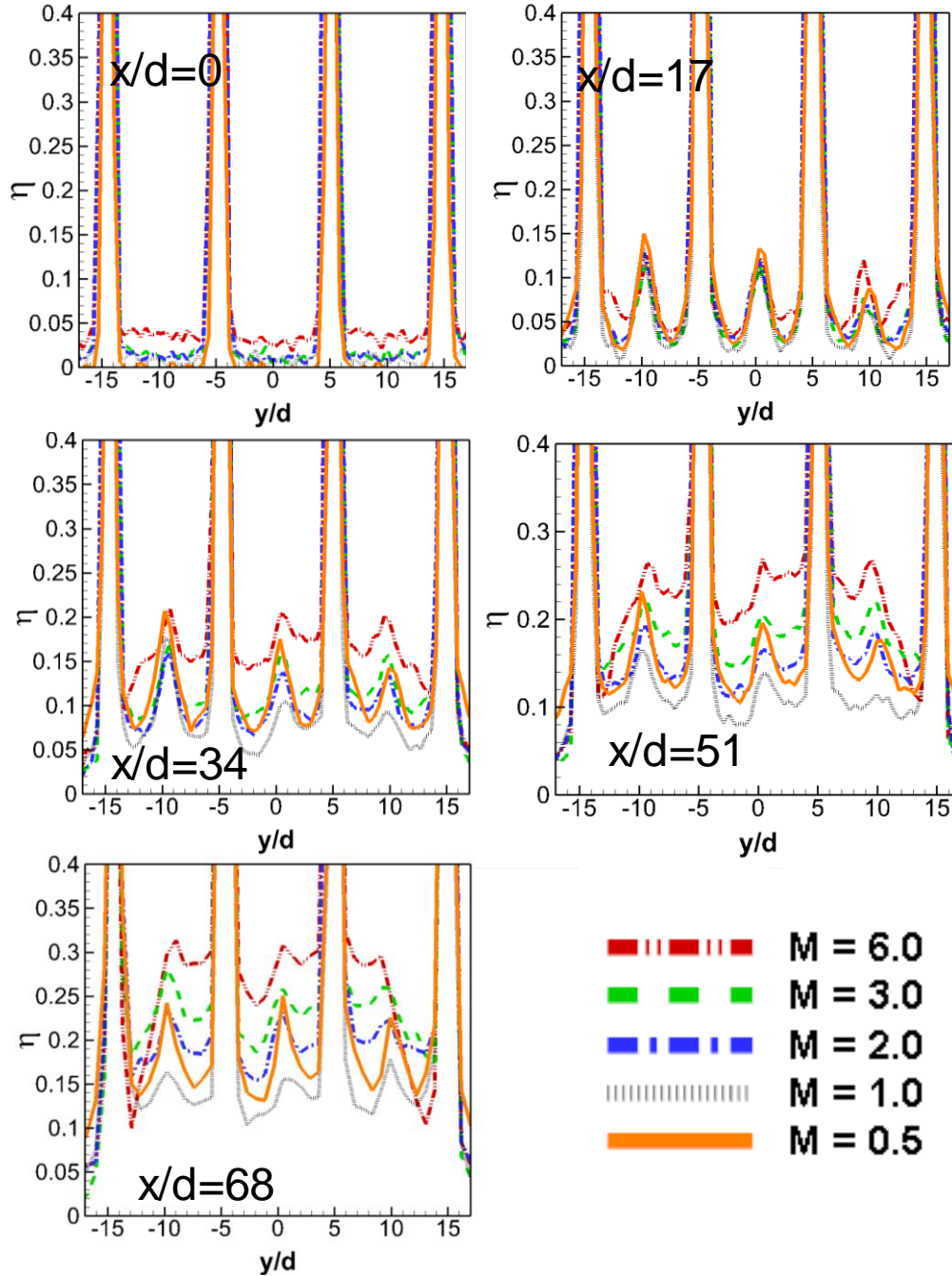


Figure 7.4: Local film cooling effectiveness for all blowing ratios at varying streamwise locations

streamwise hole location. The effectiveness in the area between each hole would be nearly zero in single row applications, so it can show clear effects of row interaction. For  $x/d < 34$ , there is no meaningful difference between all blowing ratios in the area between holes. However, for  $x/d \geq 34$ , the coolant spread is dependent on blowing ratio. The relationship between blowing ratio and downstream coolant spread is caused by the increased row interaction that occurs at higher blowing ratios. Row interaction increases with blowing ratio because the coolant is traveling faster and reaches the next row, which results in increased lateral spread of the coolant.

Increasing the blowing ratio also results in more coolant blowing into the mainstream boundary layer, which results in boundary layer thickening. The thicker boundary layer helps higher momentum coolant stay attached to the surface. This increased attachment results in increased row interaction, which also increases the spread of coolant. This causes the raised effectiveness between holes seen for  $x/d \geq 34$  that is increased with blowing ratio. The blowing ratio of  $M = 1.0$  performs the worst at all streamwise locations because the coolant and mainstream have equal momentum flux, which causes the coolant to be more easily mixed with the mainstream. Coolant injected at  $M = 1.0$  does not receive significant benefit from the effusion effects noted previously because there is significantly reduced shear between equal momentum flows. Coolant at all other blowing ratios does not have the same momentum flux as the mainstream, which causes the development of a shear layer between the two flows. This shear layer protects the coolant and keeps it attached to the surface. Increasing coolant attachment at high blowing ratios allows the coolant to reach the subsequent row of holes, which causes more coolant spread and raises effectiveness in the area between holes. This can be seen

most clearly at  $x/d = 68$ , where there have been more rows and more interactions. The blowing ratio has the strongest impact on effectiveness for this streamwise location because the amount of row interaction is directly dependent on the blowing ratio.

The overall, surface average effectiveness is used to simplify the analysis by showing the average cooling in a region, making it easier to distinguish the overall effect of blowing ratio in effusion film cooling. The overall, area averaged effectiveness region is defined by  $17 < x/d < 84$ ,  $-14.7 < y/d < 14.7$ , which limits the data to exclude the first row of sacrificial holes, so that effusion cooling is emphasized. The overall averages are shown in *Figure 7.5*. The overall effectiveness is elevated at  $M = 0.5$  despite the minimal effusion film cooling effects due to the optimum performance of round holes at that blowing ratio. In general, a blowing ratio of  $M = 0.5$  would not likely outperform higher

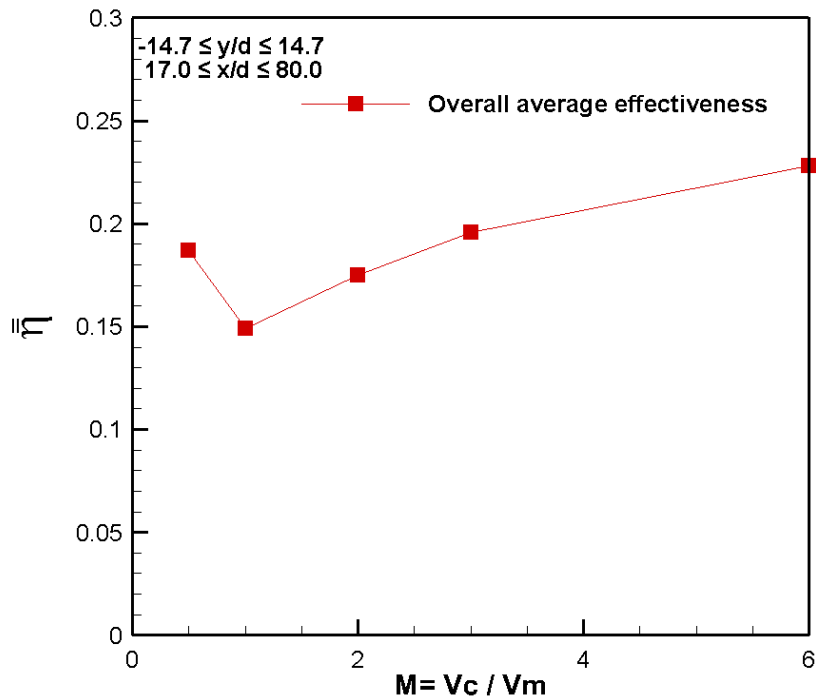


Figure 7.5: Overall, area averaged film cooling effectiveness for all blowing ratios

blowing ratios for other hole geometries where  $M = 0.5$  is not the optimum for the shape. The overall average decreases dramatically as the blowing ratio is increased from  $M = 0.5$  to  $M = 1.0$  because single rows of round holes perform worse at blowing ratios of  $M = 1.0$  and a protective shear layer is not formed at this blowing ratio. As the blowing ratio increases, the overall average also increases because effusion effects such as the lateral spread of coolant and the formation of a protective shear layer increase with blowing ratio.

The trends shown in the present study are similar to the trends shown in literature discussed in chapter two, as shown in *Figure 7.6*. For effusion film cooling, the laterally

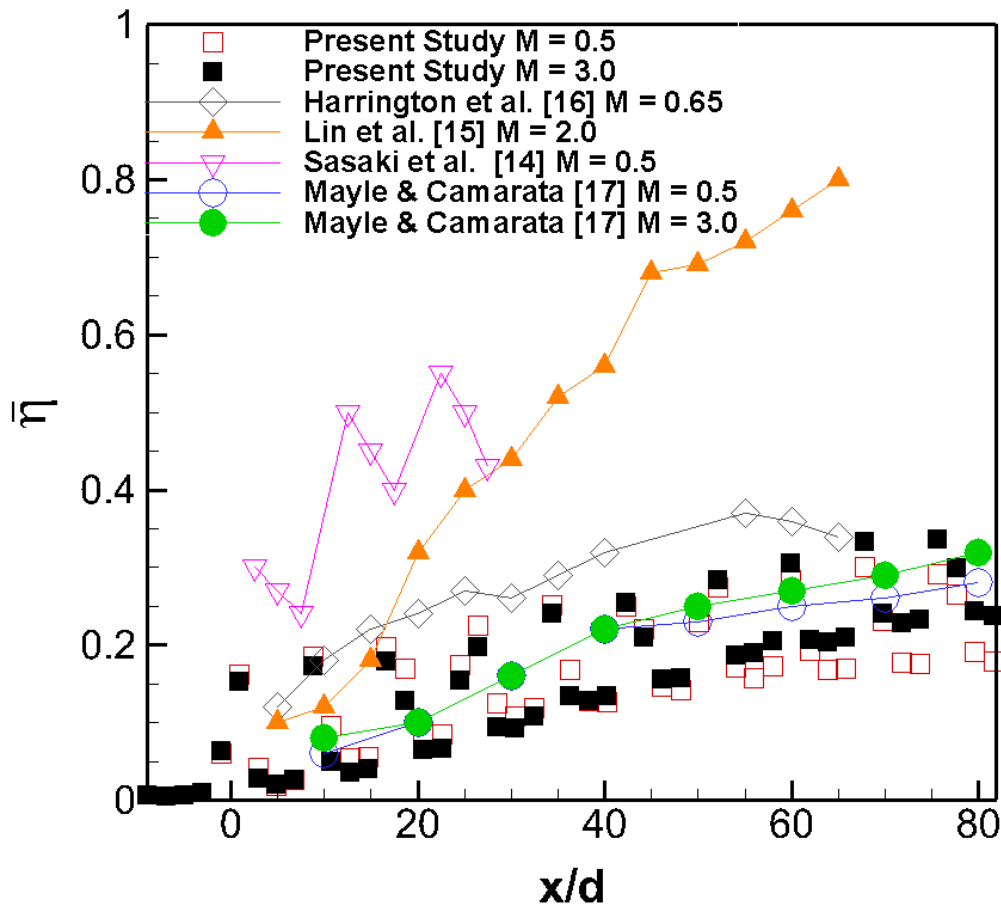


Figure 7.6: Literature comparison for lateral average film cooling effectiveness for blowing ratios ranging from  $M = 0.5$  to 3.0

averaged film cooling effectiveness increases with  $x/d$ . As shown in *Table 7.1*, this occurs for a wide variety of hole geometries and flow conditions. While the geometry of the DMLS plate does not match any previous study, there are sufficient similarities to assume that previous data and the present study should have reasonable agreement. Figure 7.6 shows that there is a non-negligible difference in the magnitude of the laterally averaged effectiveness of the present study when compared with previous full coverage investigations. The present work is not claiming that those previous investigations are inaccurate, but the PSP technique has been thoroughly validated and the tests were performed multiple times to confirm the reliability of the results. The one glaring difference between the investigated baseline round coupon and previous effusion cooling studies is the manufacturing of the cooling coupon. By physical inspection, it was clear that the DMLS technique had introduced roughness into the film cooling hole and the surface of the coupon.

The discrepancy in the magnitude of film cooling effectiveness led to further investigation of the hole roughness, which could potentially reduce film cooling

Table 7.1: Details of previous effusion cooling investigations

Authors	Sasaki et al. [14]	Lin et al. [15]	Harrington et al. [16]	Mayle & Camarata [17]	Present Study
Hole Arrangement	staggered	staggered	staggered	staggered	staggered
Row Spacing (S/D)	10	8	7.14	10	8.5
Hole Spacing (P/D)	3	4	7.14	8.66	9.8
Injection angle ( $\theta$ )	45	30	90	$\theta = 30, \beta = 45$	20
Blowing Ratio (M)	0.5	2	0.65	0.5, 1.5	0.5 - 6.0
Density Ratio (DR)	0.94	1.03 - 1.08	1.7	1	1
Turbulence Intensity	1.5	12.2	0.5	n/a	7.5

effectiveness magnitude. Bunker [87] has demonstrated that accumulation of surface roughness in the exit area of round and shaped holes can have a drastic impact on film cooling effectiveness. It was demonstrated that the centerline effectiveness for a round hole could be reduced by as much 50-60% for a blowing ratio of  $M = 1.0$ . Bunker [87] has only investigated a single row of holes, but showed that the effect of roughness is strongest in the first 20 diameters downstream of the initial hole. This is especially relevant to the present work because there are only 17 diameters between holes. The increased roughness allows more turbulent mixing which creates coolant separation from the plate. Stimpson et al. [88] also showed a similar effect in an investigation of roughness effects in additively manufactured channels. This study showed that increased surface roughness resulted in an earlier than predicted transition to turbulent flow within the channel, leading to increased friction factors. Schmidt et al. [89] investigated the impact of increased plate surface roughness on film cooling effectiveness and heat transfer. The study showed that elevated surface roughness did not have a meaningful effect on the film cooling effectiveness, which was decreased by less than 10% for all flow conditions investigated. While roughness on the surface of the DMLS plate is not likely to have a strong impact, roughness within the film cooling hole may explain the reduced film cooling magnitudes observed.

The surface and hole interior roughness of the DMLS plate used in the present study have been investigated with scanning electron microscopy (SEM). For scanning electron microscopic analysis, the DMLS plate was mounted with aluminum stubs and imaged by a Versa 3D scanning electron microscope (FEI company, Hillsborough, USA) at low vacuum conditions (0.5 mbar), with 5keV, and a working distance ranging

from 15 to 20 mm. A sample image demonstrating the surface roughness for the unpainted side of the DMLS plate is shown in *Figure 7.7*. The surface roughness is on the order of ten micrometers, which is about one percent of the hole diameter ( $\epsilon/d \sim 0.01$ ). While surface roughness location and relative size are mostly random in nature, the average size and maximum size of roughness elements are caused by the manufacturing technique. Several surface roughness images were taken on the painted and unpainted side in order to account for the random nature of the roughness. The order of magnitude of the roughness does not change across the surface of the plate, so only a single representative image is presented.

While roughness of one percent of the diameter is not insignificant, it is negligible compared to the hole interior roughness. The roughness on the interior of the holes caused by the DMLS manufacturing technique is shown in *Figure 7.8* for various hole locations. The images presented have been taken on the bottom surface of various holes, attempting to see as far into the interior of the hole as possible. These SEM images show

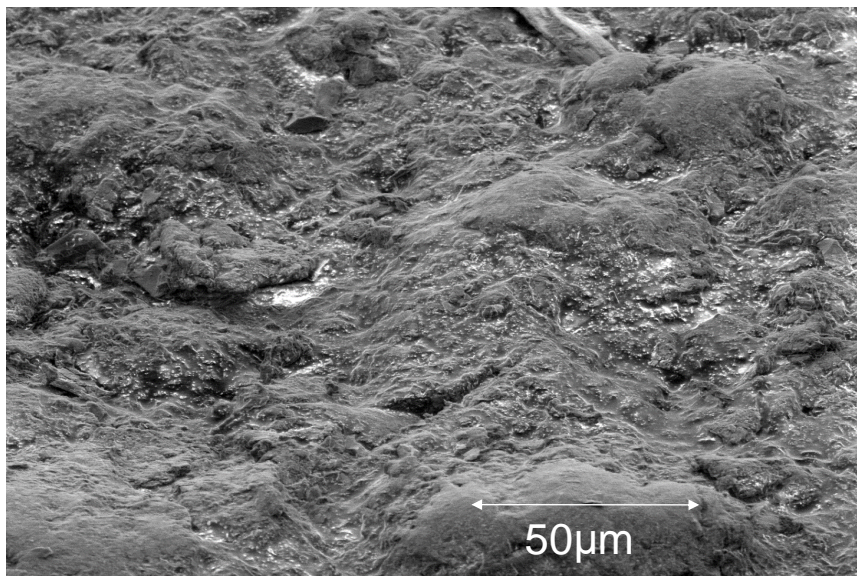


Figure 7.7: Sample of plate surface roughness

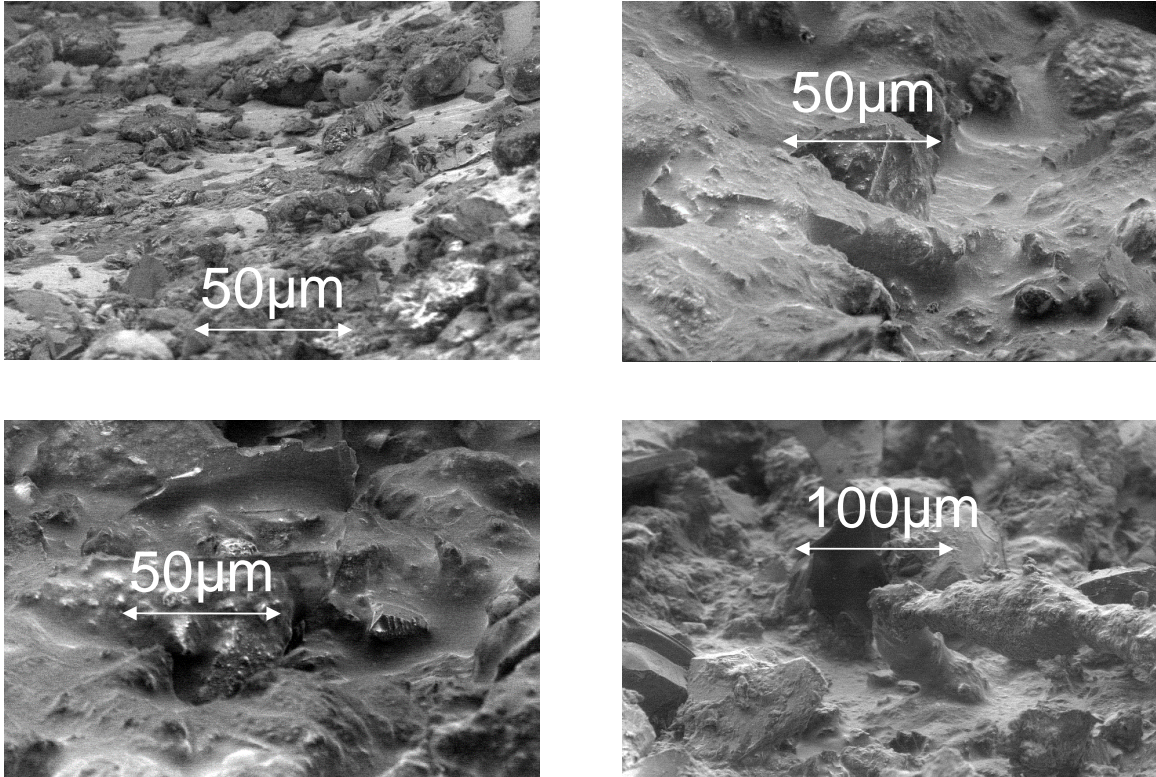


Figure 7.8: Sample roughness on the interior of holes

that the hole interior roughness elements can be on the order of 50-100 micrometers. Roughly five to ten percent of the hole diameter is blocked ( $\epsilon/d \sim 0.05 - 0.1$ ) by roughness elements of this size. Roughness of this size is extreme and helps to explain the diminished effectiveness of the effusion film cooling. Hole interior roughness would increase turbulence that would cause the coolant to separate from the interior wall of the film cooling hole and be more apt to mix with the mainstream air. Roughness elements of this magnitude also cause a significant increase in frictional losses. If the roughness is increased from smooth to  $\epsilon/d = 0.05$ , which is conservative for the roughness elements discovered, the friction factor is doubled at a Reynolds number of 6000 ( $M = 6.0$ ). Doubling the friction factor doubles the pressure drop through the hole. In a real engine, the blowing ratio is determined by the pressure differential across the film cooling hole,

so doubling the pressure loss would also decrease the effective blowing ratio for each hole. In order to maintain the blowing ratio designed based on smooth holes, the pressure difference between the coolant and mainstream flow must be increased. Increasing the pressure difference would have a detrimental impact on engine performance.

In order to more clearly quantify the effect of the roughness, a smooth plate was made using traditional printing techniques with dimensions matching the DMLS part. The traditional part was then tested using the exact same experimental setup as previously discussed. The relatively smooth test coupon was created on a Stratasys Objet 30 Pro printer. The film cooling plate was fabricated from Polyjet Rigid Opaque White material (VeroWhite Plus) that approximates the material properties of ABS plastic. The printer uses a spatial resolution of 16  $\mu\text{m}$  with a build layer thickness of 28  $\mu\text{m}$ . The build was oriented such that layers were added to the test coupon in the z-direction. After the part was printed, a 1.27 mm drill bit was used (at the 20° angle of inclination) to carefully remove any major surface defects within the holes in an effort to decrease the effect of roughness. While this does not provide a completely smooth surface, the printing and treatment provide a clear contrast in the roughness of the two additive manufacturing techniques.

The exact same PSP experimental setup was utilized to obtain film cooling effectiveness distributions for blowing ratios ranging from  $M = 0.5$  to  $M = 3.0$ . The results from the coupon printed with the Objet 30 Pro printer are directly compared to the PSP results from the DMLS coupon to determine the film cooling effectiveness degradation caused by the DMLS manufacturing technique. This comparison is shown in *Figure 7.9*, where centerline plots have been utilized to show the effect of roughness

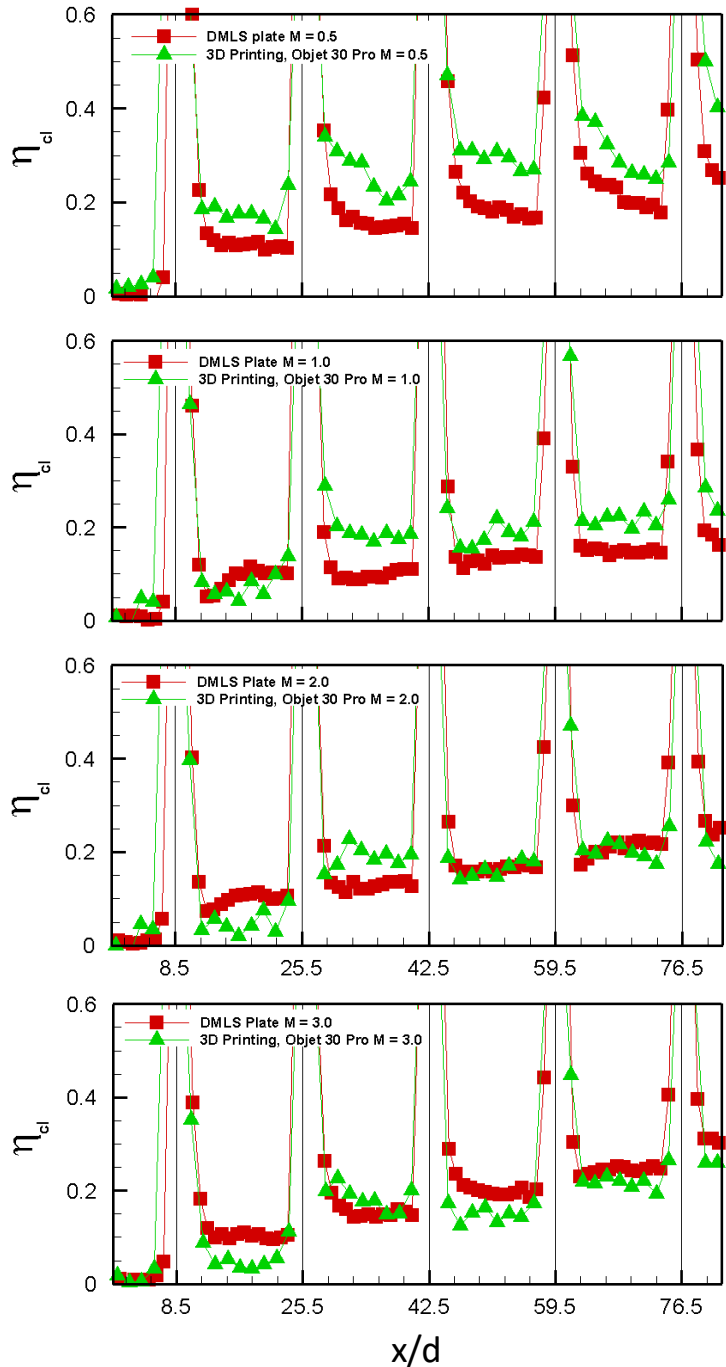


Figure 7.9: Centerline effectiveness comparison for DMLS and Objet ABS test plates

most clearly. Figure 7.9 shows that the roughness is most detrimental to film cooling at the lowest blowing ratio. For  $M = 0.5$ , the centerline effectiveness of the DMLS test coupon is approximately half of the effectiveness for the Objet 30 Pro coupon. The

effectiveness is also decreased by roughness for a blowing ratio of  $M = 1.0$ , but not as significantly as  $M = 0.5$ . The impact of roughness decreases for increasing blowing ratio. This occurs because higher blowing ratios have higher Reynolds numbers. As the Reynolds number is increased, the boundary layer formed inside the length of the hole becomes thinner, and any size defect on the surface protrudes from the boundary layer and influences the flow through the hole. At the lowest blowing ratio of  $M = 0.5$ , the reduced roughness within the Objet part is not significant enough to protrude outside the sublayer thickness, and therefore, the smoother Objet part provides improved film cooling protection on the surface. With the large roughness elements created by the DMLS part, the features alter the flow within the hole resulting in reduced coverage downstream of the hole. For thinner boundary layers associated with higher blowing ratios, both the Objet and DMLS roughness are large enough to effect the flow development inside of the hole, resulting in reduced film cooling effectiveness on the flat plate.

The roughness caused by the DMLS technique has also been investigated by Snyder et al. [90] and Stimpson et al. [88]. Snyder et al. [90] used a CT scanner to quantify the effect of DMLS build direction on both the surface and hole interior roughness. The study showed a vertical build direction could be used to reduce surface roughness, but hole interior roughness was significantly increased in comparison with traditional manufacturing techniques regardless of build direction. Stimpson et al. [88] also used a CT scanner to show that channels created with the DMLS technique can have large deviations from the specified hydraulic diameter. The study also demonstrated a significant increase in the friction factor within the channel, which suggests the flow

transitions to turbulent earlier than predicted by smooth models. The present study has used SEM technology to visualize individual roughness elements on the surface of the plate and within the hole interior. The SEM showed significant blockages caused by the roughness that would lead to earlier turbulent transition. The film cooling effectiveness was reduced by nearly 50% along the centerline at the lowest blowing ratio from this effect of DMLS roughness.

The DMLS technique must undergo further evaluation in order to determine the viability of the new manufacturing technique for film cooling applications. At present, the DMLS manufacturing technique applied to round holes leads to a significant reduction in film cooling effectiveness at low blowing ratios. The technique certainly shows potential for creating more complex hole geometries, but the drawbacks of the roughness resulting from the DMLS technique must be considered and eliminated or mitigated.

#### *Baseline Round Results*

The same PSP experimental setup was used to evaluate the baseline round hole at blowing ratios commonly used for combustor liner film cooling. Blowing ratios of  $M = 6.0, 7.5,$  and  $8.5$  have been investigated at a density ratio of  $DR = 1.0$  to determine the impact of higher blowing ratios in effusion film cooling applications, and create a baseline for determining the performance of shaped holes at higher blowing ratios in effusion film cooling applications. The results will be presented in terms of the effectiveness distributions, and then further presented as the centerline and laterally averaged effectiveness to aid in analysis of the data.

The PSP validation results along with the work of Andrews et al. [48] suggest that increasing the blowing ratio above  $M = 6.0$  will not have further benefit. *Figure 7.10* shows the film cooling effectiveness distributions for the three blowing ratios investigated. The effectiveness results clearly confirm that continuing to increase the blowing ratio above  $M = 6.0$  does not improve film cooling effectiveness. The difference

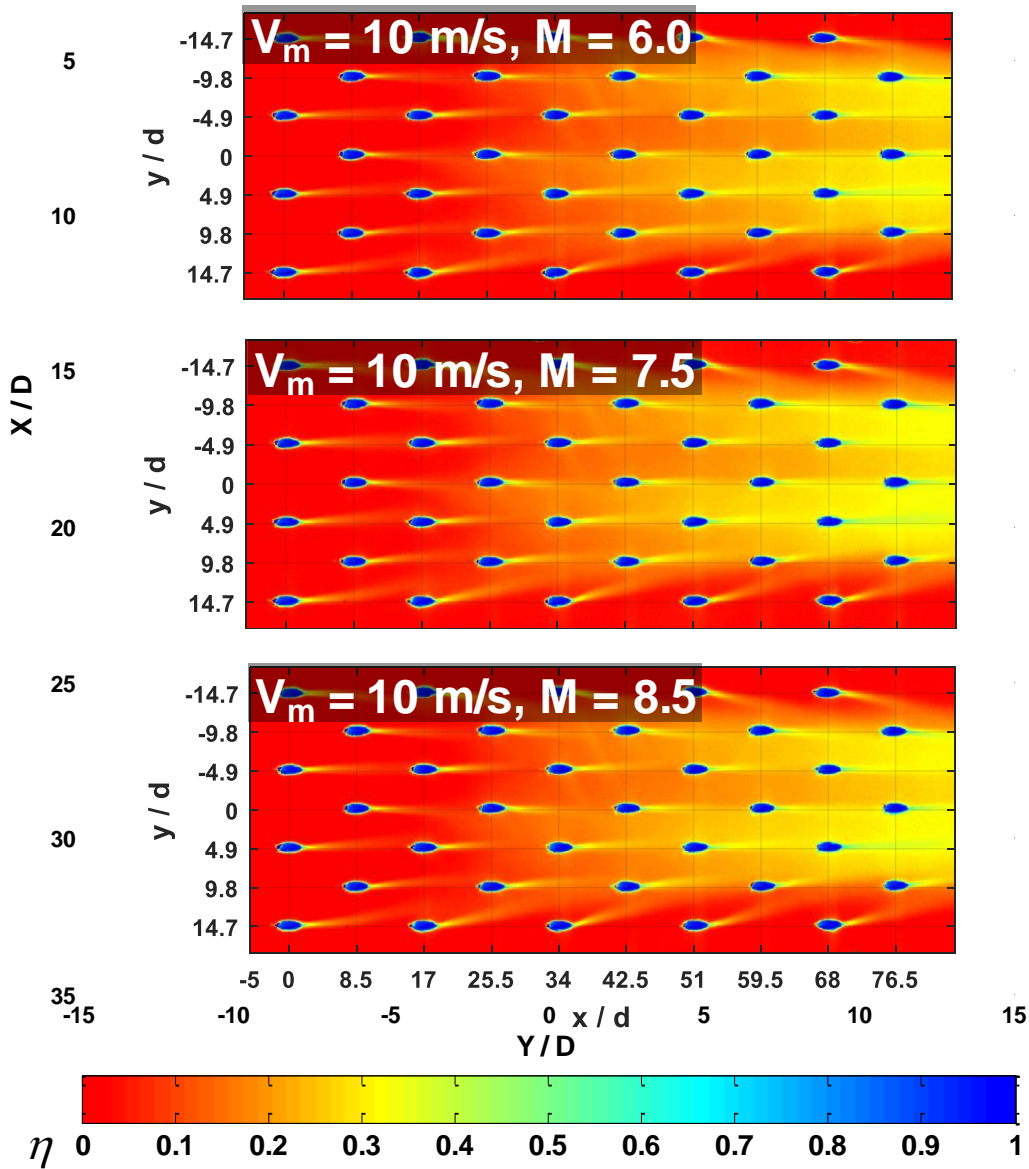


Figure 7.10: Film cooling effectiveness distributions for round holes at engine realistic blowing ratios

between the three blowing ratios is negligible. The effects of effusion film cooling mentioned previously are still present, as the initial row of holes acts as a sacrifice. The initial row blows into the boundary layer, and increased momentum coolant further thickens the boundary layer. This allows each successive row of jets to stay more closely attached, and therefore, more of the coolant stays attached to the surface long enough to collide with the next row of jets. This collision causes the coolant to spread laterally, and with each successive row, the effectiveness in between the holes is raised substantially. However, increasing the blowing ratio beyond  $M = 6.0$  does not have the same impact that it did at the lower blowing ratios investigated previously. This suggests that there is some limit to the benefit of blowing into the boundary layer in the initial rows and allowing higher momentum coolant to stay attached to the surface and cause increased lateral spread. Above  $M = 6.0$ , the boundary layer thickness has already been increased substantially, and further increases will not have any significant effect. The additional coolant is not colliding with the subsequent holes, as the coolant velocity is so high that the added coolant at the higher blowing ratios is lifting off the surface of the coupon.

*Figure 7.11* shows the centerline effectiveness for the three blowing ratios investigated. The negligible impact of increasing the blowing ratio above  $M = 6.0$  is further illustrated by the fact that the effectiveness is reduced to the same value regardless of the blowing ratio. Increasing the blowing ratio of coolant increases the coolant momentum in the normal and tangential directions to the surface. Increasing normal momentum means that the coolant will separate from the surface, while increasing tangential momentum allows more coolant to reach the successive row of holes and spread out over the surface. These effects counteract each other, so the net effect of

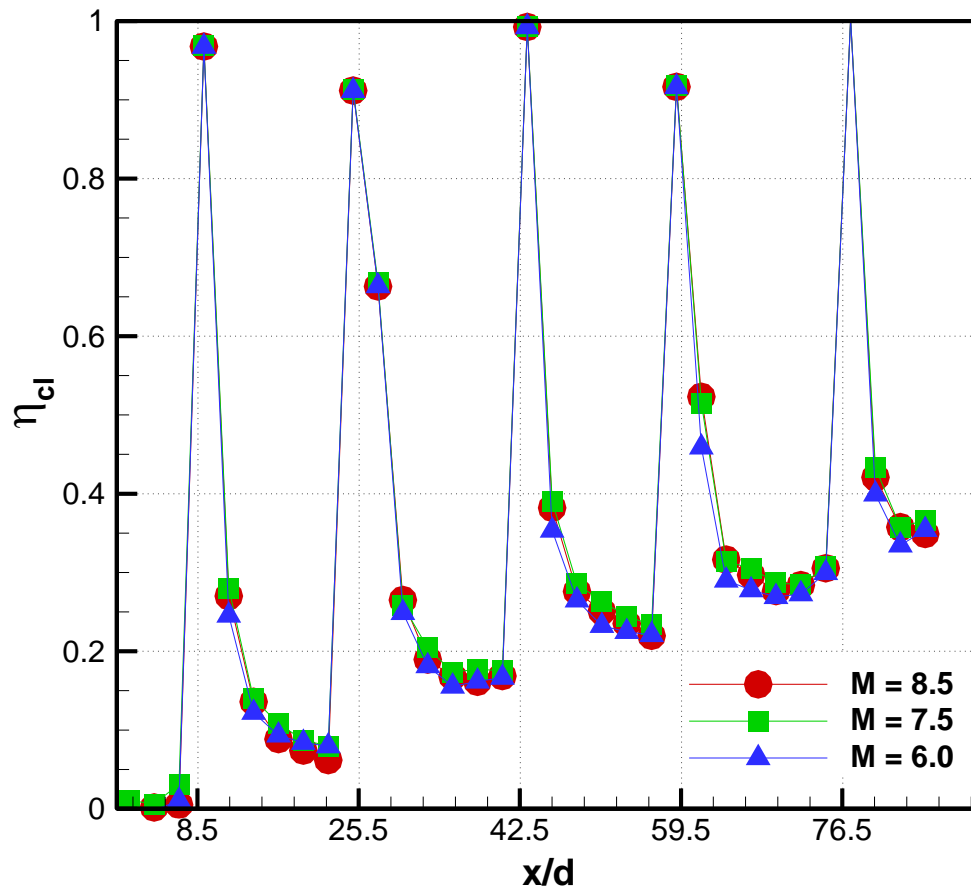


Figure 7.11: Centerline film cooling effectiveness for round holes at engine realistic blowing ratios

increasing the blowing ratio above  $M = 6.0$  is negligible. It should also be noted that the minimum centerline effectiveness does not reach a maximum value for the rows investigated. The increase in minimum effectiveness that occurs with each passing row is leveling off, but does not reach the “fully developed” region observed by Harrington et al. [51], wherein the coolant has passed a sufficient number of holes in the streamwise direction such that additional superposition and coolant spread is no longer beneficial.

The distributions are also analyzed in terms of the laterally averaged effectiveness, which is shown in *Figure 7.12*. For round holes, increasing the blowing ratio does not have any further effect on film cooling. The coolant does not spread any further and increase the lateral average effectiveness because increasing the mass flow of

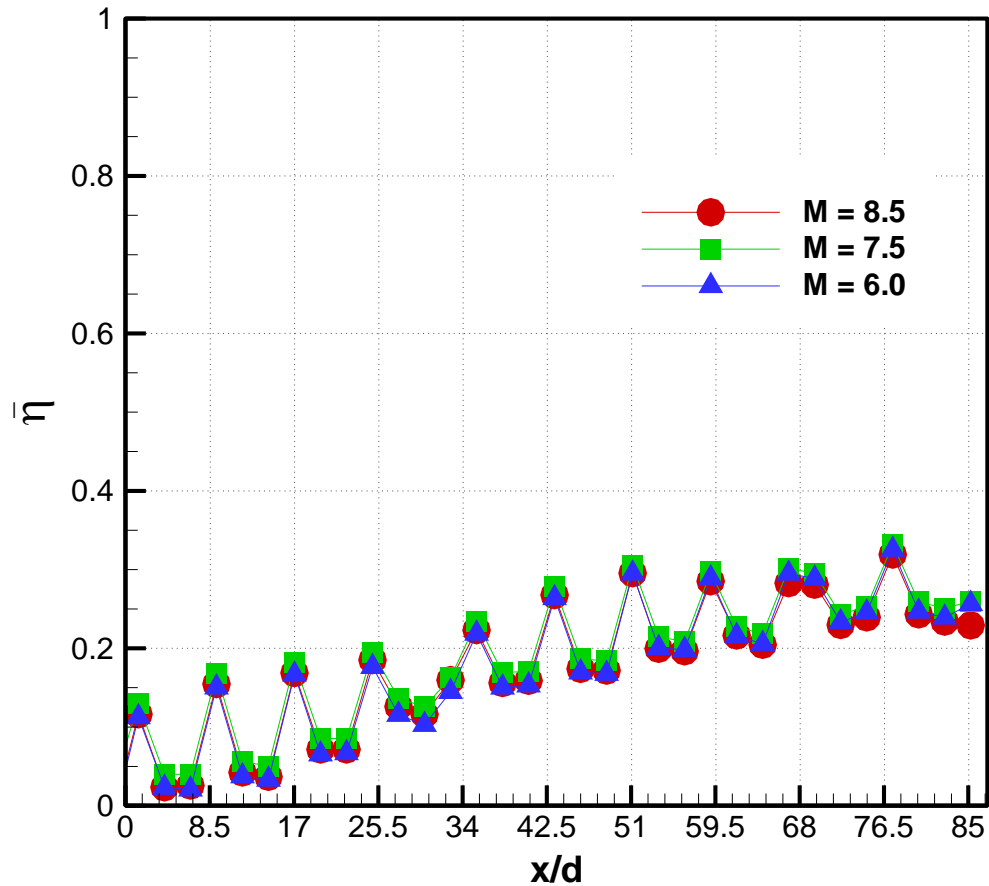


Figure 7.12: Laterally averaged film cooling effectiveness for round holes at engine realistic blowing ratios

coolant is counteracted by the increased jet momentum, causing more coolant to separate from the surface and not collide with the successive row of holes. The lateral average does level off, which suggests that ten rows is approximately the number required to reach the fully developed region, even though the centerline effectiveness has not fully leveled off by this point.

#### *Baseline Shape Results*

An innovative shaped hole geometry (Fig. 5.3) has also been tested using the same experimental setup as the round plates. The outlet of the hole is similar to a standard diffuser shaped hole, although with lower angle of inclination. The inlet and

inner workings of this non-line of sight hole are not exactly known, but for the purposes of this study, the hole can be considered similar to a laidback, fanshaped hole. It should also be noted that the DMLS roughness noted in the experiment verification is still present for the shaped hole. This roughness reduces the film cooling effectiveness, so the data presented might under-predict the film cooling effectiveness if the DMLS roughness could be minimized.

*Figure 7.13* shows the effectiveness distributions for the shaped holes. It is immediately clear that effusion cooling with shaped holes is extremely effective. After just four rows, the entire plate is uniformly covered with coolant. As previously known from single row film cooling literature, shaped holes outperform round holes because the expanded outlet area slows the coolant down so that it stays more closely attached to the surface. These particular shaped holes have a lower angle of inclination than traditional shaped holes, which makes the hole much longer. This helps the coolant to stay attached inside of the hole, and also means that the coolant does not travel as far along the surface of the plate before reaching the next row of holes. This allows more coolant to collide with the succeeding jet, increasing the spread and blanketing effect over the entire plate. It can also be clearly seen that the blowing ratio has a negligible effect over the range investigated. Increasing the mass flow rate through the shaped holes does not affect film cooling because enough coolant is already blowing into the boundary layer for  $M = 6.0$ . The boundary layer is already thick enough to protect the downstream rows, and any further coolant mass flow just separates from the surface.

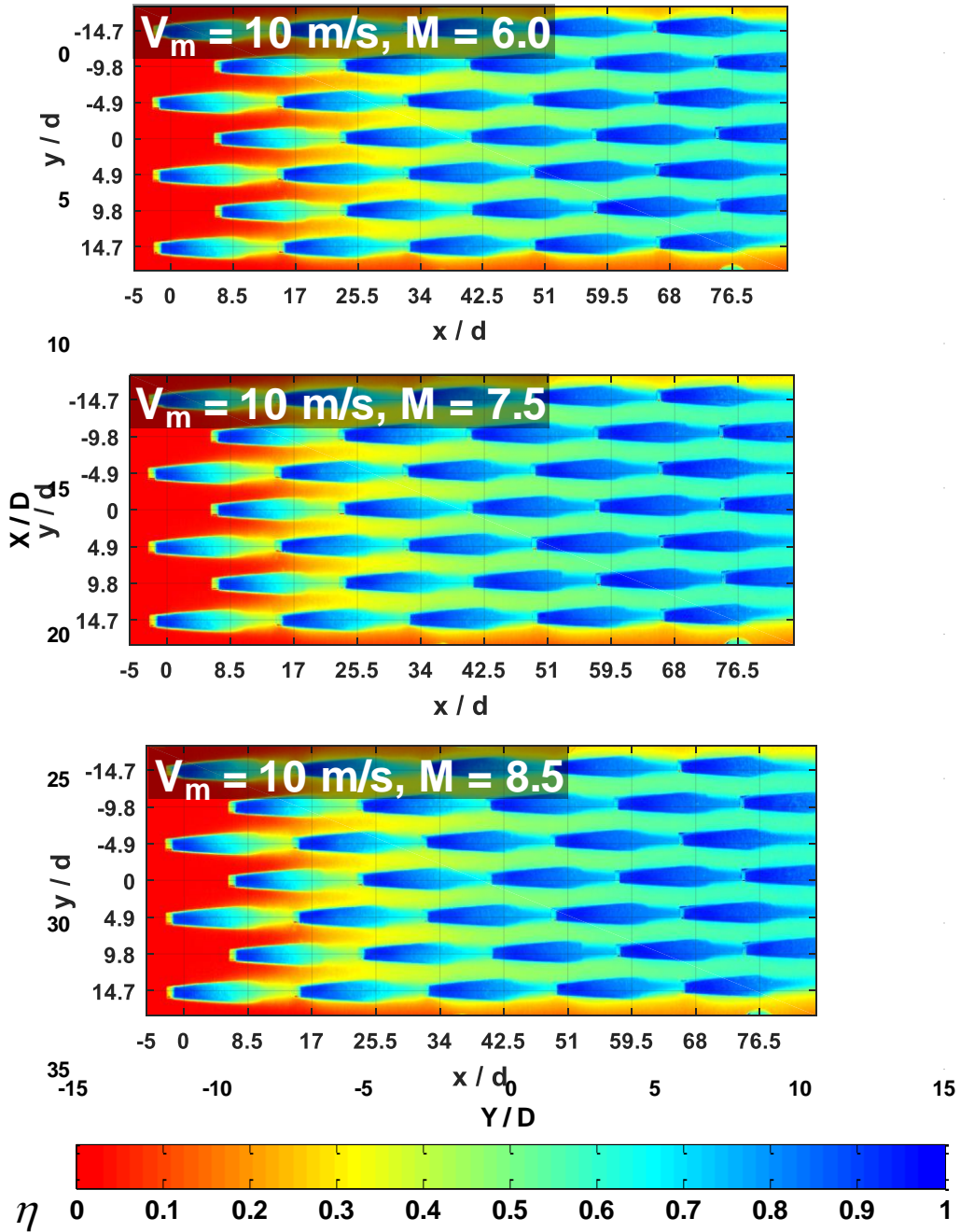


Figure 7.13: Film cooling effectiveness distributions for shaped holes at engine realistic blowing ratios

The film cooling effectiveness distributions are analyzed by the centerline effectiveness, as shown in 7.14. The minimum effectiveness increases from  $\eta = 0.5$  to  $\eta = 0.7$  after just one row of holes. After the second row, the minimum effectiveness

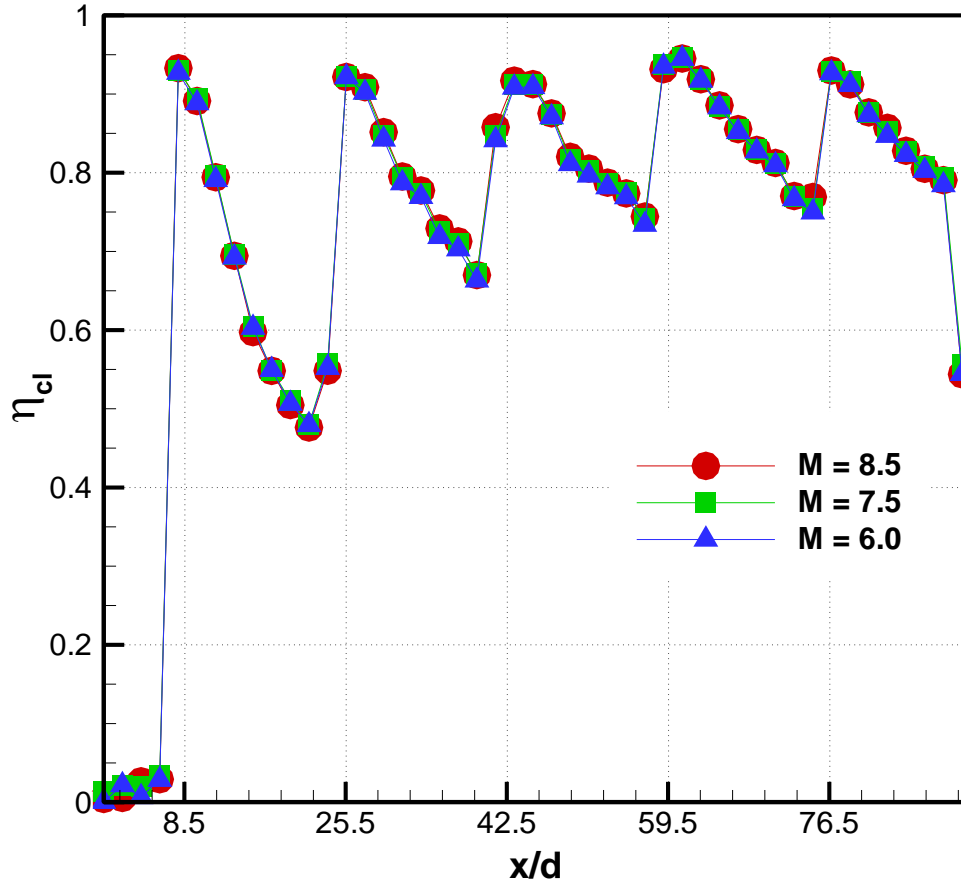


Figure 7.14: Centerline film cooling effectiveness for shaped holes at engine realistic blowing ratios

increases slowly before reaching a maximum of  $\eta = 0.8$  after the fifth row. This demonstrates that the first row of holes does act as a sacrifice row at these high blowing ratios just as it does for round holes. More coolant stays attached to the surface of the plate in the rows downstream of the initial row because the initial row blows into the boundary layer, which thickens it. The thickened boundary layer allows the coolant protection from the mainstream flow. As the coolant has increased streamwise momentum at a low inclination angle, the coolant can more easily maintain the path without separating from the surface.

Figure 7.15 reveals how effective this film cooling geometry is at these high blowing ratios. The laterally averaged effectiveness reaching above  $\eta = 0.7$  is nearly three times better than round hole film cooling. It is important to note that after four rows of holes, the difference between the maximum and minimum film cooling effectiveness for each row is reduced to nearly zero. This occurs for the same reason that the centerline effectiveness quickly reaches a “fully developed” region. The length of the hole allows so much coolant to reach the subsequent row of holes that it spreads evenly across the holes. Almost all of the coolant makes it to the next row and spreads out, and approaches a maximum. Increasing the coolant flow rate would not help more because there are some

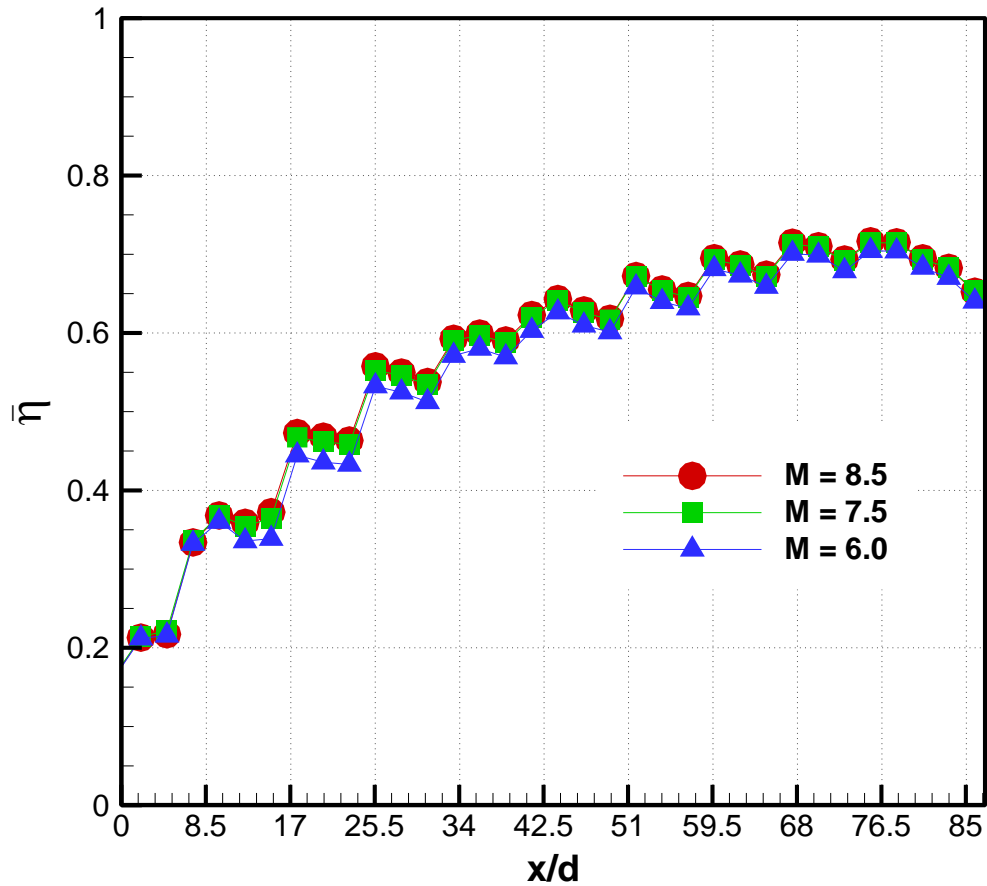


Figure 7.15: Lateral average film cooling effectiveness for shaped holes at engine realistic blowing ratios

losses associated with these spreading collisions. The turbulence generated that helps to spread the coolant out also imposes an upper limit on the cooling effectiveness.

### *Double Hole Results*

The other innovative geometry studied is a double hole geometry as shown in Fig. 5.4. The double hole geometry has a single inlet hole, and splits into two holes inside of the plate. Each of the two double holes is similar to the shaped hole, but with smaller lateral expansion and laidback angles. The same effect of DMLS roughness likely applies to this geometry as well, so reducing the DMLS roughness could further improve these results.

The film cooling effectiveness distributions for the double hole geometry are presented in *Figure 7.16* for the three blowing ratios investigated. While the impact of blowing ratio is minimal, the double hole geometry actually outperforms the shaped hole geometry. Since each hole is split into two, the flow rate of coolant through each hole is half of the flow rate through each baseline round or shaped hole. The coolant exiting the double hole geometry does not stay attached to each hole as well as it does for shaped holes, as the shaped holes are more optimum for single row film cooling. However, this means that more coolant blows into the boundary layer in the initial row and protects the coolant downstream. Furthermore, the double hole geometry effectively creates one much wider hole. While the small area between each hole is not perfectly covered, the width of the double hole means that there is no area between the holes. The top edges in the first row of the staggered array line up with the bottom edges of the second row of double holes. This results in the same blanketing coverage as the shaped hole, without the need

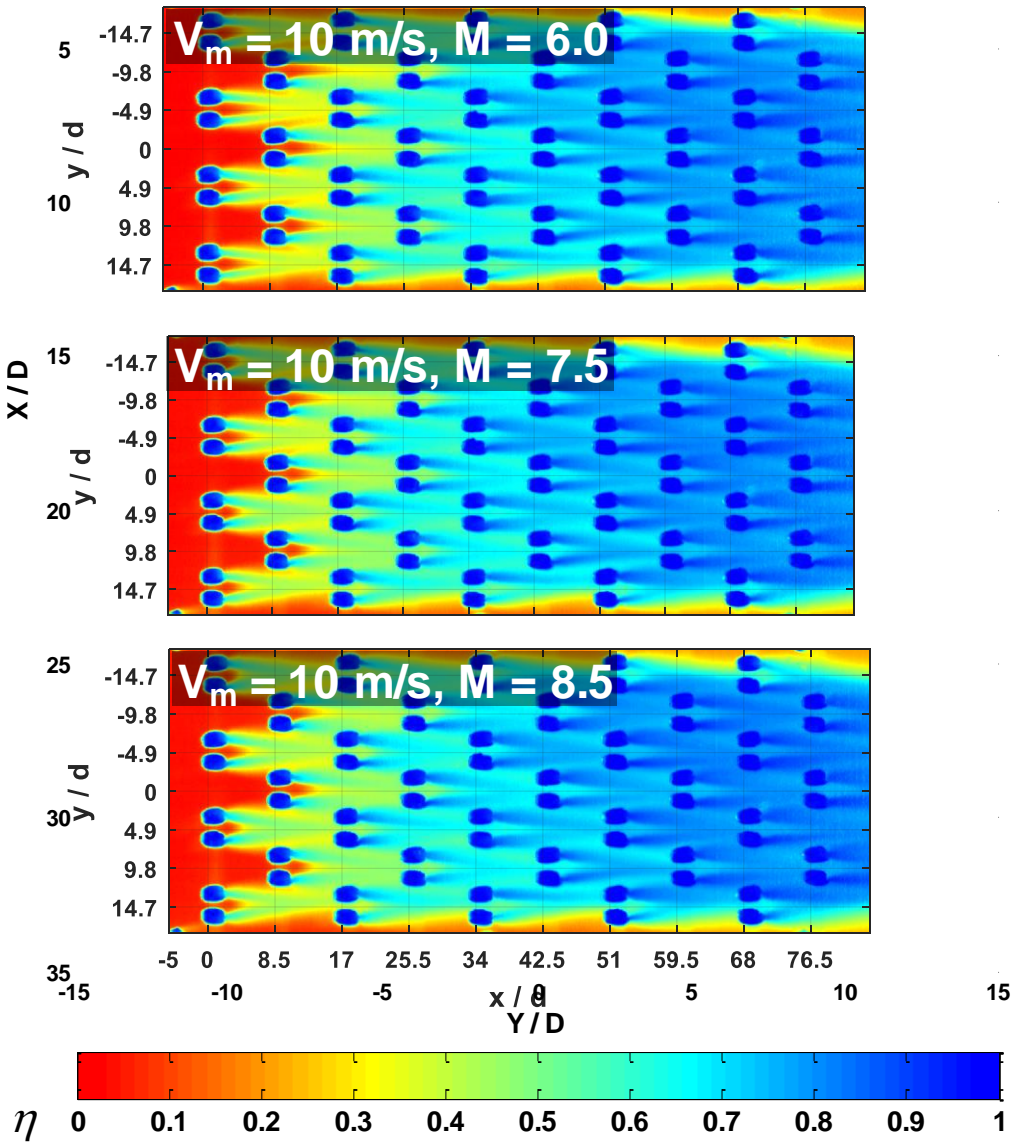


Figure 7.16: Film cooling effectiveness distributions for double holes at engine realistic blowing ratios

for collisions to spread the coolant. The impact of blowing ratio is negligible, as it has been for the baseline round and shaped holes. Increasing the blowing ratio just means further thickening of the boundary layer as more coolant blows off of the surface. While boundary layer thickening is beneficial, the film cooling effectiveness is so close to  $\eta = 1.0$ , that further thickening of the boundary layer to protect the downstream rows of holes has a negligible impact.

Figure 7.17 shows the centerline effectiveness of the double hole geometry at the three blowing ratios. The double hole geometry does not actually have a film cooling hole along the centerline, so the spikes seen in effectiveness for the shaped and round hole film cooling are not present. The lowest blowing ratio ( $M = 6.0$ ) does have slightly reduced centerline effectiveness in the initial rows of holes because the increased coolant velocity and mass flow rate leads to increased mixing between the two holes in the double hole geometry. After the initial rows, the blowing ratios converge fully because the blanketing effect fully covers the area between the holes.

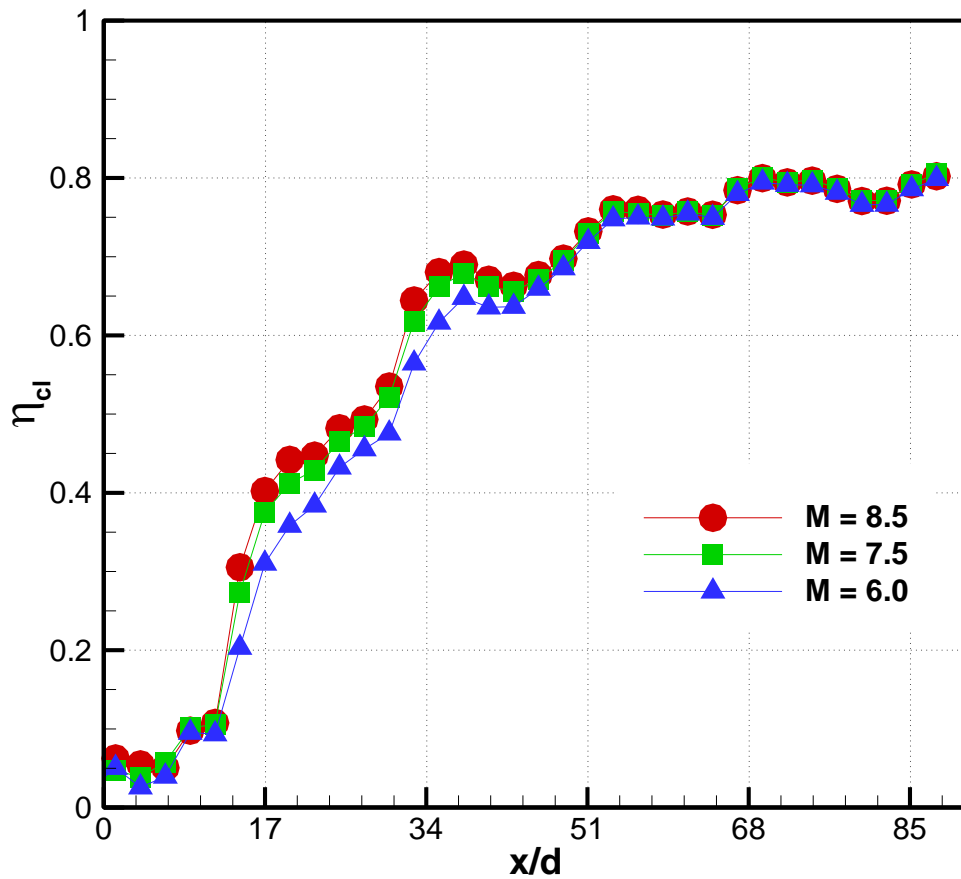


Figure 7.17: Centerline film cooling effectiveness for double holes at engine realistic blowing ratios

The laterally averaged effectiveness of the double hole geometry is shown in *Figure 7.18*, which further demonstrates the high film cooling effectiveness for the double hole geometry. The lateral average reaches above  $\eta = 0.8$ , showing that the coupon is almost completely blanketed in the film coolant. After about five rows, the laterally averaged effectiveness is no longer increasing as the coolant travels further downstream. This occurs because the blanketing of the downstream section is caused by collisions. The collisions help to spread the coolant and achieve high downstream coverage, but the effectiveness is also capped by these row interactions. The collisions do cause some coolant to separate from the surface instead of spreading further over the surface.

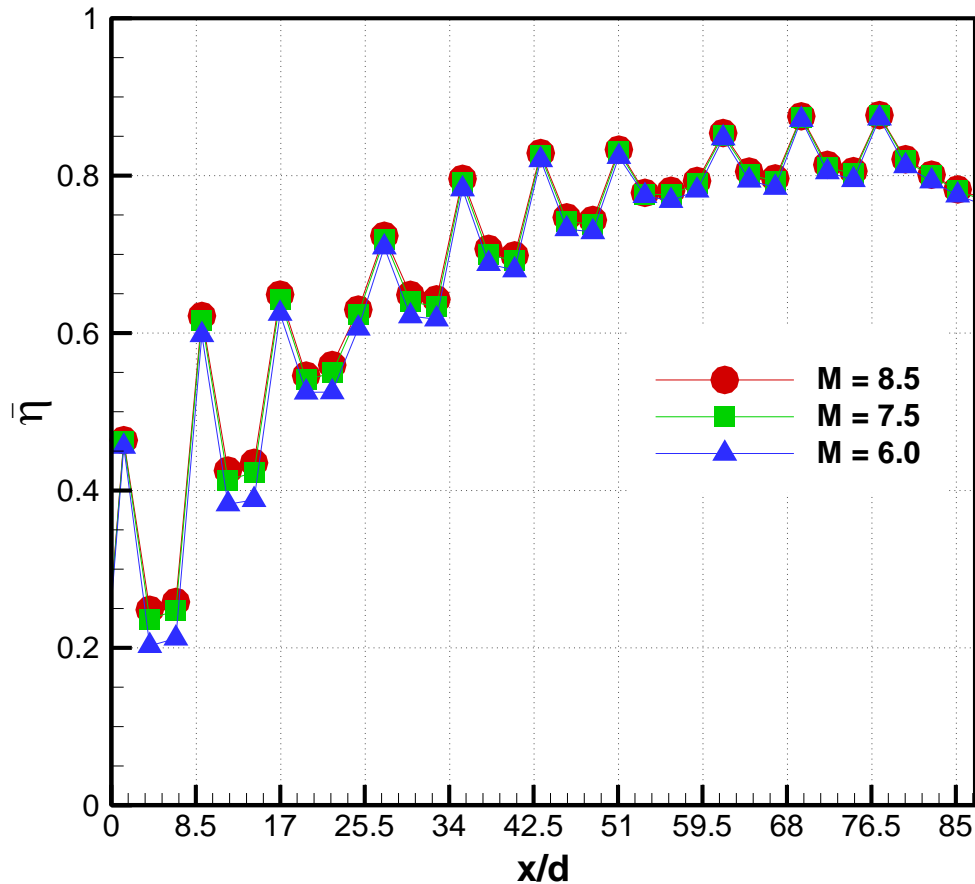


Figure 7.18: Lateral average film cooling effectiveness for double holes at engine realistic blowing ratios

### Comparison of Three Geometries

The difference between the advanced shaped holes (single shaped and double hole) and the baseline round holes reveals the tremendous potential of the DMLS shaped holes. *Figure 7.19* shows the comparison of the lateral average effectiveness of the shaped holes compared with the round holes. The double hole performs the best, but the shaped hole also shows an improvement of approximately three times over the round hole. This improvement is remarkable, and clearly shows the potential of effusion cooling with shaped holes in combustor applications. Shaped holes allow more coolant to stay attached to the surface and collide with the subsequent row. Interactions between rows of

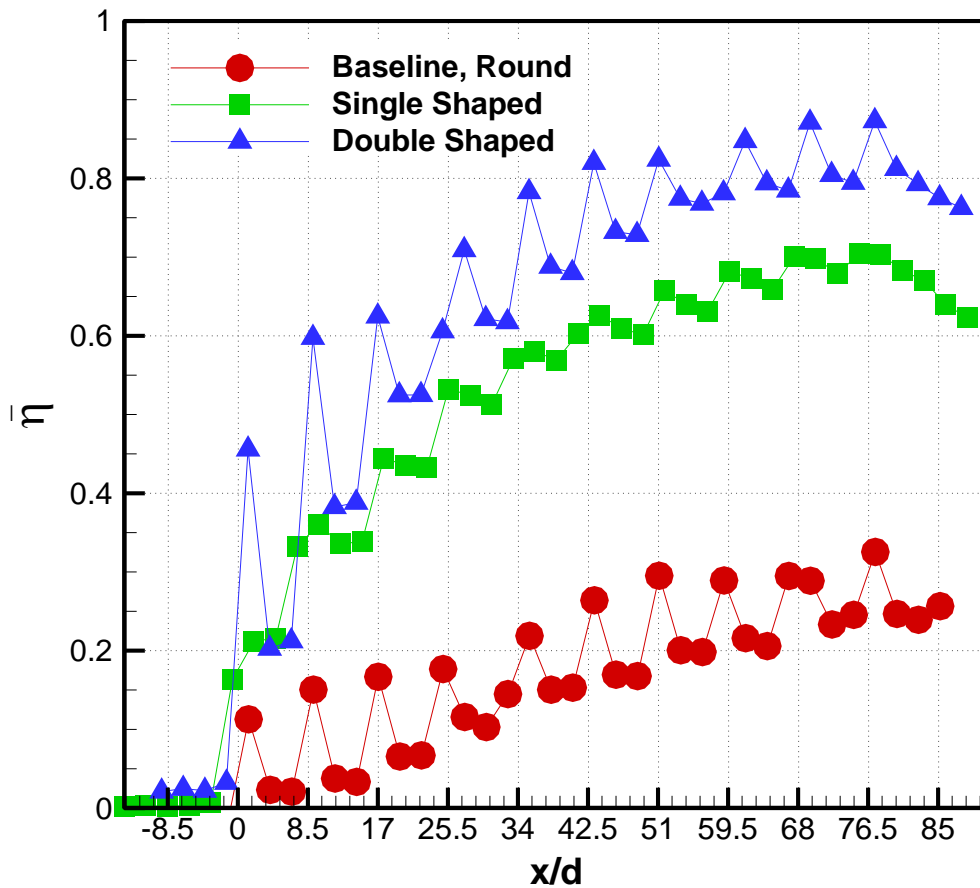


Figure 7.19: Lateral average film cooling effectiveness for all three shapes for  $M = 6.0$

film cooling holes are the primary factor in the improvement of film cooling in the downstream region. Increased row interactions lead to increased superposition, so the effectiveness immediately downstream of the hole is raised. The increased collisions also lead to improved spread of the coolant, which is most clearly illustrated in *Figure 7.20*. The figure shows the three hole shapes for a blowing ratio of  $M = 6.0$  at  $y/d = 2.45$ , which is the exact middle of two holes, where the effectiveness would be zero for single row film cooling applications and minimized for full coverage applications. The double hole is so wide that there is a slight overlap at  $y/d = 2.45$  but the difference between the

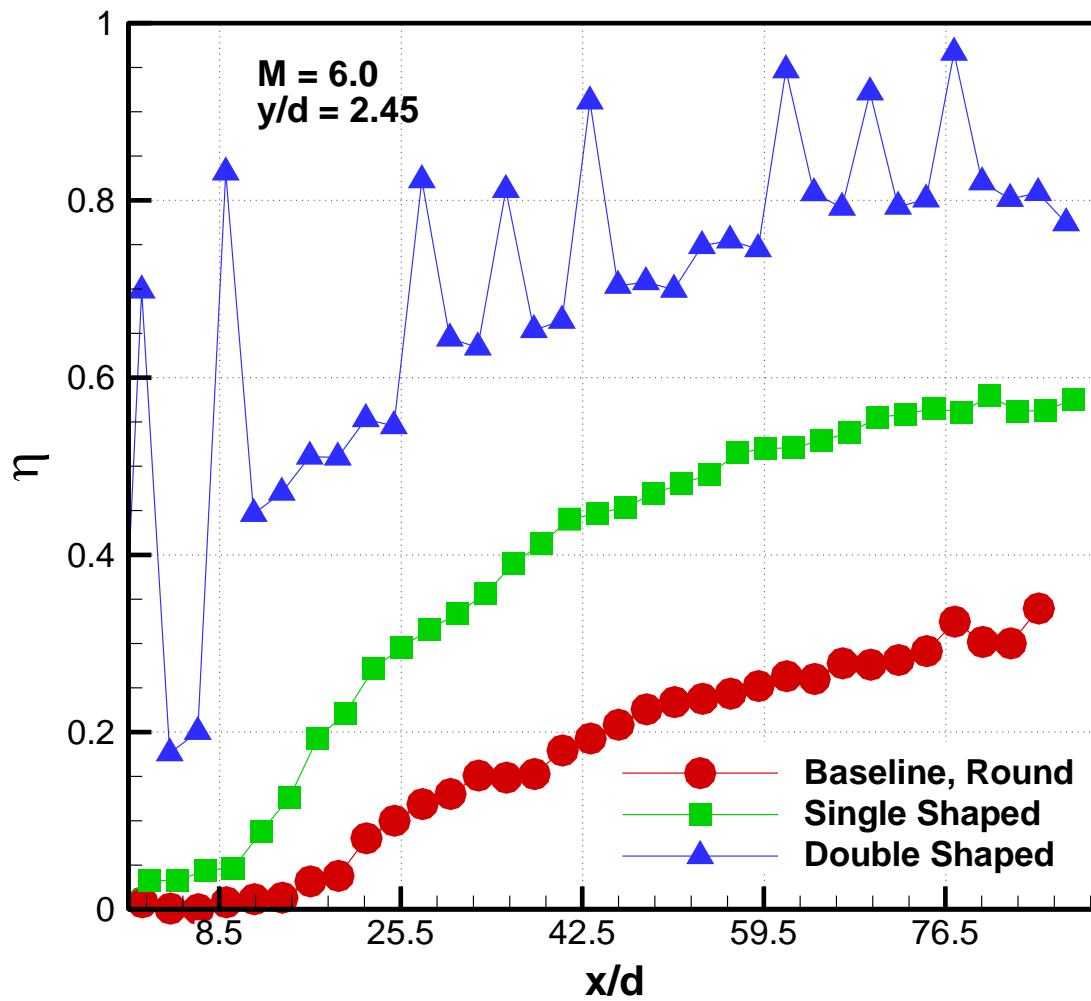


Figure 7.20: Local film cooling effectiveness for all three shapes for  $M = 6.0$  at  $y/d = 2.45$

shaped hole and round hole is clear. At first, both holes show the expected effectiveness of zero, but after one row has passed, the effectiveness between the shaped holes rises much faster than round holes. The shaped holes allow more coolant to reach the next row and collide with the new jet and spread laterally. The primary benefit of these shaped holes in effusion film cooling scenarios is that the effectiveness in between the holes reaches to  $\eta = 0.6$ . By the fully developed region, the minimum effectiveness, which should occur at the exact middle of two holes, is 0.6. The entire plate is blanketed in uniformly high amounts of coolant when the shaped holes are used for effusion cooling. This has the potential to significantly reduce the thermal gradients across combustor lining surfaces.

It is already well established that shaped holes outperform round holes, so it can be assumed that standard shaped holes would still offer dramatic improvements over round holes in effusion cooling scenarios. While the DMLS holes have additional effects that may be specific to the advanced manufacturing technique, the substantial improvement from shaped holes to round holes is not limited to DMLS shapes. Shaped holes perform better, especially with higher momentum coolant. In effusion cooling, the improvement offered by shaped holes is compounded because the jets interact and spread, causing coolant to accumulate. Nevertheless, it would be beneficial to study shaped holes made with standard manufacturing techniques to confirm that the non-line of sight holes were not the only cause of the improvement.

### *Summary of Effects*

The effects of full coverage film cooling have been investigated for both round and advanced shaped holes over a wide range of blowing ratios, including elevated blowing ratios relevant to combustor cooling. The difference between effusion cooling and single row cooling is the interaction that occurs between rows of holes. The results from the three shapes investigated revealed two effects caused by row interaction, as well as three factors that influence row interaction.

The first effect of row interaction is superposition. Coolant from the preceding row that stays attached to the surface of the plate and reaches the subsequent row is added by superposition. This results in raised effectiveness immediately downstream of the subsequent row. The more coolant that reaches the next row, the more beneficial the superposition effect is to the film cooling effectiveness. Designing the hole shape to keep coolant attached and allow more row interaction results in increased superposition effects.

The second effect of row interaction is increased lateral spreading of coolant. As the coolant collides with the subsequent row, some of it is spread laterally over the plate instead of being added by superposition. This effect is clearly seen by the raised effectiveness in the area halfway between the holes. The effectiveness should be near zero between holes for single row film cooling, but the lateral coolant spread from the collisions accumulates with each passing row. This area of minimum effectiveness reaches as high as  $\eta = 0.3$  for the round holes,  $\eta = 0.6$  for the shaped holes, and  $\eta = 0.8$  for the double hole.

The first factor that influences row interaction is the thicker downstream boundary layer caused by the initial rows of holes. In single row applications, high blowing ratio coolant would immediately separate from the surface and never reach 17 diameters downstream to interact with the subsequent row. Effusion cooling enables these interactions because the first row of holes blows coolant directly into the boundary layer. This causes boundary layer thickening, which means that coolant ejected from downstream holes is protected from the mainstream, and only interacts with the thickened boundary layer. This allows the higher momentum coolant ejected from the downstream holes to be protected from the mainstream and stay attached to the surface and reach the subsequent rows of holes.

The second factor that influences row interaction is the blowing ratio. Varying the blowing ratio for the round holes revealed the connection between the blowing ratio and previously mentioned effusion effects. For a blowing ratio of  $M = 0.5$ , the effectiveness is raised downstream of the initial rows of holes, but less coolant is blown into the boundary layer so the boundary layer is not thickened as it is for higher blowing ratios. At higher blowing ratios, more coolant is blown into the boundary layer, which results in lower effectiveness downstream of the initial row of holes but also allows more coolant interaction between the downstream rows. As the blowing ratio is increased above  $M = 6.0$ , there is no further effect of increasing the blowing ratio, as the boundary layer thickness is already thick enough to protect the downstream rows. Increased coolant simply blows off of the surface and has no impact on the film cooling effectiveness.

The third effect that influences row interaction is hole shape. It is well established that shaped holes improve jet attachment, so this improvement should be magnified by

row interaction. The PSP results confirm that shaped holes allow improved jet attachment, which causes more row interaction, which leads to extremely high effectiveness in the downstream regions. The laterally averaged effectiveness in the final rows of the plate was between  $\eta = 0.7$  and  $0.8$  for the shaped holes, while only around  $\eta = 0.25$  for the round holes. The shaped hole film cooling caused an improvement of nearly three times in the fully developed region, far downstream of the initial holes.

## CHAPTER EIGHT

### Filmx Cooling with Shaped Holes and FPG

Turbine blade film cooling has been investigated by combining the PSP and S-PIV techniques to evaluate film cooling effectiveness and flow fields related to the interaction of the film cooling jet and the mainstream flow. The effect of hole geometry has been investigated by evaluating the performance of the round and laidback, fanshaped holes to create a baseline for the more advanced shapes, which include Honeywell Shaped 1 (HWS1), Honeywell Shaped 2 (HWS2), Duckfoot 1 (DF1), and Duckfoot 2 (DF2). The shapes were evaluated for varying blowing ratios and density ratios to clarify the effect of changing the hole shape at various ranges of possible flow conditions. All of this data has been previously determined by Watson [91], but the present work reconsiders the effect of hole geometry with the added impact of a favorable pressure gradient. The impact of freestream acceleration is important because turbine airfoils induce a strong pressure gradient which can affect the interaction between the film cooling jet and mainstream. The effect has been previously investigated as detailed in chapter two, but the literature has conflicting results and should be clarified. The effectiveness, velocity, and vorticity distributions will be presented for all cases and shapes investigated with the pressure gradient and then compared directly to the previous results from Watson [91]. Both investigations were performed in the same facility, with the exception of the foam insert used to induce the pressure gradient. The film cooling effectiveness results are able to identify the path of the coolant, but they cannot explain the flow interaction between the coolant and mainstream that caused that coolant path.

Therefore, the PSP results are presented first, and then the S-PIV data will be used to clarify and explain the physical mechanisms for the measured effectiveness trends caused by varying hole shape and freestream acceleration.

### Round Hole PSP Results

Film cooling effectiveness distributions are shown for round holes under a favorable pressure gradient at a density ratio of one with a varying blowing ratio in *Figure 8.1*. The distributions show that adding the pressure gradient does not change the trends expected for round hole film cooling at  $DR = 1.0$ . Cooling is most effective at  $M = 0.5$ , and the effectiveness is severely reduced at  $M = 1.0$  and  $1.5$  because the jet

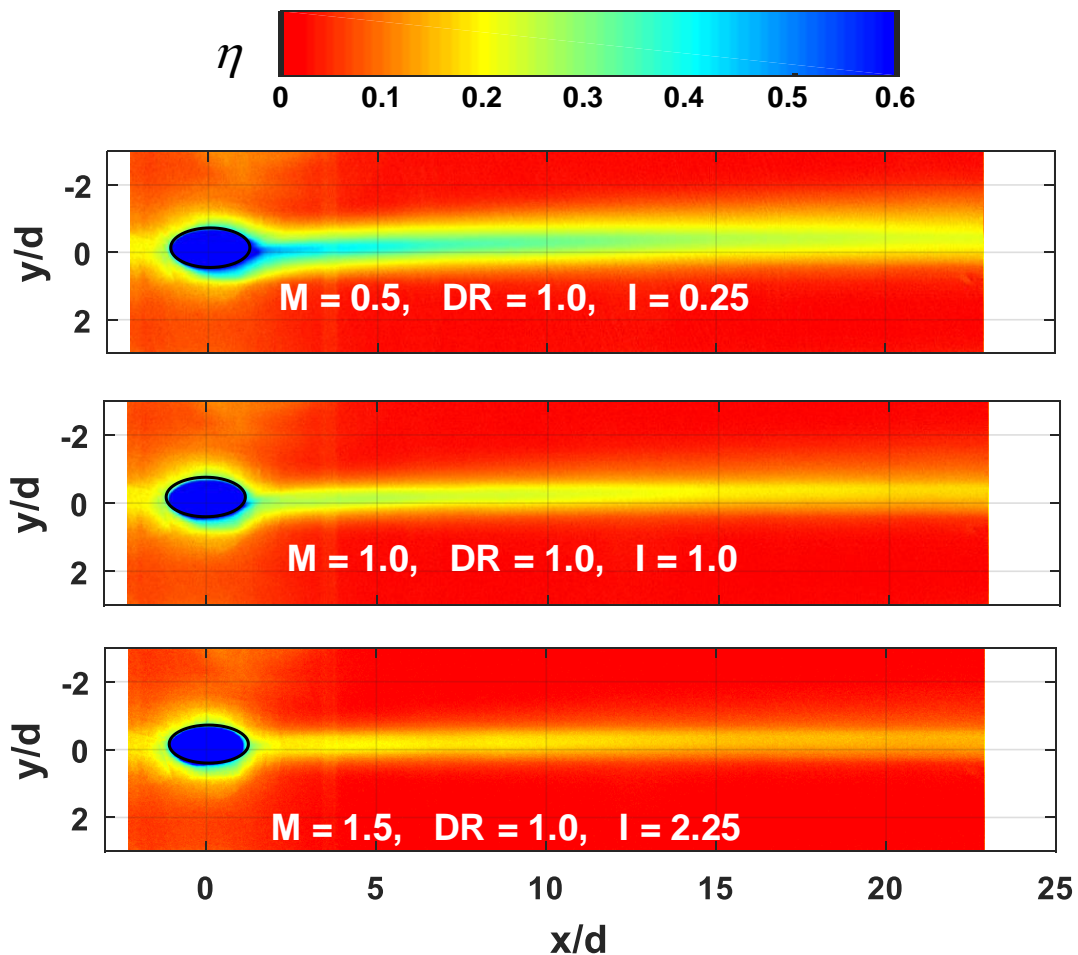


Figure 8.1: Round hole film cooling effectiveness distribution under a favorable pressure gradient: blowing ratio effect

momentum is sufficient for the jet to separate from the surface. This is the expected trend from the zero pressure gradient (ZPG) results, as well as previous literature, which predict that round hole effectiveness will be maximized for  $M = 0.5$  and blowing ratios greater than 1.0 will lift off of the surface. Adding the favorable pressure gradient has not changed the expected trend. *Figure 8.2* shows the film cooling distributions broken down into centerline and laterally averaged effectiveness distributions to aid in quantifying the effect of blowing ratio under a favorable pressure gradient. The lateral average is defined by averaging the film cooling effectiveness for one period ( $-2.5 < y/d < 2.5$ ). The centerline effectiveness shows that all three blowing ratios end near the same effectiveness level, despite the fact that the centerline effectiveness is so much better in the first ten diameters. The centerline effectiveness immediately downstream of the hole is higher at  $M = 0.5$  because the slower velocity prevents detachment of the coolant. However, the coolant that does stay attached to the surface at higher blowing ratios travels further downstream before getting swept off the surface because it has enough momentum to maintain the original path. The laterally averaged effectiveness quickly

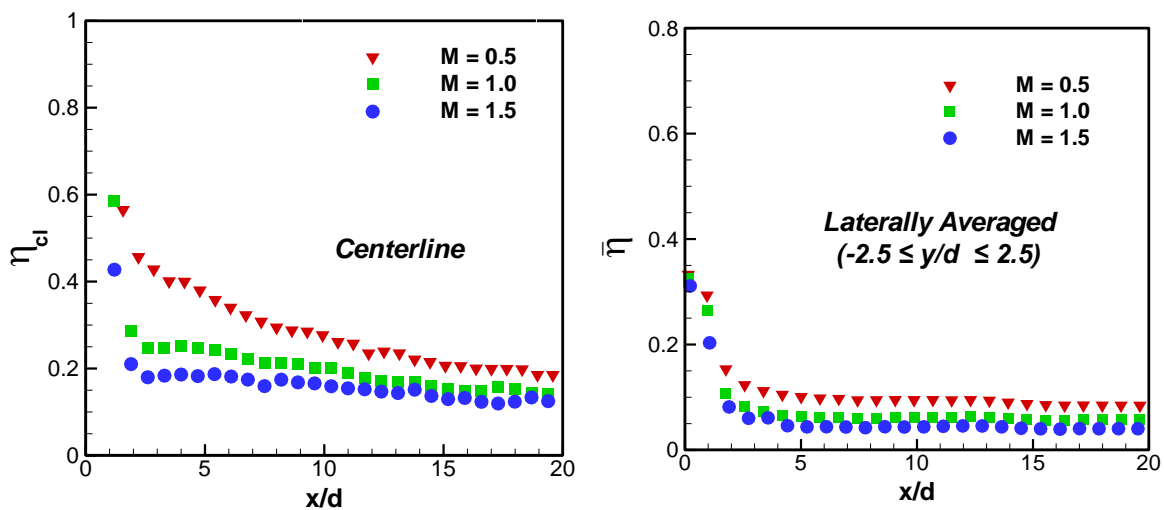


Figure 8.2: Round hole centerline and laterally averaged film cooling effectiveness under a favorable pressure gradient: blowing ratio effect

recedes in the first five diameters as the coolant jet separates from the surface, but is approximately constant for the final fifteen diameters shown.

The effect of increasing the density ratio from  $DR = 1.0$  to  $DR = 3.0$  on round hole film cooling under a favorable pressure gradient is shown in *Figure 8.3* with effectiveness distributions for  $M = 0.5$  and  $M = 1.5$ . Increasing the density ratio by a factor of 3 reduces the coolant velocity by a factor of 3 for a given blowing ratio. This causes a significant improvement in film cooling effectiveness near the hole for both blowing ratios, but also results in reduced effectiveness further downstream. The reduced velocity and increased density of the coolant results in less jet separation immediately downstream of the hole, raising effectiveness, but the lower velocity also means that the coolant cannot maintain attachment as far downstream as the higher velocity. It is also noteworthy that the lateral spread of coolant is increased for  $DR = 3.0$ . The heavier coolant is pushed towards the surface and spreads out farther, which results in better coverage downstream. *Figure 8.4* shows the effect of density ratio on centerline and laterally averaged film cooling effectiveness for  $M = 0.5$  and  $1.5$  and  $DR = 1.0 - 4.0$ . The centerline plots show that the centerline effectiveness is increased with density ratio for

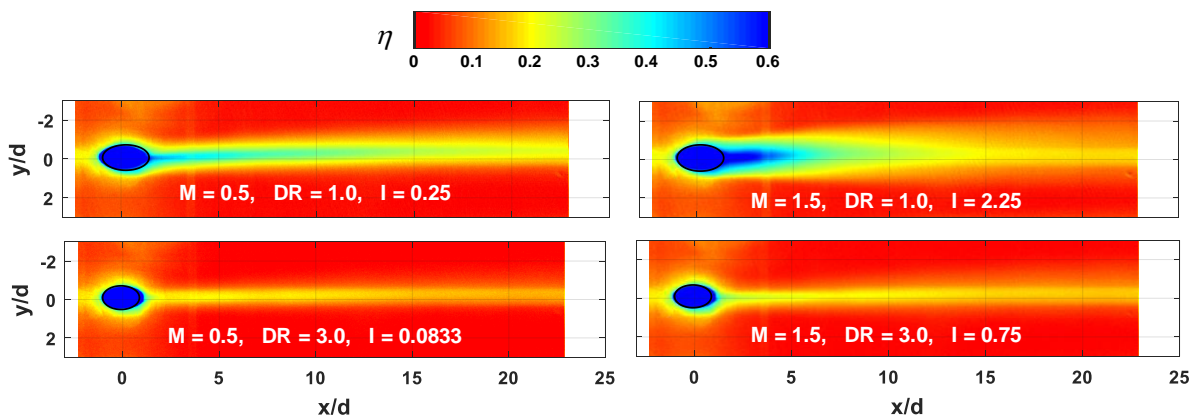


Figure 8.3: Round hole film cooling effectiveness distribution under a favorable pressure gradient: density ratio effect

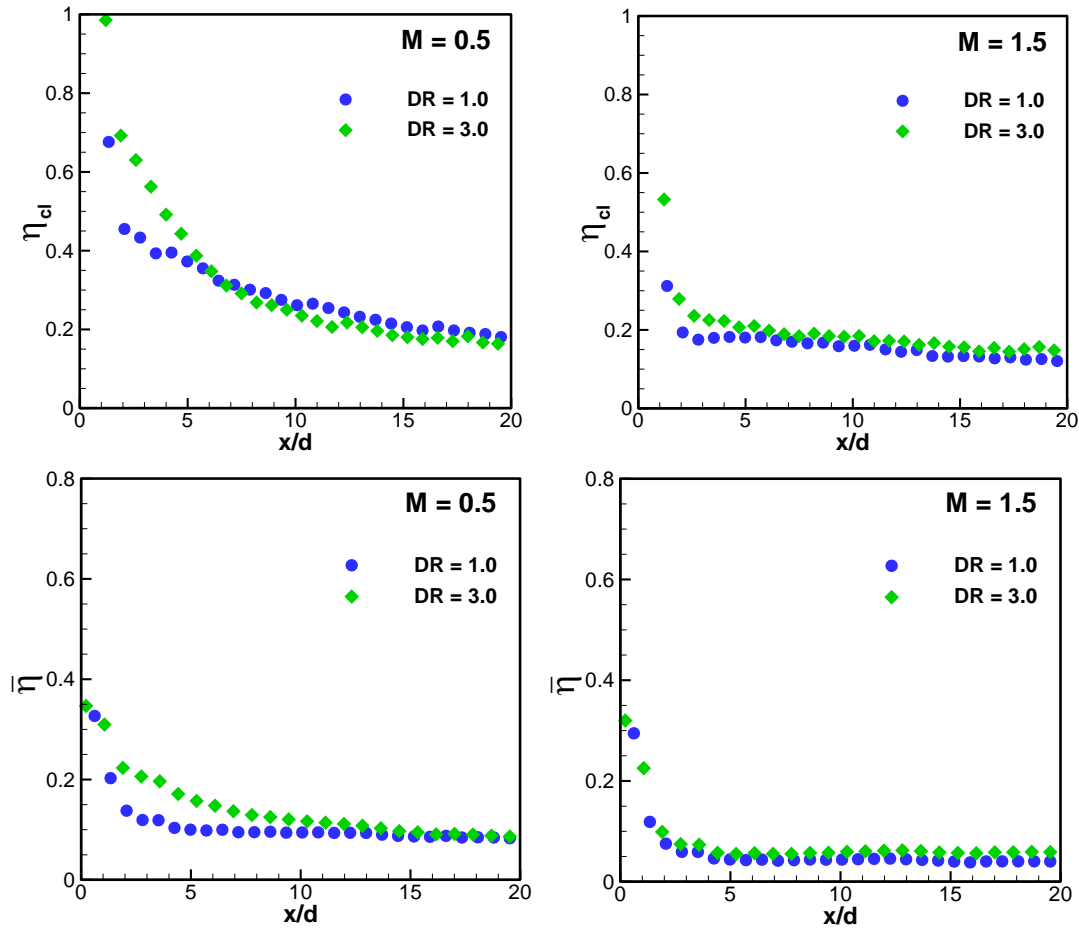


Figure 8.4: Round hole centerline and laterally averaged film cooling effectiveness under a favorable pressure gradient: density ratio effect

$x/d < 5$ , as the lower velocity coolant does not separate from the surface as quickly.

Further downstream, there is no effect of density ratio. The lower density ratio coolant has relatively higher velocity, which does help the coolant travel further downstream. The two effects cancel each other in the downstream region. The same trends are shown with the laterally averaged effectiveness, where it is increased near the hole at higher density ratios, but increasing the density ratio reduces the coolant velocity such that it provides limited downstream coverage.

The film cooling effectiveness of round holes under FPG is compared directly to the ZPG distributions in *Figure 8.5*. The FPG and ZPG distributions are split in half, and

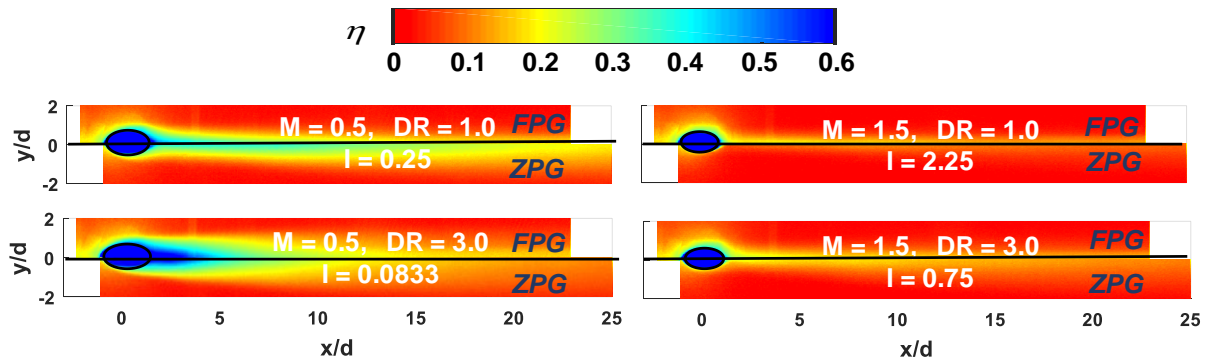


Figure 8.5: Round hole film cooling effectiveness distributions: FPG effect

the top half of the FPG distribution is the top half of each combined distribution, and the bottom half of the ZPG distribution is the bottom half of each combined distribution. It is assumed that the distributions are symmetrical about  $y/d = 0$ , and all data was checked to ensure this assumption proved reasonable. The distributions are shown for  $DR = 1.0$  and  $3.0$ , and  $M = 0.5$  and  $1.5$ . These distributions show that the effect of the pressure gradient is not negligible, but also does not change any of the basic trends shown previously. The most noteworthy difference between the distributions is the increase in coolant spread caused by the FPG. This can be most clearly seen at  $M = 0.5$  where the coolant is still attached to the surface. The width of the coolant on the surface is increased near the hole when the FPG is compared directly the ZPG. This is caused by the reduction in boundary layer thickness caused by the FPG. The thinner boundary layer offers more resistance to the coolant jet and causes it to stay closer to the surface, which increases lateral spread as the same mass flow is confined closer to the surface.

The effect of pressure gradient on round hole film cooling is also evaluated by comparing the overall, area averaged effectiveness, which is calculated by averaging the film cooling effectiveness over one period ( $-2.5 < y/d < 2.5$ ) for the length of the plate

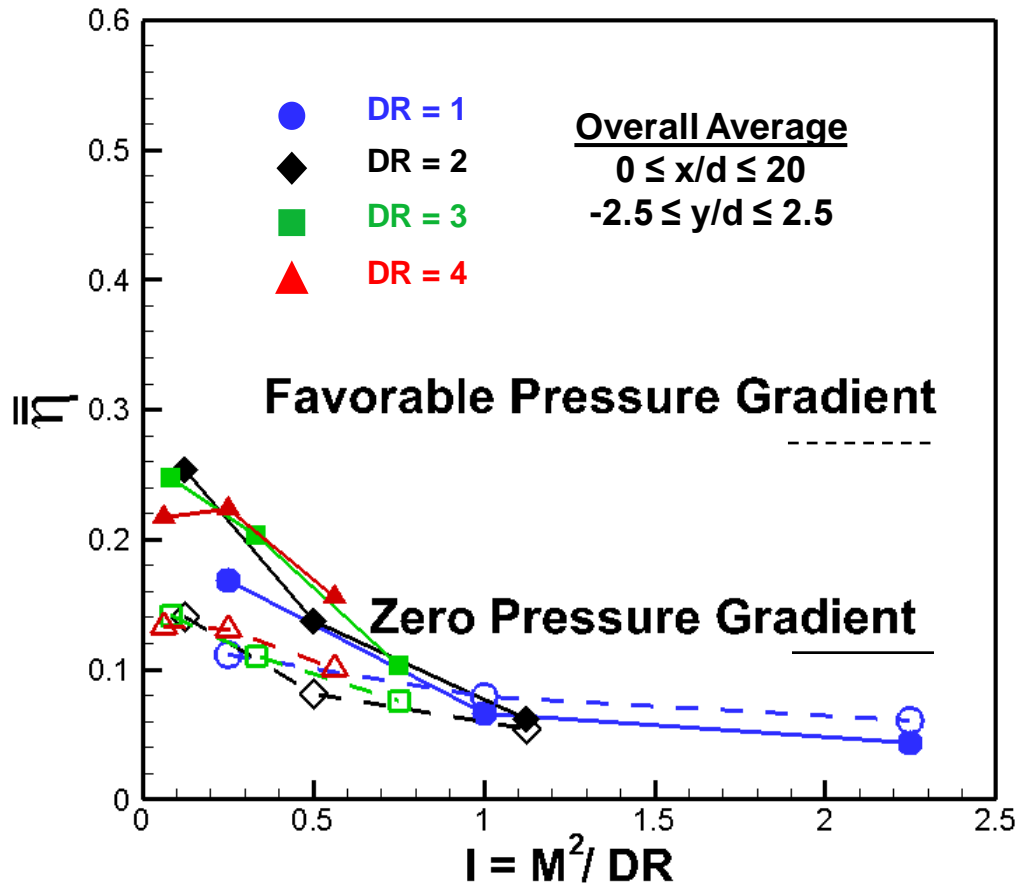


Figure 8.6: Round hole overall average film cooling effectiveness: FPG effect

visible through the viewing window in the insert ( $0 < x/d < 20$ ). The overall average is a good tool to measure the impact of FPG flow in general, and *Figure 8.6* shows that for round hole film cooling at  $DR = 1.0$ , the overall effect of the pressure gradient is limited. At the lowest blowing ratio, the ZPG performs best for  $DR = 1.0$ , but for  $M = 1.0$  and  $1.5$  the FPG is slightly better. However, at higher  $DR$ , the effect of the FPG is less favorable. The lower velocity coolant is pushed towards the surface and spreads out, which raises the effectiveness near the hole. However, this reduces the concentration and velocity of the coolant along the centerline, which causes the coolant to be more easily swept into the mainstream for the FPG case.

### Round Hole S-PIV Results

The S-PIV technique has been used to determine velocity and vorticity distributions with freestream acceleration using the same methods previously used by Watson [91] to determine these distributions for ZPG mainstream flows. The FPG and ZPG results are directly compared for a varying blowing ratio at a constant DR = 1.0 in *Figure 8.7*. The data is presented for the downstream edge (DSE), where the coolant has begun to separate from the surface and can be clearly observed with S-PIV. The velocity is non-dimensionalized by dividing by the average velocity of the mainstream ( $V/V_{avg}$ ), and presented with the color contours. The vorticity is similarly non-dimensionalized by multiplying by the hole diameter and dividing by the average velocity of the mainstream ( $\omega d/V_{avg}$ ), and is shown with topographic contours superimposed on the color contours.

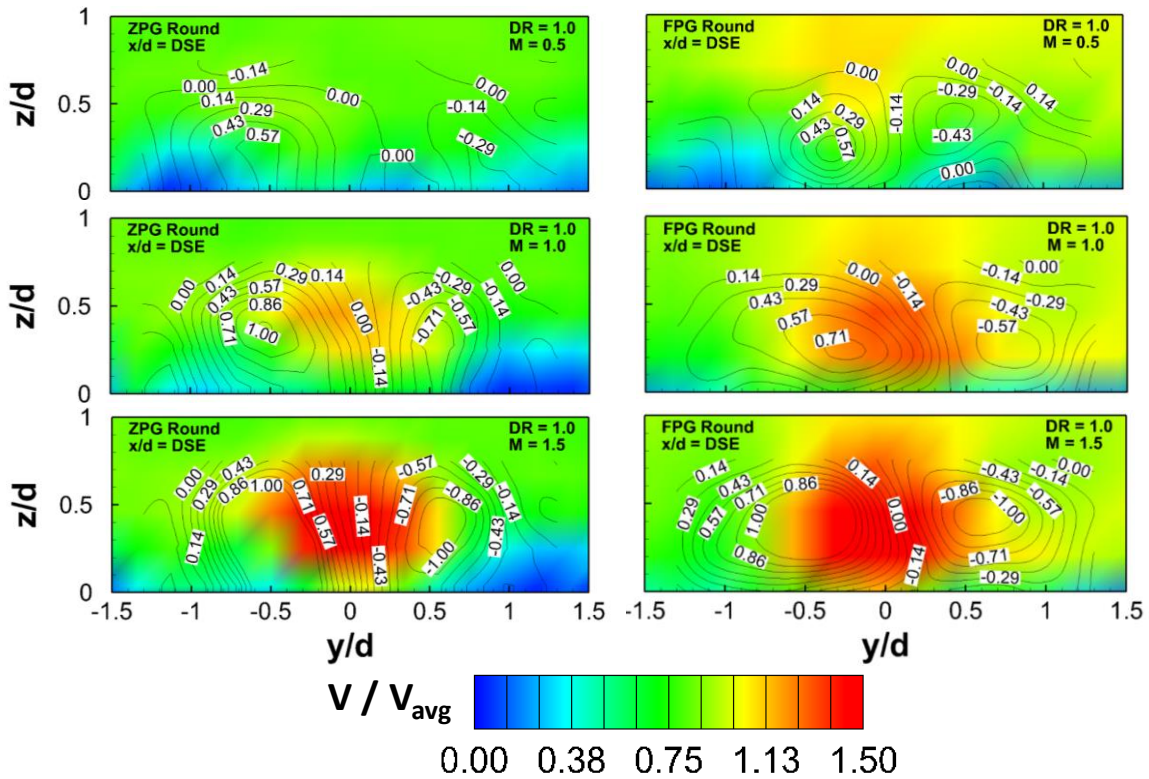


Figure 8.7: Effect of blowing ratio and freestream acceleration for round holes ( $x/d = DSE$ , DR = 1.0)

Figure 8.7 clearly shows the three primary effects of increasing the blowing ratio under accelerating freestream flows. The core of the jet lifts further above the surface as  $M$  is increased, which can be demonstrated by comparing  $M = 1.5$  and  $M = 1.0$ . For  $M = 1.5$ , the jet core extends a full diameter above the surface, but for  $M = 1.0$ , the jet core is contained within the first half diameter above the surface of the plate. The counter rotating vortex pair (CVP) increases in maximum magnitude as  $M$  is increased. The maximum magnitude of vorticity is approximately doubled as the blowing ratio is increased from  $M = 0.5$  to  $M = 1.5$ . Furthermore, the width of the CVP is increased, as the area of elevated vorticity only extends approximately one half diameter for  $M = 0.5$ , but the width of the CVP is wider than a full hole diameter for  $M = 1.0$  and  $M = 1.5$ .

When the FPG results are directly compared to the ZPG results of Watson et al. [28], it can be seen that the flows are similar, but with several non-negligible differences. Both sets of data show the same three effects detailed previously as the blowing ratio is increased. However, direct comparison at a given blowing ratio shows that the CVP is wider under favorable pressure gradient, which results in a wider jet as more mainstream air is pulled in and mixed with the coolant. Additionally, the jet stays closer to the surface with a favorable pressure gradient flow. It is well established that favorable pressure gradients reduce the boundary layer thickness and prevent boundary layer separation. The reduction in boundary layer thickness means that there is less low momentum mainstream flow colliding with the cooling jet. The higher momentum boundary layer reduces jet liftoff. This reduction in jet liftoff results in a widening of the jet and spreading of the CVP, as flow must be conserved.

The impact that the favorable pressure gradient has on vorticity is correlated with the film cooling effectiveness, and is shown in *Figure 8.8* for varying blowing ratios. The vorticity is plotted at the downstream edge, for a quarter diameter above the surface. The location of vorticity plotting is chosen because the film cooling effectiveness measurements are surface measurements, so the vorticity close to the surface is most important. One quarter diameter above the surface was closest to the core of the jet for most cases while maintaining close proximity to the surface. The film cooling effectiveness data is plotted at the downstream edge, and all data is for a density ratio of  $DR = 1.0$ . The peak effectiveness is approximately the same for all blowing ratios, regardless of the presence of the pressure gradient. However, the lateral spread of the coolant decreases with blowing ratio. Furthermore, the lateral spread of the coolant increases for a given blowing ratio under the presence of freestream acceleration. The point of minimum effectiveness (the edge of the jet) closely coincides with the point of maximum vorticity. As the point of maximum vorticity is spread by the FPG, the jet spreads wider and cooling effectiveness is increased outside of the width of the ZPG jet. The effectiveness results are supported by the S-PIV results which show the impact of the thinner boundary layer on the spreading of the CVP.

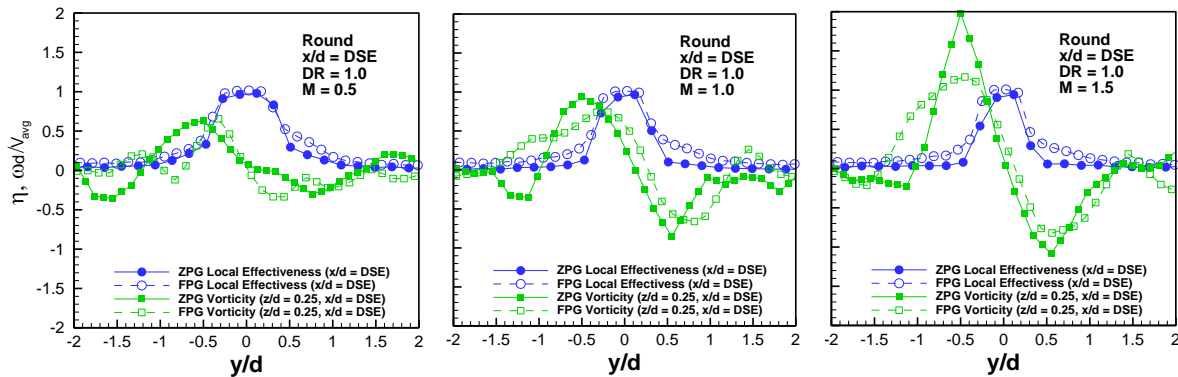


Figure 8.8: Influence of flow vorticity on surface film cooling effectiveness from round holes ( $x/d = DSE$ ,  $DR = 1.0$ )

The velocity and vorticity magnitudes are shown in *Figure 8.9* for a varying density ratio at the DSE for  $M = 1.5$  to directly compare the FPG and ZPG flows for round holes. The effect of increasing density ratio is clearly seen as the jet velocity is substantially reduced. For the ZPG case, the jet velocity is reduced to the same velocity as the mainstream, but under the freestream acceleration, the jet velocity is not reduced as substantially. These effects are correlated with the film cooling effectiveness at the DSE in *Figure 8.10*. The film cooling effectiveness data shows that the FPG also increases the spread of the coolant at elevated density ratios. However, as previously shown in Fig. 8.9, the jet velocity for the FPG case is higher than the ZPG case, which indicates that the effectiveness should be reduced. On the other hand, Fig. 8.10 shows that while the maximum vorticity remains similar, the width of rotation is significantly increased, which increases the spread of the coolant. As previously shown, this is caused by the thinner boundary layer, which pushes the jet down and spreads and strengthens the CVP.

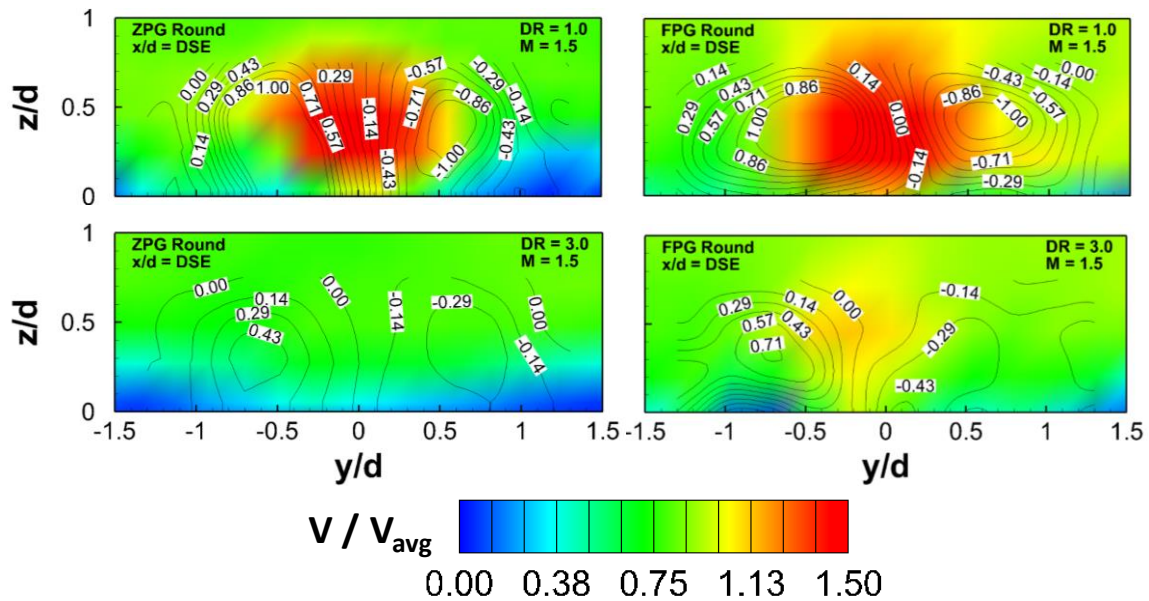


Figure 8.9: Effect of density ratio and freestream acceleration for round holes ( $x/d = DSE$ ,  $M = 1.5$ )

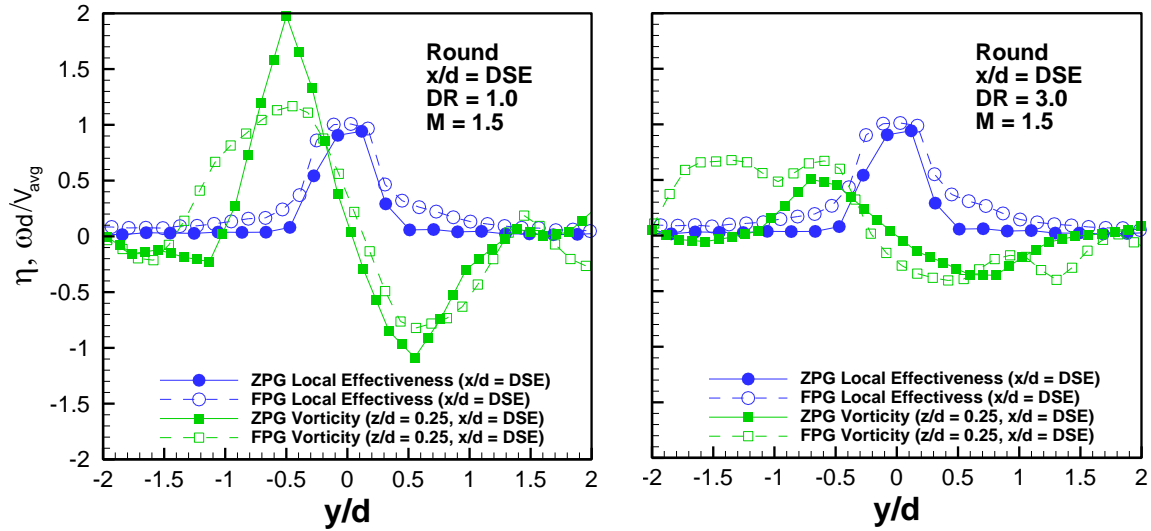


Figure 8.10: Influence of flow vorticity on surface film cooling effectiveness from round holes ( $x/d = DSE$ ,  $M = 1.5$ )

The velocity and vorticity contours were also presented for  $x/d = 0$  and compared to the results at the downstream edge, with  $DR = 1.0$  and  $M = 1.5$  in *Figure 8.11*. The jet is much closer to the surface for  $x/d = 0$ , as the jet is still inside the hole, and has not yet separated from the surface. For the FPG case, the maximum magnitude of vorticity is reduced. *Figure 8.12* shows that this reduction in vorticity magnitude results in an increase in film cooling effectiveness at  $x/d = 0$ . The increase in vorticity width also causes the increase in lateral spread of the coolant, just as shown in the other cases.

The favorable pressure gradient causes the jet to stay more closely attached to the surface. Furthermore, the FPG causes a spreading of the CVP, which leads to non-negligible increases in the lateral spreading of the coolant. These effects can be attributed to the thinner boundary layer caused by the FPG, which leads to the jet being pushed closer to the surface and spreading laterally.

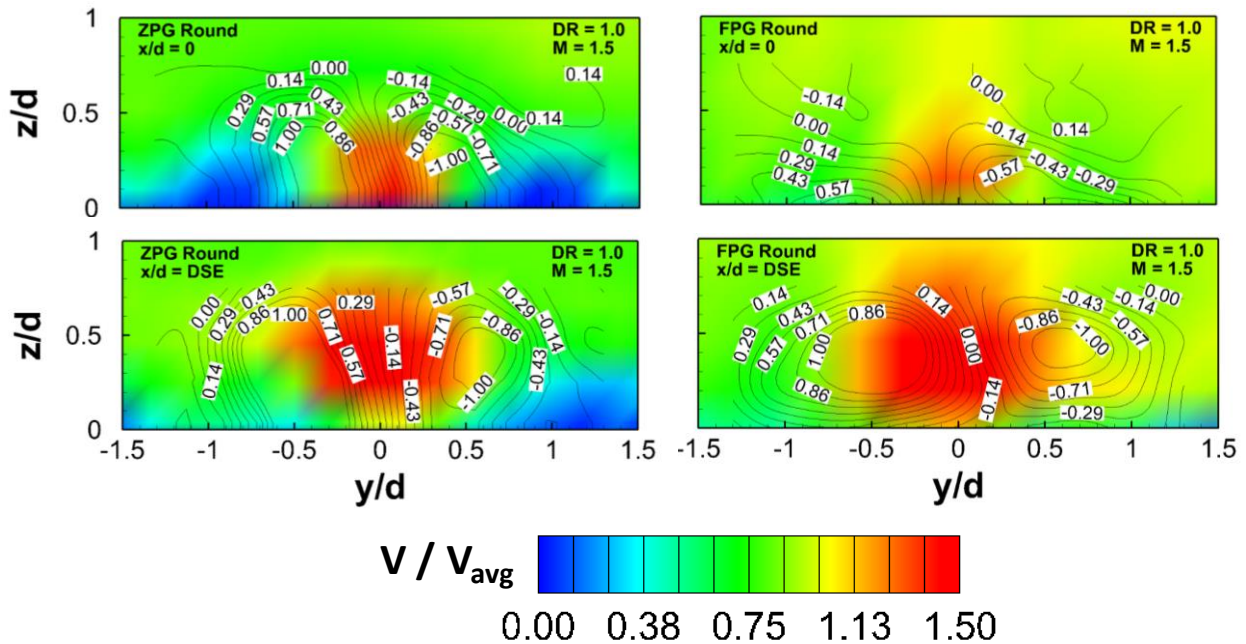


Figure 8.11: Effect of downstream location and freestream acceleration for round holes ( $M = 1.5$ ,  $DR = 1.0$ )

#### *Laidback, Fanshaped Hole PSP Results*

The laidback, fanshaped hole is also evaluated to create a baseline for more advanced shaped holes. The zero pressure gradient results were consistent with shaped film cooling literature, showing that the film cooling effectiveness is improved in comparison with round holes and that the shaped holes are less effected by blowing and density ratios over the range investigated. Film cooling effectiveness distributions have been obtained for the FPG case, and are shown for the laidback, fanshaped shaped hole in *Figure 8.13*. The distributions are presented for a varying blowing ratio at  $DR = 1.0$  to show that shaped holes also yield the same general trends under a favorable pressure gradient. The diffuse outlet of the shaped hole reduces the velocity of the coolant exiting the hole, which allows it to stay more closely attached to the surface. Increasing the blowing ratio does not cause the coolant to separate from the surface, but the increased

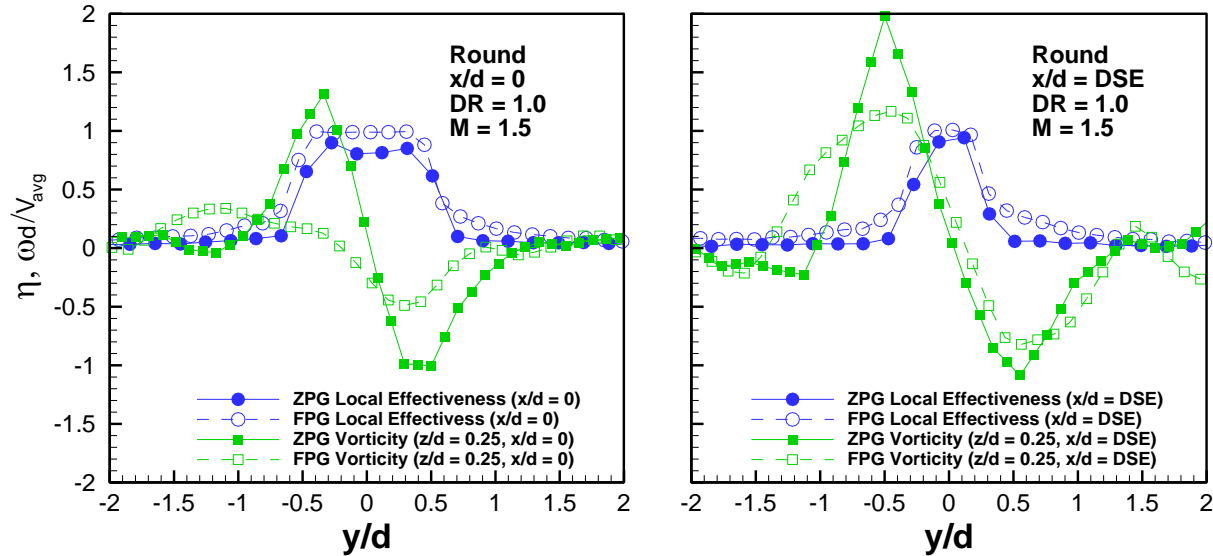


Figure 8.12: Influence of flow vorticity on surface film cooling effectiveness from round holes ( $M = 1.5$ ,  $DR = 1.0$ )

momentum allows the coolant to travel further along the plate to provide improved downstream coverage. These general trends are the same for the ZPG and FPG cases. The film cooling effectiveness distributions are analyzed quantitatively with the centerline and laterally averaged effectiveness, as shown in *Figure 8.14*. The effect of blowing ratio is minimal, but the film cooling effectiveness is slightly increased with blowing ratio inside of the hole ( $x/d < 3$ ), while reduced with blowing ratio downstream of the hole. This is a similar effect to the round hole, where the higher velocity coolant blows off of the surface, but the effect is much less pronounced.

The effect of increasing density ratio for shaped holes under the FPG case is shown through film cooling distributions in *Figure 8.15* for  $M = 0.5$  and  $1.5$ . For  $M = 0.5$ , the coolant velocity is lowered by the increased density ratio. This results in increased coolant lateral spread within the hole, but the downstream effectiveness is significantly reduced. The coolant velocity is too low for the coolant to reach as far downstream

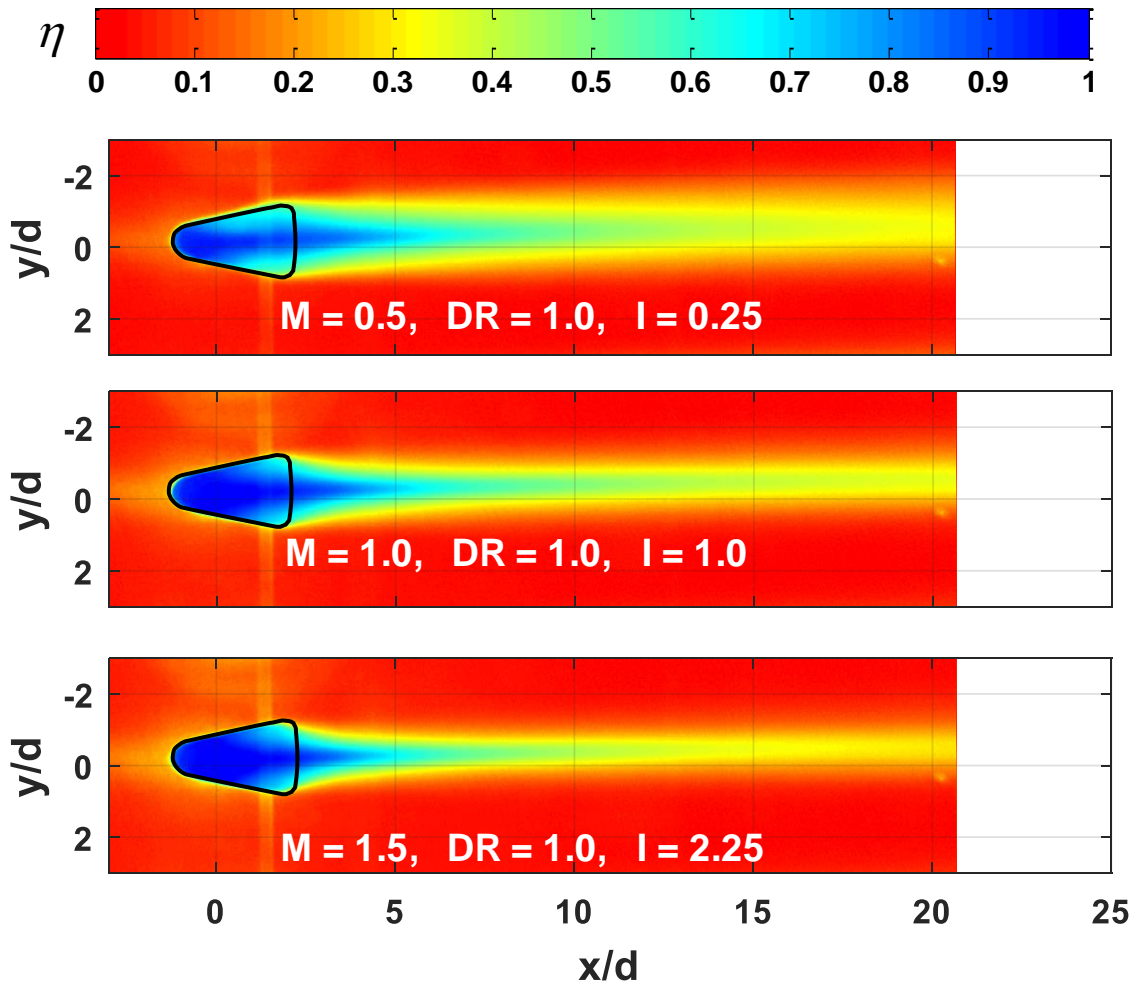


Figure 8.13: Shaped hole film cooling effectiveness distribution under a favorable pressure gradient: blowing ratio effect

without getting mixed with the mainstream. For  $M = 1.5$ , the coolant still maintains sufficient velocity to reach downstream. Furthermore, the higher density coolant is pulled towards the surface and spreads laterally, resulting in increased lateral coverage downstream. *Figure 8.16* shows the same density ratio effect. For  $M = 0.5$ , increasing the density ratio decreases film cooling effectiveness, but for  $M = 1.5$  increasing the density ratio increases film cooling effectiveness. This difference occurs because the coolant at a high density ratio for  $M = 0.5$  is moving so slowly out of the fanshaped outlet. The coolant does not stay attached because the velocity is extremely low and the coolant is

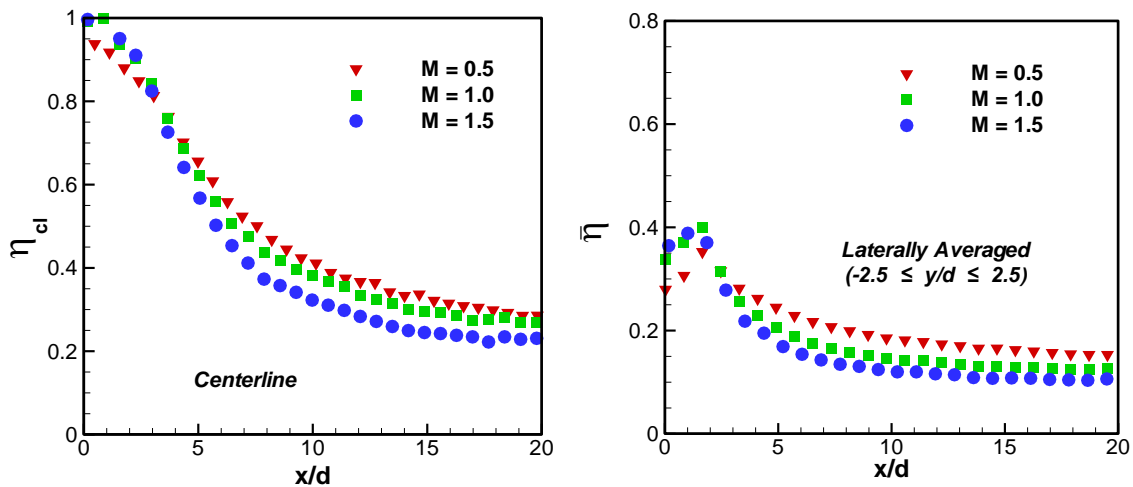


Figure 8.14: Shaped hole centerline and laterally averaged film cooling effectiveness under a favorable pressure gradient: blowing ratio effect

more easily mixed with the mainstream. However, at  $M = 1.5$  the centerline effectiveness is not a function of density ratio. The coolant velocity is high enough to keep the coolant from being mixed with the mainstream, even for  $DR = 4.0$ . However, the lateral average shows the effect of increasing density ratio as the coolant is spread further across the plate. The lateral average is increased with density ratio even though the centerline effectiveness is unchanged, which demonstrates that increasing  $DR$  causes increased lateral spreading.

The effect of a favorable pressure gradient on shaped hole film cooling is presented in *Figure 8.17*, which shows the same combined plot format used previously for the round hole. Comparing the distributions over the range of flow conditions presented shows that there is a negligible impact of the FPG on shaped hole film cooling effectiveness. The lack of the FPG effect on shaped holes is confirmed with the overall average plotted in *Figure 8.18*. The overall film cooling effectiveness is increased by less than 10% for the FPG case over the range of flow conditions investigated. The overall

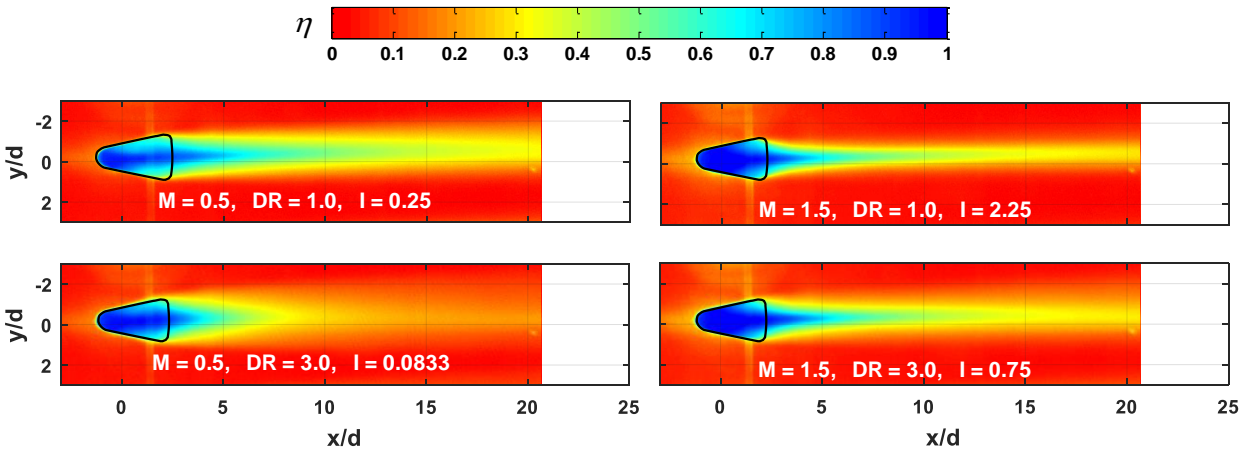


Figure 8.15: Shaped hole film cooling effectiveness distribution under a favorable pressure gradient: density ratio effect

effect of the FPG is minimal because the increased spreading of the coolant caused by the FPG also increases the interaction with the sidewall of the shaped hole which increases secondary flows, leading to increased mixing.

The laidback, fanshaped hole is directly compared to the baseline round hole to show the expected improvement caused by the expanded outlet area. The shapes are compared with the lateral average for the FPG case at DR = 1.0 and 3.0 and M = 0.5 and 1.5 in *Figure 8.19*. It is immediately clear that the laidback, fanshaped hole results in substantially increased film cooling effectiveness. For all of the flow conditions investigated, the film cooling effectiveness is approximately doubled. The laterally averaged film cooling effectiveness is approximately the same at  $x/d = 1$  (DSE of the round hole), but the coolant quickly separates from the surface downstream of the round hole. The coolant separates from the surface more gradually downstream of the shaped hole. This occurs because the coolant exiting the shaped hole has lower velocity than the round hole for a given flow condition. The difference between round and shaped hole film cooling is consistent across the flow conditions investigated, except for extremely

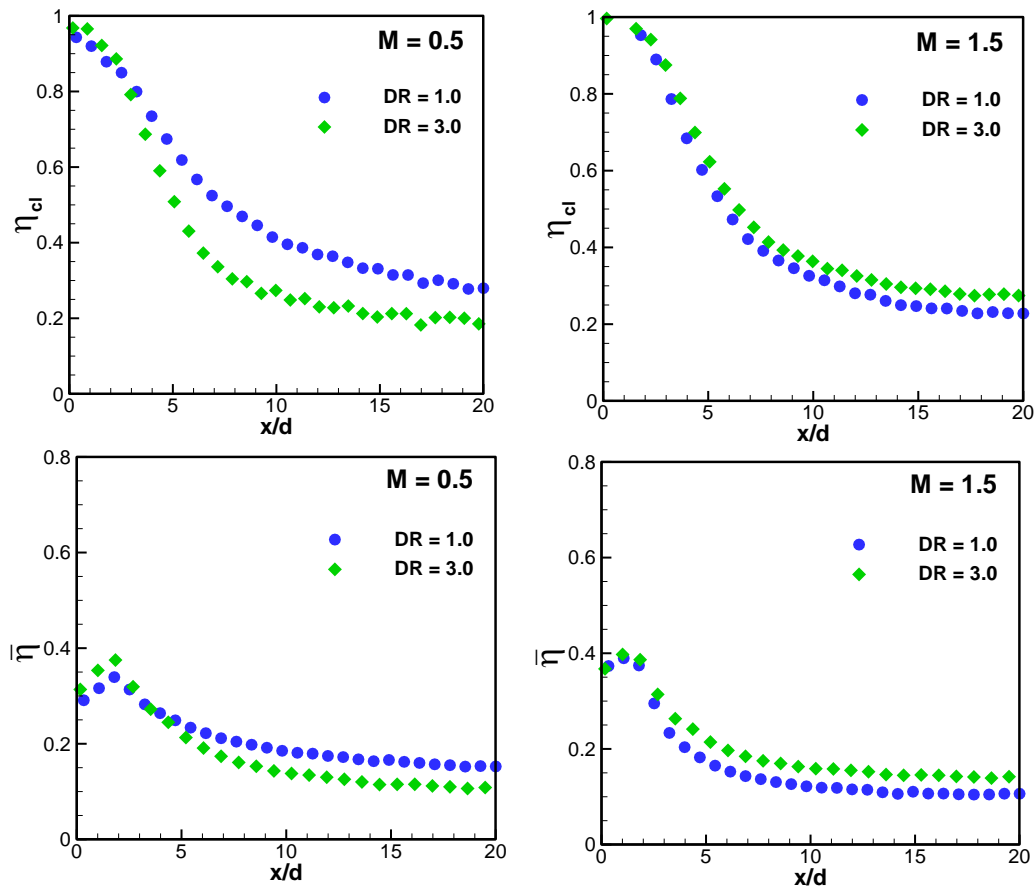


Figure 8.16: Shaped hole centerline and laterally averaged film cooling effectiveness under a favorable pressure gradient: density ratio effect

low coolant velocities such as  $DR = 3.0$ ,  $M = 0.5$ . The coolant velocity is low enough that jet separation is resisted for the round hole, such that the effectiveness of the round and shaped hole are similar. The coolant velocity for the shaped hole at this flow condition is actually too slow, so less coolant reaches farther downstream, so the round and shaped holes perform equally in the region farther downstream ( $x/d > 10$ ).

*Figure 8.20* shows the same general differences between round and shaped holes using the overall average effectiveness as comparison. While the overall average cannot clarify the locations of effective cooling, it is a useful tool for observing general

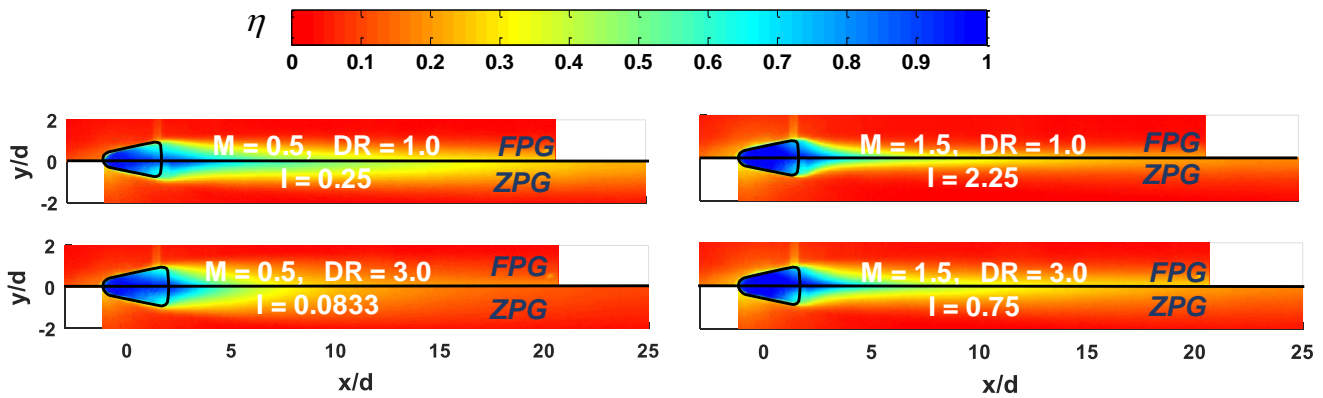


Figure 8.17: Shaped hole film cooling effectiveness distributions: FPG effect

differences caused by the different hole outlets. The shaped hole shows approximately double the average film cooling effectiveness, except in flow conditions with extremely low momentum flux. The low momentum coolant stays attached for round holes, but slightly reduces the cooling effectiveness for shaped holes because the coolant lacks sufficient velocity to provide downstream coverage.

#### *Laidback, Fanshaped S-PIV Results*

The shaped hole geometry is evaluated and analyzed with the exact same methods as the round holes. The effect of mainstream acceleration on the flow field of shaped holes has not been previously investigated, so there is no previous data for comparison. *Figure 8.21* shows the impact of accelerating mainstream flow for the range of blowing ratios investigated at the downstream edge and  $DR = 1$ . The velocity of the jet and the magnitude of the CVP are increased with increasing  $M$ , but not nearly as significantly as the ZPG case. This difference is clearly seen for  $M = 1.5$ , where the jet is much closer to the surface for the FPG, but also the CVP is intensified and spread further apart. *Figure 8.22* shows that these effects negate each other for  $M = 1.5$ . The film cooling

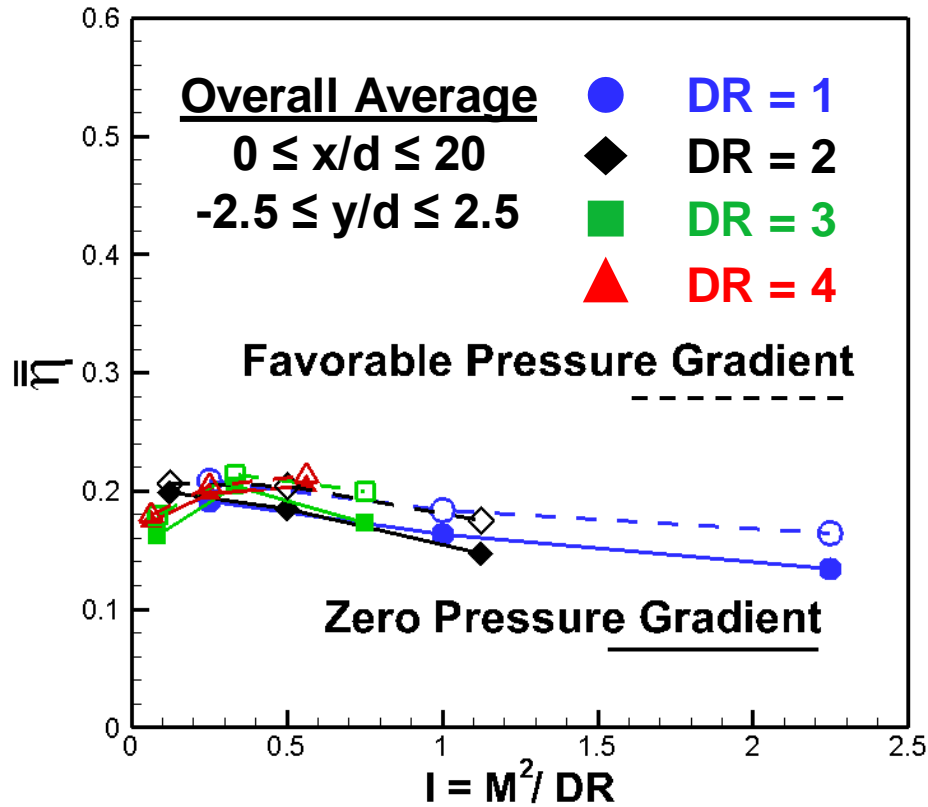


Figure 8.18: Shaped hole overall average film cooling effectiveness: FPG effect

effectiveness is almost identical at the DSE for  $M = 1.5$ , but the ZPG case has more jet liftoff, while the FPG has increased vorticity magnitude and CVP spread. The shaped hole reduces the local velocity of the coolant exiting the jet, but the higher blowing ratio case still has enough momentum to penetrate the lower momentum boundary layer of the ZPG. However, for  $M = 0.5$  and  $1.0$ , the ZPG case shows improved lateral spread within the hole, as the film cooling effectiveness remains near 1.0 for the width of the hole. The jet velocities are similar for these two cases, which indicates that differences in vorticity cause the differences in effectiveness. At the two lower blowing ratios, the vorticity is significantly increased for the FPG case, resulting in reduced effectiveness within the hole, but improved effectiveness outside of the width of the holes. The increase in

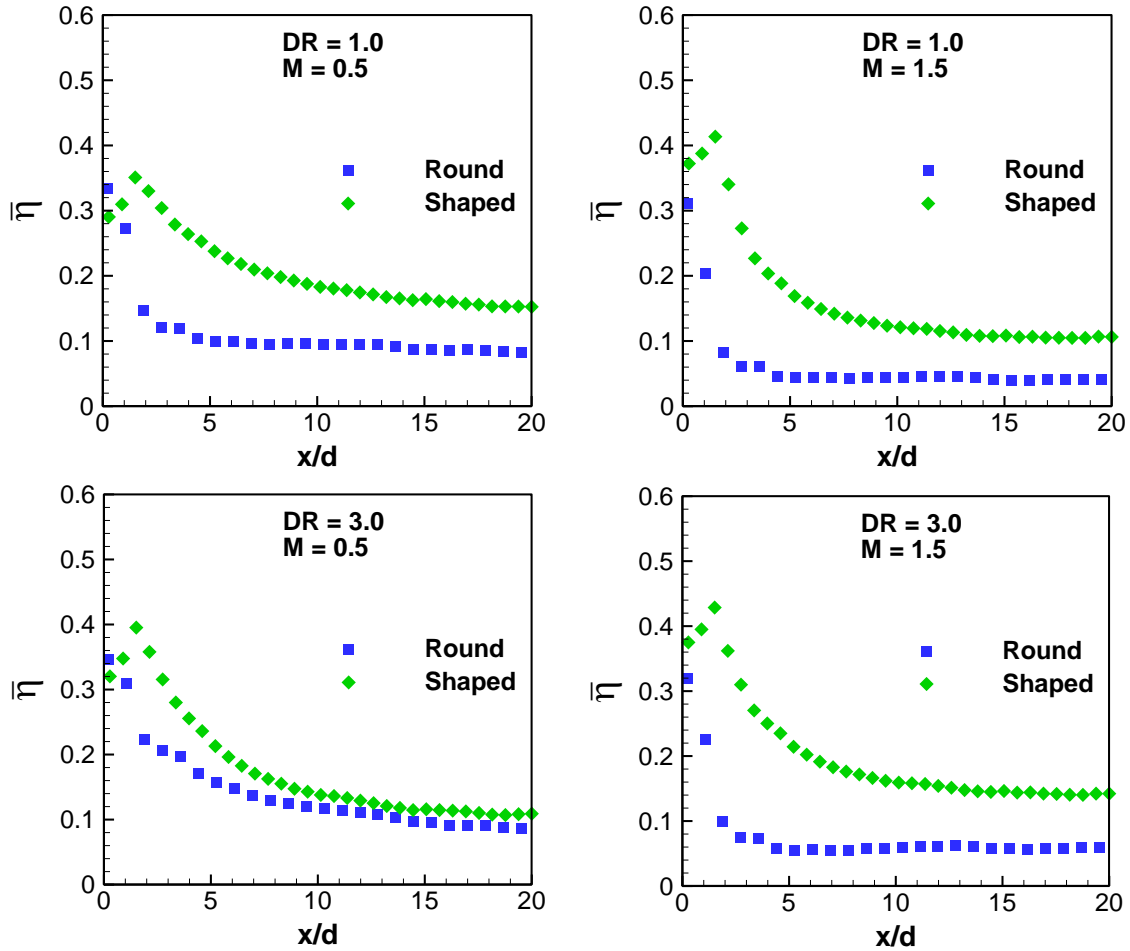


Figure 8.19: Comparison of baseline shaped and round with laterally averaged effectiveness under FPG

vorticity for the FPG case ( $M = 0.5$  and  $1.0$ ) occurs because the lateral spread of the coolant within the hole is increased for the FPG flow. The lateral spread of coolant results in increased interaction between the coolant and the sidewall, which produces increased secondary flows to increase rotation of the coolant.

*Figure 8.23* shows that for elevated density ratios, the difference between FPG and ZPG flows is minimal. Increasing the density ratio to  $DR = 3.0$  for shaped hole film cooling shows that the jet is almost completely removed and the velocity above the hole is equal to the mainstream. The vorticity magnitude is minimal for both the FPG and ZPG cases. *Figure 8.24* shows that the flow acceleration has a negligible effect on the film

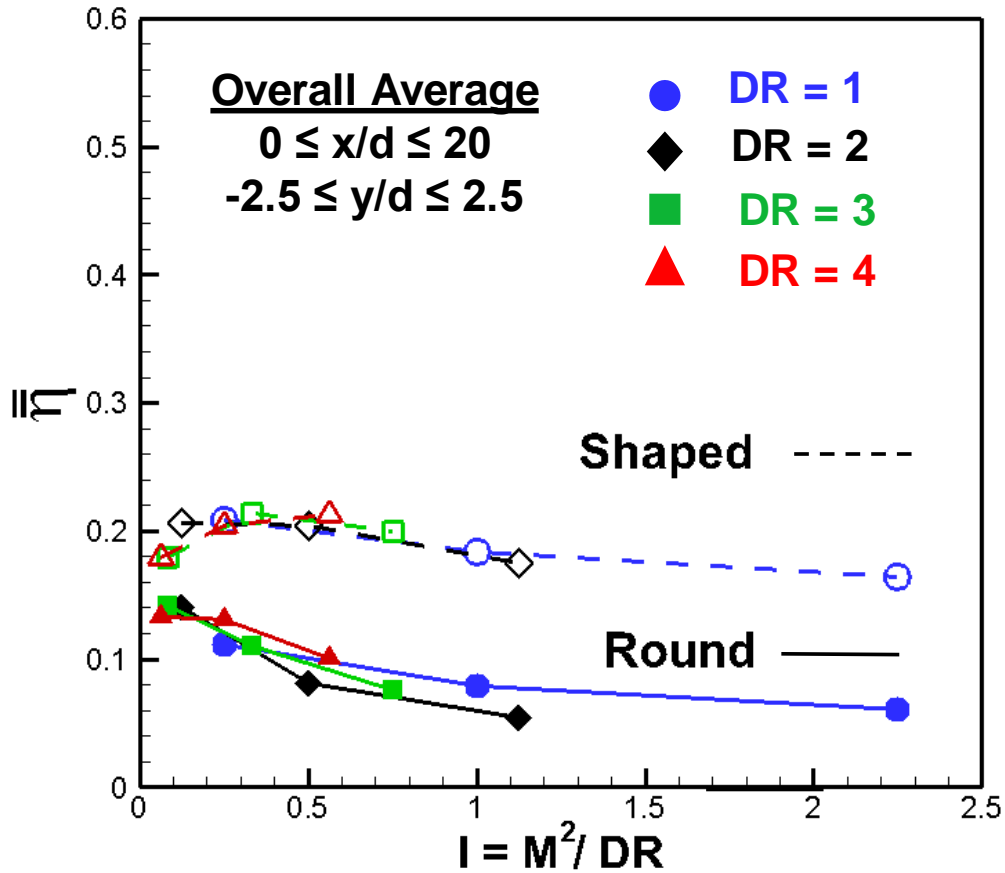


Figure 8.20: Favorable pressure gradient overall average film cooling effectiveness: shape effect

cooling effectiveness, which corroborates the flow field data that shows the negligible impact of the FPG. For  $DR = 3.0$ , the coolant momentum is so low that it cannot penetrate the boundary layer for either the ZPG or the FPG case, so the fact that the FPG has thinned the boundary layer is irrelevant.

The impact of the FPG is presented at both  $x/d = 0$  and the DSE in *Figure 8.25*. The jet is moved much closer to the surface, and the jet intensity and width are greatly reduced. The CVP is more spread out under the FPG case for both locations, which reduces the effectiveness and counteracts the increased jet liftoff for the ZPG case. *Figure 8.26* shows that there is negligible impact of pressure gradient on film cooling

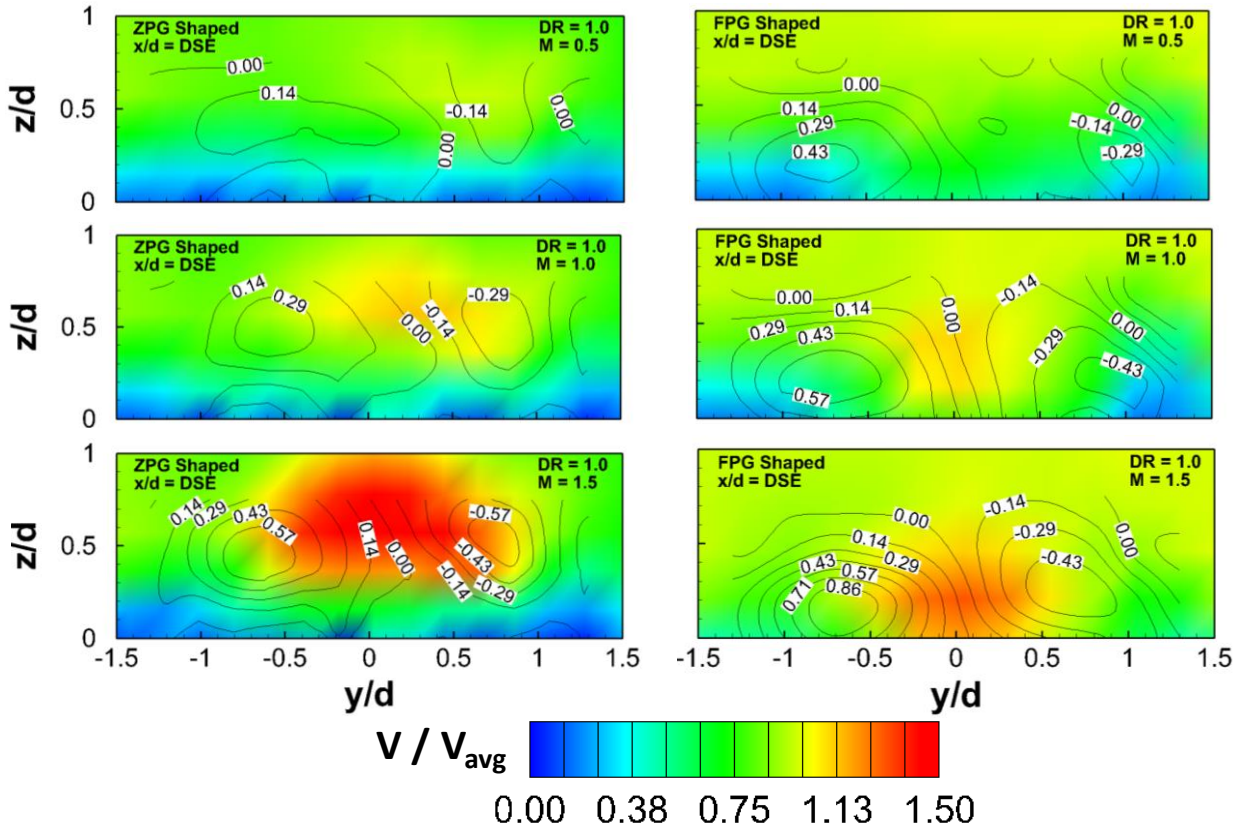


Figure 8.21: Effect of blowing ratio and freestream acceleration for shaped holes ( $x/d = DSE$ ,  $DR = 1.0$ )

effectiveness at the two locations for  $M = 1.5$ ,  $DR = 1.0$ . While the FPG moves the jet closer to the surface, it also increases the spread of the CVP, and the two effects negate each other.

The S-PIV results for the laidback, fanshaped and round holes are directly compared at the downstream edge of each hole to show the difference in the flow fields created by the two different hole shapes. The velocity and vorticity distributions are presented for the FPG case for  $DR = 1.0$  for the various blowing ratios investigated in *Figure 8.27*. It can be clearly seen that the shaped hole results in the coolant jet being pushed closer to the surface, and the magnitude of the vorticity is substantially reduced. Both of these effects result in improved film cooling effectiveness. The relationship

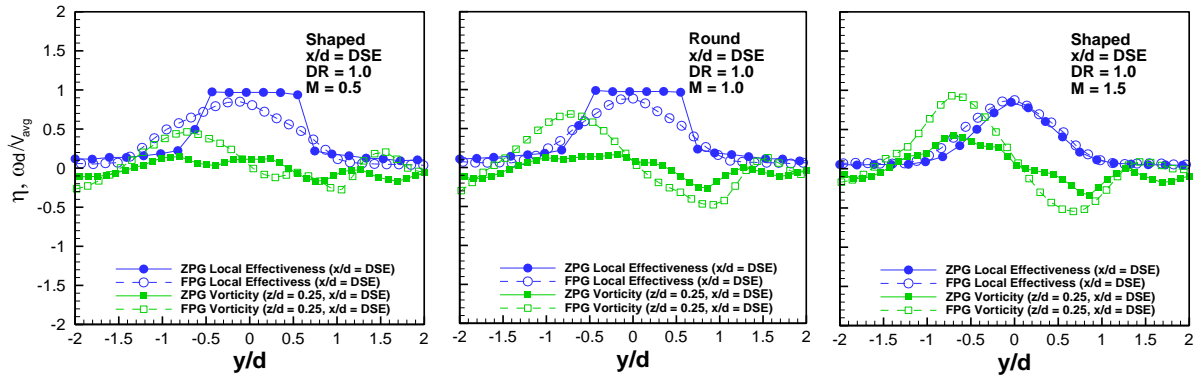


Figure 8.22: Influence of flow vorticity on surface film cooling effectiveness from shaped holes ( $x/d = DSE$ ,  $DR = 1.0$ )

between vorticity and effectiveness at the downstream edge for round and shaped holes is directly compared in *Figure 8.28* for the same flow conditions. While the round holes do have slightly increased peak film cooling effectiveness at the DSE, the spread of the coolant is significantly increased for the shaped hole. The magnitude of the CVP is substantially reduced by the diffuse outlet of the shaped hole, which results in slightly less coolant pushed towards the center but dramatically reduced jet separation and improved coolant spread.

The favorable pressure gradient causes the jet to remain closer to the surface. This effect is even more prominent for shaped holes than for round holes. However, increased vorticity magnitude counteracts the impact of the jet staying closer to the surface. It is important to note that the fundamental effects of the FPG are consistent for round and shaped holes. The jet is pushed towards the surface and the CVP spread is increased. This consistency affirms the idea that boundary layer thinning caused by the FPG explains these effects.



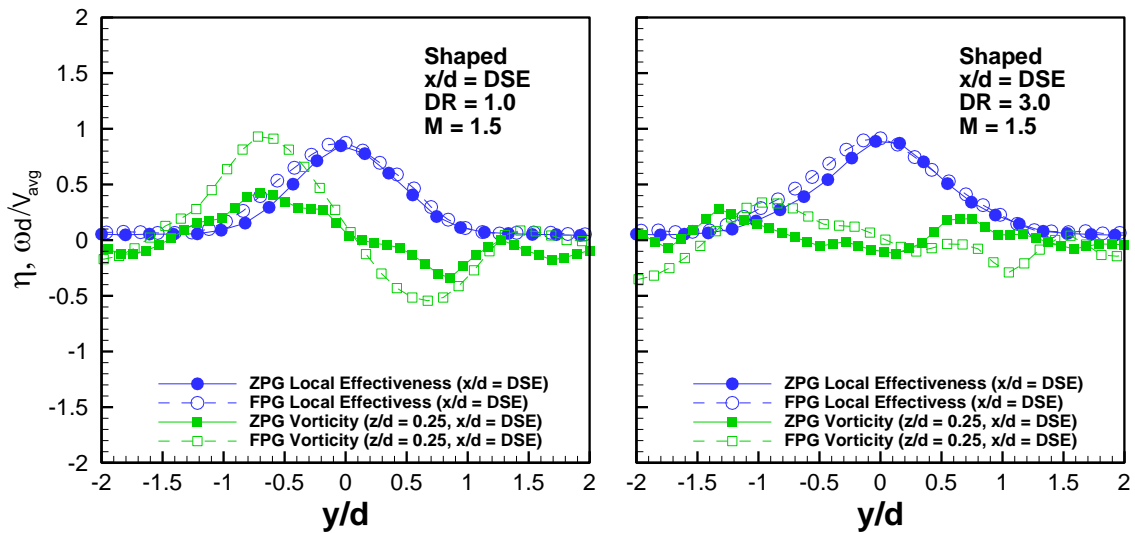


Figure 8.24: Influence of flow vorticity on surface film cooling effectiveness from shaped holes ( $x/d = DSE$ ,  $M = 1.5$ )

#### *Advanced Cooling Shapes*

The previously investigated round and laidback, fan-shaped holes have been used to establish the validity of the PSP and S-PIV setup, and to help form a baseline to compare the four unique geometries. The four geometries include Honeywell Shaped 1, Honeywell Shaped 2, Duckfoot 1, and Duckfoot 2. Each hole offers various changes in an effort to improve upon the baseline shaped hole. Honeywell Shaped 1 (HWS1) simply increases the hole outlet area. Honeywell Shaped 2 (HWS2) uses the same exit shape as HWS1, but with a racetrack shaped inlet as opposed to the standard round. Duckfoot 1 (DF1) also has the more expanded outlet area, but also introduces two contours shaped similar to the webbing of duck feet. The goal of this geometry is to generate vorticity that acts contrary to the counter-rotating vortex pair. Duckfoot 2 (DF2) has the same outlet as DF1, but also uses the same racetrack shaped inlet as used in HWS2, so the DF2 geometry is used to evaluate both effects.

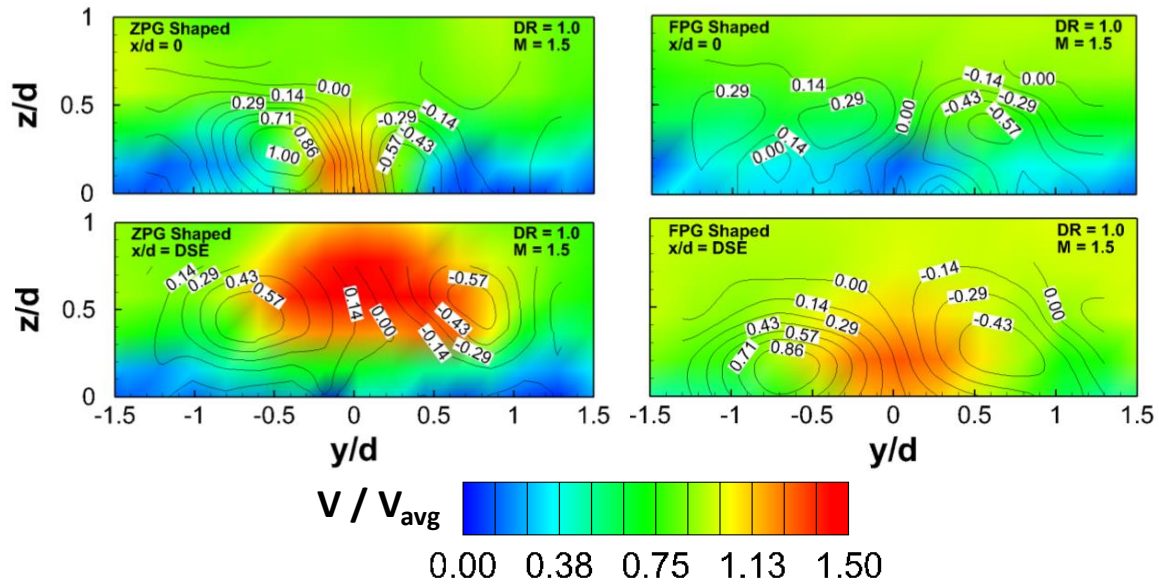


Figure 8.25: Effect of downstream location and freestream acceleration for shaped holes ( $M = 1.5$ ,  $DR = 1.0$ )

### *Honeywell Shaped 1 PSP Results*

Honeywell Shaped 1 is Honeywell’s baseline shaped hole. It is similar to the laidback, fanshaped hole tested previously, but with a 12 degree lateral expansion angle increased from 10 degrees along with a 12 degree laidback expansion increased from 10 degrees for the baseline shaped. The holes are otherwise identical, so the film cooling effectiveness distributions should be relatively similar.

The film cooling effectiveness distributions for HWS1 and  $DR = 1.0$  are shown for a varying blowing ratio in *Figure 8.29*. The effect of blowing ratio is primarily shown in the region inside of the hole. Increasing the blowing ratio specifically increases the lateral spread of coolant within the hole. At the low blowing ratio, with such a high lateral expansion angle, the low velocity coolant is unable to stay attached to the outer walls of the holes. Even at the highest blowing ratio, the coolant is only able to stay well attached to the walls of the hole for the first half of the hole. Increasing the blowing ratio has little

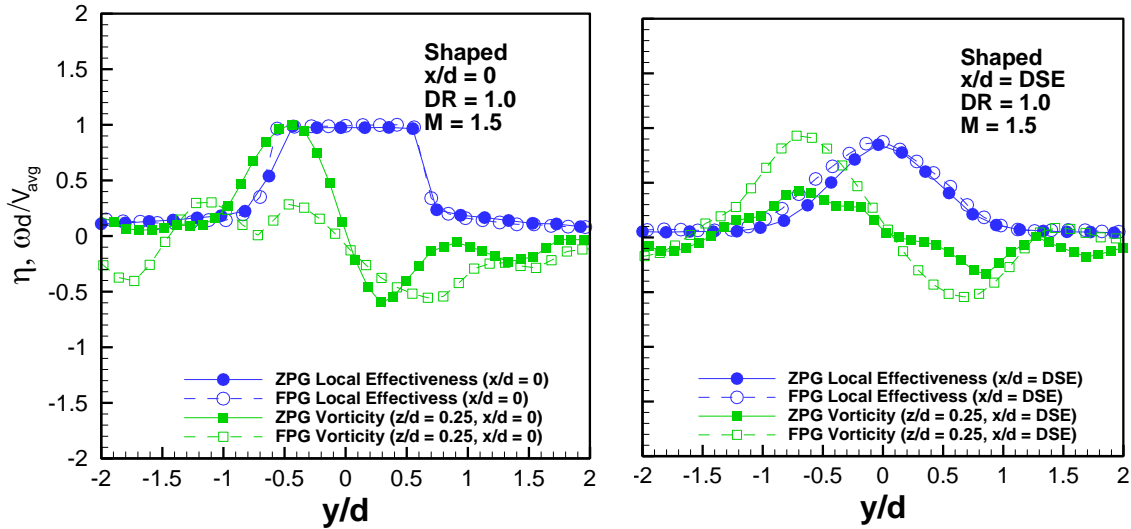


Figure 8.26: Influence of flow vorticity on surface film cooling effectiveness from shaped holes ( $M = 1.5$ ,  $DR = 1.0$ )

impact on the effectiveness downstream of the hole. *Figure 8.30* shows the centerline and laterally averaged effectiveness for  $DR = 1.0$  as a function of blowing ratio. Within the hole ( $x/d < 3$ ), the centerline effectiveness is strongly dependent on blowing ratio. The effectiveness decreases along the centerline for  $M = 1.0$  and  $M = 1.5$ , but actually increases within the hole for  $M = 0.5$ . The coolant velocity is so low for  $M = 0.5$  that the coolant is actually pulled towards the centerline.

The effect of density ratio is shown in *Figure 8.31*, which shows the limited impact of density ratio. The coolant spread within the hole is completely unaffected by the increased density and decreased velocity of the coolant. At lower  $DR$ , the coolant stays slightly more attached to the surface along the centerline. *Figure 8.32* shows these effects quantitatively for the centerline and laterally averaged effectiveness. The centerline effectiveness is slightly reduced with increasing density ratio far downstream of the hole.

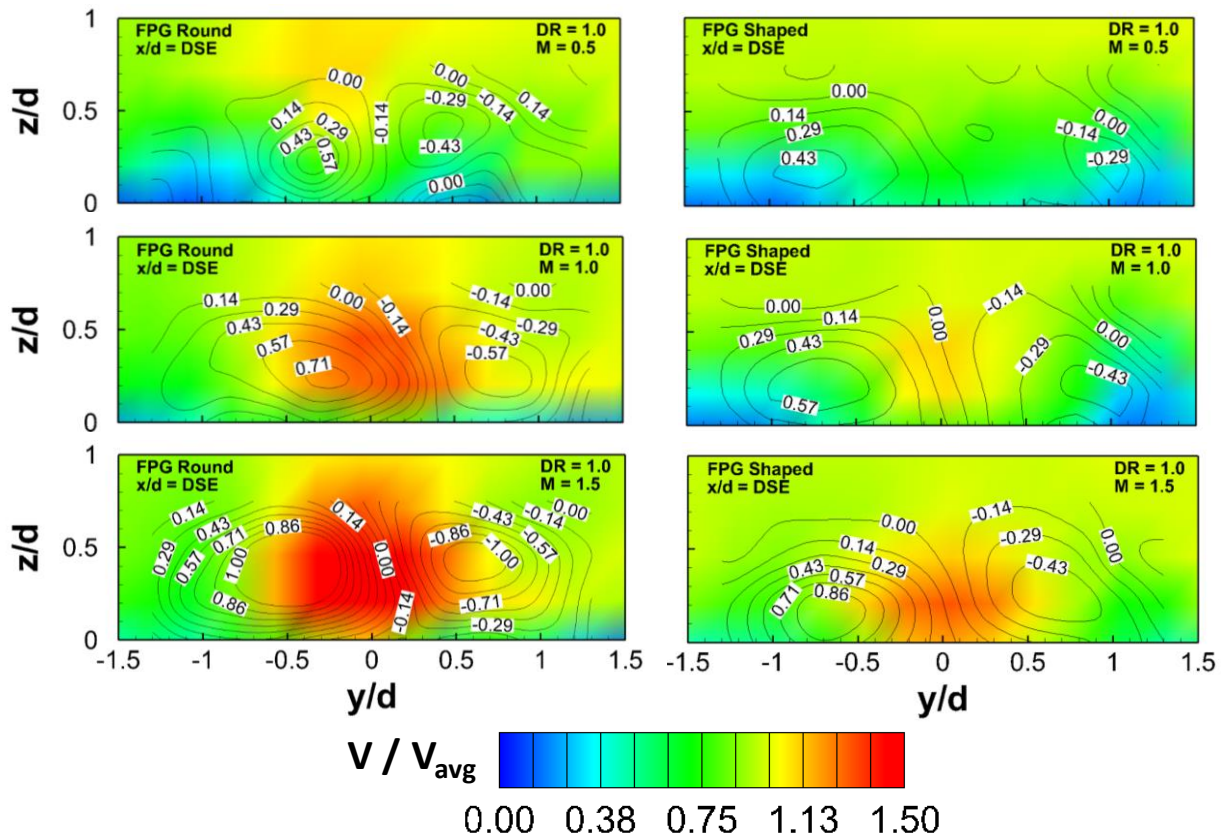


Figure 8.27: Comparison of round and shaped holes for varying blowing ratio ( $x/d = DSE$ ,  $DR = 1.0$ , FPG)

Figure 8.33 shows the film cooling effectiveness distributions plotted to directly compare FPG and ZPG at  $x/d = DSE$  and  $DR = 1.0$ . The baseline shaped hole showed minor improvement under the favorable pressure gradient, and it is expected that the HWS1 geometry should show a similar FPG effect. This assumption is correct as the distributions, along with the overall average plots in Figure 8.34 show that there is a slight increase in overall average effectiveness at lower momentum flux ratios, but for  $I > 1$ , the effect of the FPG is minimal. This occurs because the FPG causes increased coolant spread, which improves the film cooling effectiveness at lower momentum flux

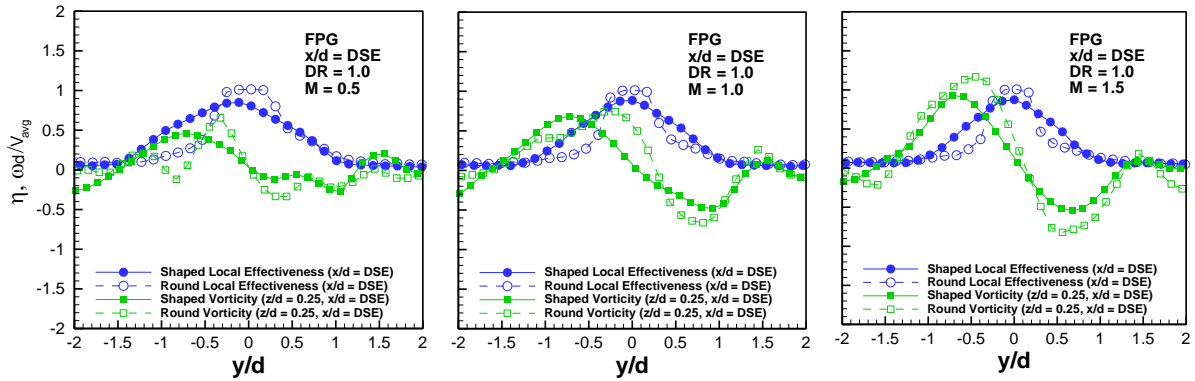


Figure 8.28: Comparison of round and shaped holes through the influence of flow vorticity on surface film cooling effectiveness ( $x/d = DSE$ ,  $DR = 1.0$ , FPG)

ratios because the low velocity coolant is able to travel farther downstream under the slight protection of the FPG.

The effect of the slight increase in lateral expansion and laidback angles is shown in *Figure 8.35*, which compares the laterally averaged film cooling effectiveness of the baseline shaped hole and the HWS1 hole. For the flow conditions investigated, the difference between the two geometries is nearly negligible. In the downstream region, HWS1 slightly outperforms the shaped hole, especially at the  $DR = 1.0$  and  $M = 1.5$ . This occurs because the marginal increase in hole exit area of the HWS1 hole is able to slow down the higher momentum flows and cause slight improvements in the rate of jet separation. For most flow conditions investigated, the coolant velocity was already in the range where jet separation is approximately constant, but for the highest momentum flows investigated, the HWS1 geometry offered marginal improvements through the increased reduction in coolant velocity.

*Figure 8.36* presents the difference between the two geometries in terms of the overall, area averaged film cooling effectiveness. The overall average film cooling effectiveness is not affected by increasing the lateral and fanshaped angles by two

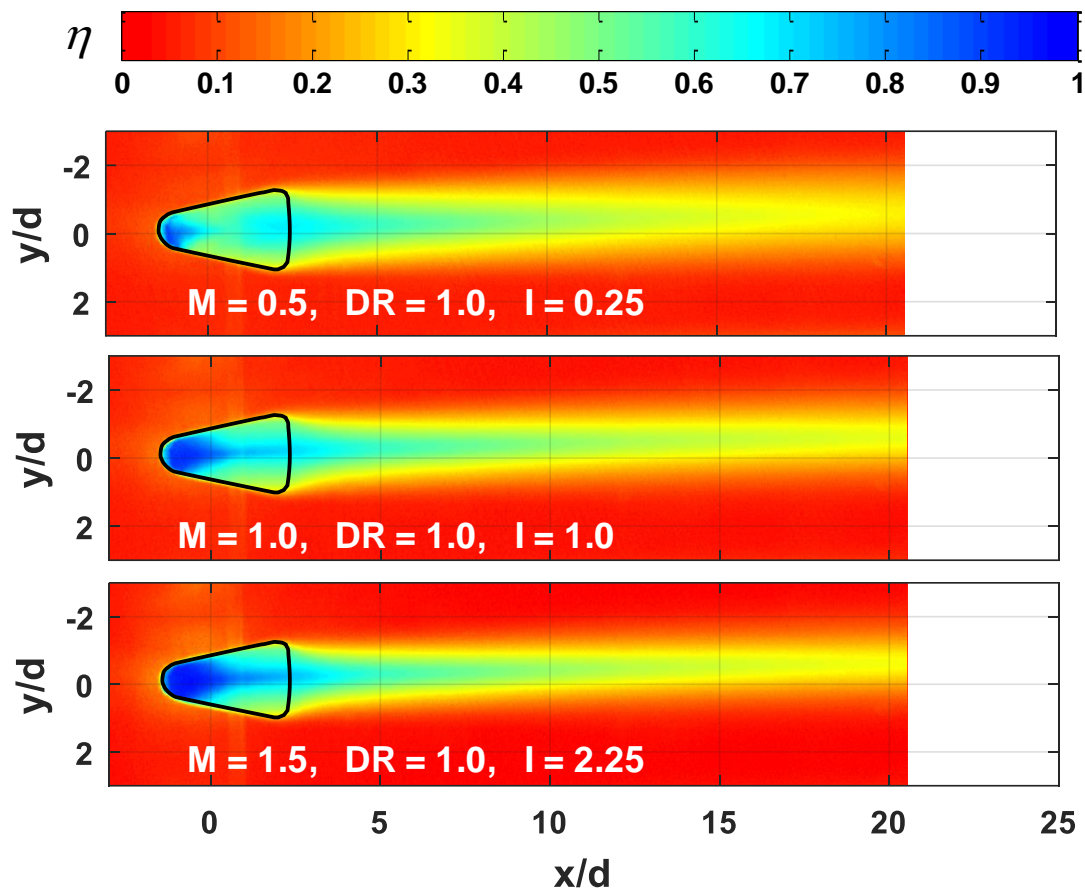


Figure 8.29: Honeywell Shaped 1 hole film cooling effectiveness distribution under a favorable pressure gradient: blowing ratio effect

degrees. HWS1 and the laidback, fanshaped hole result in similar performance for all flow conditions investigated.

#### *Honeywell Shaped 1 S-PIV Results*

As previously shown from the PSP results, the advanced film cooling hole entitled Honeywell Shaped 1 (HWS1) performs similarly to the baseline laidback, fanshaped film cooling hole. HWS1 has an increased lateral expansion angle (12 degrees compared to 10) and laidback angle (12 degrees compared to 10), but is otherwise identical to the

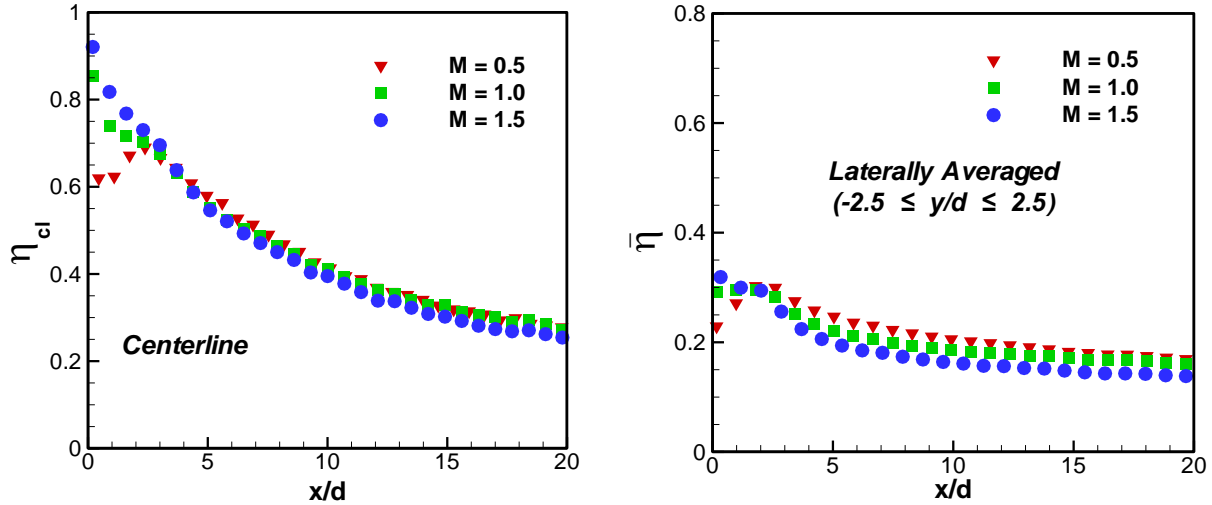


Figure 8.30: Honeywell Shaped 1 centerline and laterally averaged film cooling effectiveness under a favorable pressure gradient: blowing ratio effect

baseline shaped hole. Increasing the lateral expansion and laidback angles by 2 degrees has a similarly small impact on the flow field near the hole.

*Figure 8.37* shows the velocity and vorticity distributions for both ZPG and FPG flows as a function of blowing ratio. The density ratio is maintained at one, and flow fields are shown for the plane at the downstream edge of the HWS1 hole ( $x/d = 3$ ). The pressure gradient causes a similar effect as shown previously for the round and baseline shaped holes, where the film cooling jet is pushed closer to the surface and the CVP is spread wider. *Figure 8.38* shows the same blowing ratio effect with the effectiveness and vorticity at the downstream edge. The velocity contours suggest that the biggest difference in effectiveness should occur at  $M = 1.5$ , where the FPG causes a dramatic change in the separation and strength of the jet. However, the increasing vorticity magnitude caused by the FPG counteracted this reduced jet separation, so the effectiveness at the DSE is unaffected by the pressure gradient for  $M = 1.5$ , along with

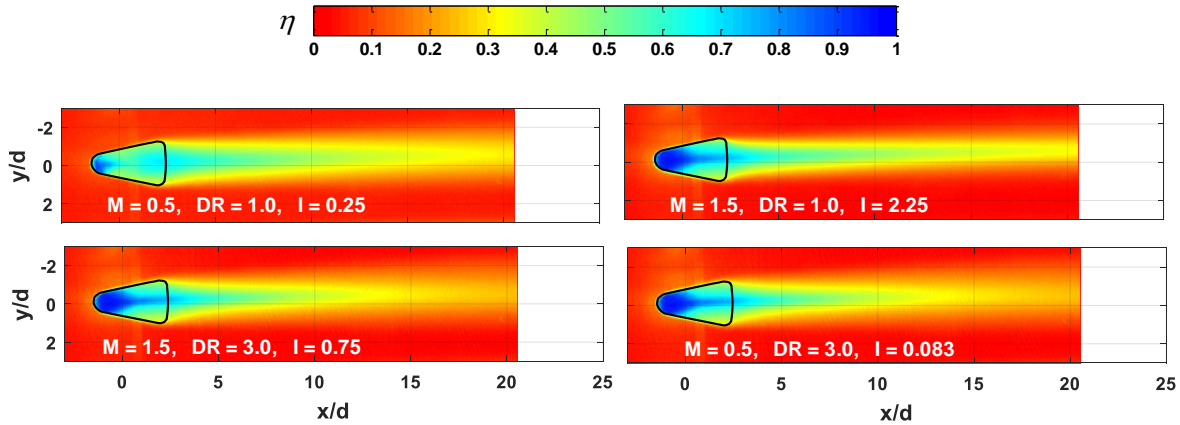


Figure 8.31: Honeywell Shaped 1 hole film cooling effectiveness distribution under a favorable pressure gradient: density ratio effect

the other two locations. This is expected, as the PSP results also showed that the pressure gradient had a small effect on the HWS1 cooling geometry.

*Figure 8.39* presents the effect of density ratio, which is the same for FPG and ZPG flows. The coolant is slowed down dramatically, which means there is no jet or vorticity to be seen with which to make comparisons. This is the same effect previously seen for the baseline shaped hole, where increasing the density ratio resulted in no visible jet and a substantial reduction in vorticity. *Figure 8.40* shows that the film cooling effectiveness at the DSE is not a function of the pressure gradient, which supports the previous figure that showed similar flow fields for the ZPG and FPG flows at the elevated density ratio of 3.0.

The effect of moving from the origin to the downstream edge of the HWS1 hole is presented in *Figure 8.41*, which shows the velocity and vorticity at a constant  $DR = 1.0$  and  $M = 1.5$ . At  $x/d = 0$ , the coolant liftoff is substantially reduced because the location is still inside of the hole, and the coolant has not had sufficient time to separate from the surface. When the ZPG and FPG flows are compared directly at  $x/d = 0$ , it can be seen

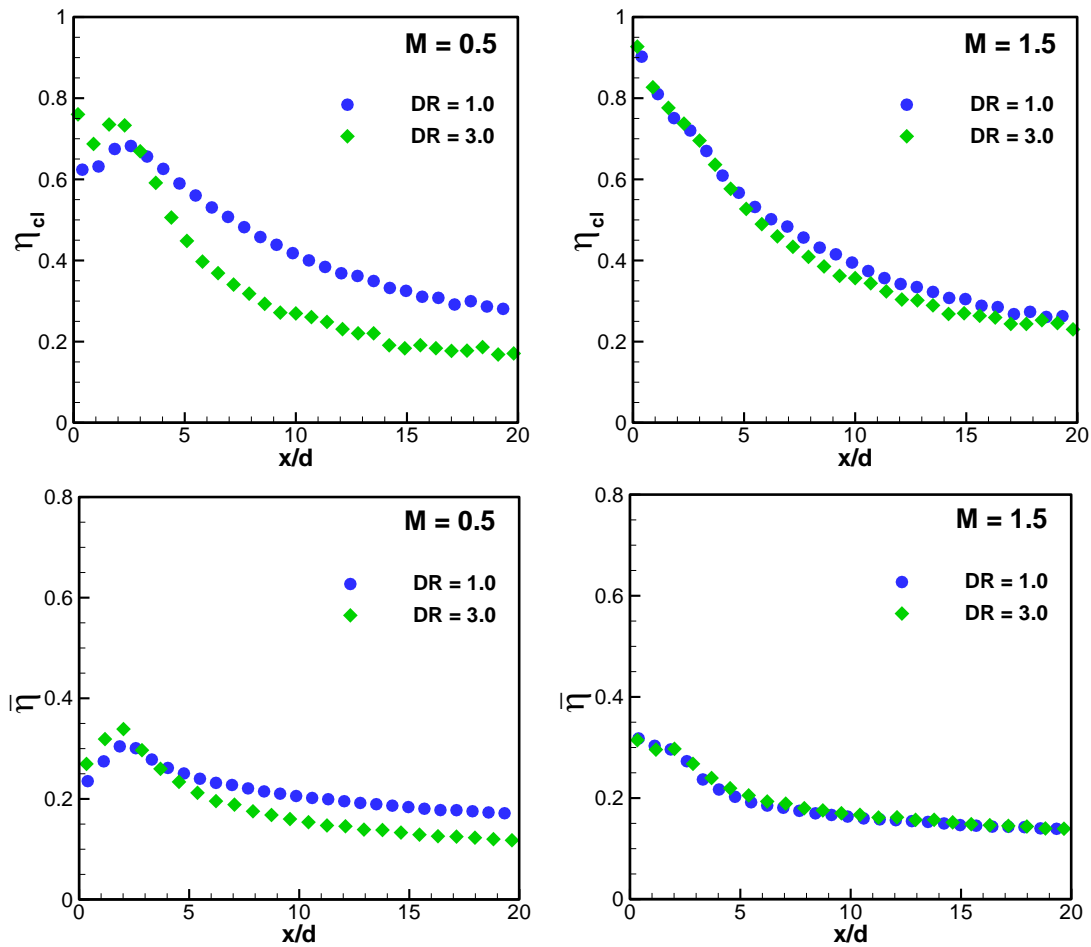


Figure 8.32: Honeywell Shaped 1 hole centerline and laterally averaged film cooling effectiveness under a favorable pressure gradient: density ratio effect

that the vorticity magnitude is significantly reduced by the FPG, as the jet is pushed towards the surface and completely inside of the hole. The formation of secondary flows is limited because the jet has been pushed low enough that it does not impede the flow of the mainstream to generate secondary flows. *Figure 8.42* shows the impact of the lack of secondary flow formation on film cooling effectiveness. The FPG allows the coolant to fill the hole more completely, as the effectiveness near the edges of the hole is significantly increased by the FPG. As less coolant is separating, more coolant is

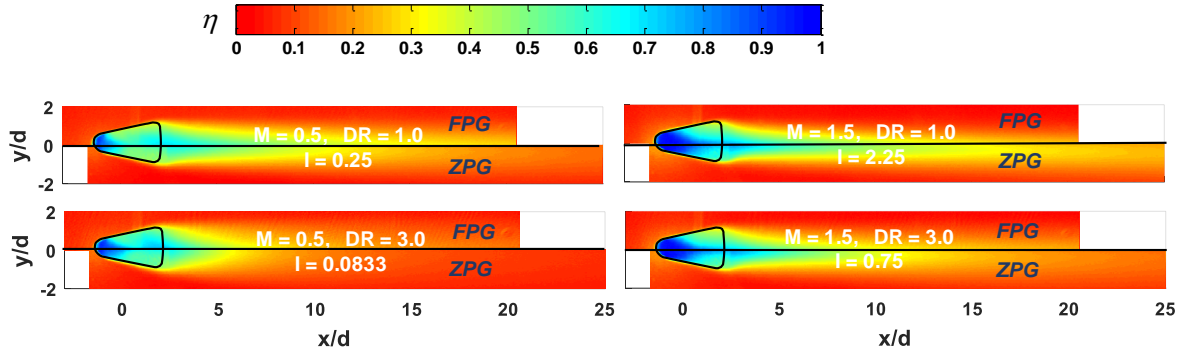


Figure 8.33: Honeywell Shaped 1 film cooling effectiveness distributions: FPG effect

available to expand and fill the larger expansion area of the HWS1 hole. The jet being pushed closer to the surface also dictates that it must spread more widely throughout the hole to maintain conservation of mass. For the ZPG, the thicker boundary layer at  $x/d = 0$  offers less resistance, allowing the jet to protrude into the mainstream, which then further increases the vorticity generation, causing increased coolant liftoff and mixing with the mainstream.

The S-PIV results of the HWS1 and baseline shaped geometries are directly compared to show the effect of increasing the hole expansion area with a FPG. *Figure 8.43* presents the distributions of velocity and vorticity at the DSE with  $DR = 1.0$  for a varying blowing ratio. The velocity and vorticity distributions are similar for both hole shapes, confirming the PSP results which showed the limited impact of increasing the hole outlet area beyond the baseline shaped hole. There are a few small but noteworthy differences caused by the increased hole outlet area of the HWS1 geometry. The velocity of the jet is slightly reduced, which can be seen most clearly for  $M = 1.5$ , where the jet is separated from the surface. This is expected, as the increased area should reduce the

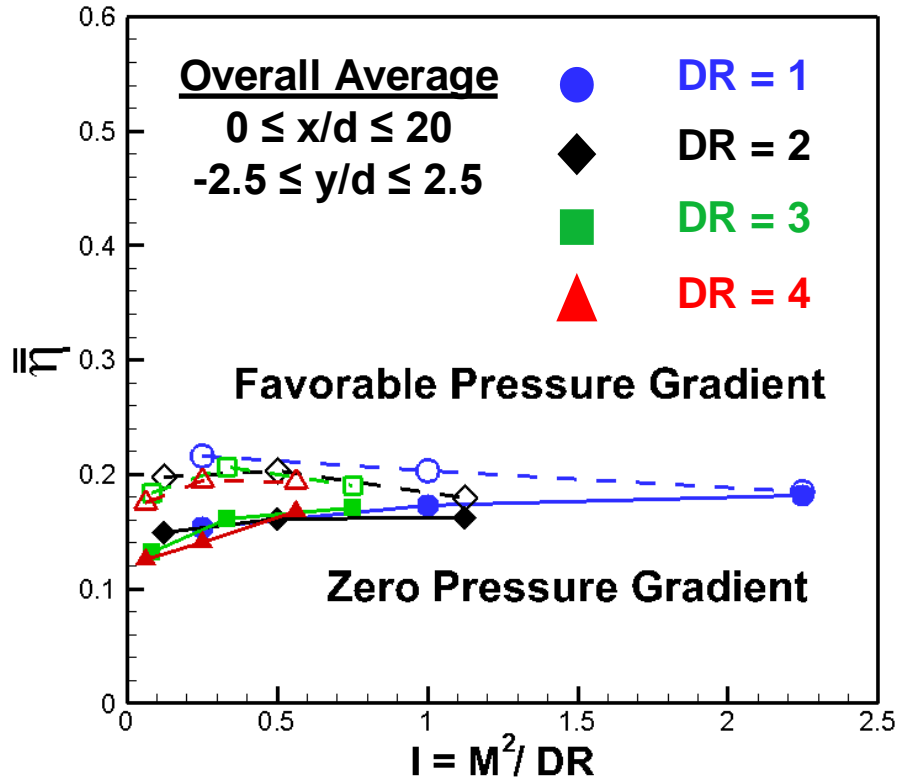


Figure 8.34: Honeywell Shaped 1 overall average film cooling effectiveness: FPG effect

coolant velocity. The magnitude and spread of the CVP is also reduced by increasing the hole outlet area. Due to the increased lateral expansion angle, the sidewalls of the HWS1 hole are farther apart, which means that the vortices generated by the interaction of sidewalls and the coolant are spread further apart and have less influence on the center jet. *Figure 8.44* shows the impact that these trends have on the film cooling effectiveness at the DSE. The effectiveness is slightly reduced for the HWS1 geometry at the DSE, but the increased vorticity of the baseline shaped hole results in increased mixing with the mainstream, and reduced downstream effectiveness.

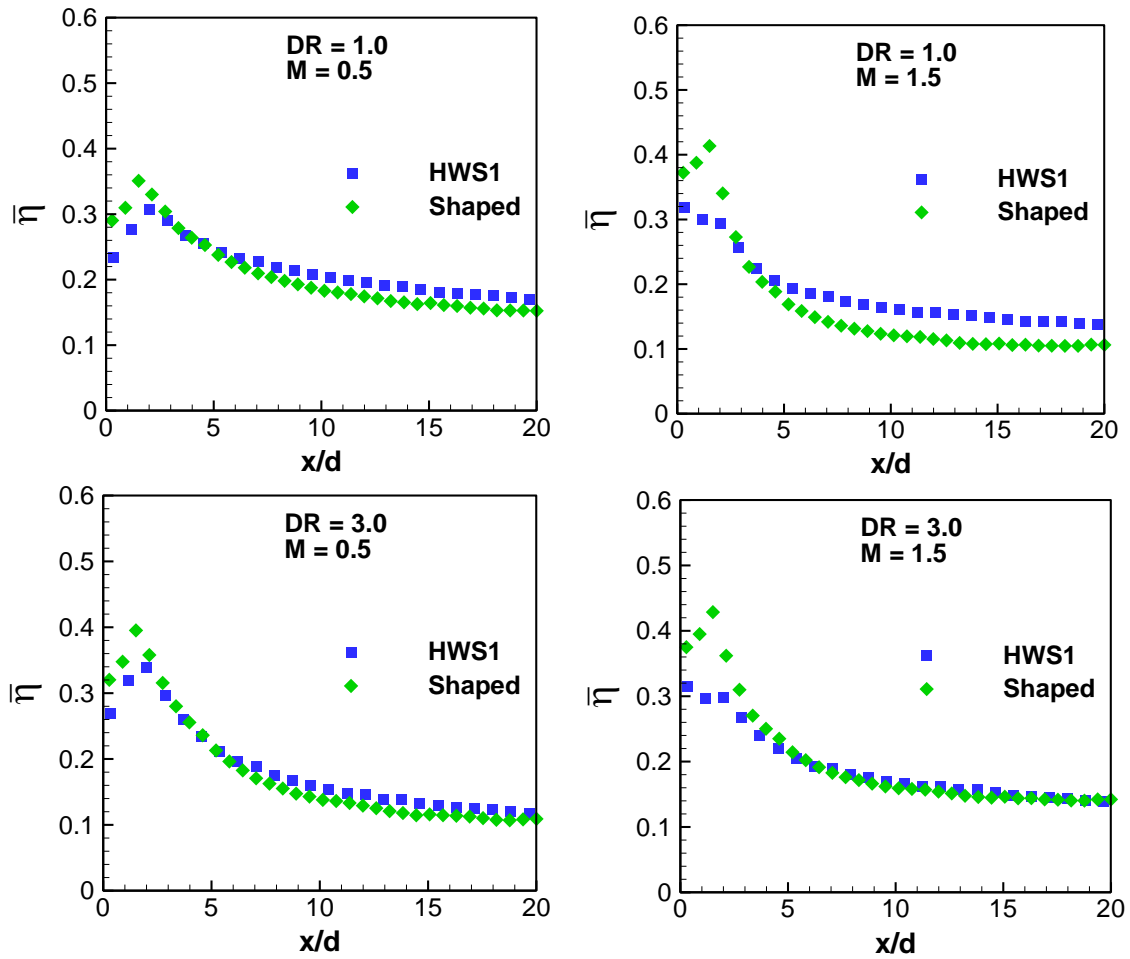


Figure 8.35: Comparison of baseline shaped and HWS1 with laterally averaged effectiveness under FPG

### *Honeywell Shaped 2 PSP Results*

The Honeywell Shaped 2 geometry matches the outlet shape of the Honeywell Shaped 1 geometry, but has an oval, or racetrack, shaped inlet as opposed to the standard round inlet of the HWS1 geometry. Watson [87] showed that for ZPG flows, the racetrack inlet slightly reduces the centerline effectiveness, but dramatically improves the lateral average, especially in the first 15 diameters. The racetrack inlet allows the coolant to spread out throughout the hole.

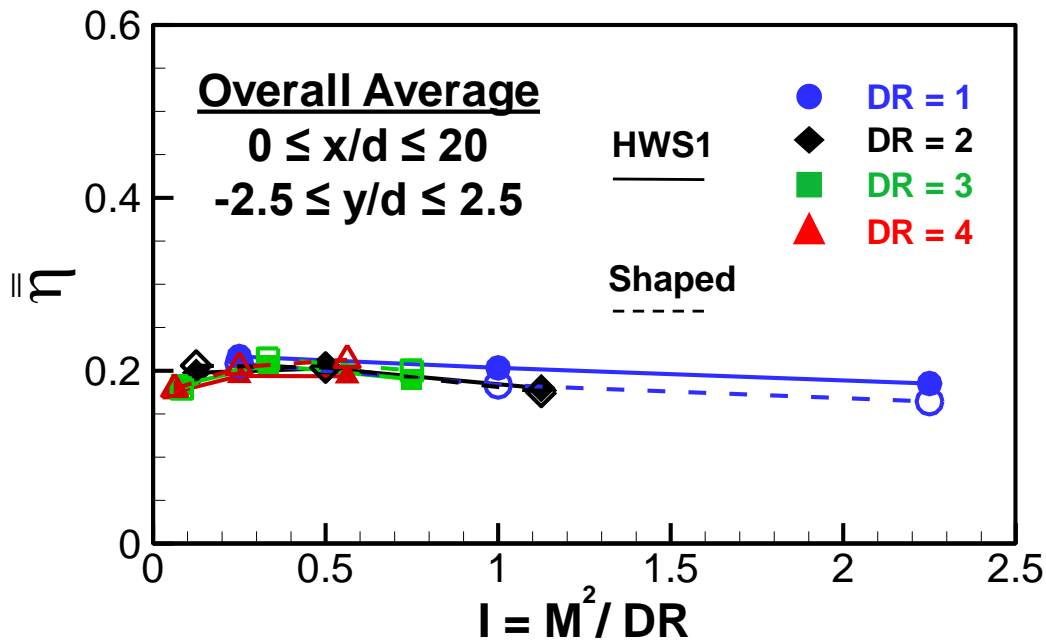


Figure 8.36: Comparison of HWS1 and shaped with overall average film cooling effectiveness

The effect of blowing ratio on the HWS2 geometry with an FPG mainstream flow is presented in *Figure 8.45*. The DR is maintained at 1.0, showing that the increase in coolant velocity reduces the spread of coolant within the hole, but improves downstream coverage dramatically. The increase in blowing ratio from  $M = 1.0$  to  $1.5$  has a negligible impact on the downstream film cooling effectiveness, but does slightly decrease the lateral spread of coolant within the HWS2 hole. *Figure 8.46* clearly shows that downstream of the hole, the higher blowing ratios have almost identical effectiveness while  $M = 0.5$  has significantly reduced effectiveness downstream of the hole. The increased length of the HWS2 hole and the increased hole exit area caused by expanding from the racetrack inlet result in an extreme reduction in coolant velocity from the hole inlet to the hole outlet. For  $M = 0.5$ , the inlet velocity is not high enough for the coolant to exit the hole with enough momentum to provide coverage downstream. The

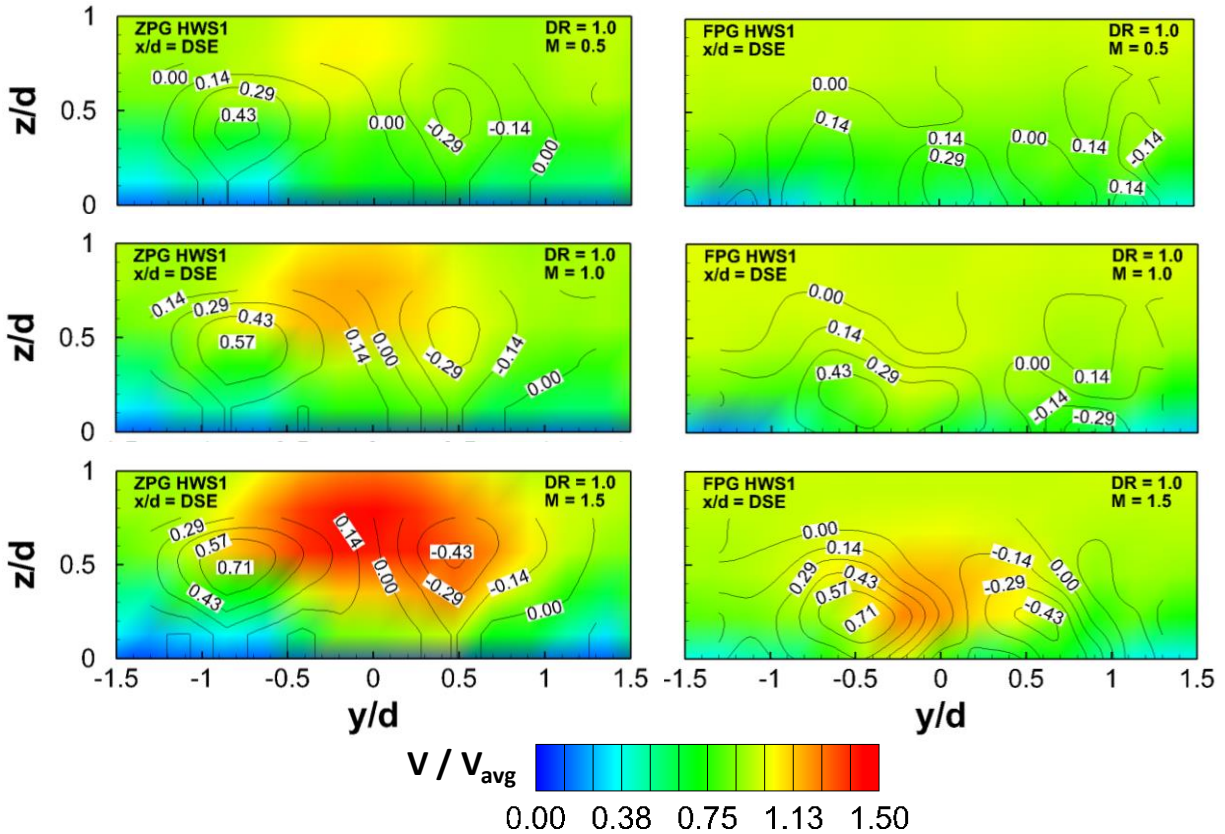


Figure 8.37: Effect of blowing ratio and freestream acceleration for Honeywell Shaped 1 hole ( $x/d = DSE$ ,  $DR = 1.0$ )

effectiveness within the hole is increased at the lower blowing ratio because the coolant is traveling slow enough to diffuse within the hole and cover the wide outlet area.

The density ratio effect is shown in *Figure 8.47* with a constant blowing ratio of  $M = 0.5$  and  $1.5$ . The slower velocity coolant at  $DR = 3.0$  does not have sufficient velocity to cover the area downstream of the hole, as it gets swept into the mainstream more easily. The HWS2 geometry is long, with over five diameters from the upstream edge to the downstream edge. The hole length, combined with the wide expansion angle that slows the coolant significantly, requires high velocity coolant to exit the hole without separating from the surface. *Figure 8.48* further illustrates this effect of density ratio for the HWS2 geometry, as increasing the density ratio increases the spread of coolant within

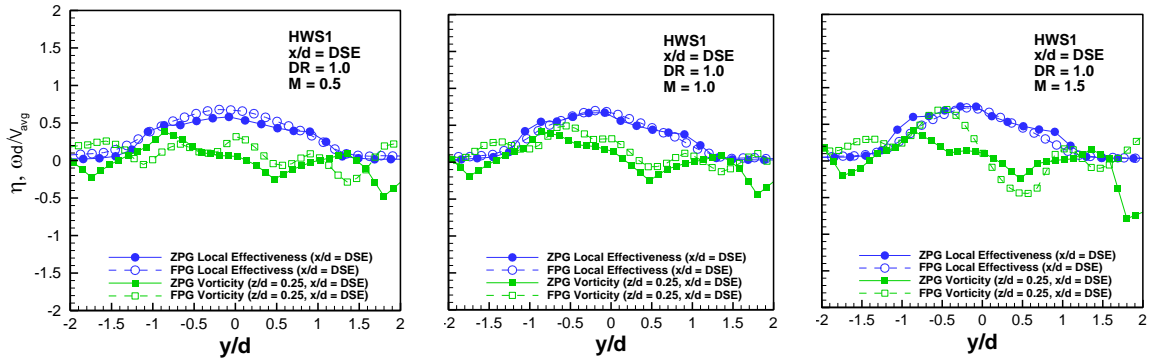


Figure 8.38: Influence of flow vorticity on surface film cooling effectiveness from Honeywell Shaped 1 ( $x/d = DSE$ ,  $DR = 1.0$ )

the hole, but the drop in velocity results in much lower film cooling effectiveness downstream.

The effect of the FPG on the HWS2 geometry is evaluated by directly comparing the ZPG and FPG distributions for  $DR = 1.0$  and  $3.0$  and  $M = 0.5$  and  $1.5$ . *Figure 8.49* shows that the FPG results in significantly improved film cooling effectiveness. The lateral spread of coolant within the hole is improved for all flow conditions, and the coolant travels farther downstream for the FPG case at all flow conditions. The spread of coolant within the hole is increased because the FPG boundary layer is thinner, which offers more resistance to jet separation within the hole. With such a long hole, keeping the jet attached inside of the hole is more important. As the jet is pushed closer to the surface of the hole, it also spreads out and provides for a wider jet of coolant exiting the hole at the DSE. *Figure 8.50* directly compares the FPG and ZPG flows for the HWS2 through the overall average. The range of  $x/d$  and  $y/d$  used to calculate the overall average are different from previous geometries because the diameter changed due to the racetrack inlet. The ranges are chosen to ensure that the same physical area is used for comparison. The overall average effectiveness is increased by 30-50% under FPG flows.

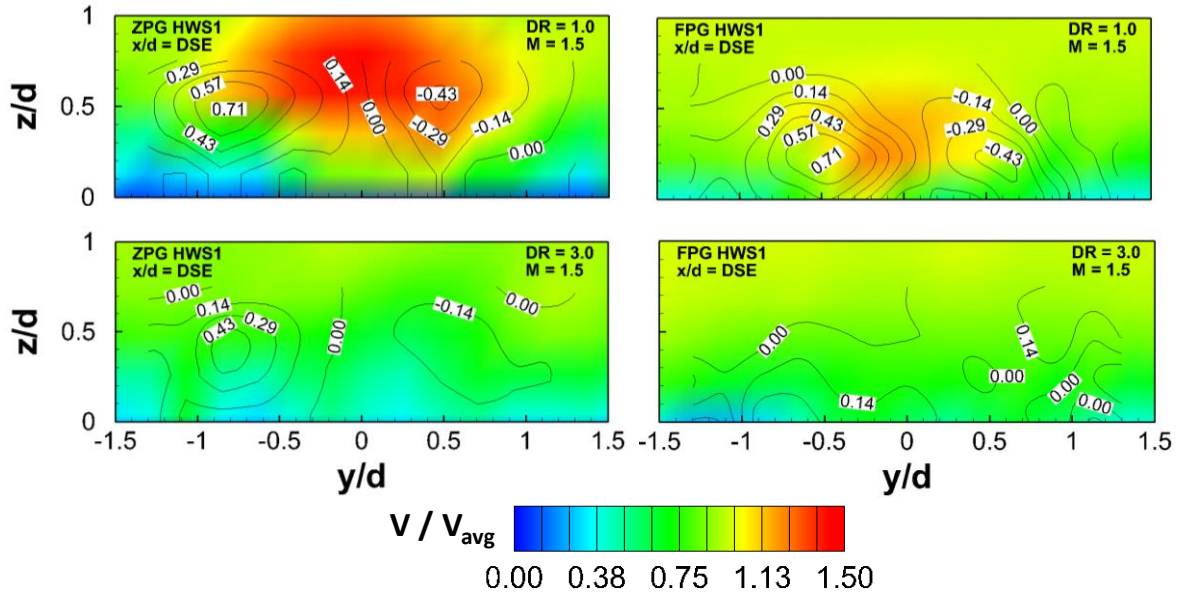


Figure 8.39: Effect of density ratio and freestream acceleration for Honeywell Shaped 1 holes ( $x/d = DSE$ ,  $M = 1.5$ )

This represents a substantial increase in effectiveness caused by the FPG that has not previously been seen for other geometries. The interaction between the jet coming through a racetrack inlet and a favorable pressure gradient mainstream flow is significantly different than the interaction with a jet through a round inlet hole. The racetrack inlet is designed to increase coolant spread and keep the jet closer to the surface, which is the same effect of the FPG. The two effects compound each other causing significant improvement compared with the ZPG. Furthermore, the HWS2 hole is two diameters longer, suggesting that the impact of the FPG is most helpful in keeping the coolant attached within the hole, which is increasingly important with the extreme length of the hole.

The effect of adding the racetrack inlet and subsequently creating a longer hole is evaluated by directly comparing the lateral average of the HWS2 and HWS1 geometries for FPG flows in *Figure 8.51*. It is clear that the HWS2 geometry dramatically

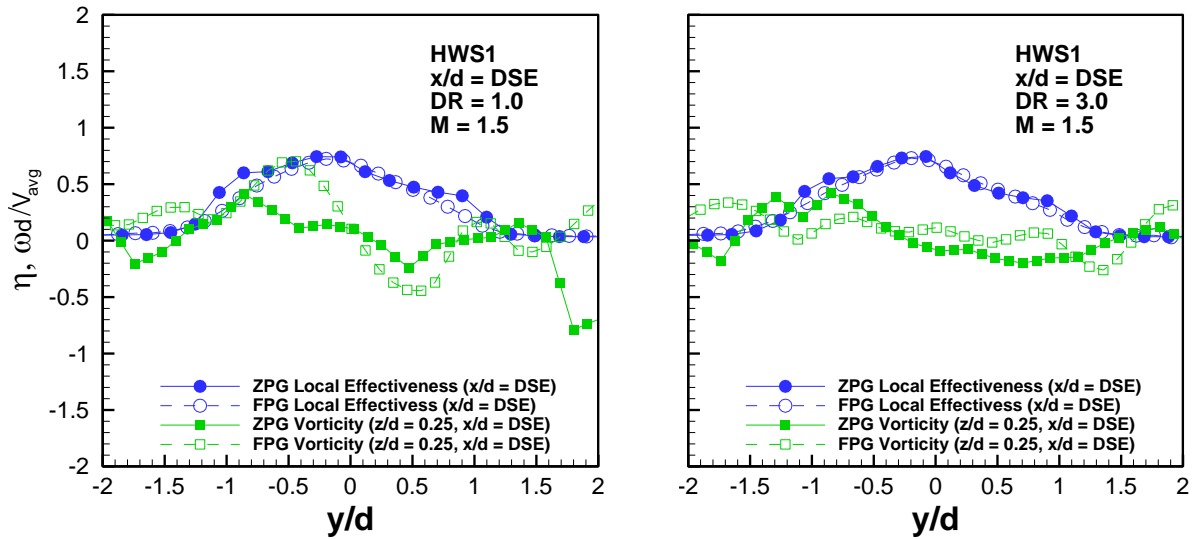


Figure 8.40: Influence of flow vorticity on surface film cooling effectiveness from Honeywell Shaped 1 holes ( $x/d = \text{DSE}$ ,  $M = 1.5$ )

outperforms the HWS1 geometry for the entire range of flow conditions investigated. The difference is also shown in *Figure 8.52*, which shows that the overall average effectiveness is approximately double for HWS2. The two possible differences that could account for this are the racetrack inlet and the longer hole shape caused by expanding from the racetrack shape. It was previously determined that the HWS2 geometry is improved by the FPG, while the HWS1 geometry is not significantly affected. However, this does not account for the entire difference as the ZPG results also show a significant improvement from HWS1 to HWS2. The longer hole helps to explain why the pressure gradient effect is more important, but it is unlikely that increasing the hole length would improve effectiveness downstream of the hole. It seems that a longer hole would allow more time for the coolant to separate from the surface and actually reduce effectiveness. Therefore, the effect of changing the inlet shape to a racetrack is significant. The coolant spread is increased and pushed closer to the surface of the HWS2 hole by the wider and

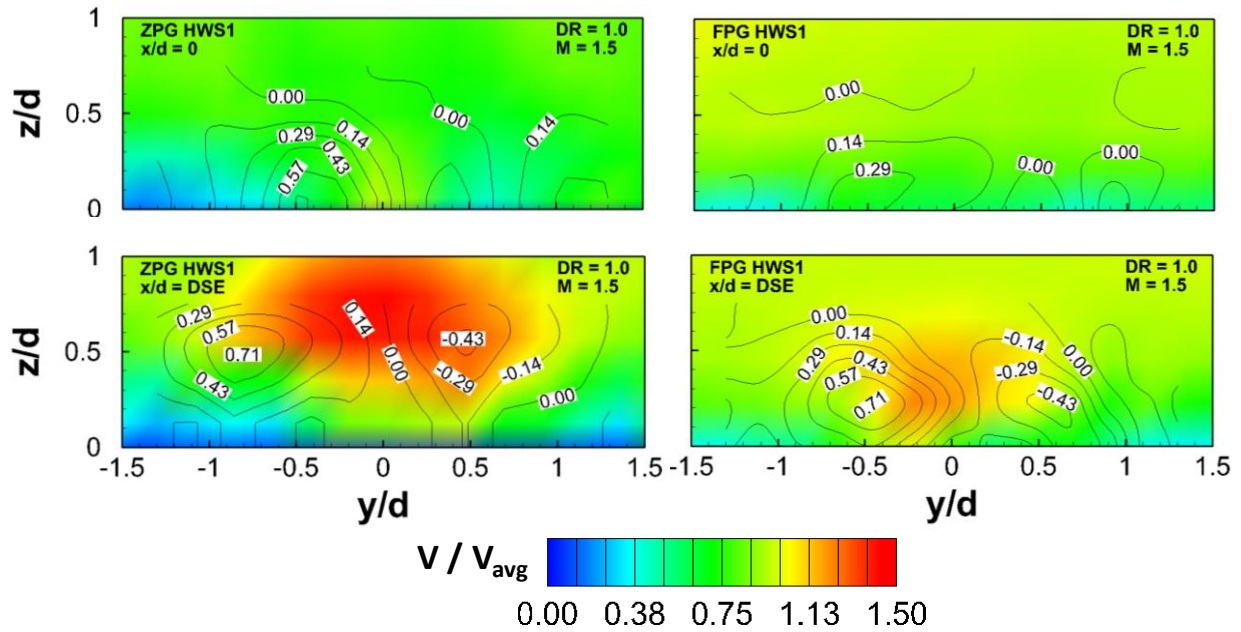


Figure 8.41: Effect of downstream location and freestream acceleration for Honeywell Shaped 1 ( $M = 1.5$ ,  $DR = 1.0$ )

shorter racetrack inlet. The core of the jet is closer to the surface because the center of the racetrack inlet is now closer to the surface.

#### *Honeywell Shaped 2 S-PIV Results*

The PSP results showing the increased effect of the FPG and the high cooling effectiveness caused by the racetrack inlet of the HWS2 geometry are further investigated using S-PIV. The velocity and vorticity distributions at the DSE for  $DR = 1.0$  with a varying blowing ratio are presented in *Figure 8.53*. The PSP results have previously shown that for  $M = 1.0$  and  $M = 1.5$ , the film cooling effectiveness is unchanged with blowing ratio, but that the effectiveness is reduced for  $M = 0.5$ . However, within the hole, the effectiveness was not significantly affected by the blowing ratio. It should be expected that the flow field at the DSE would not be a function of blowing ratio, and the ZPG and FPG results both confirm that expectation. However, the PSP results also

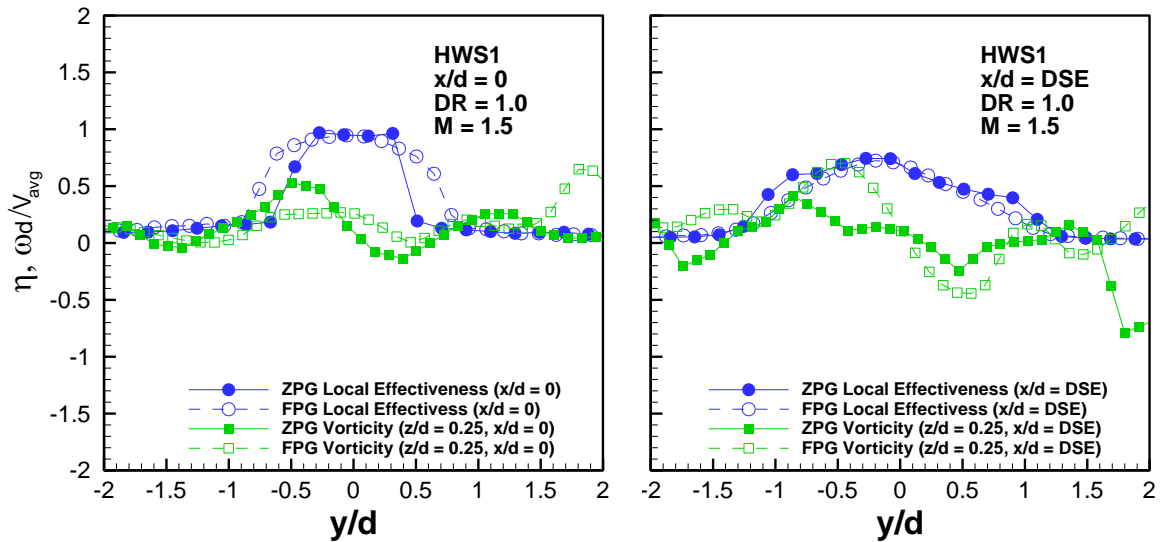


Figure 8.42: Influence of flow vorticity on surface film cooling effectiveness from Honeywell Shaped 1 holes ( $M = 1.5$ ,  $DR = 1.0$ )

showed that the film cooling effectiveness was dramatically increased by the FPG, and the flow field around the HWS2 hole should definitely be a function of the FPG. Figure 8.53 shows that the vorticity is significantly increased from the ZPG to the FPG. While there is no jet visible from the velocity contours, the vorticity contours clearly show an interaction between the coolant and mainstream. The FPG causes increased vorticity generation because the coolant is more spread within the hole. The HWS2 hole is significantly wider than previous holes due to the racetrack inlet, which results in limited coolant interaction with the sidewalls of the hole. The thinner boundary layer of the FPG flow keeps the coolant jet closer to the surface of the hole, causing increased spread of the coolant that allows for increased interaction with the sidewalls and additional vortex formation. *Figure 8.54* also shows the impact of blowing ratio in relation to the vorticity and effectiveness at the DSE. Both the lateral spread and maximum film cooling effectiveness are slightly increased at the DSE for the FPG case. This is primarily caused by the high separation that occurs in the long hole for ZPG flows. The FPG helps to

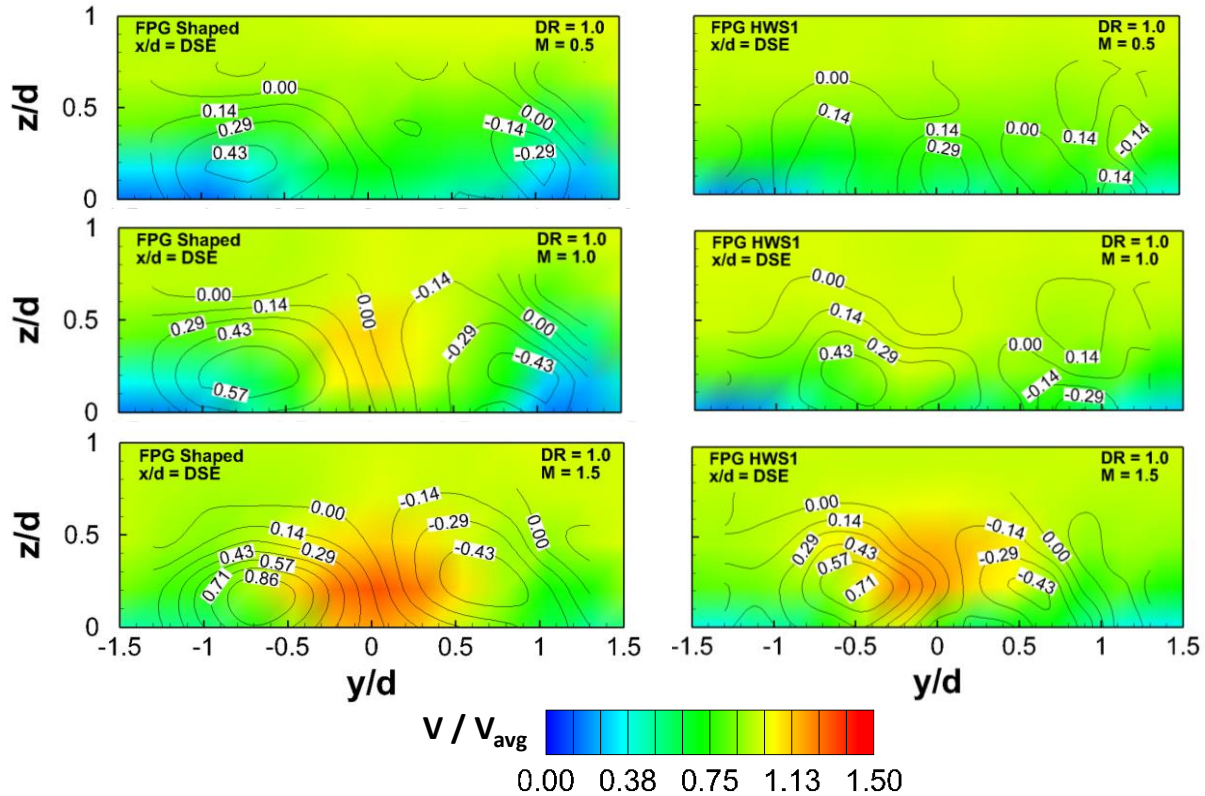


Figure 8.43: Comparison of HWS1 and shaped holes for varying blowing ratio ( $x/d = DSE$ ,  $DR = 1.0$ , FPG)

mitigate this separation by keeping the jet closer to the surface, which is more important due to the increased hole length.

The effect of increasing the density ratio from  $DR = 1.0$  to  $DR = 3.0$  is shown in *Figure 8.55*. The reduced coolant velocity caused by increasing the  $DR$  cannot be seen because the coolant velocity is lower than the mainstream. However, it is clear that the density ratio reduces the vorticity generation as the coolant is heavier and closer to the surface. With the jet closer to the surface, there is less interaction with the mainstream and the jet, resulting in reduced vorticity. *Figure 8.56* shows that the film cooling effectiveness at the downstream edge is increased by the FPG for  $DR = 3.0$ . This occurs because the coolant is traveling slowly, so protection from the mainstream within the hole

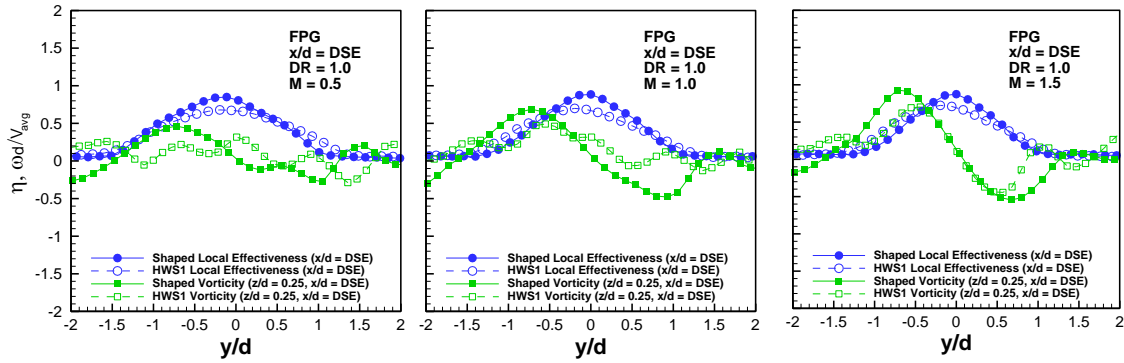


Figure 8.44: Comparison of round and shaped holes through the influence of flow vorticity on surface film cooling effectiveness ( $x/d = DSE$ ,  $DR = 1.0$ , FPG)

afforded by the FPG has a more significant effect. The slower the coolant travels, the more time it takes to reach the DSE, which offers more opportunity for mainstream mixing.

In *Figure 8.57*, the velocity and vorticity distributions are compared at  $x/d = 0, 3$ , and the DSE to show the effect of the HWS2 hole on the formation of the secondary flows through the hole. For the ZPG, there is limited vorticity formation because of the lack of interaction with the wider sidewalls. However, for the FPG, the coolant is spread within the hole to allow increased vorticity formation due to the interactions with the walls. The CVP is already clearly seen at  $x/d = 0$ , and while the strength of the CVP remains constant through the hole, the spread of the CVP is significantly increased from  $x/d = 0$  to  $x/d = DSE$ . As the coolant interacts with the sidewalls, the vortex pair spreads apart and helps to spread the coolant throughout the wider film cooling shape. *Figure 8.58* shows the effect of this vorticity generation on the film cooling effectiveness through the hole. At  $x/d = 0$ , the effectiveness is uniformly equal to one throughout the hole, so the vorticity has little impact. However, as the coolant moves down the hole, the maximum effectiveness and the spread of coolant is increased by the FPG. The increased

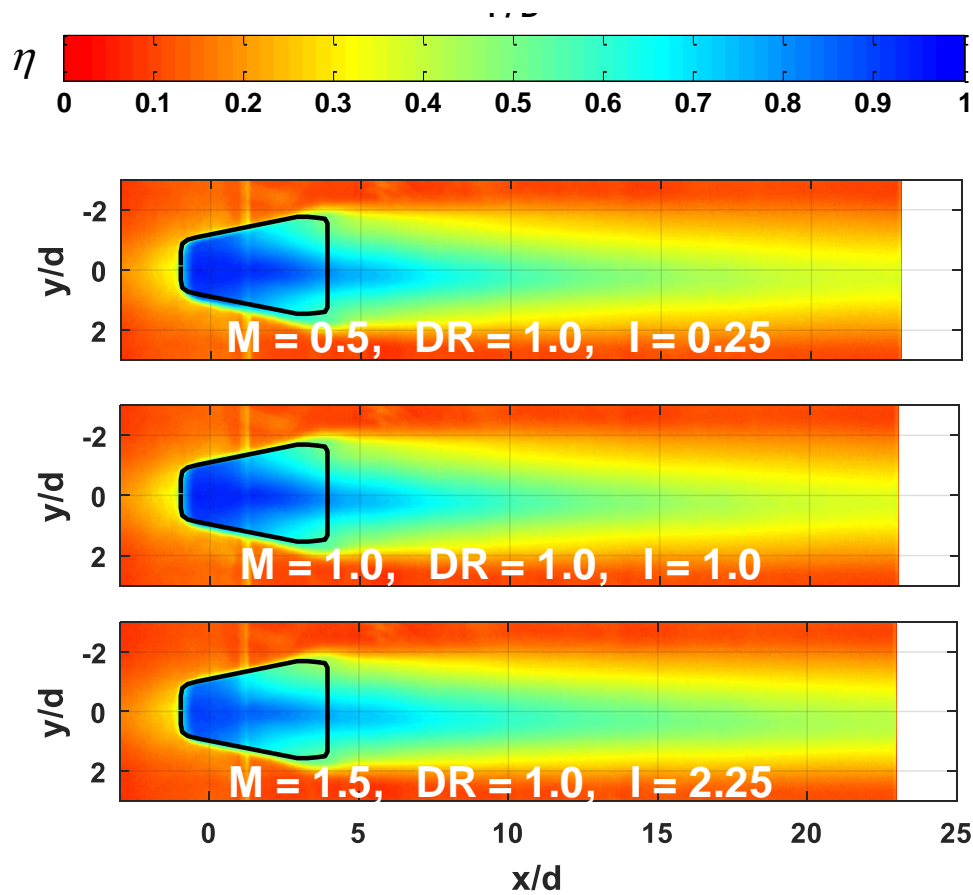


Figure 8.45: Honeywell Shaped 2 hole film cooling effectiveness distribution under a favorable pressure gradient: blowing ratio effect

vorticity causes the increased spread, and the increase in maximum is likely a result of the jet being kept closer to the surface preventing coolant liftoff.

The S-PIV results for HWS2 are also used to show the effect of the racetrack inlet by directly comparing the flow field for HWS2 and HWS1 for FPG flows in *Figure 8.59*. As previously discussed with PSP, the racetrack inlet keeps the core of the coolant jet closer to the surface, which can be clearly seen at  $M = 1.5$  where the jet is concentrated and faster than the mainstream for HWS1 but not HWS2. The magnitude of maximum vorticity is increased by the racetrack inlet, as the coolant spreads out more throughout the width of the hole and has more interaction with the sidewalls, increasing the vorticity

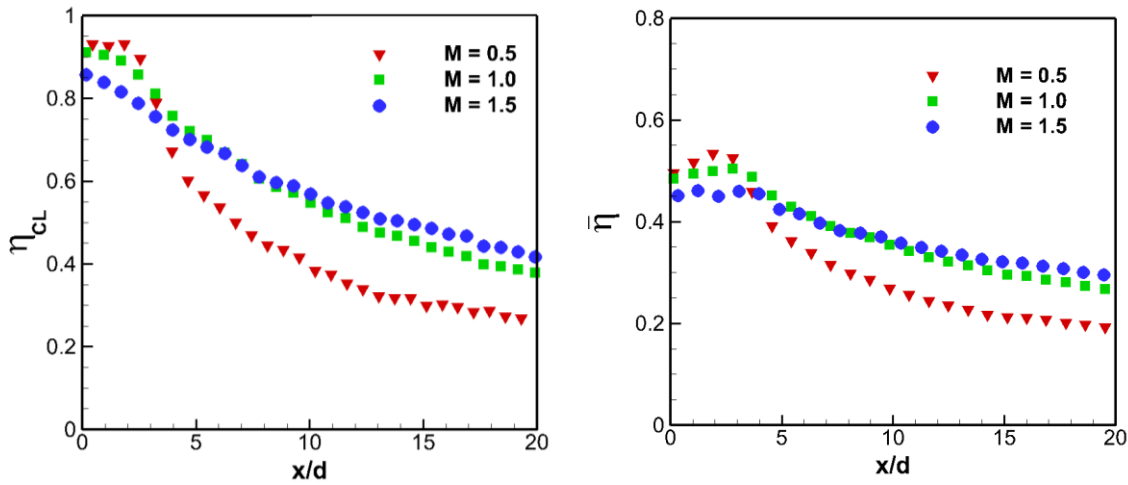


Figure 8.46: Honeywell Shaped 2 centerline and lateral average film cooling effectiveness under a favorable pressure gradient: blowing ratio effect

magnitude. Furthermore, the width of elevated vorticity is substantially increased by the racetrack inlet for essentially the same reason. The coolant is more spread out and has more interaction with the walls. *Figure 8.60* shows the impact of the additional vorticity generation on the film cooling effectiveness at the DSE. The maximum film cooling effectiveness is the same for the two geometries but the lateral spread of the coolant is dramatically increased for HWS2. This is caused by racetrack inlet as previously discussed, along with the increasing width of the vorticity that increases coolant spread.

#### *Duckfoot 1 PSP Results*

The Duckfoot 1 film cooling hole is designed to induce additional secondary flows that oppose secondary flows such as the CVP that form with baseline round and shaped film cooling. The DF1 is literally modeled after the webbing of a duck foot, with the goal of increasing coolant spread as it follows the contour of the webbing, along with generating some additional vorticity to counteract the CVP. The ZPG results have previously shown that the DF1 geometry does not result in significant improvement in

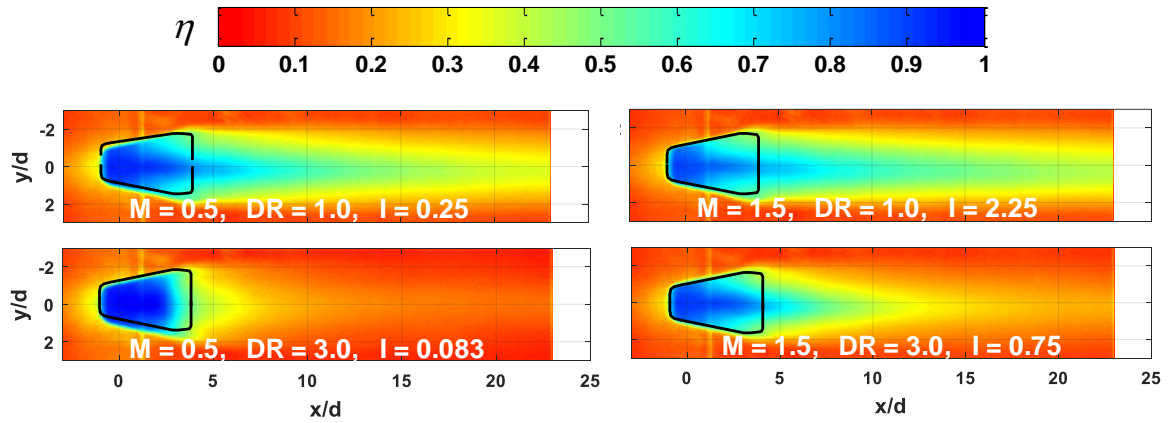


Figure 8.47: Honeywell Shaped 2 hole film cooling effectiveness distribution under a favorable pressure gradient: density ratio effect

comparison with HWS1. In order to justify the added complexity of the duckfoot hole, there should be a significant improvement to film cooling performance. The DF1 is evaluated for the FPG case to determine if it improves significantly.

The effect of blowing ratio on the film cooling effectiveness for the DF1 geometry is shown in *Figure 8.61*. Increasing the blowing ratio from  $M = 1.0$  to  $M = 1.5$  has negligible impact on the distribution of effectiveness. The effectiveness within the hole is similar for  $M = 0.5$ , but the downstream effectiveness is reduced because the coolant velocity is too low. The coolant cannot maintain attachment to the plate without getting swept into the mainstream. The blowing ratio of  $M = 0.5$  performing worse than the higher blowing ratios is caused by the increased outlet area of the duckfoot geometry. Since the duckfoot expands the hole significantly compared to the other shaped geometries, the coolant velocity is low and the coolant is barely able to make it to the downstream edge without being swept into the mainstream. *Figure 8.62* shows the distributions broken down into centerline and lateral average effectiveness. It can be clearly seen that  $M = 1.0$  and  $1.5$  perform nearly identically. This shows that the DF1

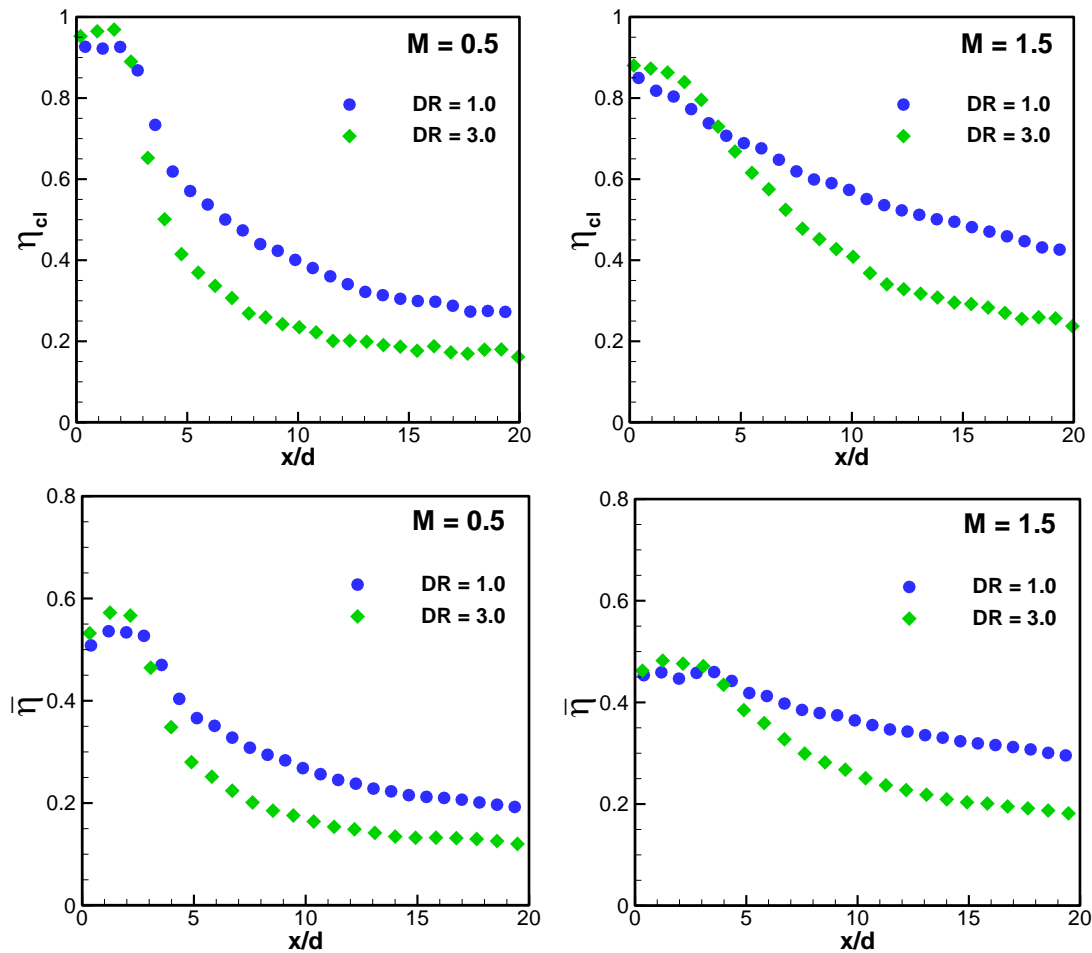


Figure 8.48: Honeywell Shaped 2 hole centerline and laterally averaged film cooling effectiveness under a favorable pressure gradient: density ratio effect

geometry performs optimally for a blowing ratio closer to  $M = 1.0$  as adding more coolant mass flow to get to  $M = 1.5$  does not improve cooling performance in any way. Figure 8.62 also shows that  $M = 0.5$  performs significantly worse downstream, especially along the centerline.

The effect of increasing the density ratio from 1 to 3 for DF1 is shown in *Figure 8.63*, for  $M = 1.5$ . The effectiveness within the hole is unchanged by increasing density ratio, which means that lowering the coolant velocity is counteracted by the increased lateral spread consistent with higher DR. However, downstream of the hole, the higher

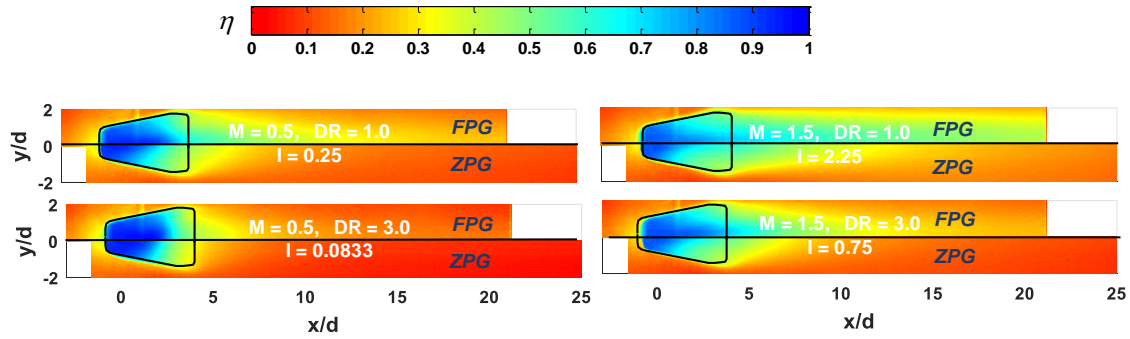


Figure 8.49: Honeywell Shaped 2 film cooling effectiveness distributions: FPG effect

density ratio cooling scheme does not have sufficient momentum to travel downstream.

*Figure 8.64* shows the effect of density ratio on the centerline and lateral average effectiveness. Increasing the density ratio reduces film cooling effectiveness downstream of the hole.

The effect of the FPG on the film cooling effectiveness for the Duckfoot 1 hole is shown by plotting the ZPG and FPG distributions side by side for direct comparison. *Figure 8.65* shows that the spread of coolant within the hole and the downstream effectiveness is not changed significantly by the FPG. *Figure 8.66* also shows the limited effect of the FPG on the overall average film cooling effectiveness. The DF1 geometry is not significantly impacted by the FPG similarly to the HWS1 geometry shown previously. The effect of reducing the boundary layer thickness is less significant because of the shorter length of the hole. Furthermore, the coolant is already slowed down by the expanding area and the contours help increase the coolant spread.

The DF1 geometry was designed to improve the cooling effectiveness of the HWS1 hole, so the geometries are compared directly to determine the improvement provided by the DF1 geometry under FPG flows. *Figure 8.67* shows that the DF1 does

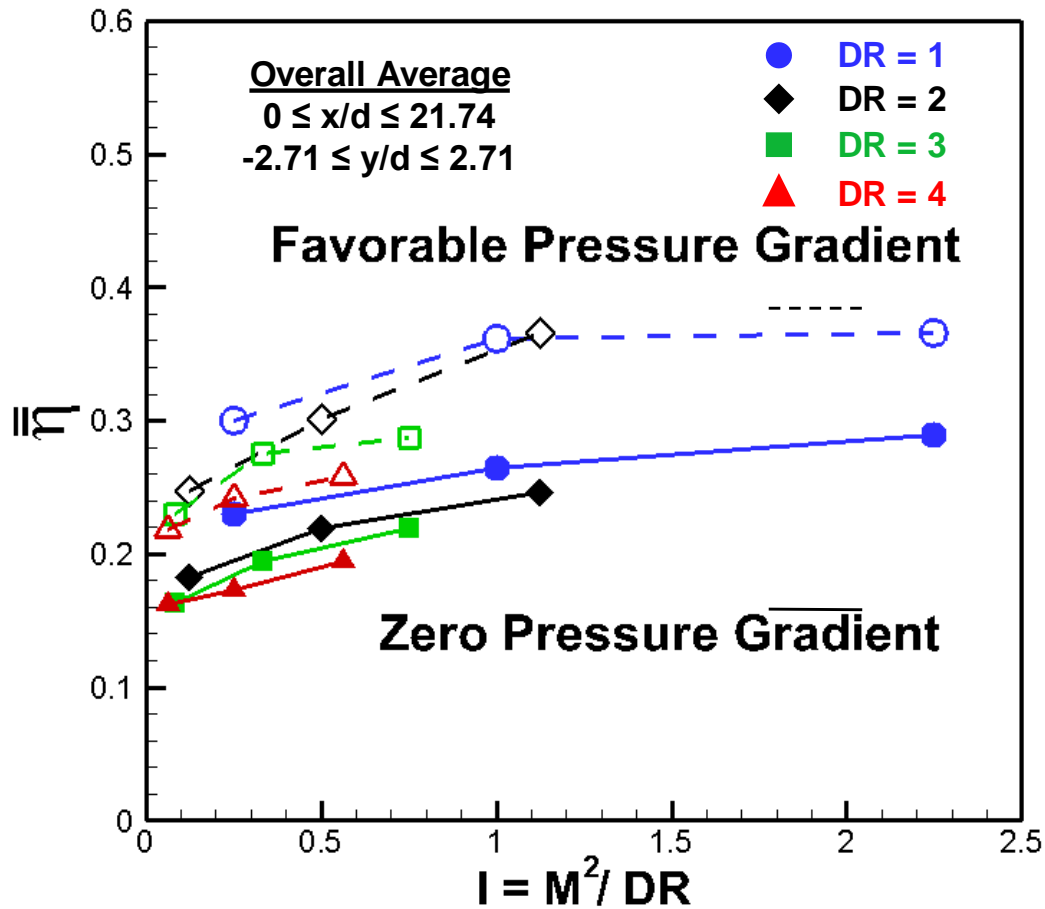


Figure 8.50: Honeywell Shaped 2 overall average film cooling effectiveness: FPG effect

not offer any meaningful improvement. For higher velocity coolant, the DF1 is slightly better because the outlet area is larger for the DF1 hole, but at lower coolant velocities, the HWS1 hole performs better because the slower coolant spreads wider within the DF1 hole. The raised lateral average within the hole for DF1 is clearly shown at  $M = 0.5$ , but this also means that the coolant is moving too slowly and interacting too much with the sidewall contours which reduces the downstream effectiveness. *Figure 8.68* shows the same results, where the DF1 geometry results in minimal overall improvement at higher momentum flux ratios, but actually performs slightly worse for lower momentum flux

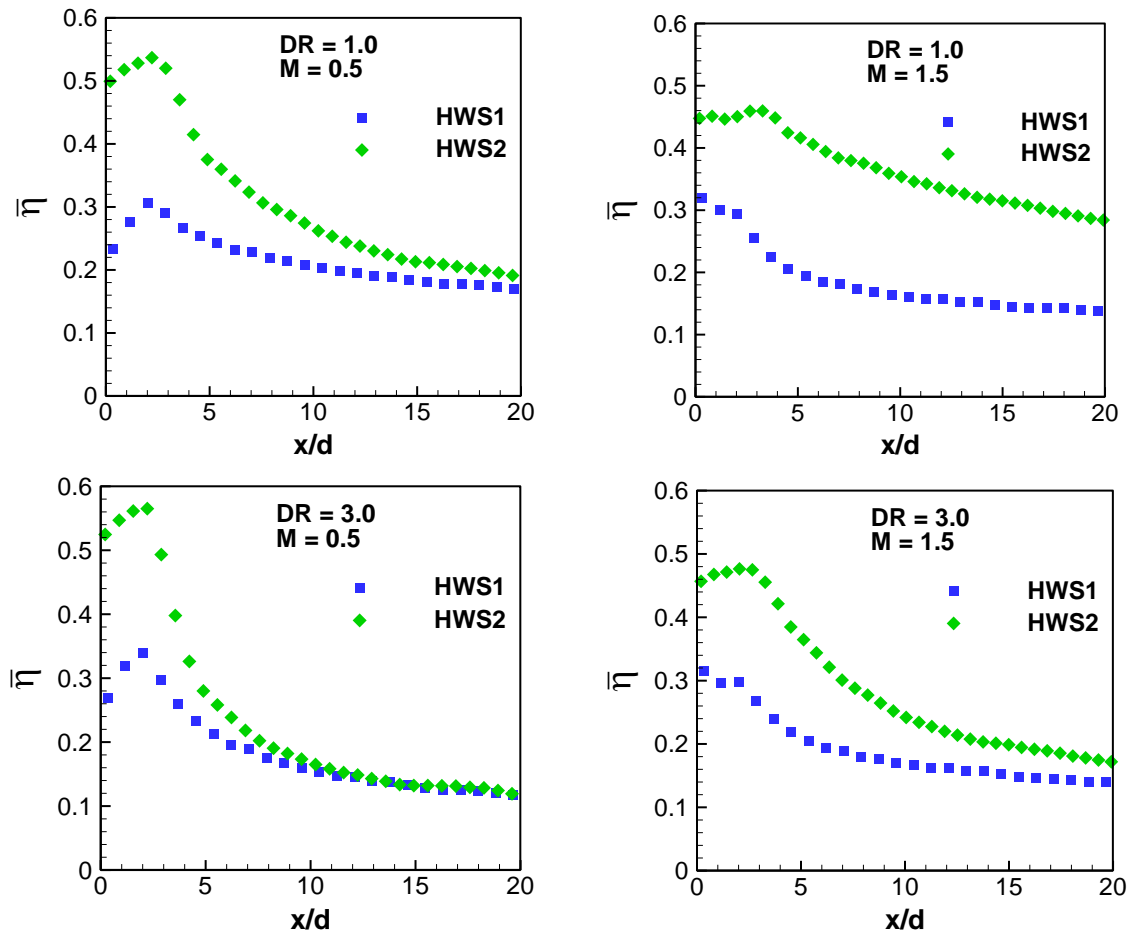


Figure 8.51: Favorable pressure gradient lateral average film cooling effectiveness: Inlet shape effect

ratios. The DF1 complex shape does not result in the increased cooling performance that was hoped for with the advanced design.

#### *Duckfoot 1 S-PIV Results*

The S-PIV results from the DF1 geometry are used to analyze the effect of the duckfoot style contours on the formation of the CVP and other secondary flows. The PSP results have previously shown that  $M = 0.5$  performs the best inside of the hole but  $M = 1.0$  and  $1.5$  are significantly better downstream of the hole. The ZPG results shown in *Figure 8.69* show no noticeable effect of blowing ratio because they show no jet or

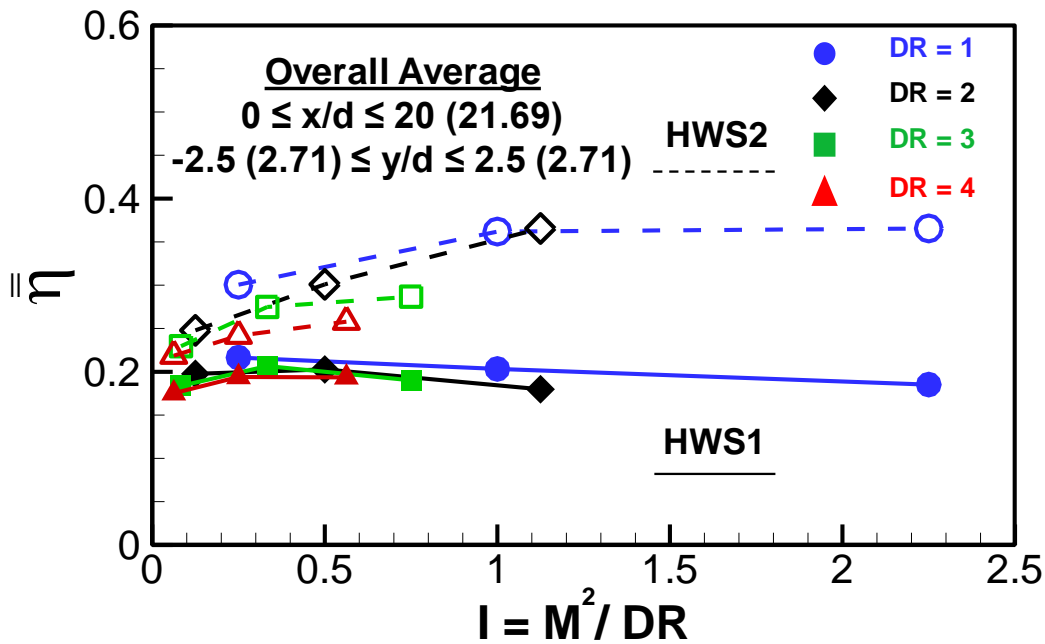


Figure 8.52: Comparison of HWS1 and HWS2 with overall average film cooling effectiveness

vorticity for any of the blowing ratios investigated. The FPG however, clearly shows the formation of a jet above the center of the DF1 as well as above one of the duckfoot toes. The jet is present for increased blowing ratios, but not  $M = 0.5$ . The FPG also shows increased vorticity magnitude with increasing blowing ratio. Increasing the blowing ratio increases the coolant velocity, which results in increased liftoff from the DF1 within the hole. This is likely a result of the increased vorticity formation from the increased surface area of the duckfoot contours. There is more vorticity present than the simple CVP normally seen, and the side vortices that are rotating counter to the CVP are clearly a result of the duckfoot contours. These additional secondary flows are present under the FPG but not the ZPG because the coolant does not spread sufficiently under the ZPG flow. The FPG increases the lateral spread of the coolant within the hole, as seen by the

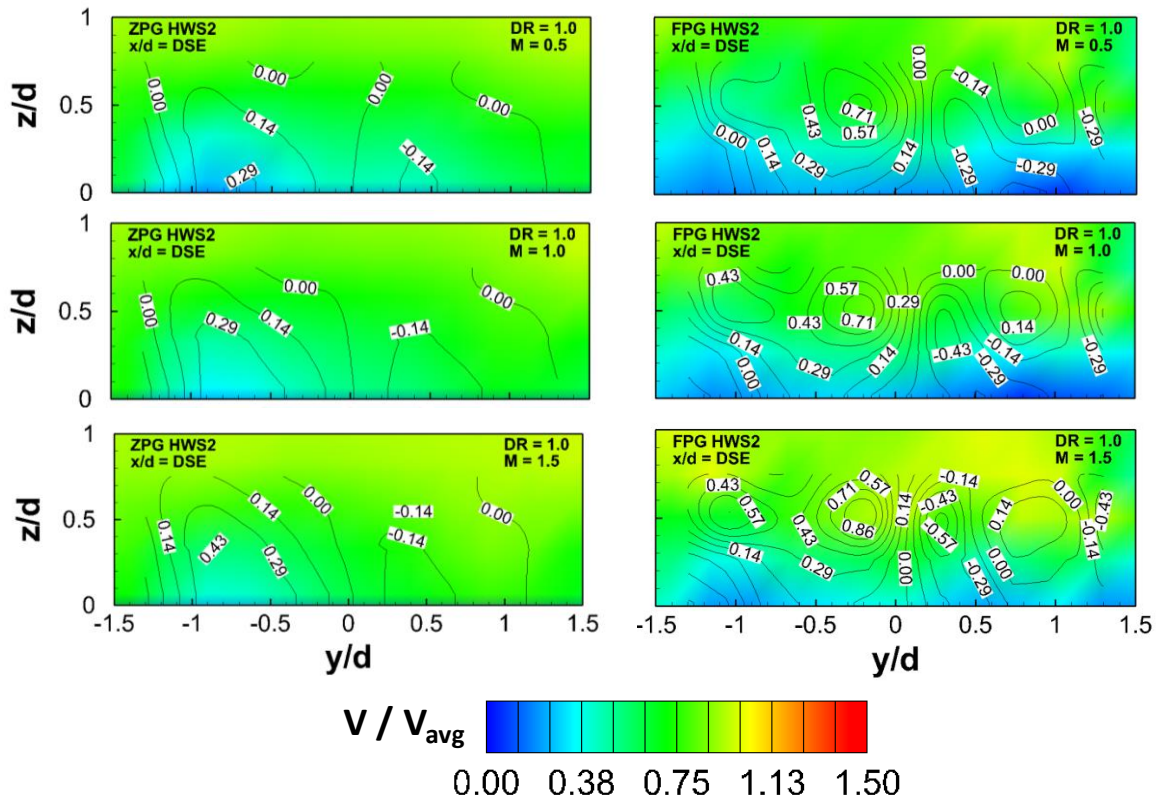


Figure 8.53: Effect of blowing ratio and freestream acceleration for Honeywell Shaped 2 hole ( $x/d = DSE$ ,  $DR = 1.0$ )

raised lateral average effectiveness within the hole for FPG flows. Increasing the lateral spread allows the coolant to interact with the contours and generate these additional secondary flows. The additional secondary flows do fulfill their intended purpose of spreading the coolant throughout the hole, but by the time the coolant reaches the downstream edge, that effect is mitigated by the increased coolant liftoff caused by increased vorticity magnitude. *Figure 8.70* shows that the film cooling effectiveness is nearly identical for FPG and ZPG flows by the downstream edge, which shows the tradeoff of increasing the spread of the coolant with additional secondary flows, as the CVP is strengthened and increases mainstream mixing.

The effect of density ratio on the DF1 shape is shown in *Figure 8.71*. The PSP results have previously shown that the effectiveness within the hole was moderately

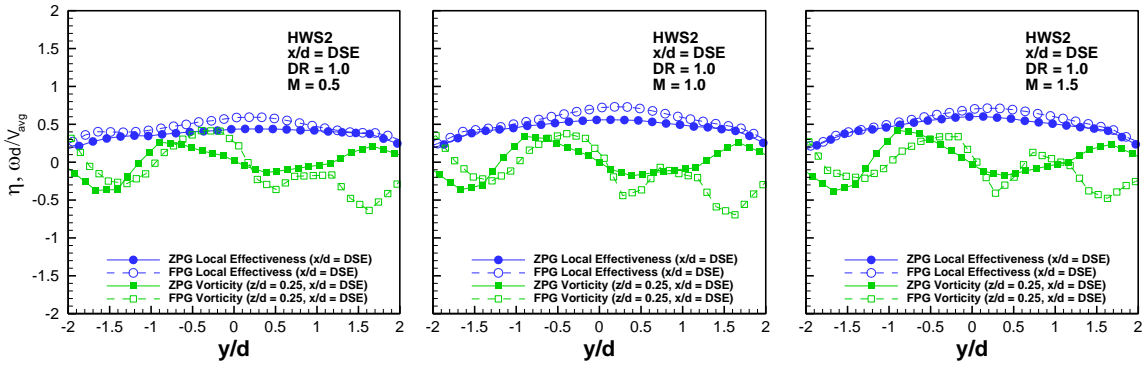


Figure 8.54: Influence of flow vorticity on surface film cooling effectiveness from Honeywell Shaped 2 ( $x/d = DSE$ ,  $DR = 1.0$ )

increased with density ratio, but that the effectiveness downstream was reduced with density ratio. The ZPG results show no jet or significant vorticity, so no effect of density ratio on the flow field can be shown. However, for the FPG, increasing the density slows down the coolant velocity, which keeps it from forming the jet present for  $DR = 1.0$  but not  $DR = 3.0$ . Also, the vorticity magnitude is slightly reduced for increasing density ratio as the slower coolant does not create as significant secondary flows. *Figure 8.72* shows that despite the strong differences in vorticity, the effectiveness results at  $DR = 3.0$  are not affected by the PG at the DSE for the same reasons previously mentioned. The coolant is more spread out but also lifts more off of the surface from the increasing magnitude of the CVP.

*Figure 8.73* shows the development of the secondary flows within the DF1 hole. The ZPG results show that the CVP is stronger at  $x/d = 0$ , but gradually reduces in strength and width at the coolant travels through the hole. This is caused by the lack of spread and lack of interaction with the duckfoot contours under the ZPG flow. However, for the FPG, the development of secondary flows is much more interesting. At  $x/d = 0$ , there is no duckfoot contour to develop further secondary flows, so the vorticity contours

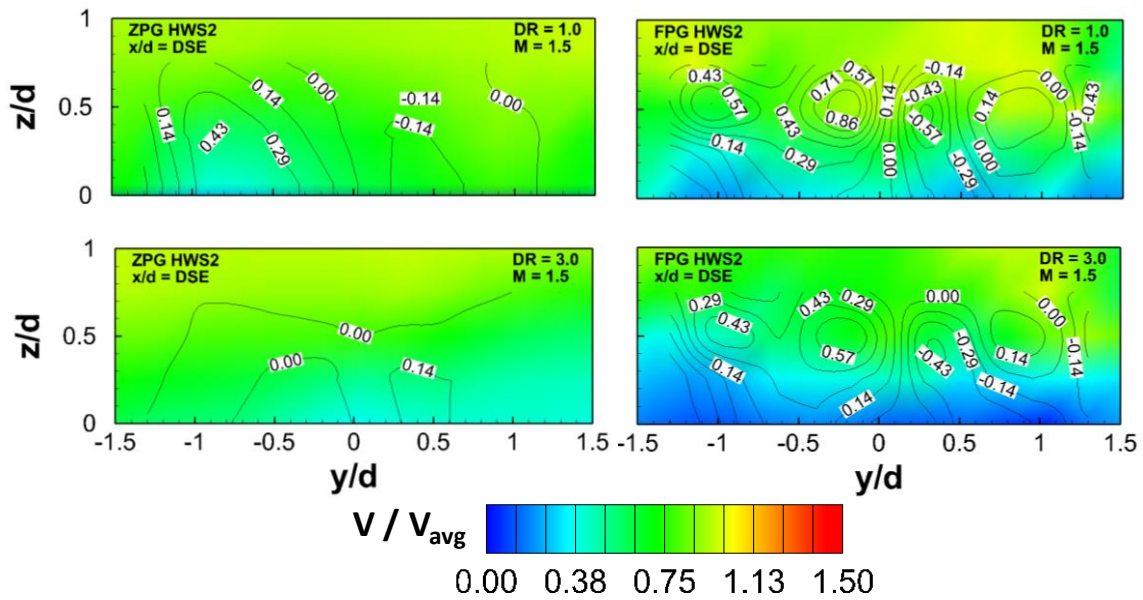


Figure 8.55: Effect of density ratio and freestream acceleration for Honeywell Shaped 2 holes ( $x/d = DSE$ ,  $M = 1.5$ )

look roughly similar to the HWS1 vorticity contours. However, as the duckfoot contours begin to affect the formation of additional vortices at  $x/d = 3$ , the CVP is pushed more towards the center as opposing vortices form on the edges of the hole. *Figure 8.74* shows how the formation of secondary flows does not have a strong impact on the cooling effectiveness because it simultaneously increases the spread and liftoff of the coolant. Furthermore, the FPG helps to mitigate the increased liftoff from increased vorticity generation due to the thinner boundary layer.

The effect of the duckfoot design on the flow field can be most clearly understood by comparing the velocity and vorticity distributions directly with the HWS1 hole, which has similar dimensions with the exception of the duckfoot outlet. *Figure 8.75* shows this direct comparison at the DSE and  $DR = 1.0$  for the range of  $M$  investigated. The secondary flows that exist for the DF1 geometry but do not exist for the HWS1 geometry can be clearly seen at the DSE for all blowing ratios. The direction of rotation of the CVP

is reversed for the DF1 geometry compared to the HWS1 geometry. This difference is caused by the anti-kidney vortices that are generated by the duckfoot toes. The anti-kidney vortices are beneficial for film cooling and push the jet towards the surface. Unfortunately, additional secondary flows are generated at the outer edges of the hole, and the increased vorticity increases mixing with the mainstream. *Figure 8.76* shows that at the DSE, the increased vorticity is more significant, resulting in reduced effectiveness for the DF1 geometry as a result of the additional secondary flows beyond the CVP that are generated by the duckfoot contour.

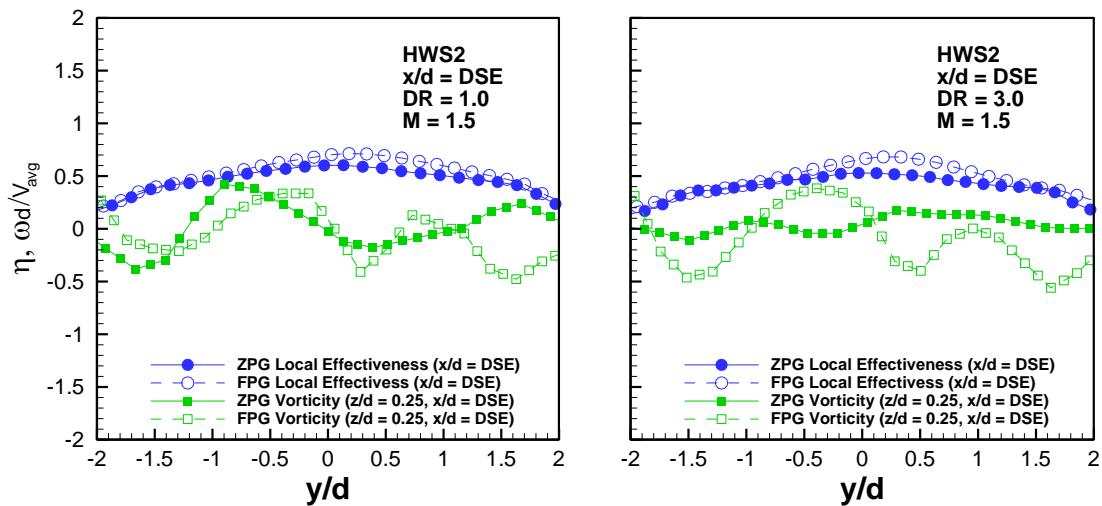


Figure 8.56: Influence of flow vorticity on surface film cooling effectiveness from Honeywell Shaped 2 holes ( $M = 1.5$ ,  $DR = 1.0$ )

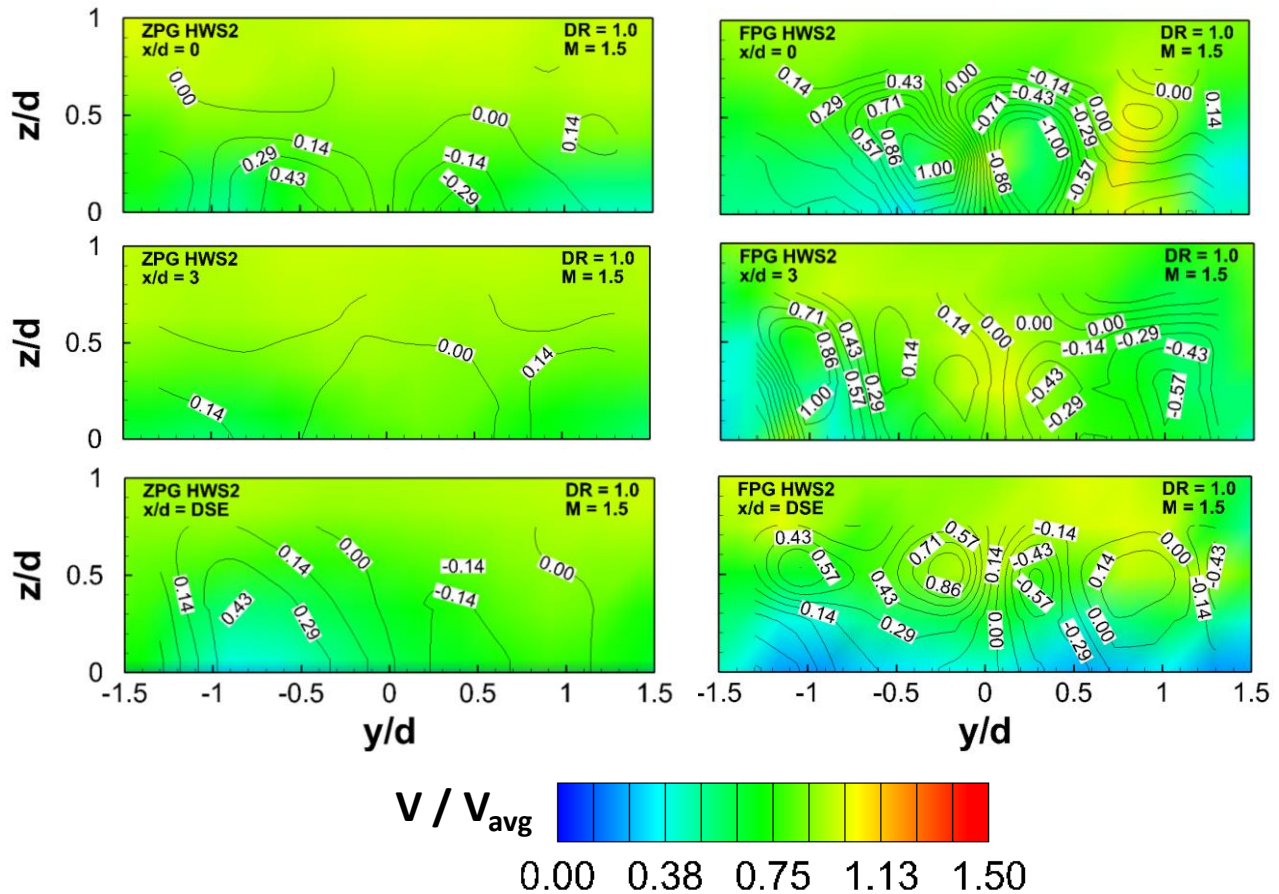


Figure 8.57: Effect of downstream location and freestream acceleration for Honeywell Shaped 2 ( $M = 1.5$ ,  $DR = 1.0$ )

#### *Duckfoot 2 PSP Results*

The Duckfoot 2 geometry is similar to the Duckfoot 1 geometry, with the same fundamental idea of having the two contours branching off to the side similar to webbed duck toes, but with a racetrack inlet just like HWS2. The geometry will be compared to HWS2 to show the effect of the duckfoot outlet over the regular shaped outlet with the same racetrack inlet. The shape will also be compared to DF1 to demonstrate the effect of adding a racetrack inlet as opposed to the standard round inlet.

The film cooling effectiveness distributions are presented as a function of blowing ratio in *Figure 8.77* with a constant  $DR$  of 1.0. The effect of blowing ratio can be clearly

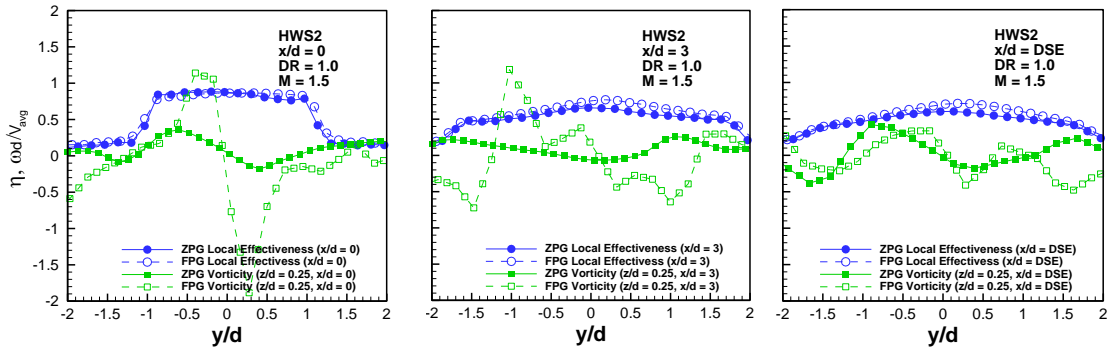


Figure 8.58: Influence of flow vorticity on surface film cooling effectiveness from Honeywell Shaped 2 holes ( $M = 1.5$ ,  $DR = 1.0$ )

seen as the coolant stays attached significantly longer at higher blowing ratios. As the blowing ratio increases, the coolant spreads less throughout the hole, but makes it much farther downstream. This relationship is clearly shown in *Figure 8.78*, which shows the centerline and laterally averaged effectiveness of the DF2 geometry as a function of blowing ratio. Inside of the hole, the lateral average is higher for  $M = 0.5$  and  $M = 1.0$ , but downstream of the hole the lateral average effectiveness is higher for  $M = 1.5$  and  $M = 1.0$ . At  $M = 0.5$ , the coolant is traveling slowly so it diffuses into the toes of the duckfoot, but the interactions with the contours and the slow coolant momentum cause the coolant to get swept into the mainstream. For  $M = 1.5$ , the coolant velocity is so high that it never diffuses outside to the middle and stays attached to the center toe. This leads to improved downstream cooling along the centerline.  $M = 1.0$  is slow enough to diffuse into the duck feet almost as well as  $M = 0.5$ , but also has enough velocity to travel downstream like  $M = 1.5$ . The lateral average downstream for  $M = 1.0$  compared to  $M = 1.5$  is almost the same, which means that the spread of coolant is better for  $M = 1.0$ , as the centerline is higher for  $M = 1.5$ .

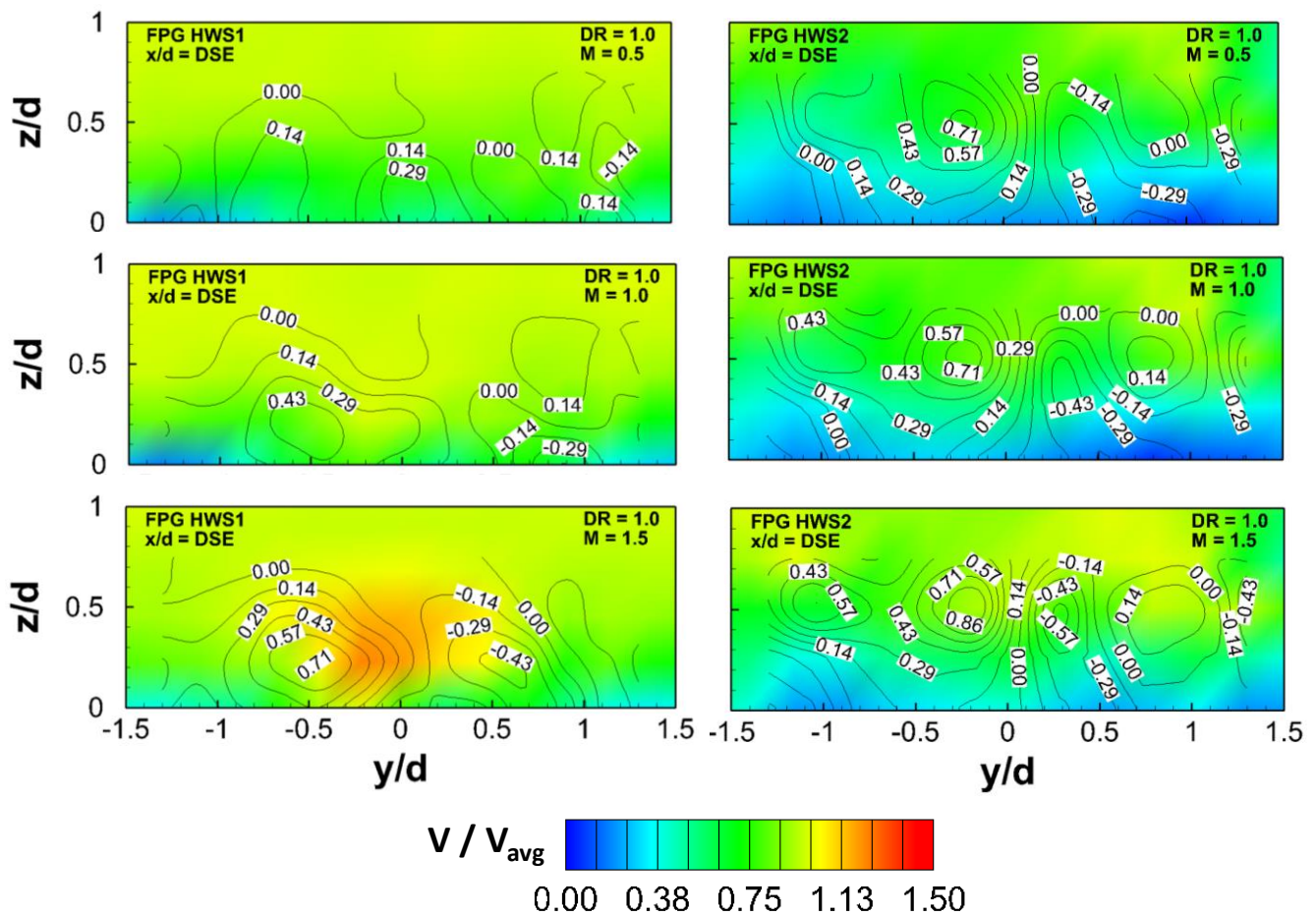


Figure 8.59: Comparison of HWS1 and HWS2 holes for varying blowing ratio ( $x/d = DSE$ ,  $DR = 1.0$ , FPG)

The effect of increasing density ratio from 1.0 to 3.0 is shown in *Figure 8.79*, with  $M = 1.5$ . The lateral spread of the coolant within the hole is increased, but the downstream effectiveness is substantially reduced. Similarly to the blowing ratio effect, the DF2 geometry requires high velocity coolant to not diffuse too much into the duck feet. Diffusing into the duck feet helps the spread of coolant within the hole, but also reduced the downstream effectiveness. The density ratio trends are further illustrated by *Figure 8.80*, which shows the clear improvement of coolant spread within the hole, but ratically reduced effectiveness downstream of the hole with increasing DR. Coolant

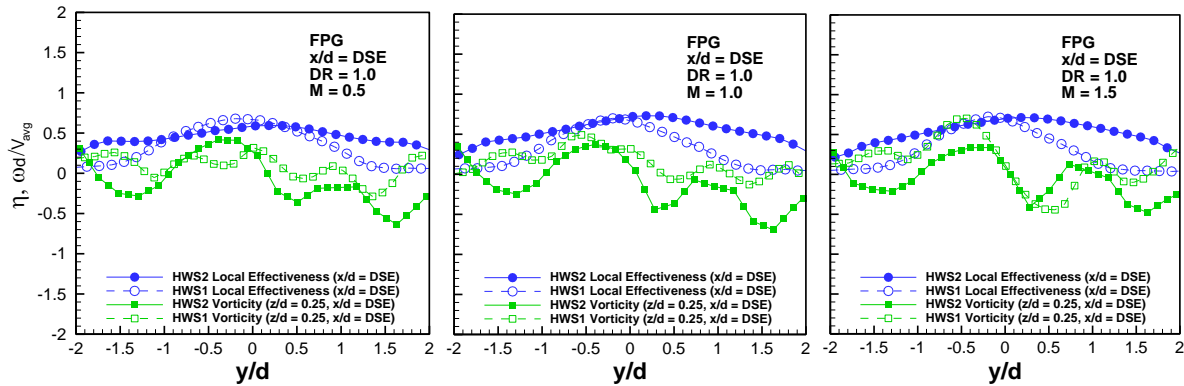


Figure 8.60: Comparison of HWS1 and HWS2 holes through the influence of flow vorticity on surface film cooling effectiveness ( $x/d = DSE$ ,  $DR = 1.0$ , FPG)

spreading into the side contours of the DF2 geometry is actually bad for downstream effectiveness.

The effect of the FPG on the DF2 film cooling effectiveness is shown in *Figure 8.81* for  $DR = 1.0$  and  $3.0$  and  $M = 0.5$  and  $1.5$ . The pressure gradient causes the jet to stay attached to the surface longer. This effect holds for all cases, but can be most clearly seen for  $DR = 3.0$  and  $M = 0.5$ . The coolant is moving so slow that it never makes it to the downstream edge of the hole before being swept into the mainstream. The coolant does travel slightly farther for the FPG case though, because the reduced boundary layer thickness of the FPG increases the resistance to the coolant separation. The overall, area averaged film cooling effectiveness shown in *Figure 8.82* shows that the FPG causes clear improvement over the ZPG, especially at lower momentum flux ratios. It is not coincidental that the only other hole to see significant improvement from the FPG was the other racetrack hole (HWS2). HWS2 and DF2 are also both significantly longer than the other hole geometries investigated. It is likely that the same effect previously discussed for the HWS2 improvement due to FPG also explains the improvement in the

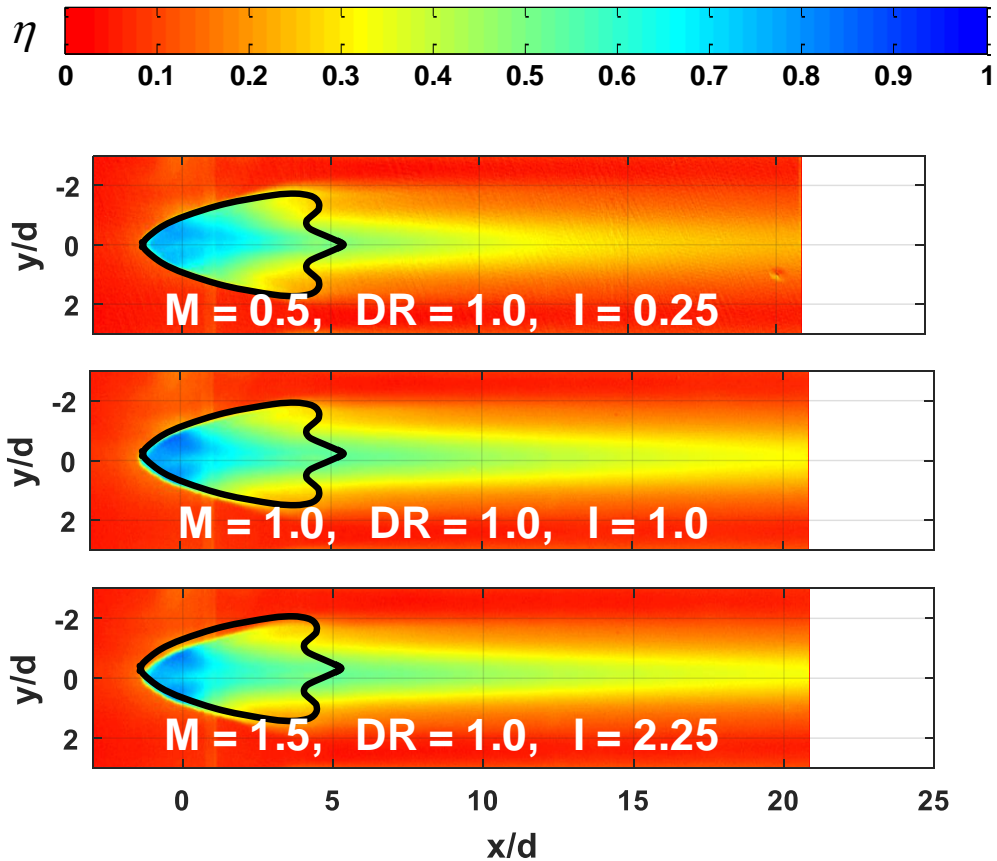


Figure 8.61: Duckfoot 1 hole film cooling effectiveness distribution under a favorable pressure gradient: blowing ratio effect

DF2 hole. The FPG effects the film cooling most significantly in protecting the coolant from the mainstream while the coolant is in the hole. Once the coolant is past the hole, the boundary layer is much thicker due to the coolant blowing into it, so the thinner boundary layer caused by the FPG would likely be irrelevant. The longer hole then allows the improvement due to the FPG to have a more significant effect. Furthermore, the FPG helps the racetrack shaped inlet further spread the coolant and keep it closer to the surface, as the FPG and racetrack shaped inlet have the same fundamental effects and work well in tandem.

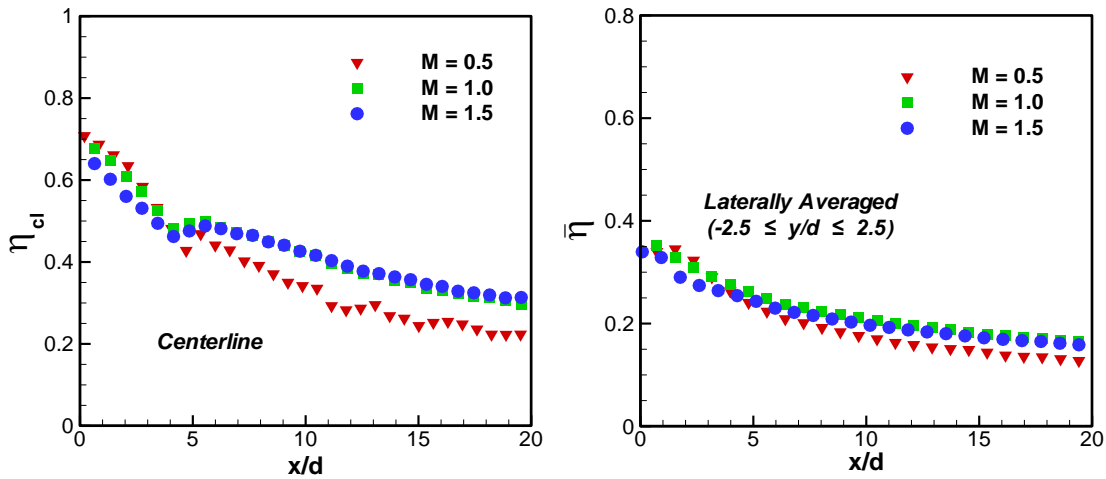


Figure 8.62: Duckfoot 1 centerline and lateral average film cooling effectiveness under a favorable pressure gradient: blowing ratio effect

The DF2 geometry is compared directly to the DF1 geometry to show the effect of the racetrack shaped inlet in the same way that the HWS2 was compared to the HWS1. *Figure 8.83* clearly shows the improved cooling effectiveness caused by the racetrack inlet. The effectiveness is especially increased within the hole ( $x/d < 5$ ) for all flow conditions, but also increased downstream by approximately 50% for  $DR = 1.0$ . The increased effectiveness is caused by the racetrack inlet increasing the spread of the coolant and keeping it closer to the surface of the hole. This occurs because the height of the hole inlet is reduced, which causes the center of the coolant jet to be closer to the surface and the lateral diffusion of the coolant to be increased. *Figure 8.84* also shows how the racetrack shaped inlet increases the overall average by as much as 50% for high momentum flux ratios, but the effect is less significant at lower momentum flux ratios because increasing the spread of the coolant just results in lower velocity coolant that does not have sufficient momentum to provide downstream coverage.

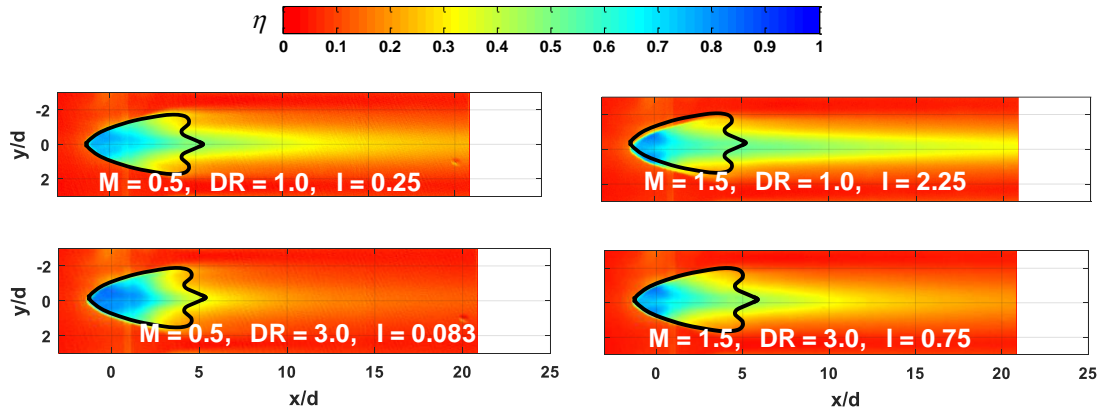


Figure 8.63: Duckfoot 1 hole film cooling effectiveness distribution under a favorable pressure gradient: density ratio effect

The effect of the duckfoot geometry is also investigated by comparing the DF2 geometry to the HWS2 geometry similarly to the way the DF1 and HWS1 geometries were compared. *Figure 8.85* shows that while the two racetrack geometries are better than the rest, the HWS2 actually outperforms the DF2. It was thought that the DF2 geometry would increase the cooling effectiveness by combining the racetrack inlet with the generation of additional secondary vortices to counteract the CVP, but the HWS2 performed better without the additional contours within the hole. The geometries performed similarly for  $M = 0.5$ , but the improvement offered by HWS2 can be seen most clearly at  $M = 1.5$ . The higher blowing ratio coolant was able to stay more closely attached to the surface for HWS2 because the area increase slowed the coolant velocity to the ideal range, while the duckfoot geometry reduced the coolant velocity too much. This caused the coolant that made it downstream of the DF2 hole to be more easily swept into the mainstream compared with the HWS2 hole which had higher velocity coolant. *Figure 8.86* shows that the overall effectiveness of the HWS2 hole was about 20% higher for the range of flow conditions investigated.

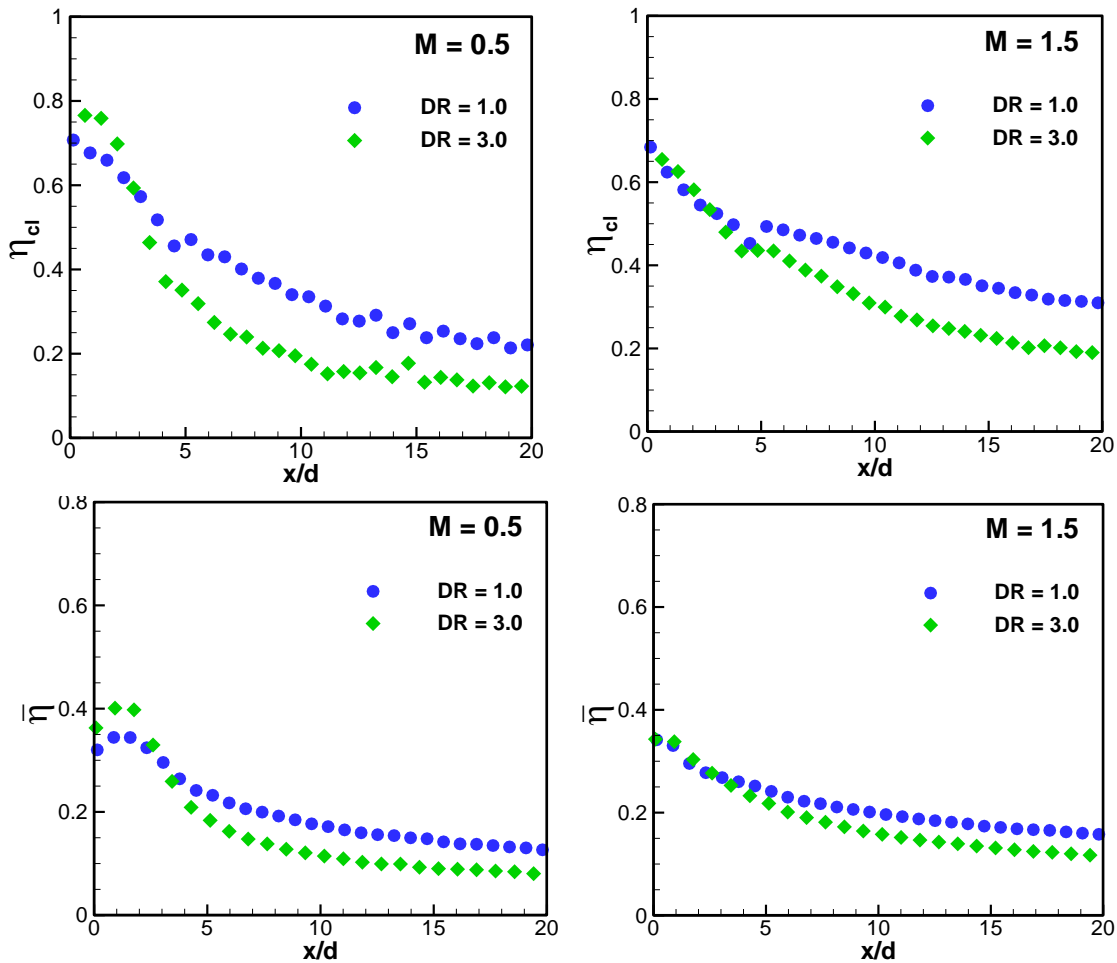


Figure 8.64: Duckfoot 1 hole centerline and lateral average film cooling effectiveness under a favorable pressure gradient: density ratio effect

### Duckfoot 2 S-PIV Results

The PSP results showed that the Duckfoot 2 film cooling geometry performed significantly better in the presence of the favorable pressure gradient. The S-PIV results are used to clarify why the DF2 geometry performs better with the thinner boundary layer caused by favorable pressure gradient flow.

The effect of blowing ratio is shown for both ZPG and FPG flows at the downstream edge of the Duckfoot 2 hole in *Figure 8.87*, where the density ratio is fixed

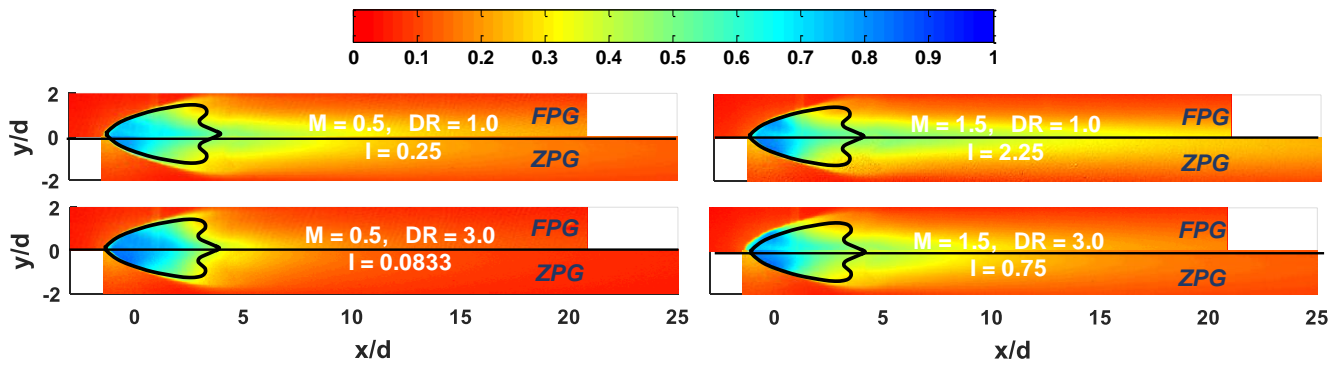


Figure 8.65: Duckfoot 1 film cooling effectiveness distributions: FPG effect

at  $DR = 1.0$ . While the ZPG showed a limited blowing ratio impact at  $DR = 1.0$ , the FPG results show that the vorticity is strongly impacted by blowing ratio. The two lower blowing ratios have significantly increased maximum vorticity magnitude. At  $M = 1.5$ , the vorticity magnitude is small for both ZPG and FPG flows. At all blowing ratios for the FPG case, it can be clearly seen that there are secondary flows generated by the duckfoot contours that cause the development of secondary flows rotating counter to the CVP on the outer edges of the hole. The secondary flows form for the FPG case but not the ZPG case for the same reason mentioned for the DF1 geometry. The FPG spreads the coolant throughout the hole and helps it stay attached to the contours, resulting in increased vortex generation. The vorticity is reduced for  $M = 1.5$  because the coolant is able to maintain sufficient velocity to prevent diffusion into the duckfoot contours.

*Figure 8.88* shows the vorticity and film cooling effectiveness at the downstream edge for the ZPG and FPG cases at  $DR = 1.0$  for the three blowing ratios investigated. The effectiveness results show the impact of the FPG on film cooling effectiveness at high blowing ratios is minimal, but at  $M = 0.5$  it can be clearly seen that the FPG helps the spread of the data. At  $M = 0.5$ , the coolant does not have sufficient momentum to stay

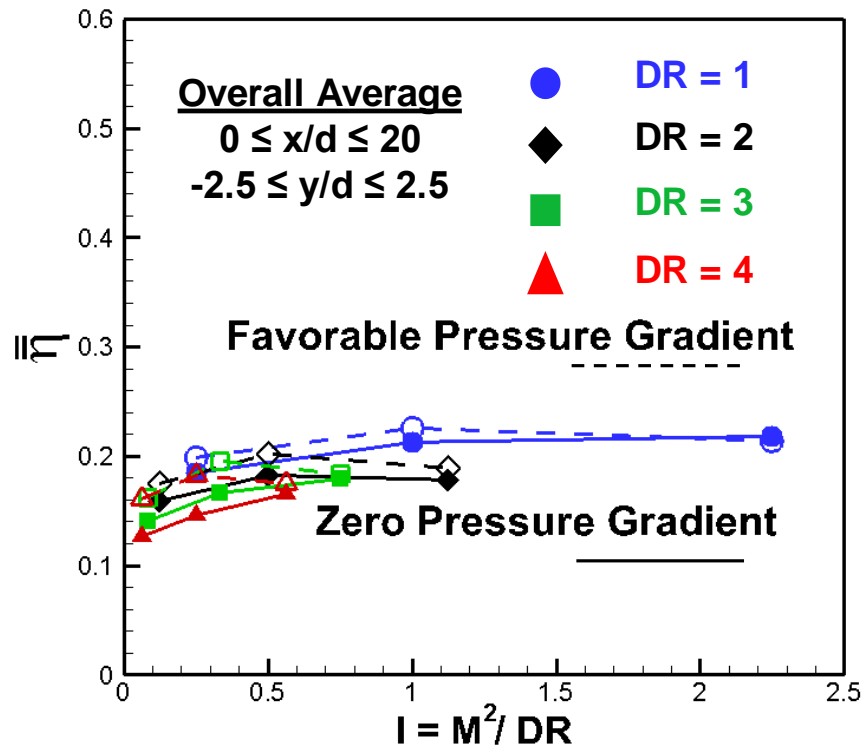


Figure 8.66: Duckfoot 1 overall average film cooling effectiveness: FPG effect

attached to the contours of the sides of the Duckfoot 2 hole. However, when the mainstream flow is accelerating, the boundary layer is thinner, which means that the coolant is pushed closer to the surface and the spread is increased. At low blowing ratios, where the coolant is moving extremely slowly with the large area expansion and the increased mainstream speed at the downstream edge of Duckfoot geometry, this effect from the FPG is significant enough to help the coolant stay attached in the outside portions of the hole. For the ZPG case, the vorticity at the outside of the hole is nearly zero at all blowing ratios, but for the FPG, the vorticity magnitude is significantly increased near the edges of the holes because the coolant is spreading out more to interact with the contours of the edges of the Duckfoot 2 geometry and increasing secondary vortex generation. The vorticity caused by the center of the Duckfoot 2 geometry is

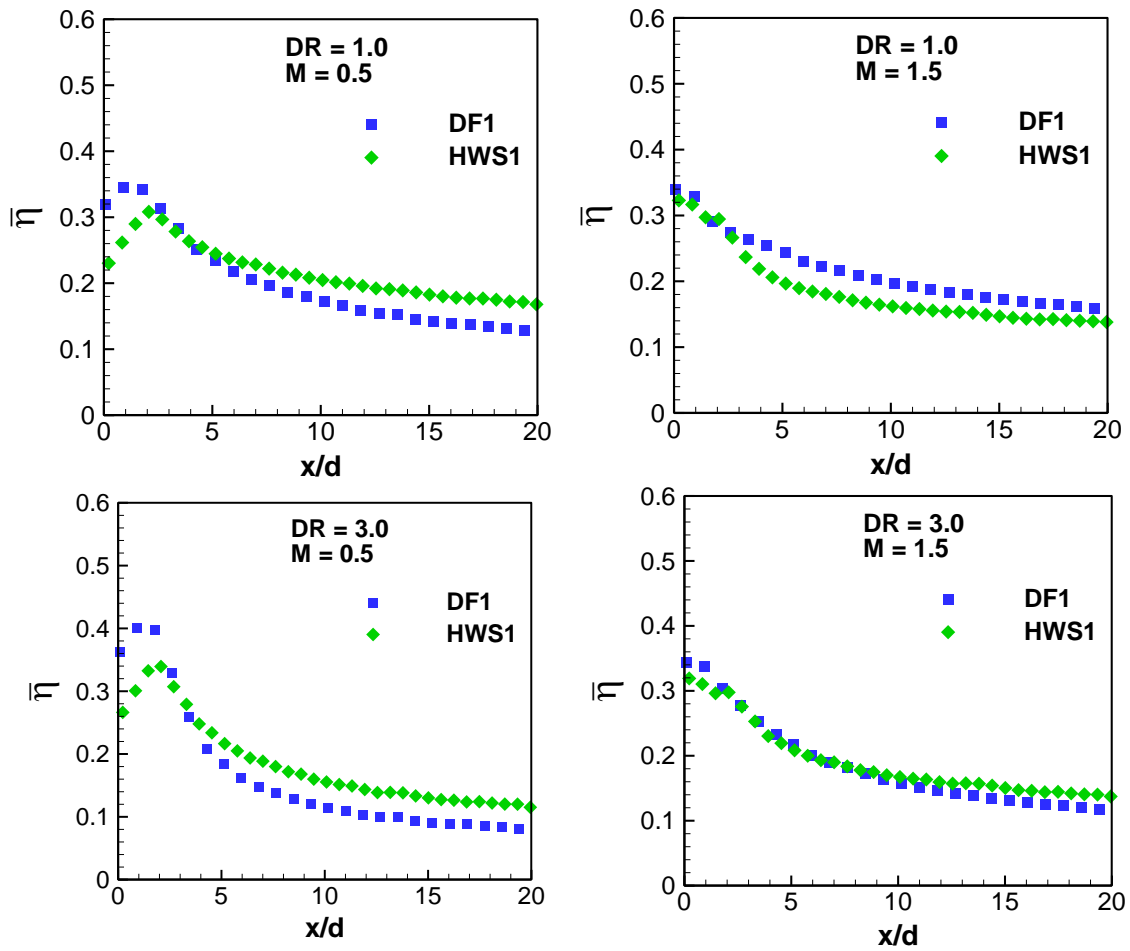


Figure 8.67: Favorable pressure gradient laterally averaged film cooling effectiveness: Duckfoot outlet effect

relatively consistent regardless of pressure gradient, because the FPG is more impactful on the spread of the coolant, especially at  $M = 0.5$ .

The effect of increasing the density ratio from  $DR = 1.0$  to  $3.0$  for the Duckfoot 2 geometry is presented for the FPG and ZPG cases in *Figure 8.89*. The data is evaluated at the downstream edge at a constant blowing ratio of  $M = 0.5$ . Increasing the density ratio for the ZPG case does not have a significant effect on the flow field at the downstream edge. The vorticity is slightly increased because increasing density ratio increases the spread of the coolant and reduces coolant velocity which allows more time for vorticity to

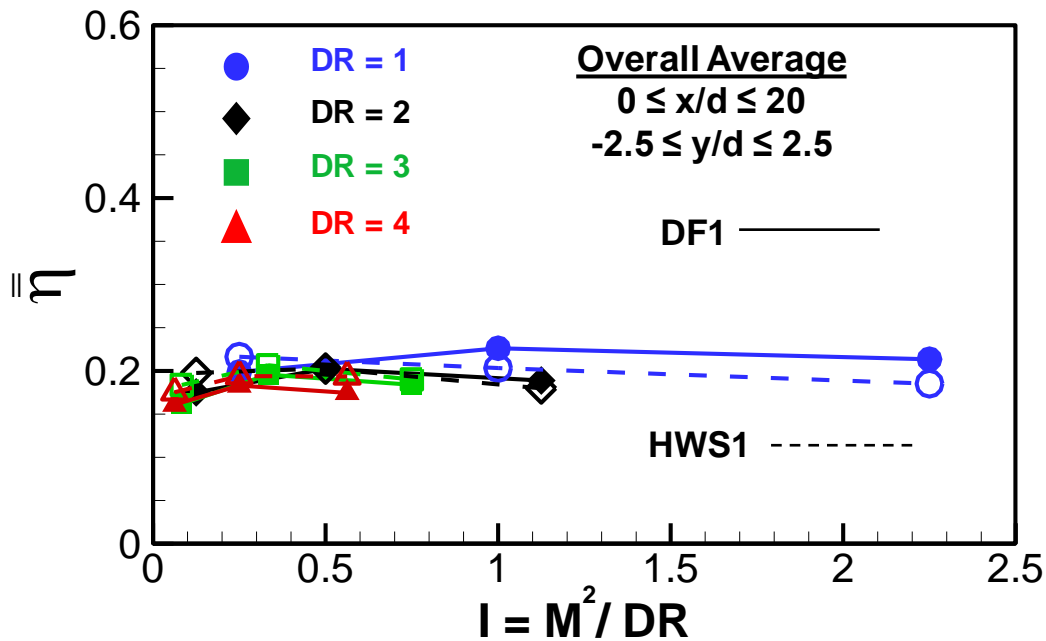


Figure 8.68: Comparison of HWS1 and DF1 with overall average film cooling effectiveness

strengthen. However, for the FPG case, increasing the DR from 1.0 to 3.0 has a more significant impact on the film cooling flow field. The heavier and slower coolant is spread more widely by the FPG, which increases the generation of secondary flows as more coolant is spread to the duckfoot contours on the outside of the coolant hole. *Figure 8.90* shows that the increased vorticity generation at DR = 3.0 for the FPG does not have a significant impact on film cooling effectiveness at the DSE because the increased lateral spread from the vorticity is counteracted by the increased mixing with the mainstream.

*Figure 8.91* shows how the flow field changes for  $x/d = 0, 3,$  and  $5.7$  (DSE). The results are presented for the FPG and ZPG cases for DR = 1.0 and M = 1.5. For DR = 1.0 and M = 1.5, there is little difference in the flow fields at the three planes investigated. Furthermore, the impact of the FPG is limited for results at DR = 1.0 and M = 1.5. *Figure*

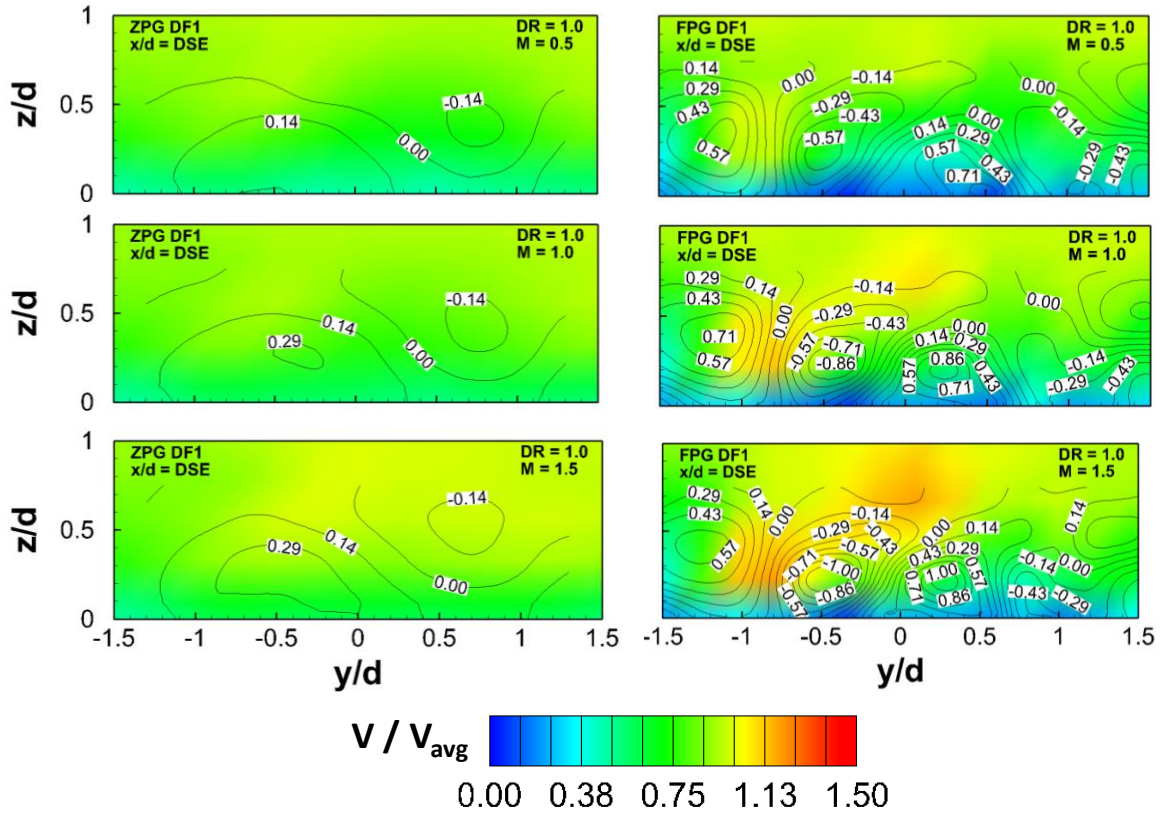


Figure 8.69: Effect of blowing ratio and freestream acceleration for Duckfoot 1 hole ( $x/d = DSE$ ,  $DR = 1.0$ )

8.92 shows that the film cooling effectiveness at the three planes investigated is almost completely independent of the presence of the favorable pressure gradient. The vorticity is similar for the FPG and ZPG cases, and with limited jet detachment from the surface, the thinner boundary layer caused by the FPG has limited impact on the interaction between the coolant and mainstream.

The effect of the racetrack shaped inlet is investigated further by comparing the velocity and vorticity distributions for the DF2 and DF1 holes as shown in *Figure 8.93*. It can be seen that jet separation is increased for the DF1 hole, as the racetrack inlet keeps the coolant more closely attached to the surface of the hole. Furthermore, the formation of additional secondary flows is present in both the DF2 and DF1 geometries, but the

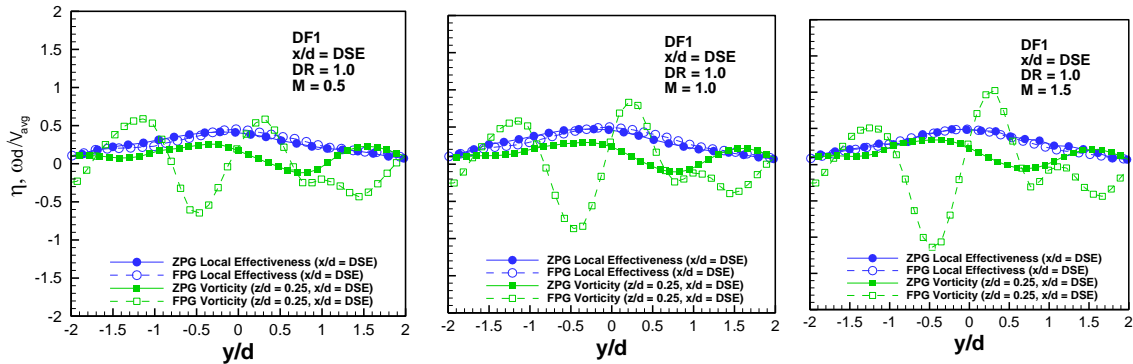


Figure 8.70: Influence of flow vorticity on surface film cooling effectiveness from Duckfoot 1 ( $x/d = \text{DSE}$ ,  $\text{DR} = 1.0$ )

secondary flows are stronger for the DF1 geometry. This is caused by the increased width of the DF2 hole as the hole expands from the racetrack shape. The sidewalls and duckfoot contours are further from the center so there is less coolant interaction compared to the DF1 hole. *Figure 8.94* shows that these effects significantly increase the film cooling effectiveness at the DSE for the DF2 hole. The reduction in the magnitude of the vorticity generated with the additional secondary flows helps to keep the coolant attached along with the improvement offered by the racetrack inlet shape.

The effect of the duckfoot shape is further considered by directly comparing the velocity and vorticity contours for the DF2 and HWS2 geometries. The PSP showed that the HWS2 geometry outperformed the DF2 geometry, and this is likely caused by the increased coolant velocity at the DSE of the HWS2 geometry. This effect cannot be seen with S-PIV as the coolant velocity would be well below the mainstream velocity, but *Figure 8.95* does show that the magnitude of vorticity is increased for HWS2, while the spread of vorticity is increased with DF2. *Figure 8.96* shows that the differences in vorticity do not result in significant changes in film cooling effectiveness at the DSE, but

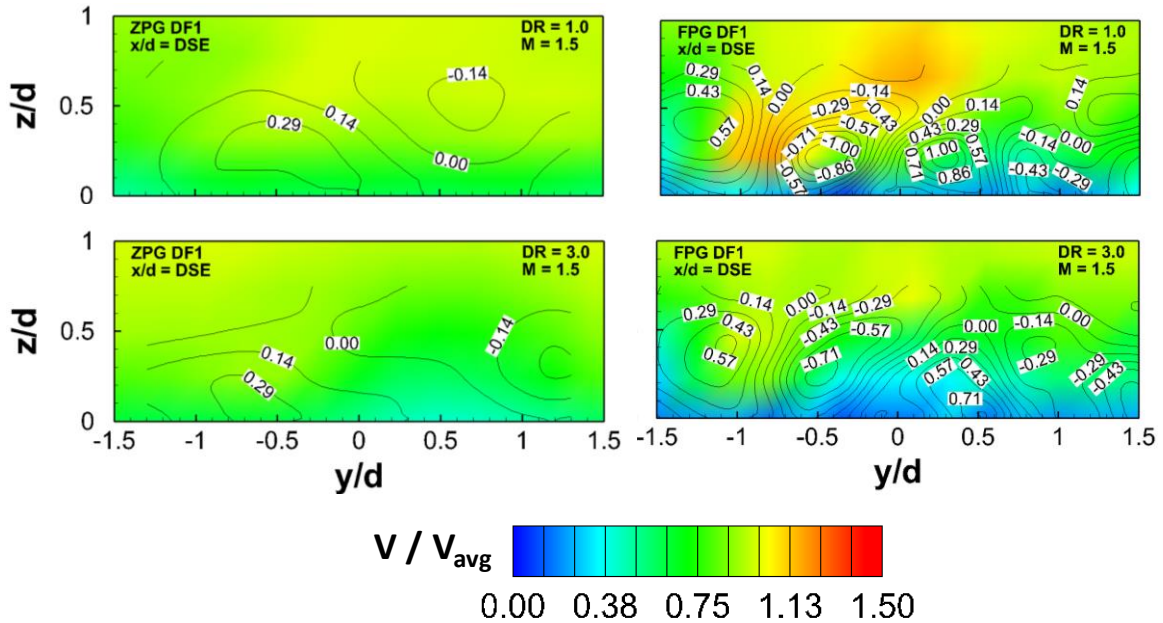


Figure 8.71: Effect of density ratio and freestream acceleration for Duckfoot 1 holes ( $x/d = DSE$ ,  $M = 1.5$ )

the lateral spread of coolant is slightly improved for HWS2. The end result is that HWS2 is a slightly more effect cooling geometry for the flow conditions investigated, and both racetrack shaped inlet holes result in significant improvements over the other shaped holes studied.

### *Summary of Effects*

The PSP and S-PIV techniques have been used to obtain film cooling effectiveness, velocity, and vorticity distributions for round, laidback fanshaped, Honeywell Shaped 1, Honeywell Shaped 2, Duckfoot 1, and Duckfoot 2 film cooling geometries. The distributions were obtained for FPG flow and compared to Watson [91] to determine the effect of mainstream acceleration. The effect of hole shape and mainstream acceleration were investigated for density ratios of  $DR = 1.0$  and  $3.0$ , and blowing ratios of  $M = 0.5$ ,  $1.0$ , and  $1.5$ . The S-PIV was performed at  $x/d = 0, 3$ , and the

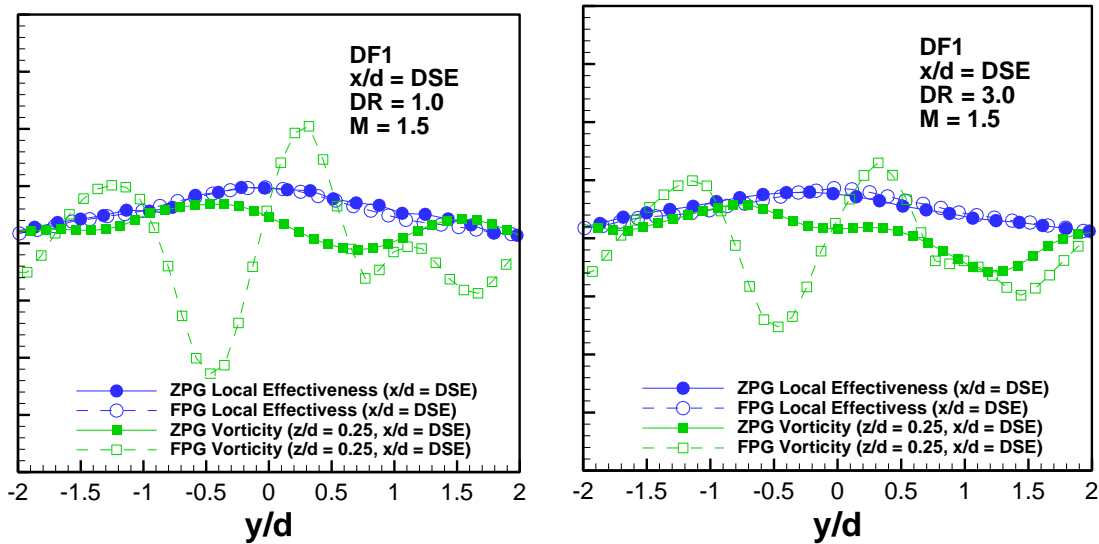


Figure 8.72: Influence of flow vorticity on surface film cooling effectiveness from Duckfoot 1 holes ( $M = 1.5$ ,  $DR = 1.0$ )

DSE of each geometry to evaluate the development of secondary flows. All of this data was coupled together to explain the fundamental, physical effects involved in these film cooling parameters.

To determine the effect of hole shape, the round and laidback, fanshaped holes were investigated to determine a baseline. The baseline shaped hole significantly outperformed the round hole as expected from film cooling literature. The four advanced shapes were then compared to the baseline shaped to evaluate the effect of increasing the hole exit area further, changing the inlet shape, and adding duckfoot shaped contours to the outlet area. The HWS1 geometry had increased lateral and laidback expansion angles compared to the baseline, and it was shown that there was no significant difference from the slightly increased hole area. The increased exit area slightly reduced jet separation and vorticity magnitude, but the effect on overall average film cooling effectiveness was negligible.

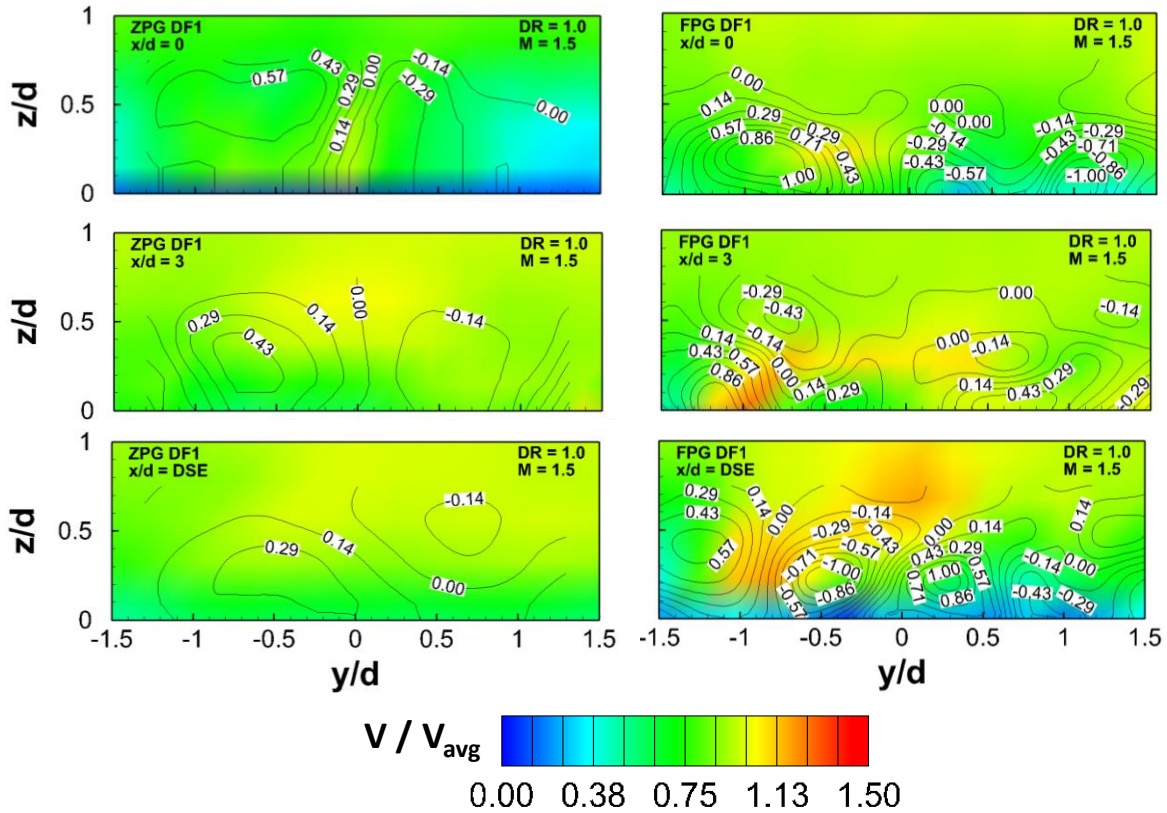


Figure 8.73: Effect of downstream location and freestream acceleration for Duckfoot 1 ( $M = 1.5$ ,  $DR = 1.0$ )

The effect of changing the inlet shape to a racetrack shape was studied with the HWS2 and DF2 holes. It was determined that the racetrack inlet causes significant improvement in film cooling effectiveness. The HWS2 and DF2 holes had the two highest overall, area averaged effectiveness values. The racetrack shape pushed the coolant closer to the surface of the hole and helped the jet spread over the surface.

The effect of adding duckfoot shaped contours to the hole outlet area was also studied with the DF1 and DF2 hole geometries. It was expected that the duckfoot contours would create some beneficial secondary flows to counteract the CVP that results in increased mixing. The duckfoot geometry did generate secondary flows that were simultaneously beneficial and harmful. The DF1 and DF2 geometries had increased

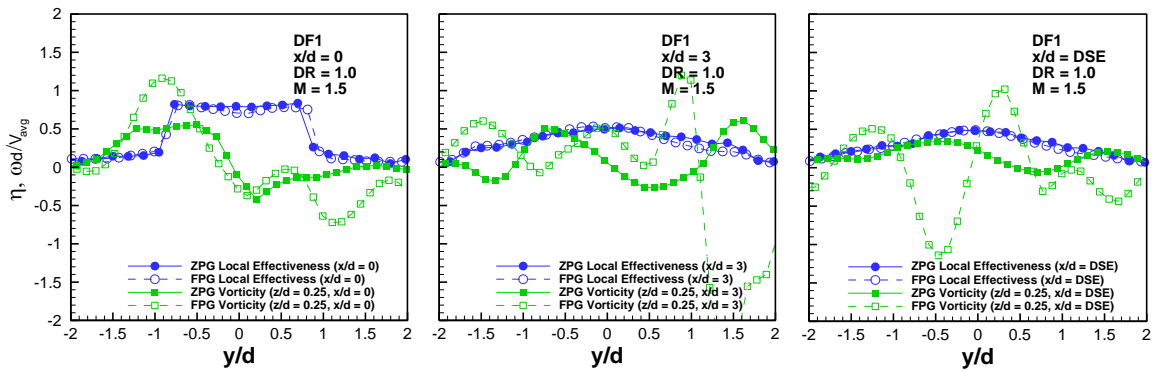


Figure 8.74: Influence of flow vorticity on surface film cooling effectiveness from Duckfoot 1 holes ( $M = 1.5$ ,  $DR = 1.0$ )

lateral spread of coolant within the hole, but the increased vorticity also increased coolant liftoff, and the net result showed that DF1 and HWS1 had nearly identical effectiveness distributions. The additional complexity of the duckfoot did not offer significant improvements to the film cooling effectiveness.

The effect of adding a favorable pressure gradient was studied for all of the shapes and flow conditions mentioned previously. The fundamental effect of the pressure gradient was consistent across all shapes and flow conditions. The accelerating mainstream flow causes the boundary layer to become thinner. The boundary layer offers less resistance to jet separation within the hole, so the thinner boundary layer would prevent jet separation. As the jet is pushed closer to the surface, it has to spread for conservation of mass. The impact of this effect varied from shape to shape. For the racetrack inlet shapes, the film cooling effectiveness was significantly improved for the flow conditions investigated. The overall average was improved by as much as 50% by the FPG for the racetrack shaped inlet holes. This occurred because the racetrack inlet and FPG have the same effects so they just compound each other. Furthermore, the

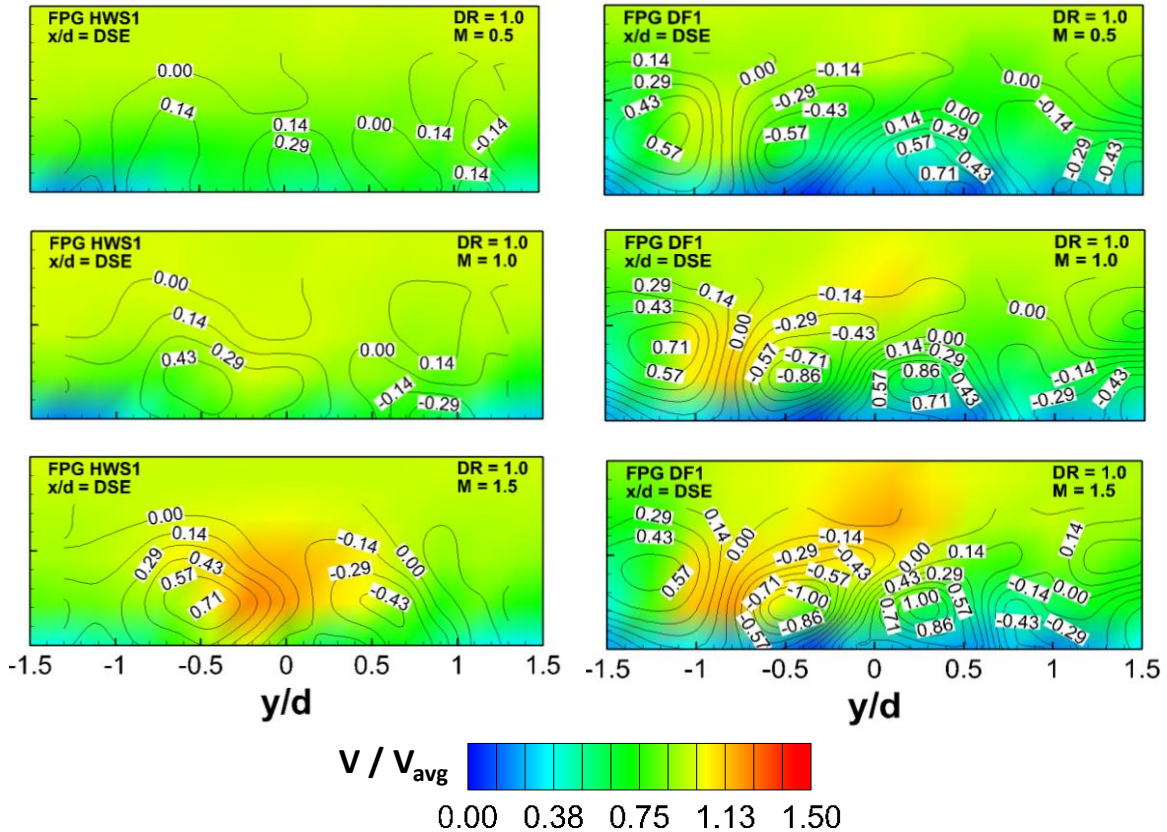


Figure 8.75: Comparison of HWS1 and DF1 holes for varying blowing ratio ( $x/d = DSE$ ,  $DR = 1.0$ , FPG)

racetrack shaped inlet holes are longer than the other film cooling holes, which makes the effect of the FPG more important for protecting the longer hole. For the other shapes, the film cooling effectiveness was raised by less than 10%, or completely unaffected. This occurs because the spreading of the CVP caused by the FPG does result in increased interaction between the walls of the hole and the jet, causing increased vorticity magnitude and mixing. Despite the FPG reducing jet separation, the film cooling effectiveness for the non-racetrack shaped inlet holes was not significantly improved for any flow condition.

The effect of blowing ratio was investigated for every hole shape and mainstream condition. The impact of blowing ratio is completely different from one hole to the next,

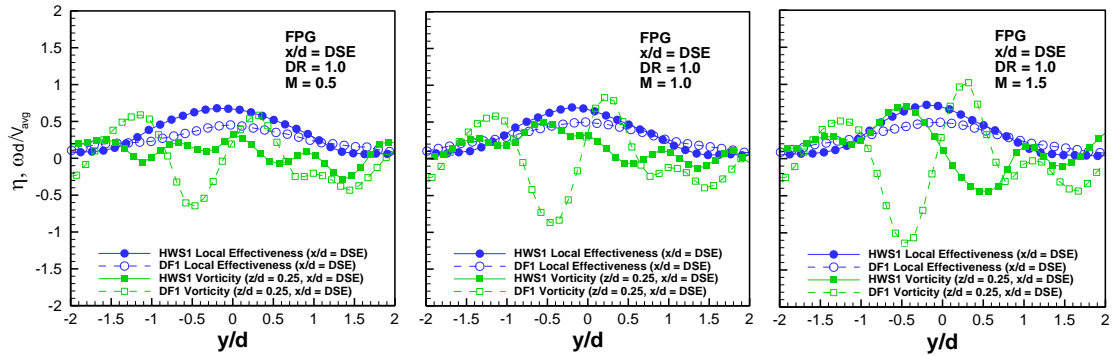


Figure 8.76: Comparison of HWS1 and DF1 holes through the influence of flow vorticity on surface film cooling effectiveness ( $x/d = DSE$ ,  $DR = 1.0$ , FPG)

especially depending on the density ratio. Increasing the blowing ratio for a set density ratio increases the coolant velocity. For some holes, especially the round hole, this velocity increase resulted in increased jet separation. However, for most shaped holes investigated, increasing the coolant velocity resulted in improved film cooling effectiveness downstream of the hole. Higher velocity coolant would actually travel downstream and protect the blade more effectively.

The effect of density ratio is similar to the effect of blowing ratio in that for a set blowing ratio, increasing DR decreases coolant velocity. Depending on the hole shape, that may improve jet attachment, or it may reduce the distance downstream the coolant can travel. The one effect of increasing DR that was consistent for all shapes and flow conditions investigated was the increased lateral spread of coolant at elevated DR. Finally, the effect of location within the hole was investigated to evaluate the formation of vorticity.  $x/d = 0, 3$ , and the DSE were investigated to show that the vorticity magnitude was significantly dependent on the location within the hole. The magnitude of the CVP increases as it develops, and the duckfoot holes show the development of

secondary flows. The duckfoot contours result in the formation of additional vortices rotating counter to the CVP on the outside edges of the holes.

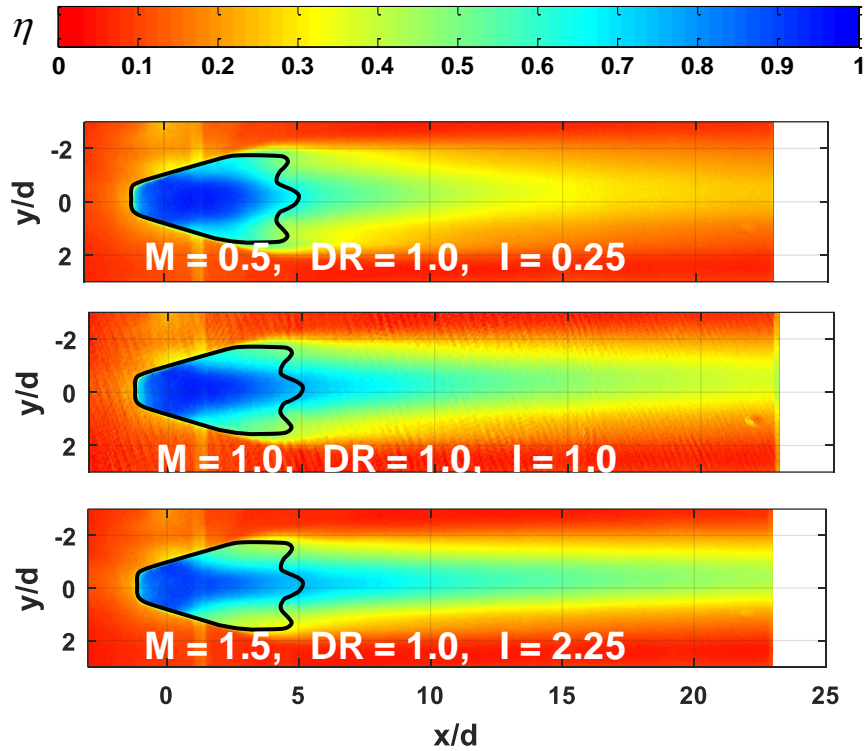


Figure 8.77: Duckfoot 2 hole film cooling effectiveness distribution under a favorable pressure gradient: blowing ratio effect

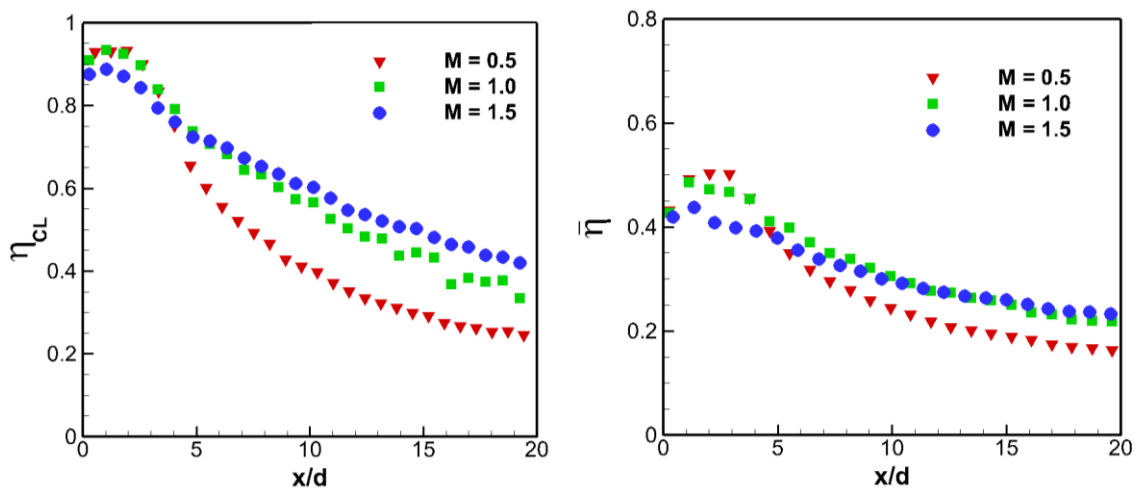


Figure 8.78: Duckfoot 2 centerline and lateral average film cooling effectiveness under a favorable pressure gradient: blowing ratio effect

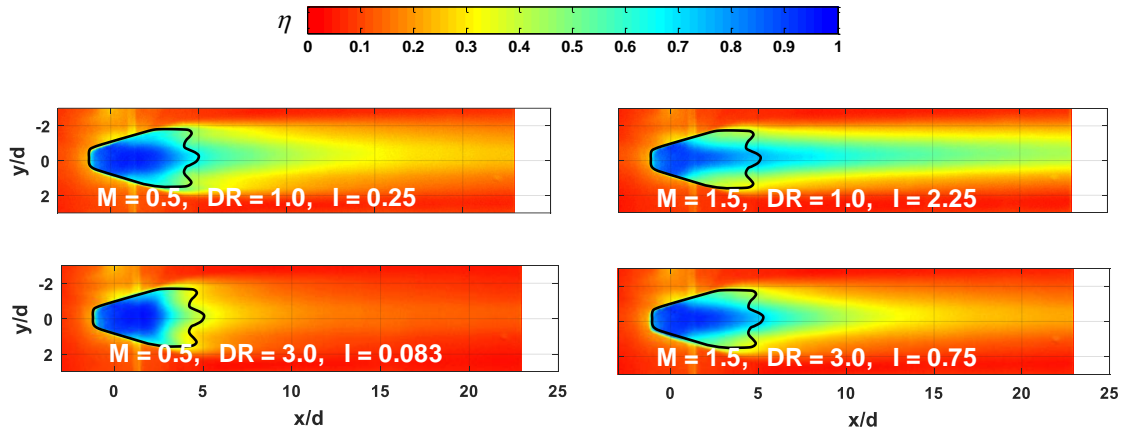


Figure 8.79: Duckfoot 2 hole film cooling effectiveness distribution under a favorable pressure gradient: density ratio effect

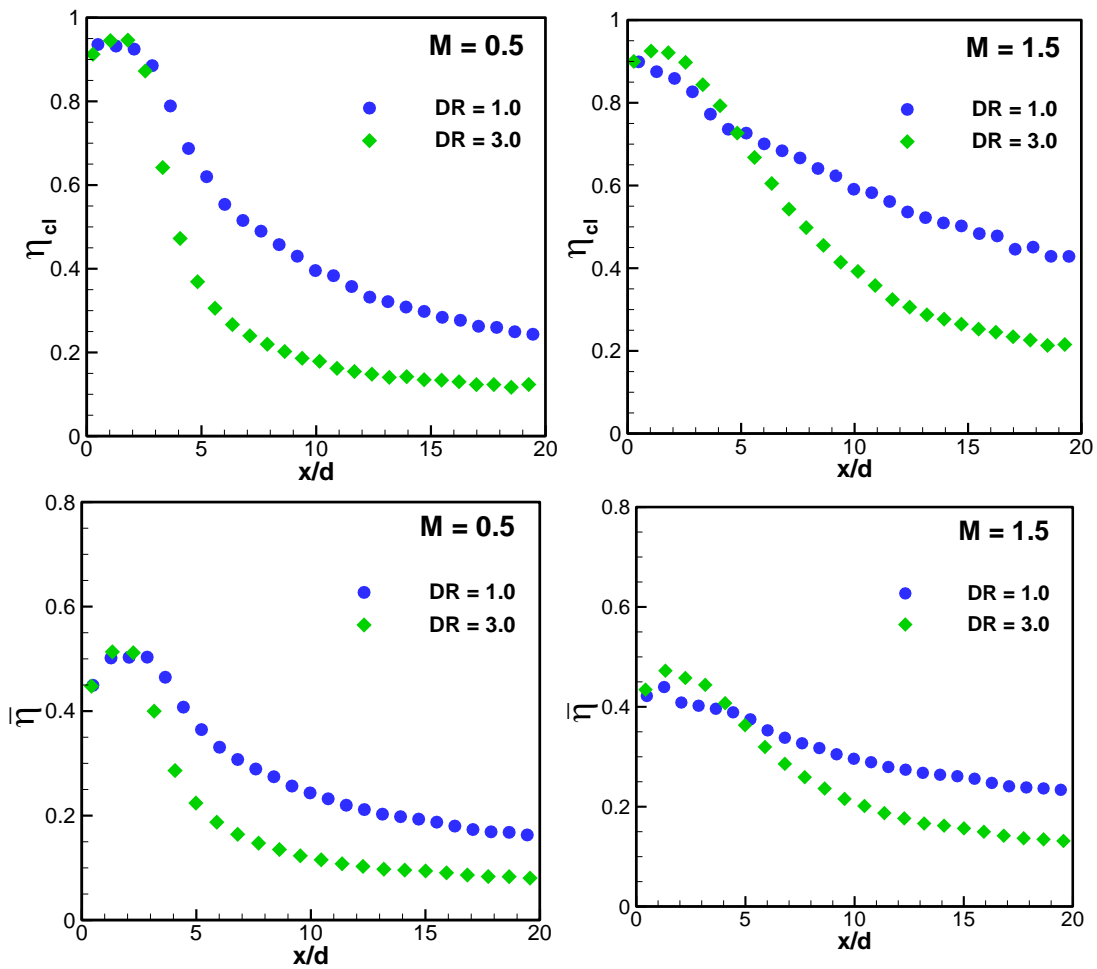


Figure 8.80: Duckfoot 2 hole centerline and lateral average film cooling effectiveness under a favorable pressure gradient: density ratio effect

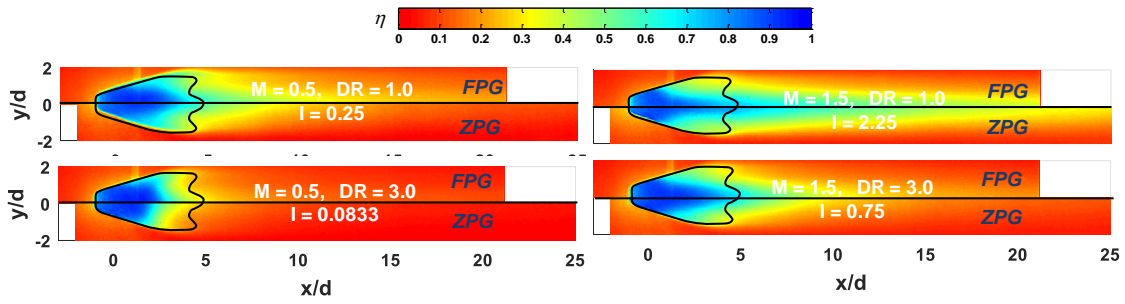


Figure 8.81: Duckfoot 2 film cooling effectiveness distributions: FPG effect

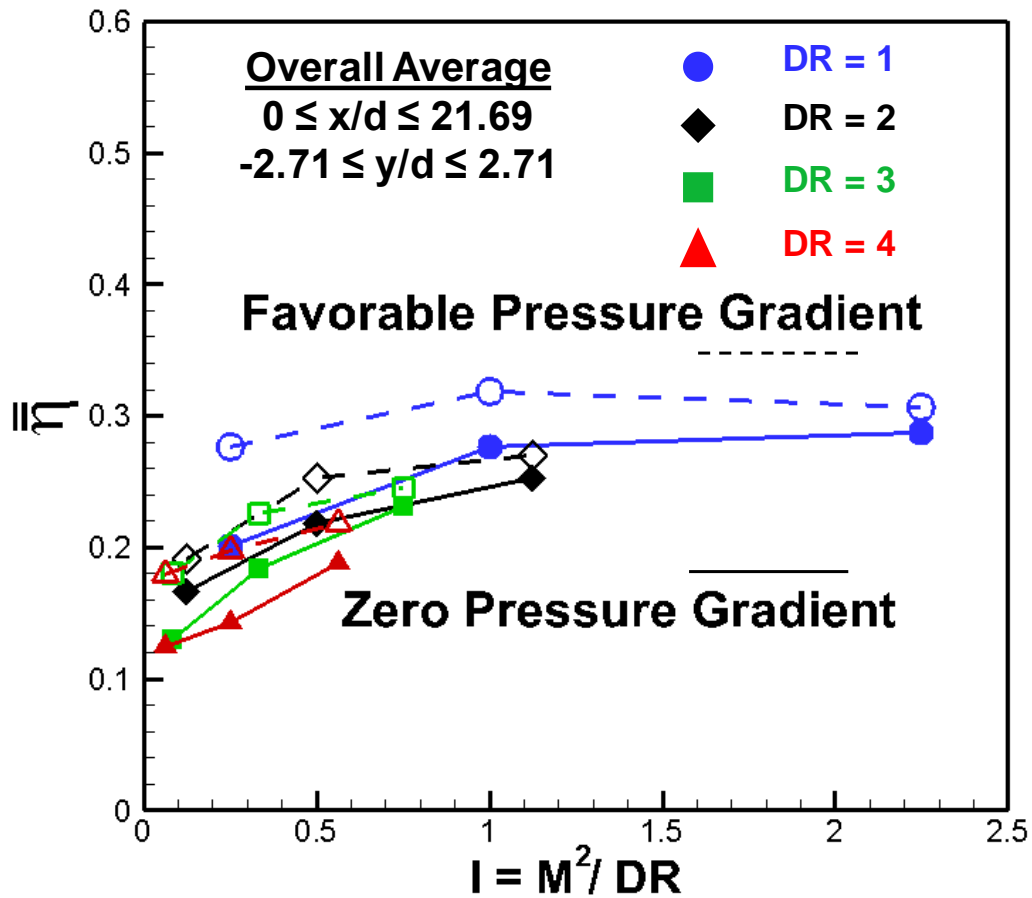


Figure 8.82: Duckfoot 2 overall average film cooling effectiveness: FPG effect

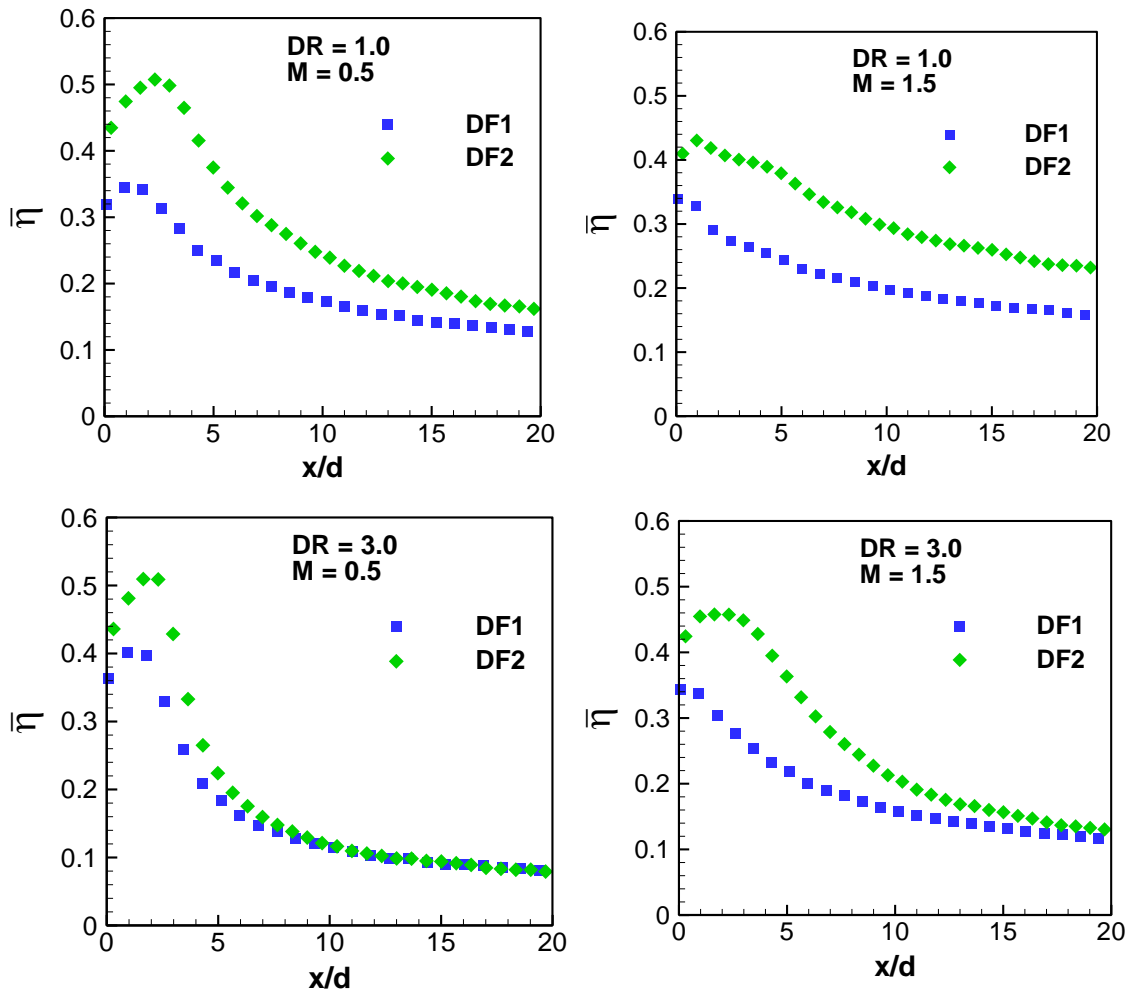


Figure 8.83: Favorable pressure gradient lateral average film cooling effectiveness: Inlet shape effect

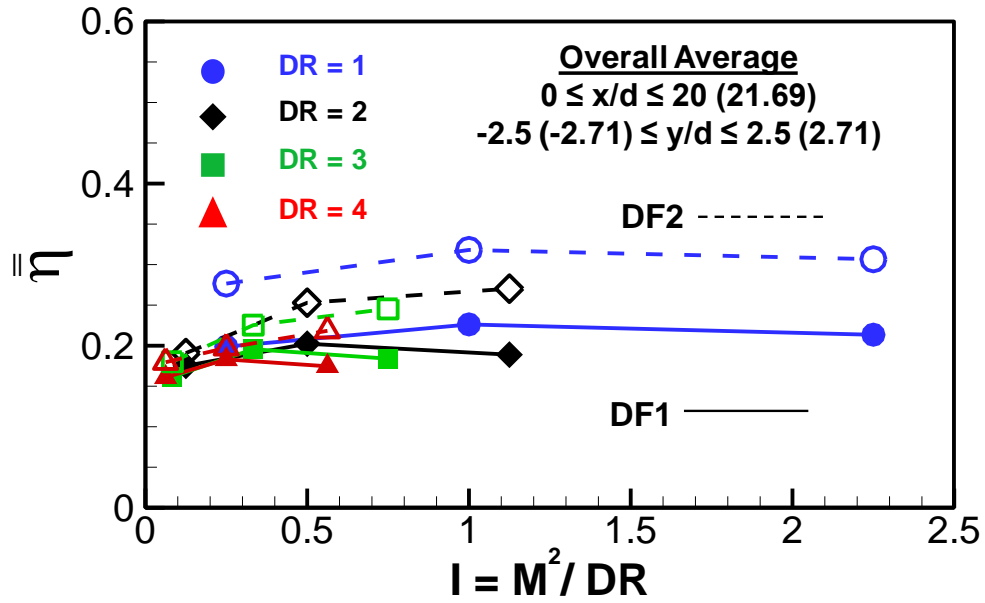


Figure 8.84: Comparison of DF1 and DF2 with overall average film cooling effectiveness

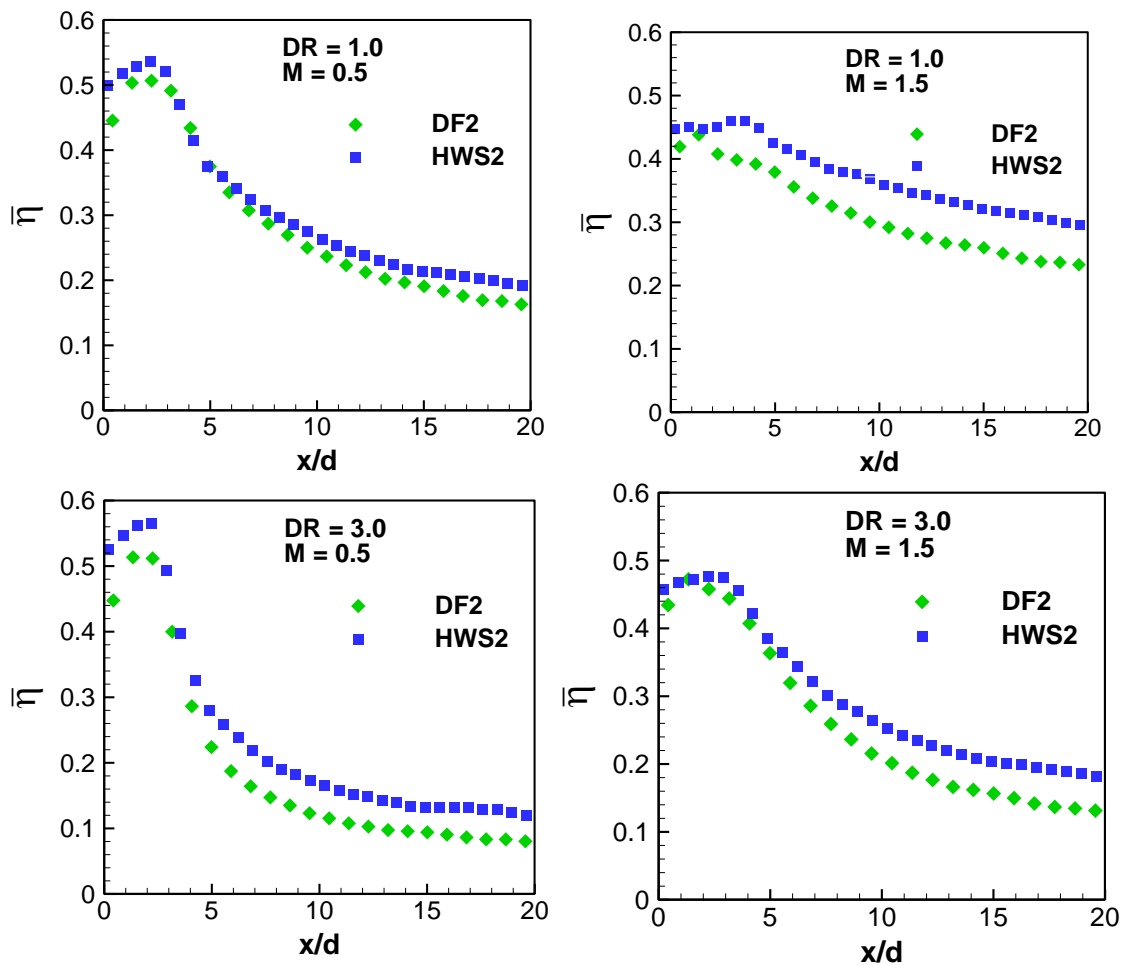


Figure 8.85: Favorable pressure gradient lateral average film cooling effectiveness: Duckfoot effect

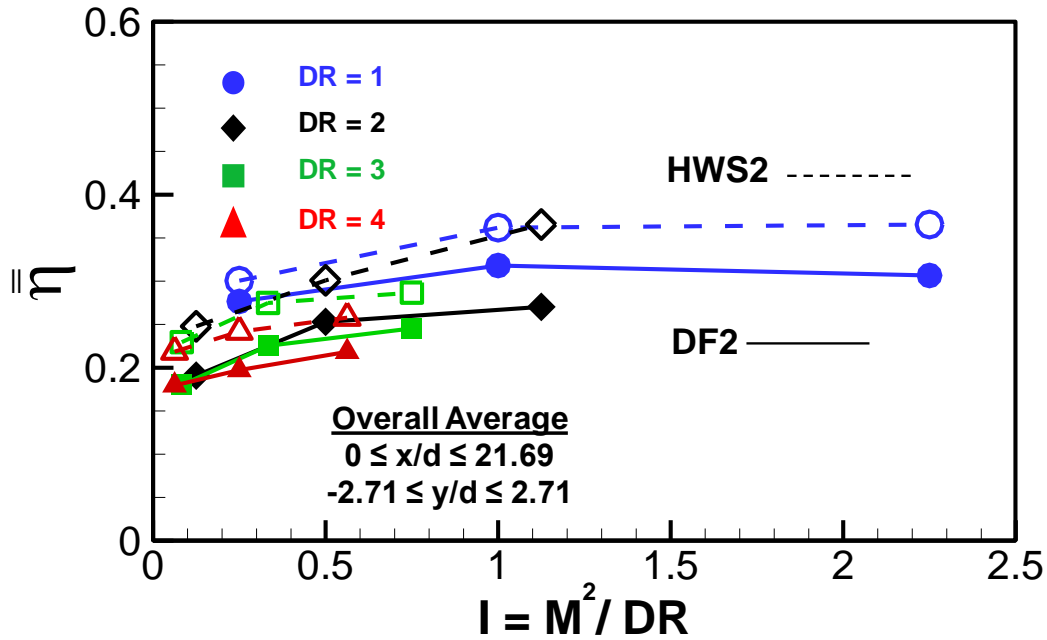


Figure 8.86: Comparison of DF2 and HWS2 with overall average film cooling effectiveness

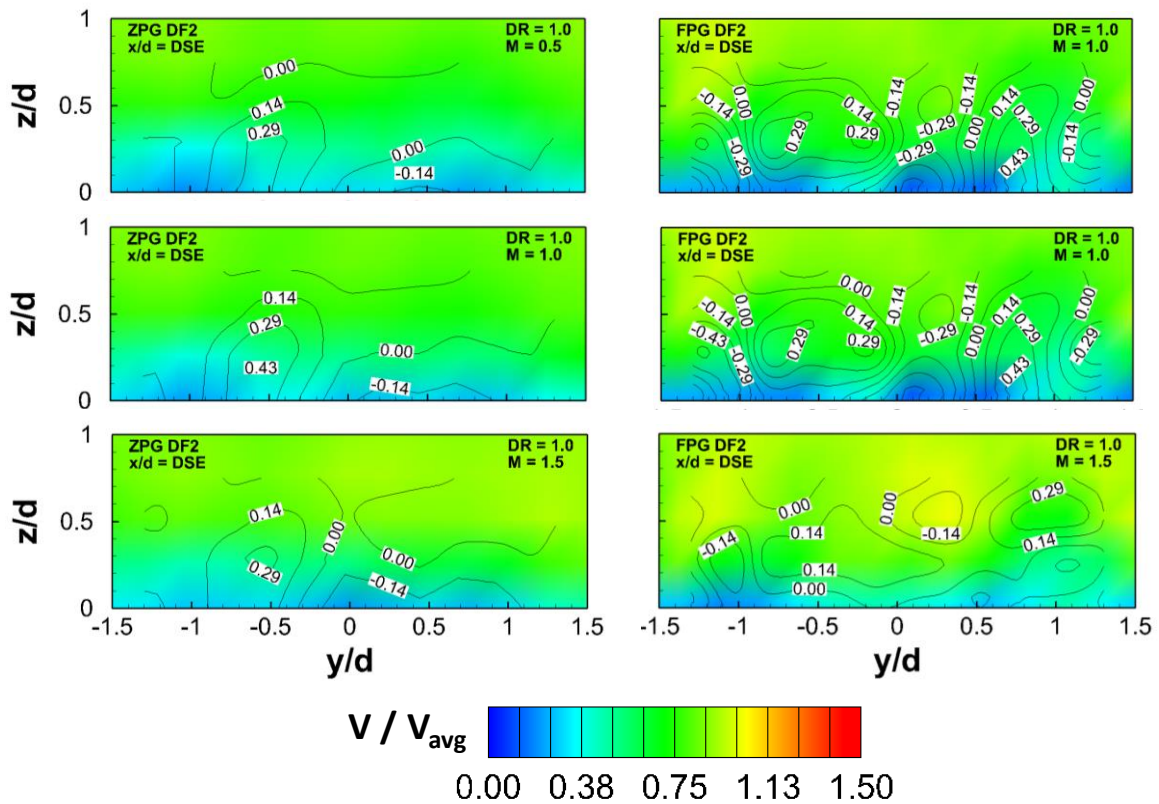


Figure 8.87: Effect of blowing ratio and freestream acceleration for Duckfoot 2 hole ( $x/d = DSE$ ,  $DR = 1.0$ )

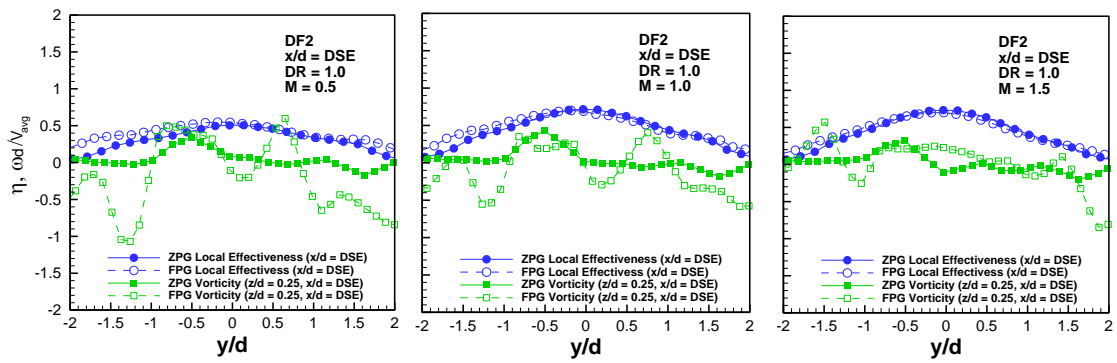


Figure 8.88: Influence of flow vorticity on surface film cooling effectiveness from Duckfoot 2 ( $x/d = DSE$ ,  $DR = 1.0$ )

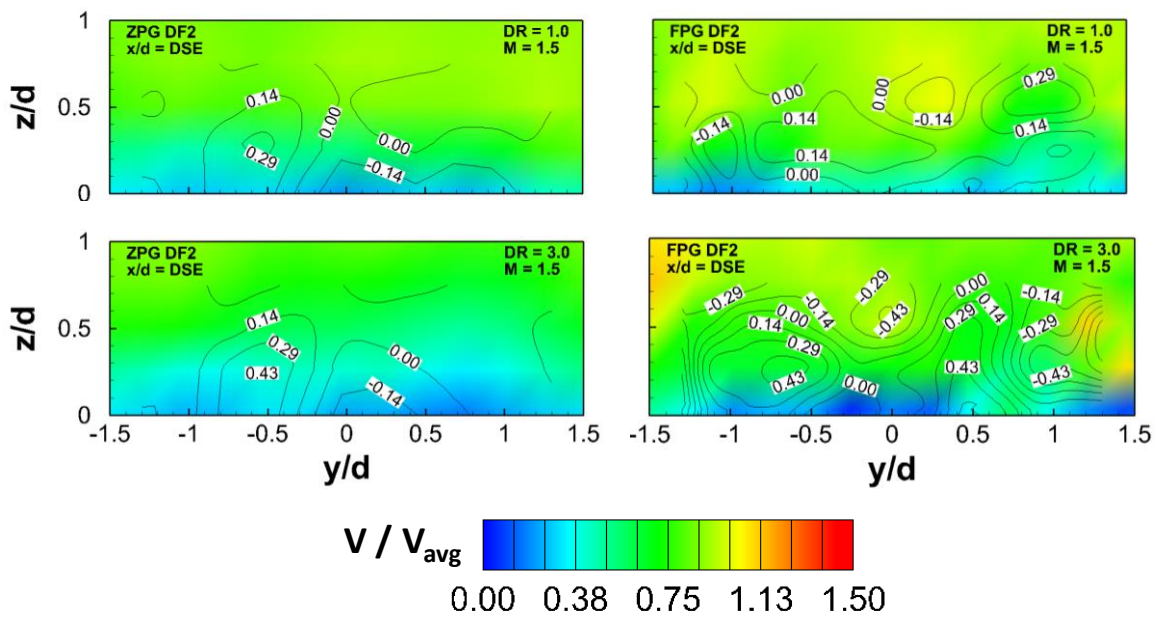


Figure 8.89: Effect of density ratio and freestream acceleration for Duckfoot 2 holes ( $x/d = DSE$ ,  $M = 1.5$ )

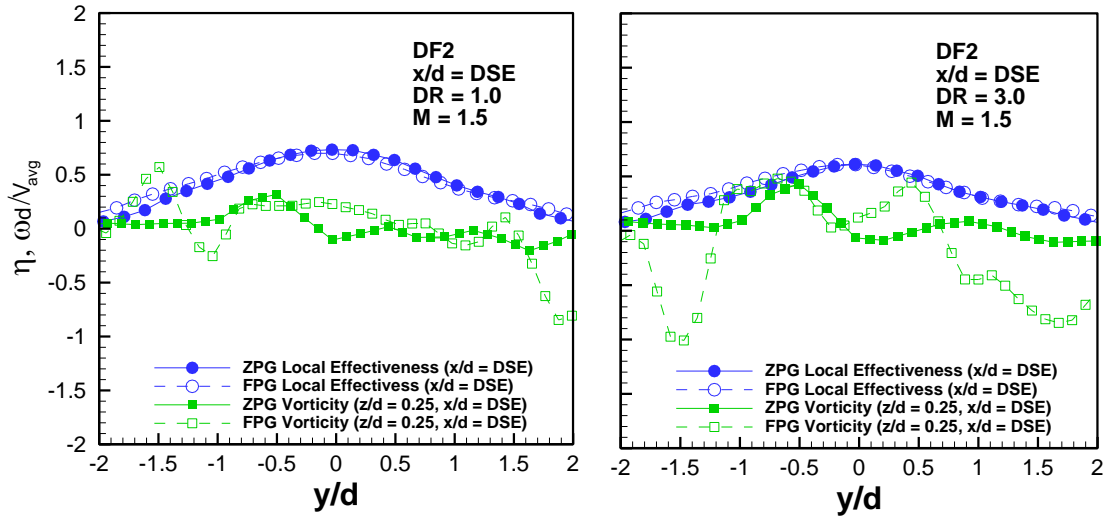


Figure 8.90: Influence of flow vorticity on surface film cooling effectiveness from Duckfoot 2 holes ( $M = 1.5$ ,  $DR = 1.0$ )

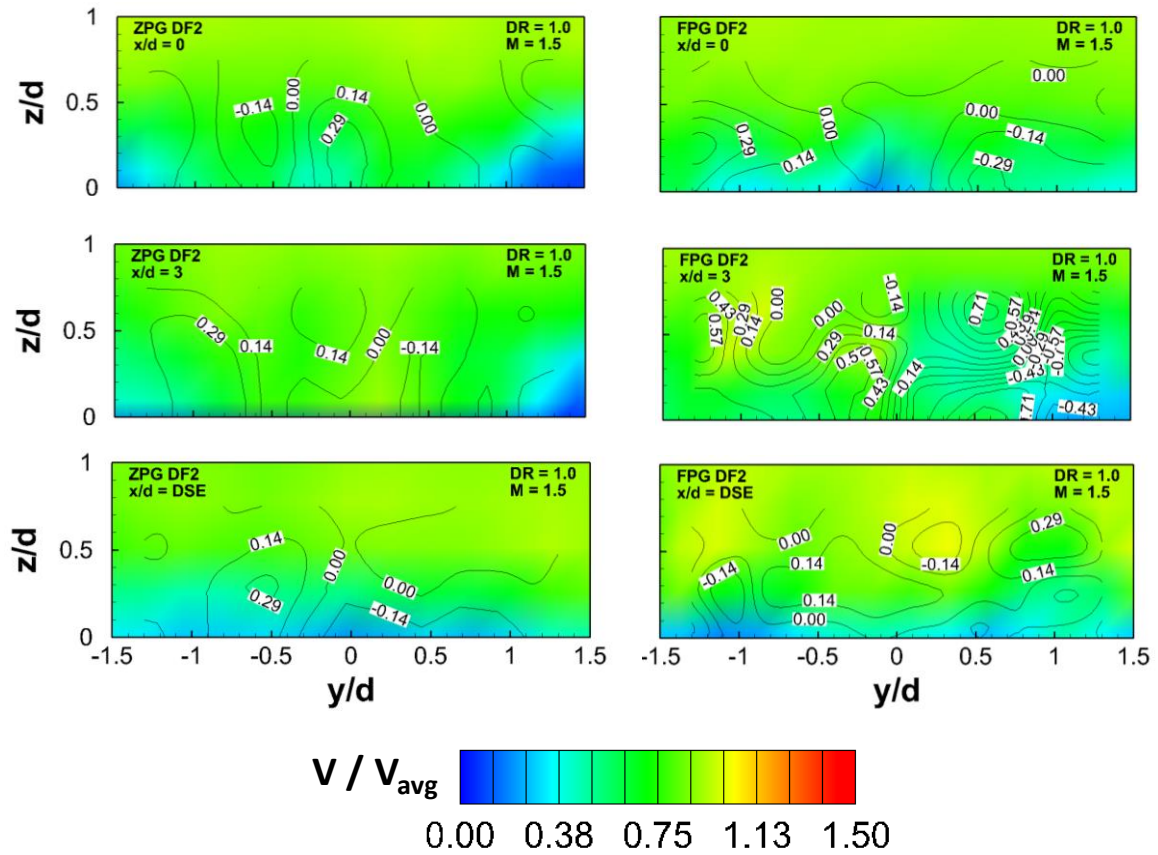


Figure 8.91: Effect of downstream location and freestream acceleration for Duckfoot 2 ( $M = 1.5$ ,  $DR = 1.0$ )

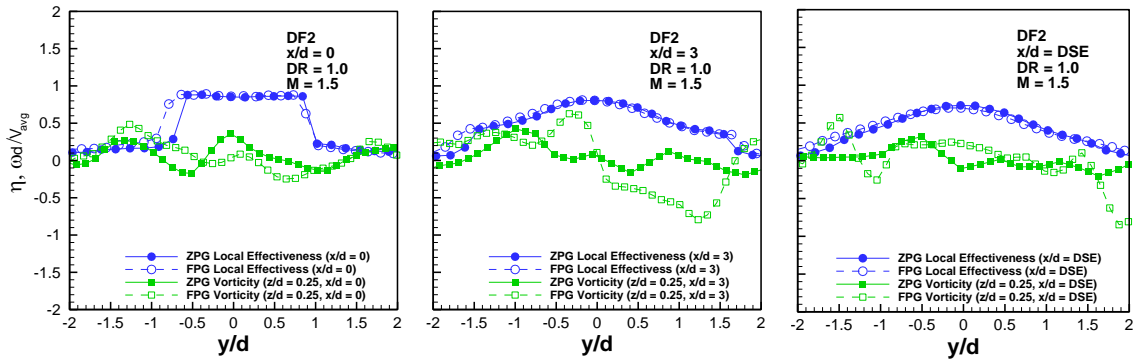


Figure 8.92: Influence of flow vorticity on surface film cooling effectiveness from Duckfoot 2 holes ( $M = 1.5$ ,  $DR = 1.0$ )

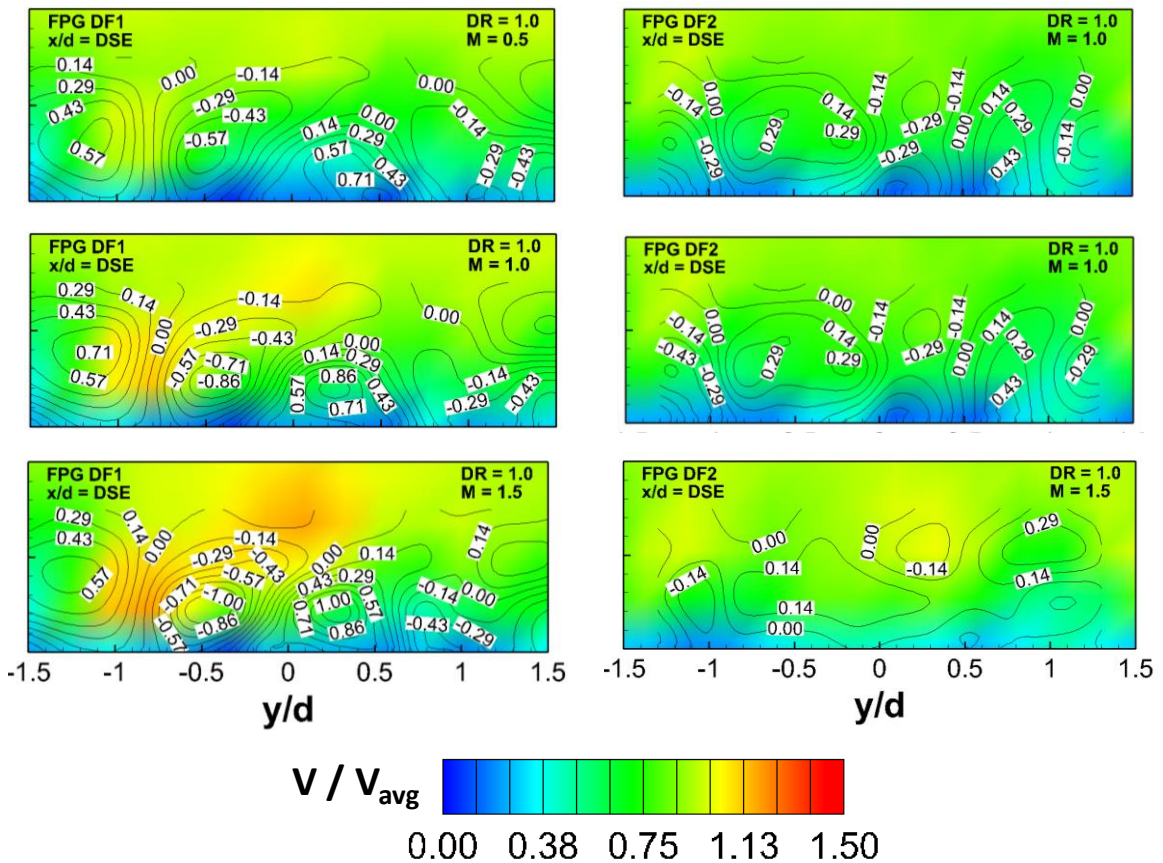


Figure 8.93: Comparison of DF2 and DF1 holes for varying blowing ratio ( $x/d = DSE$ ,  $DR = 1.0$ , FPG)

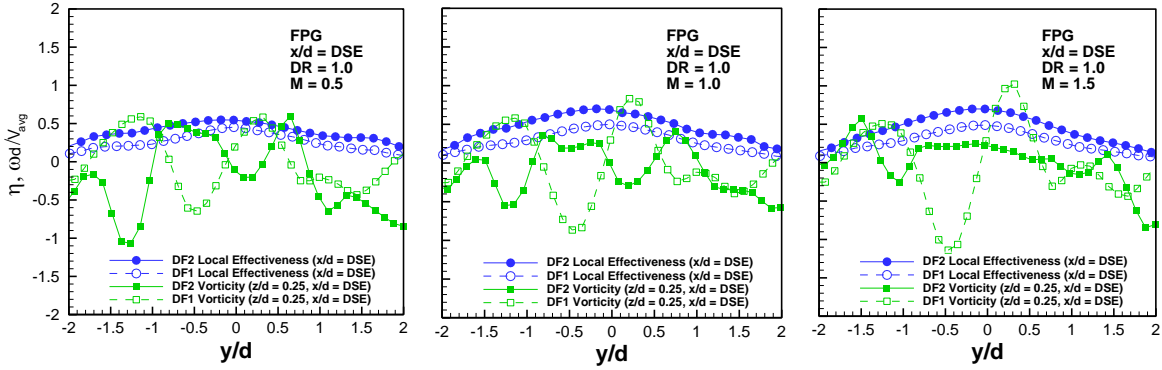


Figure 8.94: Comparison of DF1 and DF2 holes through the influence of flow vorticity on surface film cooling effectiveness ( $x/d = DSE$ ,  $DR = 1.0$ , FPG)

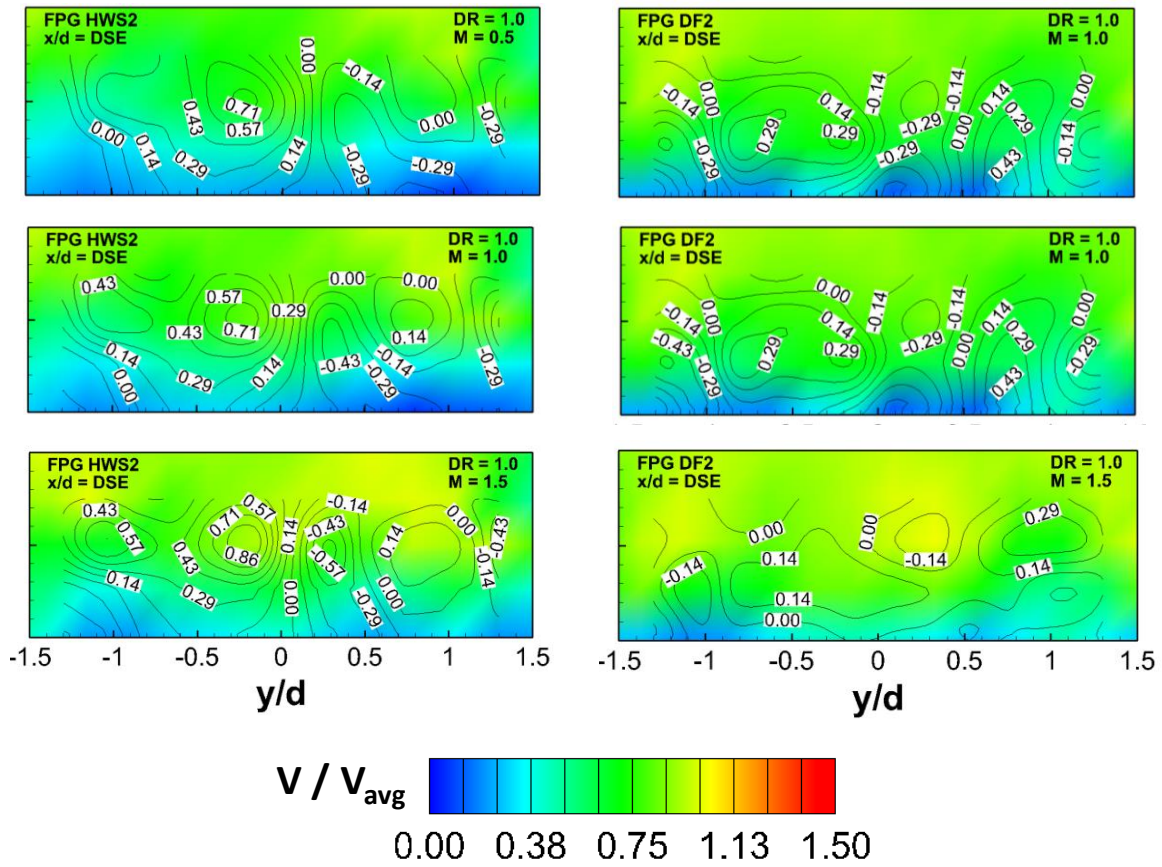


Figure 8.95: Comparison of HWS2 and DF2 holes for varying blowing ratio ( $x/d = DSE$ ,  $DR = 1.0$ , FPG)

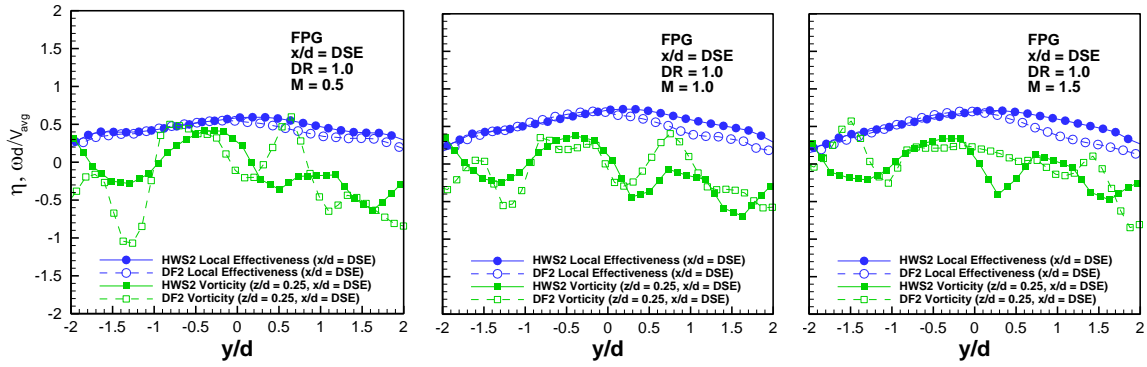


Figure 8.96: Comparison of DF2 and HWS2 holes through the influence of flow vorticity on surface film cooling effectiveness ( $x/d = DSE$ ,  $DR = 1.0$ , FPG)

## CHAPTER NINE

### Conclusions

The study has used the PSP and S-PIV techniques to evaluate film cooling in both combustor and turbine cooling applications. It is hoped that the data presented will help engine designers limit overcooling with the increased information about the interaction of the coolant and mainstream flows. If film cooling schemes can be designed with a better understanding of the complex flows related to effusion cooling, favorable pressure gradient flow, and shaped film cooling holes, then engines can achieve higher efficiencies. Air travel and power generation can be made cheaper by small improvements in film cooling design.

#### *Combustor Film Cooling*

Combustor cooling is different from turbine airfoil cooling because the combustor is stationary. This allows for significantly increased film cooling hole densities, as mechanical stress concentration is less of a constraint. This means that most combustor film cooling schemes are full coverage, or effusion cooling schemes. This means that the rows of film cooling holes are near enough that the coolant from the first row interacts with the coolant from the subsequent row. Two effects caused by row interaction were shown in this study, and three other effects were demonstrated to effect the amount of row mixing.

The first effect shown is known as superposition, which occurs when coolant from the preceding row reaches the following row and is added to the coolant exiting the

next hole. This effect is shown by the raised film cooling effectiveness immediately downstream of the second row of holes compared with the effectiveness downstream of the first row of holes. The more mixing that occurs between rows, the more that the film cooling effectiveness is increased by superposition. As more coolant is added by superposition with each passing row, the film cooling effectiveness is increasing because the film continues to accumulate.

The second effect is that coolant spreads laterally due to row interaction. The mixing of the coolant from the previous row with the coolant exiting the subsequent row causes the coolant from the previous row to spread laterally. With each passing row, more coolant reaches the subsequent row and spreads out to blanket the plate in film. This effect can lead to extremely high film cooling effectiveness across the width of the plate in the downstream region. This effect is demonstrated by the effectiveness in the area halfway between holes. The effectiveness should be near zero, as there is no interaction between holes for the first row, but the effectiveness between holes is raised with each passing row. More coolant accumulates and mixes with the next row and gets spread out, and the effect cascades.

The first effect that increases row interaction is caused by boundary layer thickening. As coolant is ejected from the first row of holes, it blows into the boundary layer. The boundary layer is thickened as a result, and the first row of holes is utilized as a sacrificial row. As the boundary layer is thickened, the coolant ejected in the downstream rows interact with the boundary layer instead of the mainstream flow. This allows high momentum coolant to stay attached to the surface and not get swept into the mainstream as it travels along the surface of the plate. This effect increased row

interaction, and any increase in row interaction increases film cooling effectiveness. As the blowing ratio increased, more coolant was blown into the boundary layer, offering improved protection downstream.

Row mixing was also increased with increasing blowing ratio in the range of  $M = 0.5$  to  $6.0$  for the round hole. Row mixing is increased at higher blowing ratios because the higher velocity coolant is able to reach the subsequent row without getting swept off the surface into the mainstream. Increasing the blowing ratio above  $M = 6.0$  is not helpful because the additional coolant immediately separates from the surface and boundary layer has already been sufficiently thickened.

The effect of using shaped holes in effusion cooling was also shown to significantly increase row interaction, and therefore film cooling effectiveness. The single shaped hole and the double shaped hole improved the laterally averaged film cooling effectiveness by 300-400%. This occurs because shaped holes increase coolant attachment, which causes increased row interaction. As previously shown, any increased row interaction is significant for effusion cooling. The shaped holes amplify each of the effects noted previously, and the film cooling surface is blanketed with uniformly high concentrations of coolant.

### *Turbine Airfoil Film Cooling*

Turbine airfoil film cooling was investigated by coupling the PSP and S-PIV techniques so that film cooling effectiveness, velocity, and vorticity distributions could be obtained with the same test scenario. There are two aspects of film cooling knowledge that are improved with this study: the effect of accelerating mainstream flow and the effect of hole shape on secondary flow generation. The literature has not clarified the

effect of accelerating mainstream flow, but turbine airfoils induce a favorable pressure gradient on the suction surface, so it is important to understand this effect. The effect of hole shape on vortex generation is also not fully understood, and that effect is investigated with S-PIV results.

The effect of the pressure gradient was shown consistently through all geometries and flow conditions investigated. Favorable pressure gradient mainstream flow results in reduced boundary layer thickness. This has two primary effects on the film cooling jet. First, resistance to jet separation is increased. The boundary layer is a lower momentum flow than the mainstream, so it is easier for the film cooling jet to separate further from the surface for zero pressure gradient flows. The favorable pressure gradient keeps the jet closer to the surface, which leads to the second effect. The jet being closer to the surface must result in increased lateral spread so that mass flow is conserved. This causes a spreading in the counter-rotating vortex pair. As the secondary flows are pushed away from the center, the coolant spreads laterally. However, this effect also results in increased vorticity magnitude. Overall the film cooling effectiveness is not significantly impacted by the favorable pressure gradient because the reduced jet separation is counteracted by the increased mixing caused by the increased spread of the counter-rotating vortex pair. The only significant impact on film cooling effectiveness is the increased lateral spread of the coolant.

Advanced shaped holes, including Honeywell Shaped 1 and 2 and Duckfoot 1 and 2 were compared to the baseline round and laidback, fanshaped film cooling holes under a favorable pressure gradient. Two primary effects were investigated. The duckfoot holes have a special webbed outlet design that was expected to generate some anti-kidney

vortices and affect the secondary flows present. The effect of adding a racetrack shaped inlet was also considered as Honeywell Shaped 2 and Duckfoot 2 were compared directly with their respective round hole inlet counterparts, Honeywell Shaped 1 and Duckfoot 1.

Under the favorable pressure gradient, the duckfoot geometries resulted in significantly different secondary flow formation. The anti-kidney vortex structures were caused by the interaction of the coolant with the sidewall contours caused by the duckfoot webbing. When Duckfoot 1 is compared to Honeywell Shaped 1, the direction of coolant rotation is reversed, which is a direct result of the anti-kidney vortices. This causes reduced jet separation as the coolant is pulled towards the surface by the anti-kidney vortex pair. However, the film cooling effectiveness is not significantly impacted because the vorticity magnitude increase and the formation of other harmful secondary flows in the outer edges of the hole results in increased mixing with the mainstream. The same effect is also seen comparing Duckfoot 2 and Honeywell Shaped 2, though the Honeywell Shaped 2 geometry actually outperforms the Duckfoot 2.

The effect of adding a racetrack shaped inlet may be the most significant result shown in this study. The Duckfoot 2 and Honeywell Shaped 2 geometries significantly outperformed all other geometries tested. The overall, area averaged film cooling effectiveness was nearly doubled by adding the racetrack inlet to Honeywell Shaped 1. This substantial improvement occurs because the racetrack inlet keeps coolant more closely attached to the surface and results in increased coolant spread. The shape of the inlet means that the center of the jet is closer to the surface because the hole inlet is shorter and wider. As the jet is pulled closer to the surface, it is also spread laterally, which are both desirable effects. The racetrack shaped inlet holes were also the only

geometries to see significant improvement from the favorable pressure gradient. This occurs because the racetrack shape and the favorable pressure gradient effect are essentially the same. They both push coolant closer to the surface and increase lateral spread, so the effects are combined in a way that improves film cooling effectiveness.

### *Future Recommendations*

The present investigation revealed several effects that should be investigated further for their potential to improve film cooling design. DMLS shaped holes were shown to cause three to four times improvement in film cooling effectiveness compared with round holes. It would be beneficial to confirm that shaped holes fabricated with more traditional manufacturing techniques would show provide similar results.

It was also shown that the adding the duckfoot shaped outlet affected the formation of secondary flows. While some effects were beneficial, others were counterproductive. Demonstrating the ability to generate anti-kidney vortices is important, but the next step is to design a hole shape that generates anti-kidney vortices without also generating further secondary flows which counteract the anti-kidney vortices. The outlet shape can be adjusted to see the effect of changing the webbing to optimize the potential for improvement by controlling the secondary flow generation. The racetrack shaped inlet holes showed substantial improvement, and this inlet shape effect should be considered further. There is no literature on this effect, but it is clearly beneficial. It seems that a racetrack shape is optimal for pushing coolant towards the surface and increasing lateral spread, but there are many other shaped inlets that could be tested. It would also be helpful to study the effect of the aspect ratio of the racetrack

shape. This is the first aspect ratio tested, and there is no evidence to suggest it would be the optimum aspect ratio.

## APPENDICES

# APPENDIX A

## CAD Model of Round Combustor Cooling Coupon

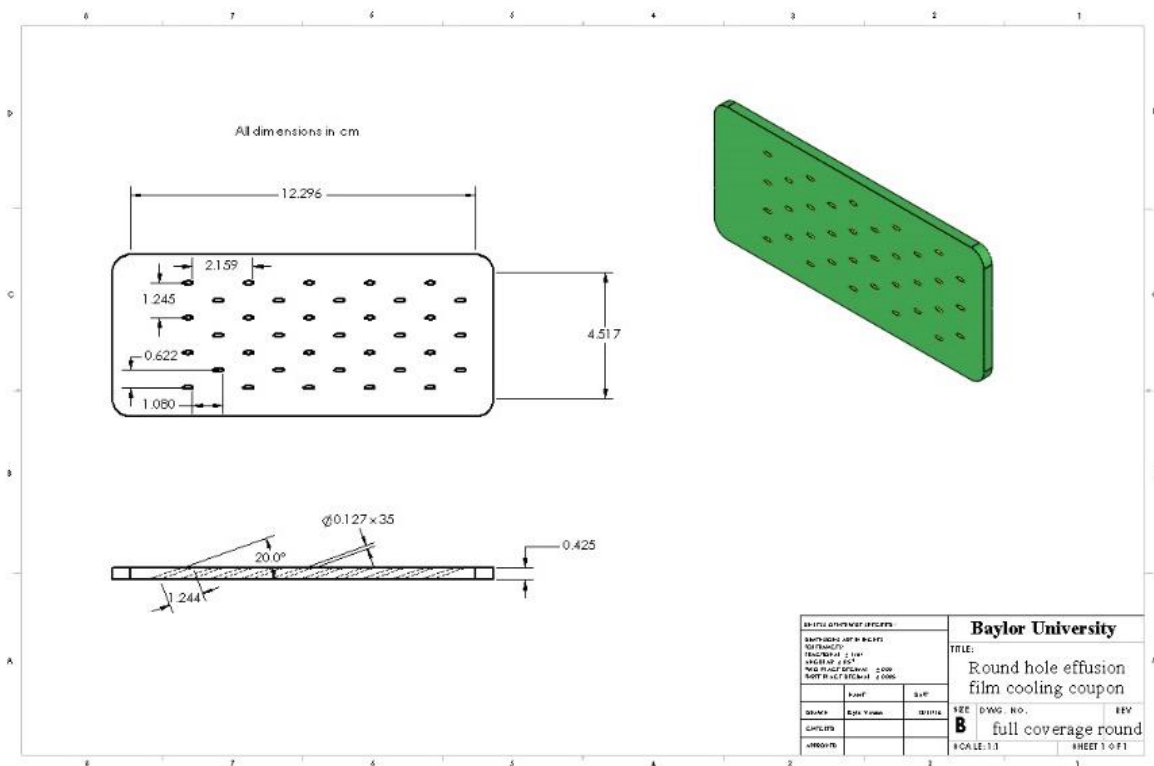


Figure A.1: CAD drawing of round hole full coverage film cooling coupon

## APPENDIX B

### CAD Models of Round and Laidback, Fanshaped Film Cooling Holes

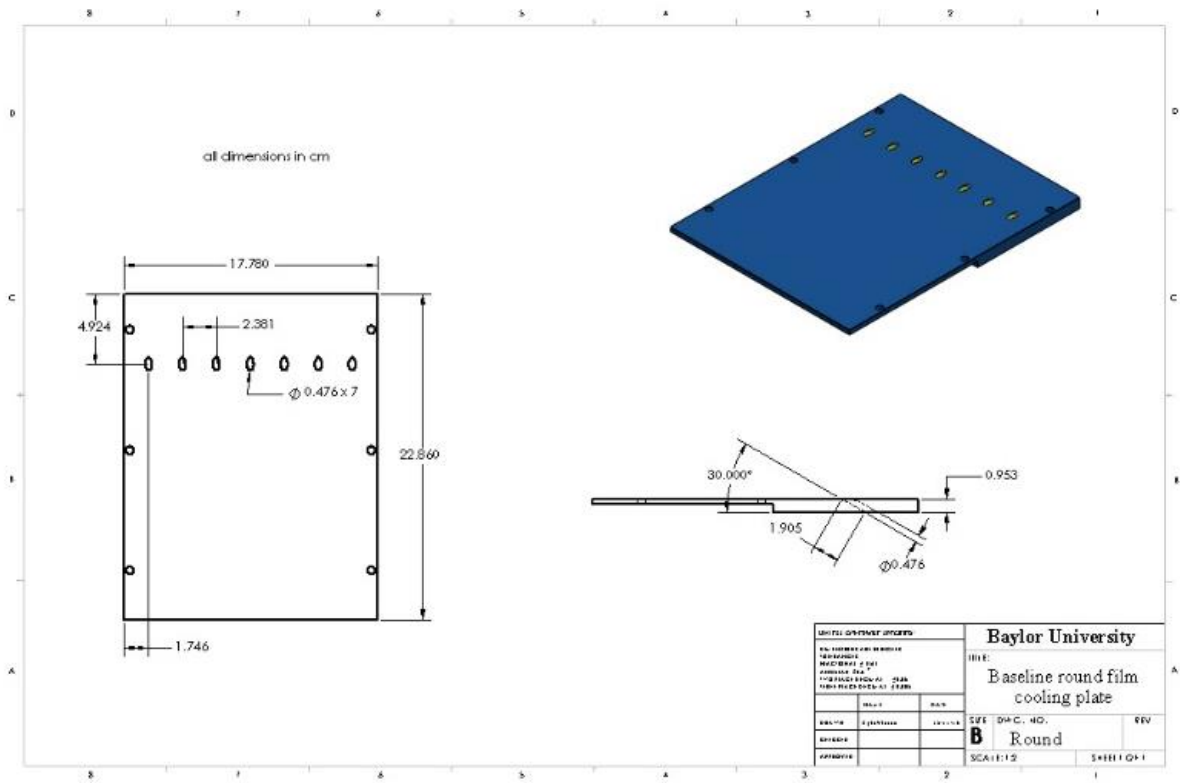


Figure B.1: CAD drawing of round film cooling hole plate

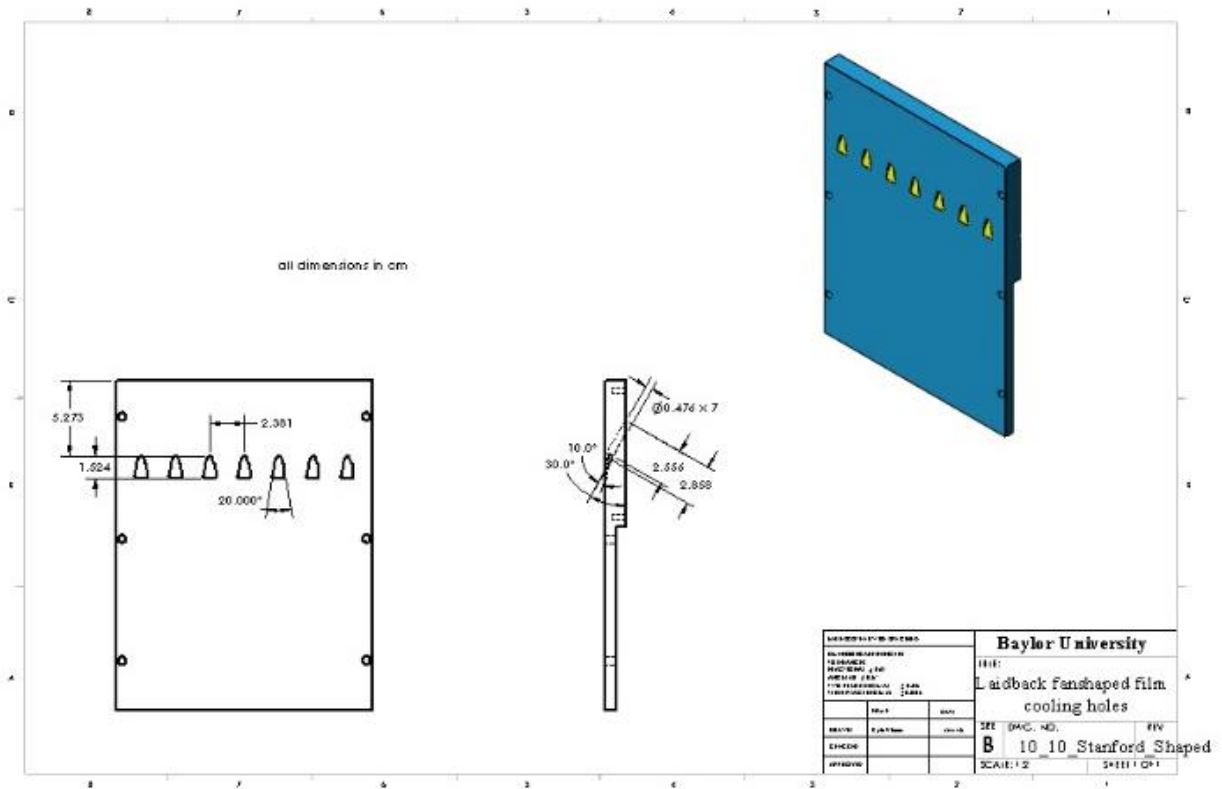


Figure B.2: CAD drawing of laidback, fan-shaped film cooling hole

## APPENDIX C

### PSP Data Analysis

```
% *****
%*           PSP EXPERIMENTAL MEASUREMENT TECHNIQUES
%* PSP - Detailed Pressure and Film Cooling Effectiveness Distributions
% *****

% ***** INTENSITY CALCULATION *****

%   From recorded images calculate the intensity at every pixel

clear all % clear all saved variables

clc      % clear command window

tic     % start internal timer

% *****
% *****
% *****
% *****

% ----- CHANGE INPUTS AS NEEDED -----

% specify area over which to determine intensity
X0 = 1; % x-coordinate of starting point
Y0 = 1; % y-coordinate of starting point

W = 822; % width of area
H = 1008; % height of area

% Define pixels to re-define coordinates (from pixels to x/D and y/D)
% film cooling hole diameter (pixels)
D = 25.5;
```

```

% x (flow) direction offset
xx = 29;

% y (lateral) direction offset
yy = 403;

% specify the file name of the save images -- ex. n1_0001.tif
name = '30sec.tif_';

% specify the file for the intensity output
ofile = 'mix1.mat'; % open (create) specified data file

% specify the starting and ending number for the saved images
Start = 1; % first image number
End = 200; % last image number

% -----          END INPUTS          -----

% establish a matrix of zeros - size H x W
sum = zeros(H,W);
inten_matrix = zeros(H,W);

% begin loop to average intensity at each pixel over the given number
% images -- do the calculations from Start (first image)
% to End (last image)

for i = Start:End

    % show progress of program by alerting user after every 10 images have
    % been completed
    if(~ mod(i,10)) % if the count is divisible by 10,
        fprintf('%d\n',End-i) % show the count in the command window
    end

    % create a character string with the image (counter, i) number,
    % preceded by zeros
    num = sprintf('%04d',i); % "0001" or "0150"

```

```

% create a string of the entire image name
% "name,num,.tif" -- "n1_0150.tif"
ifile = strcat(name,num,'.tif');

% read each image file and create a data file (I) with the
% intensity at each point (2D array)
I = imread(ifile, 'tif' );

% add the coordinates of the selected area to the data
I = I(Y0:Y0+H-1,X0:X0+W-1);
inten = double(I);
sum = sum + inten;

end

for jj = 1:W
    yD(jj) = (jj-yy)/D;
    for ii = 1:H

        xD(ii) = (ii-xx)/D;
        %inten_matrix(jj, ii) = sum(jj,ii) / (End-Start+1);
        inten_matrix(ii, jj) = sum(ii,jj) / (End-Start+1);

    end
end

%xD_new = fliplr(xD);
%I_rotate = rot90(inten_matrix);

%save(ofile, 'xD_new', 'yD', 'I_rotate');

save(ofile, 'xD', 'yD', 'inten_matrix');

% generate contour plot of intensity (with weighted pixel average)

figure
colormap([0 0 1;0 0 1;0 0.05263 1;0 0.1053 1;0 0.1579 1;0 0.2105 1;0 0.2632 1;0 0.3158
1;0 0.3684 1;0 0.4211 1;0 0.4737 1;0 0.5263 1;0 0.5789 1;0 0.6316 1;0 0.6842 1;0 0.7368
1;0 0.7895 1;0 0.8421 1;0 0.8947 1;0 0.9474 1;0 1 1;0.04545 1 0.9545;0.09091 1
0.9091;0.1364 1 0.8636;0.1818 1 0.8182;0.2273 1 0.7727;0.2727 1 0.7273;0.3182 1
0.6818;0.3636 1 0.6364;0.4091 1 0.5909;0.4545 1 0.5455;0.5 1 0.5;0.5455 1
0.4545;0.5909 1 0.4091;0.6364 1 0.3636;0.6818 1 0.3182;0.7273 1 0.2727;0.7727 1
0.2273;0.8182 1 0.1818;0.8636 1 0.1364;0.9091 1 0.09091;0.9545 1 0.04545;1 1 0;1 0.95

```

```

0;1 0.9 0;1 0.85 0;1 0.8 0;1 0.75 0;1 0.7 0;1 0.65 0;1 0.6 0;1 0.55 0;1 0.5 0;1 0.45 0;1 0.4
0;1 0.35 0;1 0.3 0;1 0.25 0;1 0.2 0;1 0.15 0;1 0.1 0;1 0.05 0;1 0 0;1 0 0));
%imagesc(yD, xD_new, I_rotate)
imagesc(yD, xD, inten_matrix)

%set(gca,'YTick',[-15 -10 -5 0 5 10 15])
%set(gca,'XTick',[-12 -8.5 -4 0 4 8.5 12])

%xlim([-38 4]);
%ylim([-15 15]);

colorbar
axis image
grid on

xlabel('Y / D','FontWeight','bold');
ylabel('X / D','FontWeight','bold');

fclose all;

toc % stop internal timer

```

```

%*****
%*           PSP EXPERIMENTAL MEASUREMENT TECHNIQUE
%* PSP - Detailed Pressure and Film Cooling Effectiveness Distributions
%*
%*****

% *STATIC PRESSURE AND FILM COOLING EFFECTIVENESS CALCULATION*

% From previously created intensity data files (Intensity.m) and input
% calibration data, calculate the static pressure and film cooling
% effectiveness at each pixel.

% STATIC PRESSURE
%  $P/P_{ref} = P/P_{ref} = a_3(I_{ref}/I)^3 + a_2(I_{ref}/I)^2 + a_1(I_{ref}/I) + a_0$ 

% Pressure Ratio is calculated based on the user defined calibration.
% Input Data Files:  black.dat
%                   ref.dat
%                   a1.dat, a2.dat, n1.dat, n2.dat, ar1.dat, ar2.dat, etc.
% Output Data Files:  a1pres.dat, etc.

% FILM COOLING EFFECTIVENESS
%  $eff = [(P/P_{ref})_{air} - (P/P_{ref})_{n2}] / (P/P_{ref})_{air}$ 
% Film Cooling Effectiveness is calculated for two density ratios based on
% coolant flows of air & nitrogen (DR = 1) and air & argon (DR = 1.5)
% Input Data Files:  a1pres.dat, a2pres.dat, n1pres.dat, n2pres.dat,
%                   ar1pres.dat, ar2pres.dat, etc
% Output Data Files:  N2effect11.dat, N2effect12.dat,
%                   N2effect21.dat, N2effect22.dat,
%                   AReffect11.dat, AReffect12.dat,
%                   AReffect21.dat, AReffect22.dat,

clear all % clear all saved variables
close all % close all open windows
clc % clear command window

tic % start internal timer

%*****
%*****
%*****
%*****

```

```

% -----          CHANGE INPUTS AS NEEDED          -----

ofile = 'eff11.mat';    % open (create) specified data file
ofile2 = 'eff11_cl.mat'; % open (create) specified data file
ofile3 = 'eff11_latavg1.5.mat'; % open (create) specified data file

% Define Size of Images
% These must match those used for black and reference
NX = 818;
NY = 993;

% Input Coefficients from PSP Calibration
%  $P/P_{ref} = a_3(I_{ref}/I)^3 + a_2(I_{ref}/I)^2 + a_1(I_{ref}/I) + a_0$ 

% Calibraton 1
a_0 = -0.0871;
a_1 = 0.6065;
a_2 = 0.2908;
a_3 = 0.1796;

% Define Y boundaries for Lateral Average
% For example spanwise average:  $-1.0 < Y/D < 1.0$ 

% Lower Limit of Average
low_yd = -2.5;

% Upper Limit of Average
high_yd = 2.5;

% Define Y boundaries for Overall Average
% For example spanwise average:  $-1.0 < Y/D < 1.0$ 
%                                $+2.0 < X/D < 14$ 

% Lower Limit of Average
low_xd = 0;

% Upper Limit of Average
high_xd = 20;

% Load Intensity Data Files (Ib, Iref, test data: Ia1, Ia2, Im1, Im2)
blackdat = load('black.mat'); % Ib
xD = blackdat.xD;
yD = blackdat.yD;
blackint = blackdat.inten_matrix;

```

```

refdat = load('ref.mat');    % Iref
refint = refdat.inten_matrix;

airdat = load('a1.mat');    % Ia1
airint = airdat.inten_matrix;

mixdat = load('mix1.mat');  % Im1
mixint = mixdat.inten_matrix;

W = size(blackint, 1);
H = size(blackint, 2);

Iratio_a1 = (refint - blackint)./ (airint - blackint);
Iratio_data = (refint - blackint)./ (mixint - blackint);

Pratio_a1 = a_3.*(Iratio_a1).^3 + a_2.*(Iratio_a1).^2 + a_1.*(Iratio_a1) + a_0;
Pratio_data = a_3.*(Iratio_data).^3 + a_2.*(Iratio_data).^2 + a_1.*(Iratio_data) + a_0;

eff = (Pratio_a1 - Pratio_data)./ Pratio_a1;

save(ofile, 'xD', 'yD', 'eff');

%-----
%-----
%-----
%-----
%-----
%-----

figure
colormap([1 0 0; 1 0 0; 1 0.0526 0; 1 0.1053 0; 1 0.1579 0; 1 0.2105 0; 1 0.2632 0; 1
0.3158 0; 1 0.3684 0; 1 0.4211 0; 1 0.4737 0; 1 0.5263 0; 1 0.5789 0; 1 0.6316 0; 1
0.6842 0; 1 0.7368 0; 1 0.7895 0; 1 0.8421 0; 1 0.8947 0; 1 0.9474 0; 1 1 0; 0.9545 1
0.0455; 0.9091 1 0.0909; 0.8636 1 0.1364; 0.8182 1 0.1818; 0.7727 1 0.2273;
0.7273 1 0.2727; 0.6818 1 0.3182; 0.6364 1 0.3636; 0.5909 1 0.4091; 0.5455 1
0.4545; 0.5000 1 0.5000; 0.4545 1 0.5455; 0.4091 1 0.5909; 0.3636 1 0.6364;
0.3182 1 0.6818; 0.2727 1 0.7273; 0.2273 1 0.7727; 0.1818 1 0.8182; 0.1364 1
0.8636; 0.0909 1 0.9091; 0.0455 1 0.9545; 0 1 1; 0 0.95 1; 0 0.9 1; 0
0.85 1; 0 0.8 1; 0 0.75 1; 0 0.7 1; 0 0.65 1; 0 0.6 1; 0 0.55 1; 0 0.5 1; 0
0.45 1; 0 0.4 1; 0 0.35 1; 0 0.3 1; 0 0.25 1; 0 0.2 1; 0 0.15 1; 0 0.10 1; 0 0.05 1;
0 0 1; 0 0 1]);

```

```

imagesc(yD, xD, eff)

colorbar
caxis([0 .8])

axis image
grid on

xlim([-12 12])
ylim([-3 36])

set(gca,'YTick',[-5 0 5 10 15 20 25 30 35])
set(gca,'XTick',[-10 -5 0 5 10])

xlabel('Y / D','FontWeight','bold');
ylabel('X / D','FontWeight','bold');

%-----
%-----
%-----
%-----
%-----
%-----

eff_rotate = rot90(eff);
eff_flip = fliplr(eff_rotate);
xD_rotate = rot90(xD,2);
yD_rotate = rot90(yD,2);

figure
colormap([0 0 0.560784339904785;0 0 0.623529434204102;0 0 0.686274528503418;0 0
0.749019622802734;0 0 0.811764717102051;0 0 0.874509811401367;0 0
0.937254905700684;0 0 1;0 0.062745101749897 1;0 0.125490203499794 1;0
0.18823529779911 1;0 0.250980406999588 1;0 0.313725501298904 1;0
0.376470595598221 1;0 0.439215689897537 1;0 0.498039215803146 1;0
0.560784339904785 1;0 0.623529434204102 1;0 0.686274528503418 1;0
0.749019622802734 1;0 0.811764717102051 1;0 0.874509811401367 1;0
0.937254905700684 1;0 1 1;0 1 0.874509811401367;0 1 0.749019622802734;0 1
0.623529434204102;0 1 0.501960813999176;0 1 0.376470595598221;0 1
0.250980406999588;0 1 0.125490203499794;0 1 0;0.125490203499794 1
0;0.250980406999588 1 0;0.376470595598221 1 0;0.501960813999176 1
0;0.623529434204102 1 0;0.749019622802734 1 0;0.874509811401367 1 0;1 1 0;1
0.937254905700684 0;1 0.874509811401367 0;1 0.811764717102051 0;1

```

```

0.749019622802734 0;1 0.686274528503418 0;1 0.623529434204102 0;1
0.560784339904785 0;1 0.501960813999176 0;1 0.439215689897537 0;1
0.376470595598221 0;1 0.313725501298904 0;1 0.250980406999588 0;1
0.18823529779911 0;1 0.125490203499794 0;1 0.062745101749897 0;1 0
0;0.937254905700684 0 0;0.874509811401367 0 0;0.811764717102051 0
0;0.752941191196442 0 0;0.690196096897125 0 0;0.627451002597809 0
0;0.564705908298492 0 0;0.501960813999176 0 0]);
imagesc(xD_rotate, yD_rotate, eff_flip)

colorbar;
caxis([0 1])

axis image
grid on

ylim([-12 12])
xlim([-3 36])

set(gca,'XTick',[-5 0 5 10 15 20 25 30 35], 'FontWeight','bold')
set(gca,'YTick',[-10 -5 0 5 10], 'FontWeight','bold')

xlabel('X / D','FontWeight','bold', 'FontSize',12);
ylabel('Y / D','FontWeight','bold', 'FontSize',12);

%-----

figure
colormap([1 0 0; 1 0 0; 1 0.0526 0; 1 0.1053 0; 1 0.1579 0; 1 0.2105 0; 1 0.2632 0; 1
0.3158 0; 1 0.3684 0; 1 0.4211 0; 1 0.4737 0; 1 0.5263 0; 1 0.5789 0; 1 0.6316 0; 1
0.6842 0; 1 0.7368 0; 1 0.7895 0; 1 0.8421 0; 1 0.8947 0; 1 0.9474 0; 1 1 0; 0.9545 1
0.0455; 0.9091 1 0.0909; 0.8636 1 0.1364; 0.8182 1 0.1818; 0.7727 1 0.2273;
0.7273 1 0.2727; 0.6818 1 0.3182; 0.6364 1 0.3636; 0.5909 1 0.4091; 0.5455 1
0.4545; 0.5000 1 0.5000; 0.4545 1 0.5455; 0.4091 1 0.5909; 0.3636 1 0.6364;
0.3182 1 0.6818; 0.2727 1 0.7273; 0.2273 1 0.7727; 0.1818 1 0.8182; 0.1364 1
0.8636; 0.0909 1 0.9091; 0.0455 1 0.9545; 0 1 1; 0 0.95 1; 0 0.9 1; 0
0.85 1; 0 0.8 1; 0 0.75 1; 0 0.7 1; 0 0.65 1; 0 0.6 1; 0 0.55 1; 0 0.5 1; 0
0.45 1; 0 0.4 1; 0 0.35 1; 0 0.3 1; 0 0.25 1; 0 0.2 1; 0 0.15 1; 0 0.10 1; 0 0.05 1;
0 0 1; 0 0 1]);

imagesc(xD_rotate, yD_rotate, eff_flip)

colorbar;
caxis([0 0.8])

axis image

```

```

grid on

ylim([-3 3])
xlim([-3 36])

set(gca,'XTick',[-5 0 5 10 15 20 25 30 35], 'FontWeight','bold')
set(gca,'YTick',[-2 0 2], 'FontWeight','bold')

xlabel('X / D','FontWeight','bold', 'FontSize',12);
ylabel('Y / D','FontWeight','bold', 'FontSize',12);

%-----

figure
imagesc(xD_rotate, yD_rotate, eff_flip)

colorbar;
caxis([0 1])

axis image
grid on

ylim([-2 2])
xlim([-1 16])

set(gca,'XTick',[-2 0 2 4 6 8 10 12 14 16], 'FontWeight','bold')
set(gca,'YTick',[-2 -1 0 1 2], 'FontWeight','bold')

xlabel('X / D','FontWeight','bold', 'FontSize',12);
ylabel('Y / D','FontWeight','bold', 'FontSize',12);

%-----
%-----
%-----
%-----

figure
colormap([0 0 1;0 0 1;0 0.05263 1;0 0.1053 1;0 0.1579 1;0 0.2105 1;0 0.2632 1;0 0.3158
1;0 0.3684 1;0 0.4211 1;0 0.4737 1;0 0.5263 1;0 0.5789 1;0 0.6316 1;0 0.6842 1;0 0.7368
1;0 0.7895 1;0 0.8421 1;0 0.8947 1;0 0.9474 1;0 1 1;0.04545 1 0.9545;0.09091 1
0.9091;0.1364 1 0.8636;0.1818 1 0.8182;0.2273 1 0.7727;0.2727 1 0.7273;0.3182 1
0.6818;0.3636 1 0.6364;0.4091 1 0.5909;0.4545 1 0.5455;0.5 1 0.5;0.5455 1
0.4545;0.5909 1 0.4091;0.6364 1 0.3636;0.6818 1 0.3182;0.7273 1 0.2727;0.7727 1

```

```
0.2273;0.8182 1 0.1818;0.8636 1 0.1364;0.9091 1 0.09091;0.9545 1 0.04545;1 1 0;1 0.95
0;1 0.9 0;1 0.85 0;1 0.8 0;1 0.75 0;1 0.7 0;1 0.65 0;1 0.6 0;1 0.55 0;1 0.5 0;1 0.45 0;1 0.4
0;1 0.35 0;1 0.3 0;1 0.25 0;1 0.2 0;1 0.15 0;1 0.1 0;1 0.05 0;1 0 0;1 0 0]);
```

```
subplot(2,2,1)
imagesc(yD, xD, Pratio_a1)
```

```
colorbar
caxis([.25 1.25])
axis image
grid on
```

```
xlim([-12 12])
ylim([-3 36])
```

```
set(gca,'YTick',[-5 0 5 10 15 20 25 30 35])
set(gca,'XTick',[-10 -5 0 5 10])
```

```
xlabel('Y / D','FontWeight','bold');
ylabel('X / D','FontWeight','bold');
```

```
subplot(2,2,2)
imagesc(yD, xD, Pratio_data)
```

```
colorbar
caxis([.25 1.25])
axis image
grid on
```

```
xlim([-12 12])
ylim([-3 36])
```

```
set(gca,'YTick',[-5 0 5 10 15 20 25 30 35])
set(gca,'XTick',[-10 -5 0 5 10])
```

```
xlabel('Y / D','FontWeight','bold');
ylabel('X / D','FontWeight','bold');
```

```
%
% %extract centerline data
%
```

```
CL_0_location = find(yD == 0);
```

```

CL_5_location = find(abs(yD - 5) <= 0.02, 1);
CL_10_location = find(yD == 10);
CL_n5_location = find(abs(yD + 5) <= 0.02, 1);
CL_n10_location = find(yD == -10);

CL_0 = eff(:,CL_0_location);
save(ofile2, 'xD', 'CL_0');

figure
subplot(2,2,1)
plot(xD, eff(:,CL_0_location), 'g', ...
     xD, eff(:,CL_5_location), 'r',...
     xD, eff(:,CL_10_location), 'b',...
     xD, eff(:,CL_n5_location), 'm',...
     xD, eff(:,CL_n10_location), 'k',...
     'LineWidth',2)

legend show
legend('Y/D = 0','Y/D = +5','Y/D = 10', 'Y/D = -5','Y/D = -10')

set(gca,'YTick',[0 0.1 0.2 0.3 0.4 0.5 0.6 0.7 0.8 0.9], 'YMinorTick', 'on')
set(gca,'XTick',[0 5 10 15 20 25 30 35], 'XMinorTick', 'on')

xlim([0 40]);
ylim([0 0.9]);

grid on

xlabel('X / D','FontWeight','bold');
ylabel('h','FontWeight','bold','FontSize',14,'FontName','Symbol');

set(legend,'Location','NorthEast','FontWeight','bold',...
     'FontSize',8);
%
% %-----
%
% %extract lateral average data

ylow_location = find(yD >= low_yd, 1);
yhigh_location = find(yD >= high_yd, 1);

xlow_location = find(xD >= low_xd, 1);
xhigh_location = find(xD >= high_xd, 1);

eff_lat_avg = eff(:,ylow_location:yhigh_location);

```

```

[lat_x, lat_y] = size(eff_lat_avg);

for jj = 1 : length(xD)
    sum(jj) = 0;

    for ii = ylow_location : yhigh_location
        sum(jj) = sum(jj) + eff(jj,ii);
    end

    lat_avg(jj) = sum(jj) / (yhigh_location - ylow_location + 1); % 1 is added to
                                                                    % ensure the endpoints are
                                                                    % included in the division
end

save(ofile3, 'xD', 'lat_avg');

figure
subplot(2,2,1)
plot(xD, lat_avg, 'LineWidth',2)

set(gca,'YTick',[0 0.1 0.2 0.3 0.4 0.5 0.6 0.7 0.8 0.9], 'YMinorTick', 'on')
set(gca,'XTick',[0 5 10 15 20 25 30 35], 'XMinorTick', 'on')

xlim([0 40]);
ylim([0 0.5]);

grid on

xlabel('X / D','FontWeight','bold');
ylabel('h','FontWeight','bold','FontSize',14,'FontName','Symbol');

% overall average

eff_overall_avg = eff(xlow_location:xhigh_location,ylow_location:yhigh_location);
stanford_overall_average = mean(mean(eff_overall_avg))

toc % stop internal timer

```

```

%*****
%*           PSP EXPERIMENTAL MEASUREMENT TECHNIQUE
%*           PSP – Centerline Film Cooling Effectiveness Profiles
%*
%*****

% ***** CENTERLINE DATA CONVERSION FOR TECPLOT *****

close all;
clear all;
clc;

% Load centerline data
data = load('Round\DR=1\M=0.5\eff11_cl.mat');
xD = data.xD;
eff_cl = data.CL_0;

% Create data file for Tecplot
fid = fopen('Watson CL Round DR_1p0_M0p5_cl.dat', 'w');
fprintf(fid, 'zone \n');

% Convert data to
for i = 1 : length(eff_cl)
    fprintf(fid, '%6.4f %6.4f \n', xD(i), eff_cl(i));
end

fclose(fid);

```

```

%*****
%*           PSP EXPERIMENTAL MEASUREMENT TECHNIQUE
%*           PSP – Laterally Averaged Film Cooling Effectiveness Profiles
%*
%*****

% ***** LATERAL AVERAGE DATA CONVERSION FOR TECPLOT*****

close all;
clear all;
clc;

% Load laterally averaged data
data = load('Round\DR = 1.0\M=1.0\eff11_latavg2p5.mat');
xD = data.xD;
eff_cl = data.lat_avg;

% Create data file for Tecplot
fid = fopen('Watson LAT Round DR_1p0_M1p0_latavg2p5.dat', 'w');
fprintf(fid, 'zone \n');

for i = 1 : length(eff_cl)
    fprintf(fid, '%6.4f %6.4f \n', xD(i), eff_cl(i));
end

fclose(fid);

```

## APPENDIX D

### Detailed PSP Uncertainty Analysis

The uncertainty of the film cooling effectiveness obtained with the PSP technique is evaluated using the technique of Kline and McClintock [78]. The following sample calculation is presented for the baseline shaped hole at DR = 1.0 and M = 1.5. *Figure D.1*

$\eta = \frac{T_{aw} - T_{inf}}{T_c - T_{inf}}$	Definition of film cooling effectiveness
$\eta = \frac{c_{mix} - c_{air}}{c_{N2} - c_{air}}$	The temperatures can be related to concentrations by the heat mass transfer analogy, where c represents the concentration of oxygen.
$\eta = \frac{c_{air} - c_{mix}}{c_{air}}$	The nitrogen used as coolant is pure nitrogen, with no more than trace amounts of oxygen.
$\eta = \frac{\left(\frac{P}{P_{ref}}\right)_{air} - \left(\frac{P}{P_{ref}}\right)_{N2}}{\left(\frac{P}{P_{ref}}\right)_{air}}$	The concentrations of oxygen can be related to the partial pressure of oxygen, where P is the pressure.
$\left(\frac{P}{P_{ref}}\right)_{air} = 0.2648 \cdot \left(\frac{I_{ref} - I_{black}}{I_{air} - I_{black}}\right)^3 - 0.181 \cdot \left(\frac{I_{ref} - I_{black}}{I_{air} - I_{black}}\right)^2 + 1.0234 \cdot \frac{I_{ref} - I_{black}}{I_{air} - I_{black}} - 0.1106$	where I is the intensity measured by the CCD camera, emitted by the PSP
$\left(\frac{P}{P_{ref}}\right)_{N2} = 0.2648 \cdot \left(\frac{I_{ref} - I_{black}}{I_{N2} - I_{black}}\right)^3 - 0.181 \cdot \left(\frac{I_{ref} - I_{black}}{I_{N2} - I_{black}}\right)^2 + 1.0234 \cdot \frac{I_{ref} - I_{black}}{I_{N2} - I_{black}} - 0.1106$	
$\eta = \frac{\left[ 0.2648 \cdot \left(\frac{I_{ref} - I_{black}}{I_{air} - I_{black}}\right)^3 - 0.181 \cdot \left(\frac{I_{ref} - I_{black}}{I_{air} - I_{black}}\right)^2 + 1.0234 \cdot \frac{I_{ref} - I_{black}}{I_{air} - I_{black}} - 0.1106 \right] \dots}{0.2648 \cdot \left(\frac{I_{ref} - I_{black}}{I_{air} - I_{black}}\right)^3 - 0.181 \cdot \left(\frac{I_{ref} - I_{black}}{I_{air} - I_{black}}\right)^2 + 1.0234 \cdot \frac{I_{ref} - I_{black}}{I_{air} - I_{black}} - 0.1106}$	All of the equations are combined to get the calculated effectiveness in terms of the measured values only in order to use the method of Kline and McLintock to determine the uncertainty of the film cooling effectiveness.

Figure D.1: Derivation of film cooling effectiveness in terms of measured effectiveness

shows the derivation of the film cooling effectiveness in terms of the measured intensity values from the four images used to determine film cooling effectiveness.

To calculate uncertainty in this sample calculation, two points are chosen with high and low effectiveness values. The intensity are entered into the Mathcad worksheet. The uncertainty of each intensity value is calculated by finding the standard deviation of the pressure ratio for the air test. The pressure ratio should be equal to one across the surface of the plate, but errors in the camera and effects of calibration error and the interference of the tunnel and other factors cause the pressure ratio to not exactly equal one. The standard deviation of the pressure ratio image is considered to be the percent uncertainty. This process is shown in *Figure D.2*.

The derivatives are then calculated using Mathcad, and that analysis is shown in *Figure D.3*. The derivatives are incredibly long, so the font is small in the text, but the symbolic derivative in Mathcad is used.

$$\omega_{\eta} = \sqrt{\left(\frac{\delta\eta}{\delta I_{\text{black}}} \cdot \omega_{I_{\text{black}}}\right)^2 + \left(\frac{\delta\eta}{\delta I_{\text{ref}}} \cdot \omega_{I_{\text{ref}}}\right)^2 + \left(\frac{\delta\eta}{\delta I_{\text{air}}} \cdot \omega_{I_{\text{air}}}\right)^2 + \left(\frac{\delta\eta}{\delta I_{\text{N2}}} \cdot \omega_{I_{\text{N2}}}\right)^2}$$

$$I_{\text{black}} := \begin{pmatrix} 390 \\ 389 \end{pmatrix} \quad I_{\text{ref}} := \begin{pmatrix} 1696 \\ 1395 \end{pmatrix} \quad I_{\text{air}} := \begin{pmatrix} 1694 \\ 1449 \end{pmatrix} \quad I_{\text{N2}} := \begin{pmatrix} 4541 \\ 1531 \end{pmatrix} \quad \begin{array}{l} \text{for } \eta = .7981 \\ \text{for } \eta = .0991 \end{array} \quad \text{stdevPratio\_air} := 0.0826$$

$$\omega_{I_{\text{black}}} := I_{\text{black}} \cdot \text{stdevPratio\_air} \quad \omega_{I_{\text{ref}}} := I_{\text{ref}} \cdot \text{stdevPratio\_air}$$

$$\omega_{I_{\text{air}}} := I_{\text{air}} \cdot \text{stdevPratio\_air} \quad \omega_{I_{\text{N2}}} := I_{\text{N2}} \cdot \text{stdevPratio\_air}$$

The % uncertainty is found by the standard deviation of the air pressure ratio, which should be uniformly one. The error in this calculation reflects calibration and camera measurement error.

Figure D.2: Derivation of uncertainty as a function of measured intensity

$$\begin{aligned}
\delta\eta_{ref} &= \left[ \frac{1.0234}{I_{air} - I_{black}} - \frac{1.0234}{(I_{N2} - I_{black})^2} + \frac{0.181(2I_{ref} - 2I_{black})}{(I_{air} - I_{black})^2} - \frac{0.181(2I_{ref} - 2I_{black})}{(I_{N2} - I_{black})^3} + \frac{0.7944(I_{ref} - I_{black})^2}{(I_{air} - I_{black})^3} - \frac{0.7944(I_{ref} - I_{black})^2}{(I_{N2} - I_{black})^4} \right] \cdot \left( -1.211 \times 10^{-5} \right) \\
\delta\eta_{air} &= \left[ \frac{1.0234I_{ref} + -1.0234I_{black}}{I_{air} - I_{black}} - \frac{0.181(I_{ref} - I_{black})^2}{(I_{air} - I_{black})^2} + \frac{0.2648(I_{ref} - I_{black})^3}{(I_{air} - I_{black})^3} - 0.1106 \right] \cdot \left( -2.284 \times 10^{-4} \right) \\
\delta\eta_{N2} &= \left[ \frac{1.0234I_{ref} + -1.0234I_{black}}{I_{air} - I_{black}} - \frac{0.181(I_{ref} - I_{black})^2}{(I_{air} - I_{black})^2} + \frac{0.2648(I_{ref} - I_{black})^3}{(I_{air} - I_{black})^3} - 0.1106 \right] \cdot \left( -1.217 \times 10^{-3} \right)
\end{aligned}$$

$$\delta\eta_{\delta I_{N2}} = \frac{\frac{1.0234 \cdot I_{ref} + -1.0234 \cdot I_{black}}{(I_{N2} - I_{black})^2} - \frac{0.362 \cdot (I_{ref} - I_{black})^2}{(I_{N2} - I_{black})^3} + \frac{0.7944 \cdot (I_{ref} - I_{black})^3}{(I_{N2} - I_{black})^4}}{\frac{1.0234 \cdot I_{ref} + -1.0234 \cdot I_{black}}{I_{air} - I_{black}} - \frac{0.181 \cdot (I_{ref} - I_{black})^2}{(I_{air} - I_{black})^2} + \frac{0.2648 \cdot (I_{ref} - I_{black})^3}{(I_{air} - I_{black})^3} - 0.1106}} = \begin{pmatrix} 7.498 \times 10^{-5} \\ 1.103 \times 10^{-3} \end{pmatrix}$$

Figure D.3: Partial derivatives used to calculate uncertainty

Following the calculation of the derivatives, the uncertainty can be directly calculated. The film cooling effectiveness is also recalculated to ensure no mistakes were made. The uncertainty is divided by the effectiveness to determine the percent uncertainty. These calculations are shown in *Figure D.4*.

The equations derived with Mathcad are then copied into a matlab code to determine uncertainty for every pixel. The Matlab code is shown below and the figures generated by the Matlab code are shown in *Figure D.5*.

$$\omega_{\eta} := \sqrt{(\delta\eta\delta I_{\text{black}} \cdot \omega_{I_{\text{black}}})^2 + (\delta\eta\delta I_{\text{ref}} \cdot \omega_{I_{\text{ref}}})^2 + (\delta\eta\delta I_{\text{air}} \cdot \omega_{I_{\text{air}}})^2 + (\delta\eta\delta I_{\text{N2}} \cdot \omega_{I_{\text{N2}}})^2} = \begin{pmatrix} 0.043 \\ 0.198 \end{pmatrix}$$

$$\eta := \frac{\left[ 0.2648 \cdot \left( \frac{I_{\text{ref}} - I_{\text{black}}}{I_{\text{air}} - I_{\text{black}}} \right)^3 - 0.181 \cdot \left( \frac{I_{\text{ref}} - I_{\text{black}}}{I_{\text{air}} - I_{\text{black}}} \right)^2 + 1.0234 \cdot \frac{I_{\text{ref}} - I_{\text{black}}}{I_{\text{air}} - I_{\text{black}}} - 0.1106 \right] \dots}{0.2648 \cdot \left( \frac{I_{\text{ref}} - I_{\text{black}}}{I_{\text{air}} - I_{\text{black}}} \right)^3 - 0.181 \cdot \left( \frac{I_{\text{ref}} - I_{\text{black}}}{I_{\text{air}} - I_{\text{black}}} \right)^2 + 1.0234 \cdot \frac{I_{\text{ref}} - I_{\text{black}}}{I_{\text{air}} - I_{\text{black}}} - 0.1106} = \begin{pmatrix} 0.798 \\ 0.1001 \end{pmatrix}$$

$$\frac{\omega_{\eta}}{\eta} = \begin{pmatrix} 0.054 \\ 1.976 \end{pmatrix}$$

Figure D.4: Determination of percent uncertainty

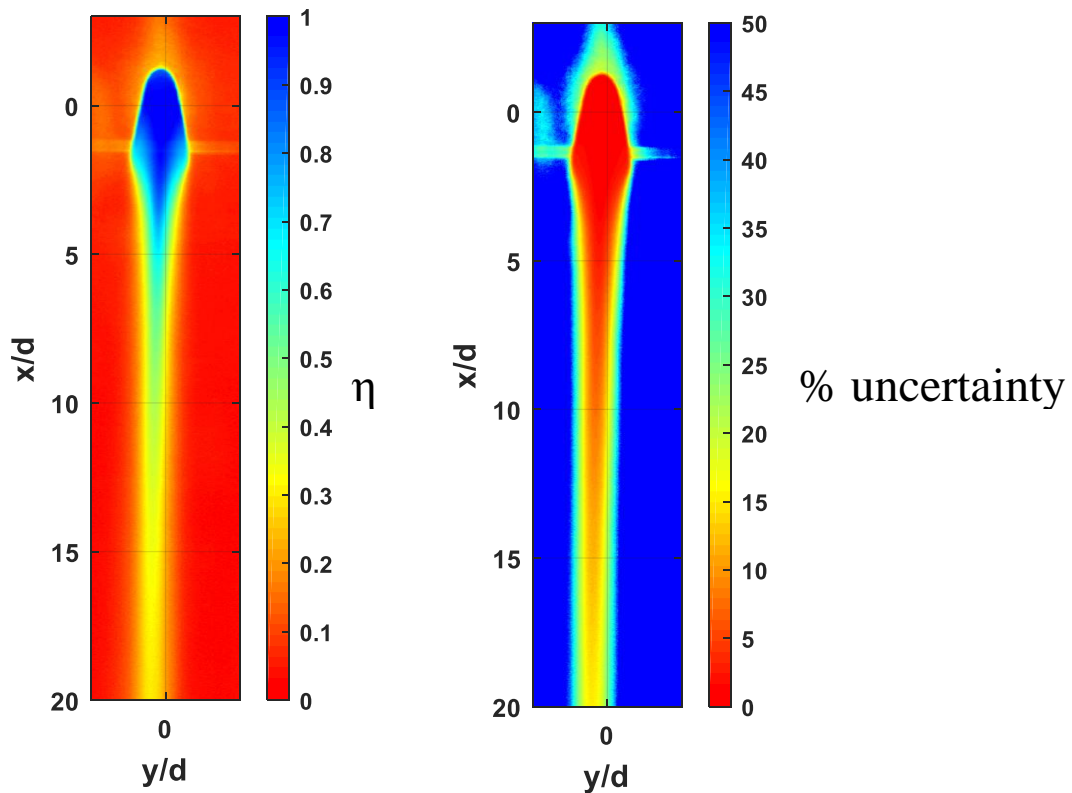


Figure D.5: Film cooling effectiveness and percent uncertainty

```

%*****
%*
%*          PSP EXPERIMENTAL MEASUREMENT TECHNIQUE
%* PSP - Detailed Pressure and Film Cooling Effectiveness Distributions
%*
%*****

% ***** PSP EXPERIMENTAL UNCERTAINTY *****

% From previously created intensity data files (Intensity.m) and input
% calibration data, calculate the static pressure and film cooling
% effectiveness at each pixel.

% STATIC PRESSURE
%          P/Pref = P/Pref = a3(Iref/I)^3 + a2(Iref/I)^2 + a1(Iref/I) +
a0

% Pressure Ratio is calculated based on the user defined calibration.
% Input Data Files:    black.dat
%                      ref.dat
%                      a1.dat, a2.dat, n1.dat, n2.dat, ar1.dat,
ar2.dat, etc.
% Output Data Files:  alpres.dat, etc.

% FILM COOLING EFFECTIVENESS
%          eff = [(P/Pref)air - (P/Pref)n2] / (P/Pref)air
% Film Cooling Effectiveness is calculated for two density ratios
based on
% coolant flows of air & nitrogen (DR = 1) and air & argon (DR = 1.5)
% Input Data Files:    alpres.dat, a2pres.dat, n1pres.dat, n2pres.dat,
%                      ar1pres.dat, ar2pres.dat, etc
% Output Data Files:  N2effect11.dat, N2effect12.dat,
%                      N2effect21.dat, N2effect22.dat,
%                      AReffect11.dat, AReffect12.dat,
%                      AReffect21.dat, AReffect22.dat,

clear all      % clear all saved variables
close all     % close all open windows
clc           % clear command window

tic          % start internal timer

% *****
% *****
% *****
% *****

% -----          CHANGE INPUTS AS NEEDED          -----
---
```

```

ofile = 'eff11.mat';      % open (create) specified data file
ofile2 = 'eff11_cl.mat';  % open (create) specified data file
ofile3 = 'eff11_latavg.mat'; % open (create) specified data file

% Define Size of Images
% These must match those used for black and reference
NX = 808;
NY = 847;

% Input Coefficients from PSP Calibration
%  $P/P_{ref} = a_3(I_{ref}/I)^3 + a_2(I_{ref}/I)^2 + a_1(I_{ref}/I) + a_0$ 
a_0 = -0.1106;
a_1 = 1.0234;
a_2 = -0.181;
a_3 = 0.2648;

% Define Y boundaries for Lateral Average
% For example spanwise average:  $-1.0 < Y/D < 1.0$ 

% Lower Limit of Average
low_yd = -2.5;

% Upper Limit of Average
high_yd = 2.5;

% Define Y boundaries for Overall Average
% For example spanwise average:  $-1.0 < Y/D < 1.0$ 
%                                      $+2.0 < X/D < 14$ 

% Lower Limit of Average
low_xd = 0;

% Upper Limit of Average
high_xd = 10.0;

% Load Intensity Data Files (Ib, Iref, test data: Ia1, Ia2, In1, In2)
blackdat = load('black.mat'); % Ib
xD = blackdat.xD;
yD = blackdat.yD;
blackint = blackdat.inten_matrix;

refdat = load('ref.mat'); % Iref
refint = refdat.inten_matrix;

airdat = load('a1.mat'); % Ia1
airint = airdat.inten_matrix;

mixdat = load('mix1.mat'); % In1
mixint = mixdat.inten_matrix;

W = size(blackint, 1);
H = size(blackint, 2);

```

```

Iratio_a1 = (refint - blackint)./(airint - blackint);
Iratio_data = (refint - blackint)./(mixint - blackint);

Pratio_a1 = a_3.*(Iratio_a1).^3 + a_2.*(Iratio_a1).^2 +
a_1.*(Iratio_a1) + a_0;
Pratio_data = a_3.*(Iratio_data).^3 + a_2.*(Iratio_data).^2 +
a_1.*(Iratio_data) + a_0;

eff = (Pratio_a1 - Pratio_data)./ Pratio_a1;

save(ofile, 'xD', 'yD', 'eff');

%-----
---

%Use standard deviation of air pressure ratio as percent uncertainty of
%measured effectiveness for all pixels
uIblack = std2(Pratio_a1)*blackint;
uIref = std2(Pratio_a1)*refint;
uIair = std2(Pratio_a1)*airint;
uImix = std2(Pratio_a1)*mixint;

%Calculate Uncertainty for Intensity Ratio for N2 and Air
dIref = 1./(mixint - blackint);
dIblack = (refint - blackint)./(mixint - blackint).^2 - dIref;
dI = -(refint - blackint)./(mixint - blackint).^2;
uIrat_N2 = sqrt((dIref.*uIref).^2 + (dIblack.*uIblack).^2 +
(dI.*uImix).^2);

dIref = 1./(airint - blackint);
dIblack = (refint - blackint)./(airint - blackint).^2 - dIref;
dI = -(refint - blackint)./(airint - blackint).^2;
uIrat_air = sqrt((dIref.*uIref).^2 + (dIblack.*uIblack).^2 +
(dI.*uIair).^2);

% Calculate Uncertainty for Pressure Ratio for N2 and Air
dIrat = 3*a_3*Iratio_data.^2 + 2*a_2*Iratio_data + a_1;
uPrat_N2 = sqrt((dIrat.*uIrat_N2).^2);

dIrat = 3*a_3*Iratio_a1.^2 + 2*a_2*Iratio_a1 + a_1;
uPrat_air = sqrt((dIrat.*uIrat_air).^2);

% Calculate Uncertainty for Film Cooling Effectiveness
dPratair = (Pratio_data-Pratio_a1)./Pratio_a1.^2+1./Pratio_a1;
dPratN2 = -1./Pratio_a1;

Ueff = sqrt((dPratair.*uPrat_air).^2 + (dPratN2.*uPrat_N2).^2);
Percent_Ueta = Ueff./eff*100;
fprintf('Experimental uncertainty of high film cooling (~0.8) is %4.2f
percent \n',Percent_Ueta(1))

```

```
fprintf('Experimental uncertainty of low film cooling (~0.1) is %4.2f
percent \n',Percent_Ueta(2))
```

```
figure
```

```
colormap([1 0 0; 1 0 0; 1 0.0526 0; 1 0.1053 0; 1 0.1579 0; 1 0.2105 0;
1 0.2632 0; 1 0.3158 0; 1 0.3684 0; 1 0.4211 0; 1 0.4737 0; 1 0.5263 0;
1 0.5789 0; 1 0.6316 0; 1 0.6842 0; 1 0.7368 0; 1 0.7895 0; 1 0.8421 0;
1 0.8947 0; 1 0.9474 0; 1 1 0; 0.9545 1 0.0455; 0.9091 1 0.0909;
0.8636 1 0.1364; 0.8182 1 0.1818; 0.7727 1 0.2273; 0.7273 1
0.2727; 0.6818 1 0.3182; 0.6364 1 0.3636; 0.5909 1 0.4091;
0.5455 1 0.4545; 0.5000 1 0.5000; 0.4545 1 0.5455; 0.4091 1 0.5909;
0.3636 1 0.6364; 0.3182 1 0.6818;0.2727 1 0.7273; 0.2273 1 0.7727;
0.1818 1 0.8182; 0.1364 1 0.8636; 0.0909 1 0.9091; 0.0455 1
0.9545; 0 1 1; 0 0.95 1; 0 0.9 1; 0 0.85 1;0
0.8 1; 0 0.75 1; 0 0.7 1; 0 0.65 1; 0 0.6 1; 0
0.55 1; 0 0.5 1; 0 0.45 1; 0 0.4 1; 0 0.35 1;0
0.3 1; 0 0.25 1; 0 0.2 1; 0 0.15 1; 0 0.10 1; 0 0.05 1; 0 0 1; 0 0 1]);
imagesc(yD, xD, Percent_Ueta)
```

```
colorbar
caxis([0 50])
```

```
axis image
grid on
```

```
xlim([-2.5 2.5]);
ylim([-3 20]);
```

```
set(gca, 'YTick', [-5 0 5 10 15 20 25 30 35], 'FontWeight', 'bold')
set(gca, 'XTick', [-15 -10 -5 0 5 10 15], 'FontWeight', 'bold')
```

```
xlabel('y/d', 'FontWeight', 'bold', 'FontSize', 12);
ylabel('x/d', 'FontWeight', 'bold', 'FontSize', 12);
```

```
figure
```

```
colormap([1 0 0; 1 0 0; 1 0.0526 0; 1 0.1053 0; 1 0.1579 0; 1 0.2105 0;
1 0.2632 0; 1 0.3158 0; 1 0.3684 0; 1 0.4211 0; 1 0.4737 0; 1 0.5263 0;
1 0.5789 0; 1 0.6316 0; 1 0.6842 0; 1 0.7368 0; 1 0.7895 0; 1 0.8421 0;
1 0.8947 0; 1 0.9474 0; 1 1 0; 0.9545 1 0.0455; 0.9091 1 0.0909;
0.8636 1 0.1364; 0.8182 1 0.1818; 0.7727 1 0.2273; 0.7273 1
0.2727; 0.6818 1 0.3182; 0.6364 1 0.3636; 0.5909 1 0.4091;
0.5455 1 0.4545; 0.5000 1 0.5000; 0.4545 1 0.5455; 0.4091 1 0.5909;
0.3636 1 0.6364; 0.3182 1 0.6818;0.2727 1 0.7273; 0.2273 1 0.7727;
0.1818 1 0.8182; 0.1364 1 0.8636; 0.0909 1 0.9091; 0.0455 1
0.9545; 0 1 1; 0 0.95 1; 0 0.9 1; 0 0.85 1;0
0.8 1; 0 0.75 1; 0 0.7 1; 0 0.65 1; 0 0.6 1; 0
0.55 1; 0 0.5 1; 0 0.45 1; 0 0.4 1; 0 0.35 1;0
0.3 1; 0 0.25 1; 0 0.2 1; 0 0.15 1; 0 0.10 1; 0 0.05 1; 0 0 1; 0 0 1]);
imagesc(yD, xD, eff)
```

```
colorbar
caxis([0 1.0])
```

```
axis image
grid on

xlim([-2.5 2.5]);
ylim([-3 20]);

set(gca, 'YTick', [-5 0 5 10 15 20 25 30 35], 'FontWeight', 'bold')
set(gca, 'XTick', [-15 -10 -5 0 5 10 15], 'FontWeight', 'bold')

xlabel('y/d', 'FontWeight', 'bold', 'FontSize', 12);
ylabel('x/d', 'FontWeight', 'bold', 'FontSize', 12);
```

## APPENDIX E

### S-PIV Uncertainty Analysis

The ability to calculate uncertainty was added to DaVis 3.2.2. The step added to the process shown by Watson [87] is shown in *Figure E.1*. The standard processing window is opened, and then the vector calculation parameter dialogue is opened. There is a new check box that allows the option to calculate uncertainty, as shown in the figure. Processing then proceeds as normal, with an additional step to calculate the uncertainty. Although no information is given about the calculation of uncertainty within DaVis, Dr. Steve Anderson from LaVision Inc. has conveyed that the uncertainty is calculated by the method established by Wieneke [85]. The uncertainty in the streamwise (x in this work, z in DaVis) direction for a sample case is presented in *Figure E.2*. The uncertainty is approximately 2 m/s in the region shown which is where the velocity and vorticity distributions were determined for this case. The lateral (y) uncertainty is shown in *Figure E.3*. The normal (z in this work, x in DaVis) uncertainty is shown in *Figure E.4*. The lateral and normal uncertainties are less than 1 m/s for the region investigated.

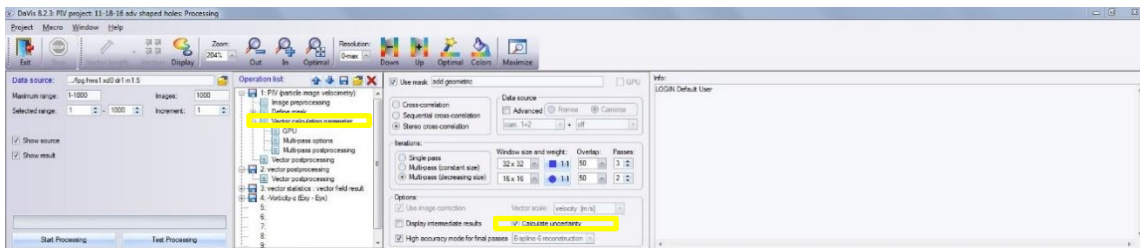


Figure E.1: S-PIV uncertainty processing

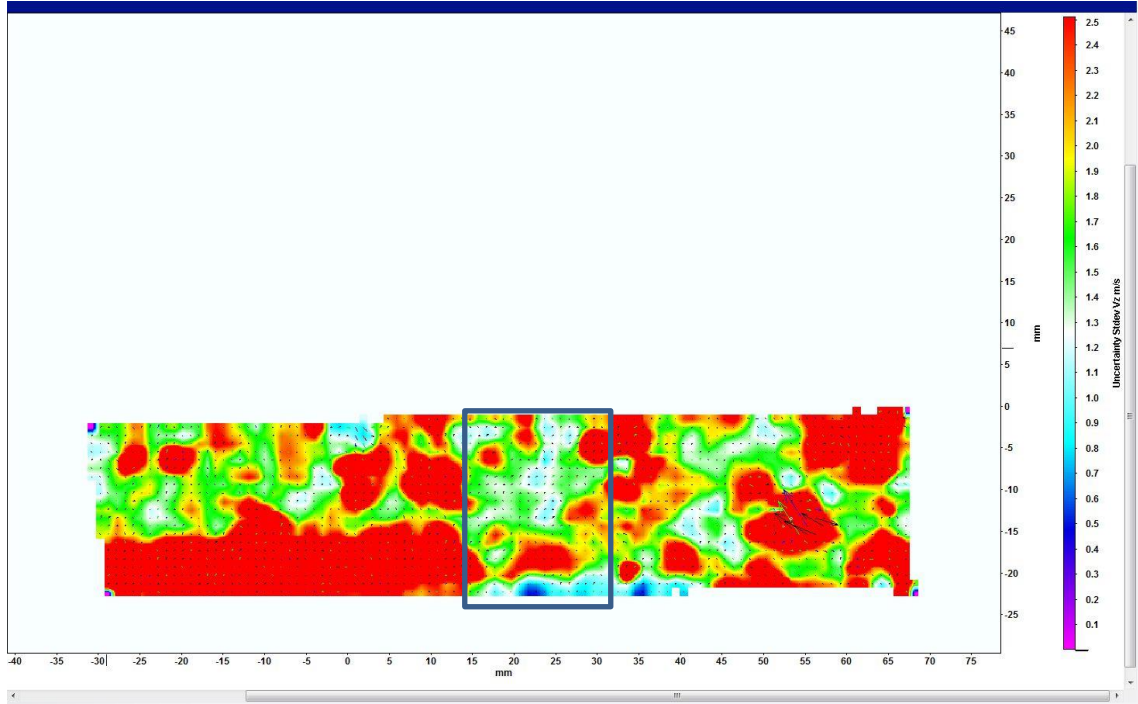


Figure E.2: Uncertainty in streamwise velocity

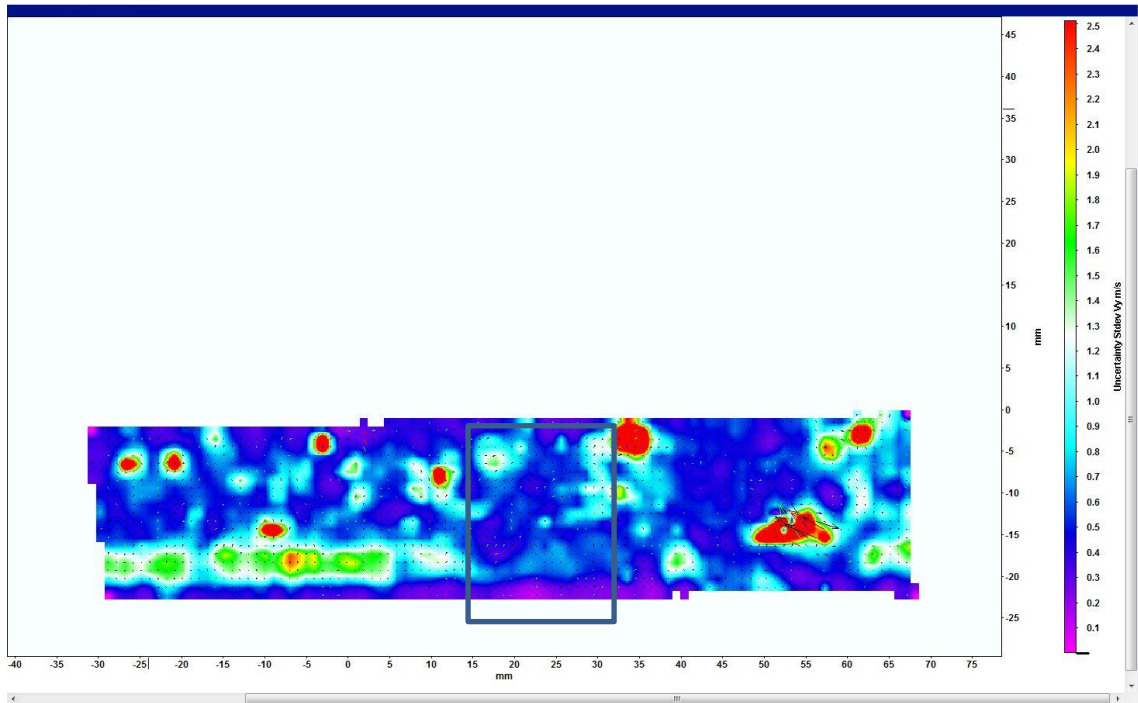


Figure E.3: Uncertainty in lateral velocity

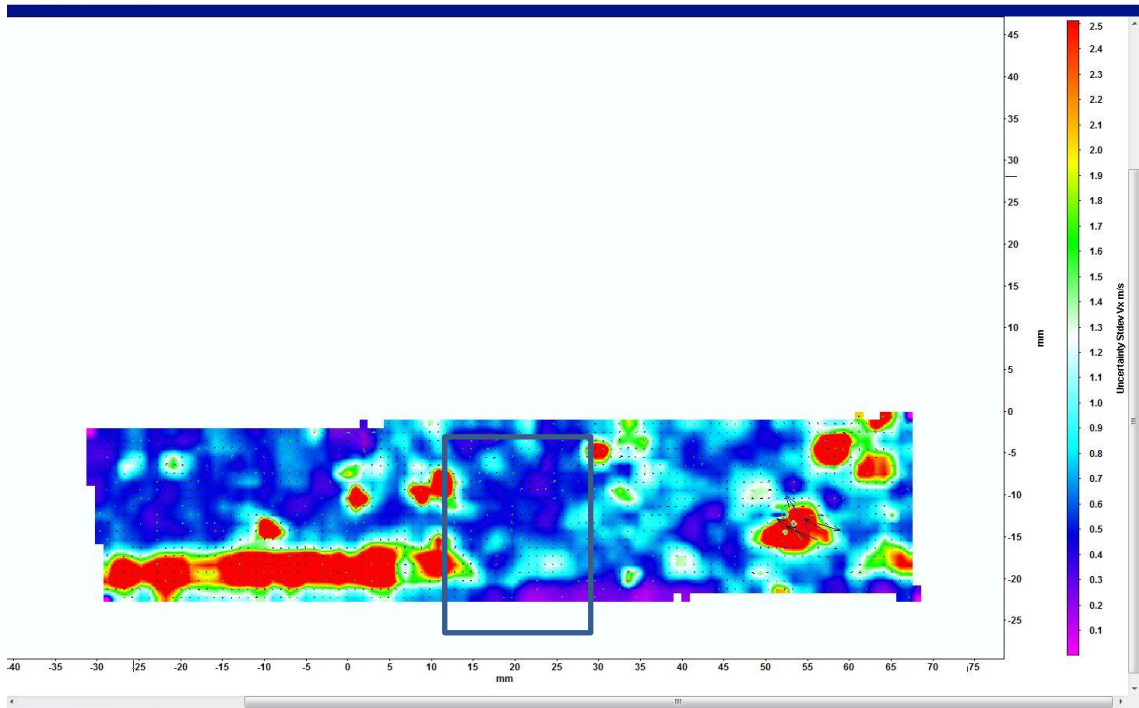


Figure E.4: Uncertainty in normal velocity

## REFERENCES

- [1] Han, J.C., Dutta, S., and Ekkad, S.V., 2000, Gas Turbine Heat Transfer and Cooling Technology, Taylor & Francis, New York, pp. 1-20, Chap. 1, pp. 531-271, Chap. 6.
- [2] Wright, L. M., Gao, Z., Varvel, T. A., and Han, J. C., 2005, "Assessment of Steady State PSP, TSP, and IR Measurement Techniques for Flat Plate Film Cooling," ASME Paper No. HT2005-72363.
- [3] Bogard, D. and Thole. K., 2005, "Gas Turbine Film Cooling," *AIAA J. Propulsion and Power*, pp. 1-3.
- [4] Baldauf, S., Schulz A., and Wittig S., 2001, "High-Resolution Measurements of Local Effectiveness from Discrete Hole Film Cooling," *ASME J. Turbomachinery*, 123(4), pp. 758-65.
- [5] Eriksen, V. L., and Goldstein, R. J., 1974, "Heat Transfer and Film Cooling Following Injection through Inclined Circular Tubes," *ASME J. Heat Transfer*, 96(2), pp. 239-45.
- [6] Russin, R.A., Alfred D., and Wright L.M., 2009, "Measurement of Detailed Heat Transfer Coefficient and Film Cooling Effectiveness Distributions using PSP and TSP," ASME Paper No. GT2009-59975.
- [7] Johnson, B., Tian, W., Zhang, K., Hu, H., 2014, "An Experimental Study of Density Ratio Effects on the Film Cooling Injection from Discrete Holes by Using PIV and PSP Techniques," *International J. Heat and Mass Transfer*, 76, pp. 337-49.
- [8] Sinha, A. K., Bogard, D. G., and Crawford, M. E., 1991, "Film-Cooling Effectiveness Downstream of a Single Row of Holes with Variable Density Ratio," *ASME J. Turbomachinery*, 113(3), pp. 442-49.
- [9] Pedersen, D. R., Eckert, E. R. G., and Goldstein, R. J., 1977, "Film Cooling with Large Density Differences between the Mainstream and the Secondary Fluid Measured by the Heat-Mass Transfer Analogy," *ASME J. Heat Transfer*, 99(4), pp. 620-627.
- [10] Thole, K. A., Sinha, A., Bogard, D. G., and Crawford, M. E., 1992, "Mean Temperature Measurements of Jets with a Crossflow for Gas Turbine Film Cooling Application," *Rotating Machinery Transport Phenomena*, pp. 69-85.

- [11] Saumweber, C. and Schulz, A., 2008, "Free-Stream Effects on the Cooling Performance of Cylindrical and Fan-Shaped Cooling Holes," ASME Paper No. GT2008-51030.
- [12] Bons, J.P., MacArthur, C.D., and Rivir, R.B., 1994 "The Effect of High Free-Stream Turbulence on Film Cooling Effectiveness," ASME Paper No. 94-GT-51.
- [13] Foster, N. W. and Lampard, D., 1980, "The Flow and Film Cooling Effectiveness Following Injection Through a Row of Holes," *ASME J. Engineering for Power*, 102, pp. 584-588.
- [14] Kohli, A. and Bogard, D., 1997, "Adiabatic Effectiveness, Thermal Fields, and Velocity Fields for Film Cooling with Large Angle Injection," *ASME J. Turbomachinery*, 119, pp. 352-358.
- [15] Schmidt, D. L., Sen, B., and Bogard, D. G., 1996, "Film-Cooling With Compound Angle Holes: Adiabatic Effectiveness," *ASME J. Turbomachinery*, 118(4), pp. 807-813.
- [16] Bunker, R S. 2005 "A Review of Shaped Hole Turbine Technology," *ASME J. Heat Transfer*, 127(4), pp. 441-53.
- [17] Goldstein, R.J., 1971, "*Film cooling. Advances in heat transfer*, 7, pp.321-379.
- [18] Zhang, L. J. and Jaiswal, R. S., 2001, "Turbine Nozzle Endwall Film Cooling Study Using Pressure Sensitive Paint," ASME Paper No. 2001-GT-0147.
- [19] Jia, R., Leger, B., Miron, P., and Sunden, B., 2005, "A Numerical and Experimental Investigation of the Slot Film-Cooling Jet with Various Angles," *ASME J. Turbomachinery*, 127, pp. 635-645.
- [20] Goldstein, R.J., Eckert, E.G., and Burggraf, R., 1974, "Effects of Hole Geometry and Density on Three Dimensional Film-Cooling," *International J. Heat and Mass Transfer*, 17, pp. 595-606.
- [21] Gritsch, M., Schulz, A., and Wittig, S., 1988, "Adiabatic Wall Effectiveness Measurements of Film Cooling Holes with Expanded Exits," *ASME J. Turbomachinery*, 123(3), pp. 549-556.
- [22] Yu, Y., Yen, C. -H., Shih, T. I. -P., Chyu, M. K., 2002, "Film Cooling Effectiveness and Heat Transfer Coefficient Distributions Around Diffusion Shaped Holes," *ASME J. Heat Transfer*, 124, pp. 820-827.
- [23] Saumweber, C. and Schulz, A., 2008, "Free-Stream Effects on the Cooling Performance of Cylindrical and Fan-Shaped Cooling Holes," ASME Paper No. GT2008-51030.

- [24] Saumweber, C., Schulz, A., and Wittig, S., 2002, "Free-Stream Turbulence Effects on Film Cooling with Shaped Holes," ASME Paper No. GT2002-30170.
- [25] Haven, B.A., Yamagata, D.K., Kurosaka, M., Yamawaki, S. and Maya, T., 1997, "Anti-Kidney Vortices in Shaped Holes and Their Influence on Film Cooling Effectiveness," ASME Paper No. 97-GT-45.
- [26] Ekkad, S., Lu, Y., and Nasir, H., 2005, "Film Cooling from a Row of Holes Embedded in Transverse Slots," ASME Paper No. GT2005-68598.
- [27] Lu, Y., Dhungel, A., Ekkad, S., and Bunker, R., 2007, "Effect of Trench Width and Depth on Film Cooling from Cylindrical Holes Embedded in Trenches," ASME Paper No. GT2007-27388.
- [28] Dorrington, R., Bogard, D.G., Bunker, R., and Dees, J., 2007, "Film Effectiveness Performance for Coolant Holes Imbedded in Various Shallow Trench and Crater Depressions," ASME Paper No. GT2007-27992.
- [29] Lu, Y., Dhungel, A., Ekkad, S., and Bunker, R., 2007, "Film Cooling Measurements for Cratered Cylindrical Inclined Holes," ASME Paper No. GT2007-27386.
- [30] Sargison, J.E., Guo, S.M., Oldfield, M.L.G., Lock, G.D., and Rawlinson, A.J., 2001, "A Converging Slot-Hole Film-Cooling Geometry. Part 1: Low-Speed Float-Plate Heat Transfer and Loss," ASME Paper No. 2001-GT-0126.
- [31] Kusterer, K., Bohn, D., Sugimoto, T., and Tanaka, R., 2006, "Double-Jet Ejection of Cooling Air for Improved Film Cooling," ASME Paper No. GT2006-90854.
- [32] Wright, L.M., Brown, C.P., Harmon, W.V., and McClain, S.T., 2013, "Assessment of a Double Hole Film Cooling Geometry Using S-PIV and PSP," ASME Paper No. GT2013-94614
- [33] Heidmann, J. and Ekkad, S., 2007, "A Novel Anti-Vortex Turbine Film Cooling Hole Concept," ASME Paper No. GT2007-27528.
- [34] Dhungel, A., Lu, Y., Phillips, A., Ekkad, S., and Heidmann, J., 2007, "Film Cooling From a Row of Holes Supplemented With Antivortex Holes," ASME Paper No. GT2007-27419.
- [35] LeBlanc, C., Narzary, D., and Ekkad, S.V., 2001, "Film Cooling Performance of an Anti-Vortex Hole on a Flat Plate," AJTEC2011-44161, 2011, AJTEC, Honolulu, HI, March 2011.
- [36] Chi, Z., Ren, J., Jiang, H., and Zang, S., 2016, "Geometrical Optimization and Experimental Validation of a Tripod Film Cooling Hole With Asymmetric Side Holes," *ASME J. Heat Transfer*, 138, pp. 1-12.

- [37] Kim, SM., Lee, KD., and Kim, KY., 2012, "A comparative analysis of various shaped film cooling holes," *J. Heat Mass Transfer*, 48, pp. 1-11.
- [38] Okita, Y. and Nishiura, M., 2007, "Film Effectiveness Performance of an Arrowhead-Shaped Film-Cooling Hole Geometry," *ASME J. of Turbomachinery*, 129, pp. 331-339.
- [39] Kollati, V. R., Srinivasan, B., Venkataramanan, J., Guntu, S., Liu, J., Crites, D. C., Tapia, L., and Malak, M. F., "Gas turbine engine components with cooling hole trenches," U.S. Patent 20130315710 A1, Nov 28, 2013.
- [40] Xu, J., Zelesky, M. F., Kholi, A., Gleiner, M. S., "Multi-lobed cooling hole and method of manufacture," WO 2013165510 A3, Feb 12, 2013.
- [41] Lutum, E., J. Wolfersdorf, V., Semmler, K., Dittmar, J., and Weigand, B., 2001, "An Experimental Investigation of Film Cooling on a Convex Surface Subjected to Favorable Pressure Gradient Flow," *International J. Heat and Mass Transfer*, 44(5), pp. 939-51.
- [42] Teekaram, A. J. H., Forth, C. J. P., and Jones, T. V., 1991, "Film Cooling in the Presence of Mainstream Pressure Gradients," *ASME J. Turbomachinery*, 113(3), pp. 484-92.
- [43] Liess, C., 1975, "Experimental Investigation of Film Cooling with Ejection from a Row of Holes for the Application to Gas Turbine Blades," *ASME J. Engineering for Gas Turbines and Power*, 97(1), pp. 21-27.
- [44] Schmidt, D. L., and Bogard, D. G., 1995, "Pressure Gradient Effects on Film Cooling," ASME Paper No. 95-GT-018.
- [45] Launder, B. E., and York, J., 1974, "Discrete-Hole Cooling in the Presence of Free Stream Turbulence and Strong Favorable Pressure Gradient," *International J. Heat and Mass Transfer*, 17(11), pp. 1403-1409.
- [46] Coletti, F., Elkins, C. J., and Eaton, J. K., 2012, "Three-Dimensional Velocity Measurements of Film Cooling Flow Under Favorable Pressure Gradient," ASME Paper No. GT2012-69402.
- [47] Wakeman, T. G., Maclin, H. M., Walker, A., "Film cooled combustor liner for gas turbine," EP0486133, May 20, 1992.
- [48] Andrews, G. E., Khalifa, I. M., Asere, A. A., and Bazdidi-Tehrani, F., 1995, "Full Coverage Effusion Film Cooling with Inclined Holes," ASME Paper No. 95-GT-274.
- [49] Sasaki, M., Takahara, K., Kumagai, T., and Hamano, M., 1979, "Film Cooling Effectiveness for Injection from Multirow Holes," *ASME Journal of Engineering for Power*, 101(1), pp. 101-108.

- [50] Lin, Y., Song, B., Li, B., and Liu, G., 2006, "Measured Film Cooling Effectiveness of Three Multihole Patterns," *ASME J. Heat Transfer*, 128(2), pp. 192-197.
- [51] Harrington, M. K., McWaters, M. A., Bogard, D. G., Lemmon, C. A., and Thole, K. A., 2001, "Full-Coverage Film Cooling with Short Normal Injection Holes," ASME Paper No. 2001-GT-0130.
- [52] Mayle, R. E. and Camarata, F. J., 1975, "Multihole Cooling Film Effectiveness and Heat Transfer," *ASME J. of Heat Transfer*, 97(4), pp. 534-538.
- [53] Morrison, G.L., and Tung, K., 1999, "Five-Hole Pitot Probe Reduction Technique and Measurement Uncertainty Analysis," ASME Paper No. FEDSM99-7155.
- [54] Zhou, D. and Wang, T., 1995, "Effects of Elevated Free-Stream Turbulence on Flow and Thermal Structures in Transitional Boundary Layers," *ASME J. Turbomachinery*, 117, pp.40-412.
- [55] Blair, M.F., and Bennet, J.C., 1984 "Hot-Wire Measurements of Velocity and Temperature Fluctuations in a Heated Turbulent Boundary Layer," ASME Paper No. 84-GT-234.
- [56] Adapted from <http://www.dantecdynamics.com/measurement-principles-of-lda>
- [57] Pietrzyk, J. R., Bogard, D. G., and Crawford, M. E., 1989, "Effects of Density Ratio on the Hydrodynamics of Film Cooling," ASME Paper No. 89-GT-175.
- [58] Thole, K., and Bogard, D.G., 1994, "Simultaneous Temperature and Velocity Measurements," *Measurement Science and Technology*, 5, pp.435-439.
- [59] ME 5338 Experimental Methods in Heat Transfer and Fluid Flow at Baylor University
- [60] Ekkad, S.V. and Han, J.C., 2000, "A Transient Liquid Crystal Thermography Technique for Gas Turbine Heat Transfer Measurements," *Measurement Science and Technology*, 11(7), pp. 957-968.
- [61] Kwak, J. S., and Han, J. C., 2003, "Heat transfer coefficient and film cooling effectiveness on a gas turbine blade tip", *ASME J. of Heat Transfer*, 125, pp. 494-502.
- [62] Ekkad, S. V., Ou, S., and Rivir, R. B., 2004, "A transient infrared thermography method for simultaneous film effectiveness and heat transfer coefficient measurements from a single test," *ASME J. Turbomachinery*, 126, 597-603.
- [63] Bogard, D. G. and Cutbrith, J. M., 2003, "Effects of coolant density ratio on film cooling performance on a vane," ASME Paper No. GT2003-38582.

- [64] Lui, T., Campbell, B.T., Burns, S.P., and Sullivan, J.P., 1997, "Temperature- and Pressure- Sensitive Luminescent Paints in Aerodynamics," *Applied Mechanics Review*, 50(4), pp. 227-246.
- [65] Kunze, M., Vogeler, K., Brown, G., Prakash, C., and Landis, K., 2009, "Aerodynamic and endwall film cooling investigations of a gas turbine nozzle guide vane applying temperature sensitive paint," ASME Paper No. GT-2009-59412.
- [66] Russin, R.A., Alfred D., and Wright L.M., 2009, "Measurement of Detailed Heat Transfer Coefficient and Film Cooling Effectiveness Distributions using PSP and TSP," ASME Paper No. GT2009-59975.
- [67] Goldstein, R. J. and Chen, H. P., 1985, "Film cooling on a gas turbine near the endwall," *ASME J. Engineering for Gas Turbines and Power*, 107, pp. 117-122.
- [68] Takeishi, K., Matsuura, M., Aoki, S., and Sato, T., 1990, "An experimental study of heat transfer and film cooling on low aspect ratio turbine nozzles," *ASME J. Turbomachinery*, 112, pp. 488-496.
- [69] Soechting, F.O., Landis, K.K., and Dobrowolski, R., 1987, "Development of Low-Cost Test Techniques for Advanced Film Cooling Technology." AIAA Paper No. AIAA-87-1913.
- [70] Friedrich, S., Hodson, H.P. and Dawes, W.N., 1996, "Distribution of Film-Cooling Effectiveness on a Turbine Endwall Measured Using the Ammonia and Diazo Technique." *ASME J. of Turbomachinery*, 118, pp. 613-612.
- [71] Zhang, L., Baltz, M. Padupatty, R., and Fox, M. 1999, "Turbine Nozzle Film Cooling Study Using the Pressure Sensitive Paint (PSP) Technique," ASME Paper No. 99-GT-196.
- [72] Gao, Z., Wright, L. M., and Han, J. C., 2005, "Assessment of Steady State PSP and Transient IR Measurement Techniques for Leading Edge Film Cooling," ASME Paper No. IMECE2005-80146
- [73] Ahn, J. Mhetras, S., and Han, J. C., 2004, "Film-Cooling Effectiveness on a Gas Turbine Blade Tip Using Pressure Sensitive Paint," ASME Paper No. GT2004-53429.
- [74] Ahn J., Schobeiri, M. T., Han J. C., and Moon, H. K., 2004, "Film Cooling Effectiveness on the Leading Edge of a Rotating Turbine Blade," ASME Paper No. IMECE2004-59852.
- [75] Ahn J., Schobeiri, M. T., Han J. C., and Moon, H. K., 2005, "Film Cooling Effectiveness on the Leading Edge of a Rotating Film-Cooled Blade Using Pressure Sensitive Paint," ASME Paper No. GT2005-68344.

- [76] Suryanarayanan, A., Mhetras, S. P., Schobeiri, M. T., and Han, J. C., 2006, "Film Cooling Effectiveness on a Rotating Blade Platform," ASME Paper No. GT2006-90034.
- [77] Wright, L.M., McClain, S.T., and Clemenson, M.D., 2011, "Effect of Density Ratio on Flat Plate Film Cooling with Shaped Holes using PSP," *ASME J. Turbomachinery*, 133(4).
- [78] Kline, S. J. and McClintock, F. A., 1953, "Describing Uncertainties in Single-Sample Experiments," *Mechanical Engineering*, 75(1), pp. 3–8.
- [79] Gogineni, S., Goss, L., Pestian, D., and Rivir, R., 1998, "Two-color Digital PIV Employing a single CCD Camera," *Experiments in Fluids*, 25, pp.320 – 328.
- [80] Wright, L.M., McClain, S.T., and Clemenson, M.D., 2010, "Effect of Freestream Turbulence Intensity on Film Cooling Jet Structure and Surface Effectiveness using PIV and PSP," ASME Paper No. GT2010-23054.
- [81] Schabacker, J., Boelcs, A., Johnson, V., 1998, "PIV Investigation of the Flow Characteristics in an Internal Coolant Passage with Two Ducts Connected by a Sharp 180 deg. Bend," ASME Paper No. 98-GT-544.
- [82] Brown, C.P., Wright, L.M., McClain, S.T., 2015, "Comparison of Staggered and In-Line V-Shaped Dimple Arrays Using S-PIV," ASME Paper No. GT2015-43499.
- [83] Jordan, C. N. and Wright, L. M., 2013, "Heat Transfer Enhancement in a Rectangular (AR = 3:1) Channel with V-Shaped Dimples," *ASME J. Turbomachinery*, 135(1), pp. 1-10.
- [84] Aga, V., Rose, M., and Abhari, R.S., 2008, "Experimental Flow Structure Investigation of Compound Angled Film Cooling," *ASME J. Turbomachinery*, 130.
- [85] Wieneke, B., 2015, "PIV uncertainty quantification from correlation statistics," *Meas. Sci. Technol.*, 26(074002), pp. 1-10.
- [86] Issakhanian, E., 2012, *3D Velocity and Scalar Field Measurements of Discrete Hole Film Cooling Flows*, Ph. D. thesis, Stanford Univ., Stanford, CA.
- [87] Bunker, R. S., 2000, "Effect of Partial Coating Blockage on Film Cooling Effectiveness," ASME Paper No. 2000-GT-0244.
- [88] Stimpson, C. K., Snyder, J. C., Thole, K. A., and Mongillo, D., 2015, "Roughness Effects on Flow and Heat Transfer for Additively Manufactured Channels," ASME Paper No. GT2015-43940.
- [89] Schmidt, D. L., Sen, B., and Bogard, D. G., 1996, "Effects of Surface Roughness on Film Cooling," , ASME Paper No. 96-GT-299.

- [90] Snyder, J. C., Stimpson, C. K., Thole, K. A., and Mongillo, D., 2015, "Build Direction Effects on Additively Manufactured Channels," ASME Paper No. GT2015-43935.
- [91] Watson, T., 2015, *Assessment of Shaped Film Cooling Holes at High Density Ratios for Gas Turbine Cooling Using S-PIV and PSP*, MS thesis, Baylor Univ., Waco, TX.